N°d'ordre NNT : 2016LYSEI115

THESE de DOCTORAT DE L'UNIVERSITE DE LYON
opérée au sein de
INSA

Ecole Doctorale N° 512
InfoMaths

Spécialité de doctorat :
Discipline : Informatique

Soutenue publiquement le 2/12/2016, par :
Ilia Prokin

Synaptic plasticity emerging from chemical reactions: modeling spike-timing dependent plasticity of basal ganglia neurons

---

Devant le jury composé de :

BESLON, Guillaume	Professeur des Universités	LIRIS, INSA-LYON	Président
KOTALESKI, Jeanette	Docteur, HDR	Institut royal de technologie	Rapporteure
TSANEVA-ATANASOVA, Krasimira	Docteur, HDR	Université d'Exeter	Rapporteure
BESLON, Guillaume	D.R.2	LIRIS, INSA-LYON	Examinateur
GRAUPNER, Michael	C.R.1	Université Paris Descartes	Examinateur
BERRY, Hugues	D.R.2	INRIA	Directeur de thèse

Département FEDORA – INSA Lyon - Ecoles Doctorales – Quinquennal 2016-2020

SIGLE	ECOLE DOCTORALE	NOM ET COORDONNEES DU RESPONSABLE
CHIMIE	**CHIMIE DE LYON** **http://www.edchimie-lyon.fr** Sec : Renée EL MELHEM Bat Blaise Pascal 3e etage secretariat@edchimie-lyon.fr Insa : R. GOURDON	M. Stéphane DANIELE Institut de Recherches sur la Catalyse et l'Environnement de Lyon IRCELYON-UMR 5256 Équipe CDFA 2 avenue Albert Einstein 69626 Villeurbanne cedex directeur@edchimie-lyon.fr
E.E.A.	**ELECTRONIQUE, ELECTROTECHNIQUE, AUTOMATIQUE** **http://edeea.ec-lyon.fr** Sec : M.C. HAVGOUDOUKIAN Ecole-Doctorale.eea@ec-lyon.fr	M. Gérard SCORLETTI Ecole Centrale de Lyon 36 avenue Guy de Collongue 69134 ECULLY Tél : 04.72.18 60.97 Fax : 04 78 43 37 17 Gerard.scorletti@ec-lyon.fr
E2M2	**EVOLUTION, ECOSYSTEME, MICROBIOLOGIE, MODELISATION** **http://e2m2.universite-lyon.fr** Sec : Safia AIT CHALAL Bat Darwin - UCB Lyon 1 04.72.43.28.91 Insa : H. CHARLES Safia.ait-chalal@univ-lyon1.fr	Mme Gudrun BORNETTE CNRS UMR 5023 LEHNA Université Claude Bernard Lyon 1 Bât Forel 43 bd du 11 novembre 1918 69622 VILLEURBANNE Cédex Tél : 06.07.53.89.13 e2m2@ univ-lyon1.fr
EDISS	**INTERDISCIPLINAIRE SCIENCES-SANTE** **http://www.ediss-lyon.fr** Sec : Safia AIT CHALAL Hôpital Louis Pradel - Bron 04 72 68 49 09 Insa : M. LAGARDE Safia.ait-chalal@univ-lyon1.fr	Mme Emmanuelle CANET-SOULAS INSERM U1060, CarMeN lab, Univ. Lyon 1 Bâtiment IMBL 11 avenue Jean Capelle INSA de Lyon 696621 Villeurbanne Tél : 04.72.68.49.09 Fax :04 72 68 49 16 Emmanuelle.canet@univ-lyon1.fr
INFOMATHS	**INFORMATIQUE ET MATHEMATIQUES** **http://infomaths.univ-lyon1.fr** Sec :Renée EL MELHEM Bat Blaise Pascal 3e etage infomaths@univ-lyon1.fr	Mme Sylvie CALABRETTO LIRIS – INSA de Lyon Bat Blaise Pascal 7 avenue Jean Capelle 69622 VILLEURBANNE Cedex Tél : 04.72. 43. 80. 46 Fax 04 72 43 16 87 Sylvie.calabretto@insa-lyon.fr
Matériaux	**MATERIAUX DE LYON** **http://ed34.universite-lyon.fr** Sec : M. LABOUNE PM : 71.70 –Fax : 87.12 Bat. Saint Exupéry Ed.materiaux@insa-lyon.fr	M. Jean-Yves BUFFIERE INSA de Lyon MATEIS Bâtiment Saint Exupéry 7 avenue Jean Capelle 69621 VILLEURBANNE Cedex Tél : 04.72.43 71.70 Fax 04 72 43 85 28 Ed.materiaux@insa-lyon.fr
MEGA	**MECANIQUE, ENERGETIQUE, GENIE CIVIL, ACOUSTIQUE** **http://mega.universite-lyon.fr** Sec : M. LABOUNE PM : 71.70 –Fax : 87.12 Bat. Saint Exupéry mega@insa-lyon.fr	M. Philippe BOISSE INSA de Lyon Laboratoire LAMCOS Bâtiment Jacquard 25 bis avenue Jean Capelle 69621 VILLEURBANNE Cedex Tél : 04.72 .43.71.70 Fax : 04 72 43 72 37 Philippe.boisse@insa-lyon.fr
ScSo	**ScSo*** **http://recherche.univ-lyon2.fr/scso/** Sec : Viviane POLSINELLI Brigitte DUBOIS Insa : J.Y. TOUSSAINT viviane.polsinelli@univ-lyon2.fr	Mme Isabelle VON BUELTZINGLOEWEN Université Lyon 2 86 rue Pasteur 69365 LYON Cedex 07 Tél : 04.78.77.23.86 Fax : 04.37.28.04.48

*ScSo : Histoire, Géographie, Aménagement, Urbanisme, Archéologie, Science politique, Sociologie, Anthropologie

Synaptic plasticity emerging from chemical reactions: modeling spike-timing dependent plasticity of basal ganglia neurons

Ilya Prokin

A thesis presented for the degree of
Doctor of Philosophy

Supervised by:
Dr. Hugues Berry

INRIA, Lyon, France
December 2016

Motivation

In XVIIth century, owing to major contributions of Isaac Newton, physics saw a huge leap toward quantification boosting its ongoing transition from the qualitative physics of Aristotle to quantitative physics as we know it today. In XXth-XXIst centuries, biology is striving to undergo a similar transformation. This time, however, the success of quantitative neurobiology might bring us not just the understanding of the fundamental forces of nature, but the understanding of the very foundation of the cognitive processes, by which, humans learn patterns and develop quantitative science itself. With the current state of knowledge, we already have strong ideas about the correlates of processes of learning and memory at the level of interacting brain cells. However, our understanding of these processes at the molecular level is still in its infancy. To contribute in filling this gap, in this thesis, we develop a molecular level mathematical model to study the cellular level basis of learning and memory: the process of synaptic plasticity, in which the efficiency of communication between neurons changes in response to a pattern of environmental conditions.

Abstract

Our brains support various forms of learning in their various subparts. This is for instance the case of the basal ganglia, a set of subcortical nuclei that is involved in action selection and a specific form of learning / memory, procedural memory (memory of skills or expertise). At the scale of single neurons, the most plausible support of learning and memory is synaptic plasticity, the process by which the efficiency of interneuronal communication changes in response to a pattern of environmental conditions. A recent focus of research is on spike-timing dependent plasticity (STDP), whereby the relative timing of activations (spikes) of connected pre- and postsynaptic neurons, determines the synaptic weight (the efficiency of synaptic connection). Notwithstanding, the dependence of STDP on underlying signaling pathways is not yet fully understood. To address this issue, we combine experimental approaches by our collaborators (pharmacology and electrophysiology) with modeling of the implicated signaling network (described by Ordinary-Differential Equations). After parameter estimation, the model reproduces much of experimental data, including the dependence of STDP on the number of paired stimuli of pre- and postsynaptic neurons and intensive pharmacological exploration (where signaling molecules are perturbed by chemicals). Furthermore, in opposition to what was widely believed in the neuroscience community, our model directly indicates that the endocannabinoid system supports bidirectional changes of the synaptic weight (increase and decrease). Moreover, we study how a range of factors including glutamate uptake regulates STDP. We expect our model to be a starting point to the elucidation of the regulation of learning and memory in the basal ganglia at the single neuron level.

Acknowledgements

Three years ago, I came to France to study the new topic in the new environment. I feel that my intellectual development during these years goes far beyond learning to be a scientist. Only one part of this development concluded in this thesis. Another, larger part reflected in the broader outlook and the range of skills and thinking tools that became an integral part of me. For both of these parts, I am thankful to many people.

My adviser, Hugues, gave me a lot of freedom and at the same time the essential feedback to refine my skills. Thanks to him, I took part in different projects of the lab and get exposed to a variety of scientific topics. As a child learns to read, write and talk to express simple ideas, a Ph.D. student learns to read and write scientific documents, and give scientific talks. Thanks to the feedback of Hugues, I grew from my scientific childhood into my scientific adolescence.

As it is always in science, this contribution is thanks to the work of many others. I am especially grateful to our experimental collaborators: Laurent Venance who was almost my second thesis adviser (not officially) and his Ph.D. student Silvana Valtcheva. Silvana explained me many nuances of experimental techniques, became a friend, and introduced me to diverse Parisian gastronomy. Thanks the project with them, I have greatly improved my knowledge of Experimental Neuroscience. Without this collaboration, the work of this thesis would not be possible. I am as well thankful to all scientists whose work I have used in this thesis, particularly to Nicolas Brunel and Kim Blackwell with whom I had fruitful discussions.

I am thankful to all senior members of the lab: Guillaume Beslon, Carole Knibbe, Christophe Rigotti, Jonathan Rouzaud-Cornabas, Hedi Soula, Eric Tanier for the scientific seminars and working environment enriched with the resources needed for an efficient number-crunching and comfortable lab life.

I am thankful to members of DRACULA and other teams with whom we sometimes shared lunchtime and had discussions. Unfortunately, I did not get to know all of you very well. Thanks to our cross-team seminars, I was exposed to a broad range of topics in Computational Biology. I am particularly thankful to Samuel Bernard with whom we worked together on a side project

and had many scientific meetings.

I am grateful to all the members of the Ph.D. committee for accepting invitations and for the great feedback during Q&A session following my Ph.D. defense presentation. Thanks to their careful reading of the manuscript and reporting all errors, the final version of this manuscript has been noticeably improved.

I am thankful to Maurizio De Pittá who taught me many practical aspects of scientific life, inspired me during hard times, and helped me to develop a sense for ideas and their presentation. I am thankful to Yulia Dembitskaya for sharing her experimental expertise and suggesting interesting ideas. Moreover, Yulia have been emotionally supporting me throughout these years and pushed me to become a better person.

I am thankful to other Ph.D. students and postdocs, with whom we shared office, large part of our time, and became friends. Thank you Alexandre Foncelle, Álvaro Mateos González and Sergio Peignier for your hospitality, humor and discussions on diverse topics. Thank you Sergio Peignier for lunchtime discussions on orthogonal scientific topics and your absurd-based sense of humor. Thank you Audrey Denizot and Priscila Biller for your funny attitude; thank you Priscila Biller for taking care of social life and commenting on my work. I am thankful to Charles Rocabert for political discussions and for his high motivation for organizing social events, to Jules Lallouette for helping me to navigate the environment during my first time in the lab, to Marine Jacquier for accepting my character, to Loic Barbarroux for the movies in "so bad that it is funny" genre, to Vincent Liard for discussions on variety of topics and for contributing to the improvement of my French. Moreover, thanks to the environment of Computer Science institute and facilitated by Anthony Rossi, I became a computer geek.

I am thankful to our lab assistant Caroline Lothe who was patiently walking me through the impassable jungle "de la bureaucratie Française".

Thank you all!

List of Publications

Publications

Cui, Y., **Prokin**, I., Xu, H., Delord, B., Genet, S., Venance, L., and Berry, H. (2016). "Endocannabinoid dynamics gate spike-timing dependent depression and potentiation". *eLife* 5, e13185.

Xu, H., Perez, S., Detraux, B., Cornil, A., **Prokin**, I., Cui, Y., Degos, B., Berry, H., Kerchove d'Exaerde, A. de, and Venance, L. (submitted, 2016). "Endocannabinoid-dopamine interactions mediate spike-timing dependent potentiation in the striatum". *Nature Communications*.

Communications

Prokin, I. (2015). "Mechanistic Modeling of Spike-Timing Dependent Plasticity of Basal Ganglia Neurons". University of Chicago, Chicago, United States of America. (**Talk**).

Prokin, I., Cui, Y., Valtcheva, S., Venance, L., and Berry, H. (2015). "Modeling spike-timing dependent plasticity of basal ganglia neurons and its bidirectional control by endocannabinoid signaling". *Advanced Lecture Course on Computational Systems Biology*. Aussois, France: (**Poster**).

Prokin, I., Valtcheva, S., Venance, L., and Berry, H. (2015). "Mechanistic Modeling of Spike-Timing Dependent Plasticity of Basal Ganglia Neurons". *Neuroscience 2015*. Chicago, United States of America: Society for Neuroscience. (**Poster**).

Table of Contents

Abbreviations

Abbreviation	Meaning
2-AG	2-arachidonoylglycerol
AC	adenylate cyclase
AEA	anandamide
AMPAR	α-amino-3-hydroxy-5-methyl-4-isoxazolepropionic acid receptor
AP	action potential
ARPP-21	cAMP-regulated phosphoprotein 21 kDa
BG	basal ganglia
CB1R	cannabinoid receptor type 1
CICR	calcium-induced calcium release
CaM	calcium/calmodulin complex
CaMKII	calcium/calmodulin-dependent protein kinase II
CaN	calcineurin
DAG	diacylglycerol
DAGLα	diacylglycerol lipase α
DHK	dihydrokainic acid
EPSC	excitatory postsynaptic current
EPSP	excitatory postsynaptic potential
ER	endoplasmatic reticulum
FS	fast-spiking
G-t-LTD	presynaptic $G_{i/o}$ and spike-timing dependent long-term depression
G-t-LTP	presynaptic $G_{i/o}$ and spike-timing dependent long-term potentiation
GABA	γ-aminobutyric acid
GPCR	G protein–coupled receptor
GPe	globus pallidus external segment
GPi	globus pallidus internal segment
HFS	low-frequency stimulation
HFS-LTD	HFS-induced long-term depression
I1	inhibitor 1
IP3	inositol (1,4,5)-triphosphate
IP3R	inositol (1,4,5)-triphosphate receptor
LFS	high-frequency stimulation
LFS-LTP	LFS-induced long-term potentiation
LTD	long-term depression
LTP	long-term potentiation
M1R	muscarinic receptors
MSN	medium-sized spiny neuron
NMDAR	N-methyl-D-aspartate receptor
NOS	(NO)-synthesizing
PIP2	phosphatidylinositol (4,5)-bisphosphate
PKA	protein kinase A
PLCβ	phospholipase Cβ
PP1	protein phosphatase 1
SERCA	sarco/endoplasmatic reticulum Ca2+-ATPase
SNc	substantia nigra *pars compacta*
SNr	substantia nigra *pars reticulata*
STDP	spike-timing dependent plasticity
STN	subthalamic nucleus
TRPV1	transient receptor potential vanilloid type-1
VSCC	voltage-sensitive calcium channels
bAP	back-propagating action potential
cAMP	cyclic adenosine monophosphate
eCB	endocannabinoid
mGluR	metabotropic glutamate receptor
t-LTD	timing-dependent long-term depression
t-LTP	timing-dependent long-term potentiation
DARPP-32	dopamine and cAMP-regulated phosphoprotein 32 kDA

Chapter 1

State of the art

1.1 Experimental investigation of synaptic plasticity

1.1.1 Background

Learning new skills and facts is an integral part of normal human experience. However, what represents learning and memory in the brain is an unsolved problem of neuroscience. From common sense perspective, one might think that, in order to learn a pattern such as "event A causes event B", a learner has to be repeatedly and persistently exposed to an environment with statistical regularities, where A occurs before and is correlated with B. At the end of the XIXth century, by repeatedly exposing dogs to an environment with artificial regularities, Ivan Pavlov managed to make them learn an association between salivation and a previous neutral sound stimulus. Half a century following Pavlov's work has brought new tools for questioning the mechanisms of learning at the level of brain biology. At the time of Pavlov's work, the invention of staining technique by Camillo Golgi allowed for visualization of structures in neural tissue under the microscope. Using this technique, Santiago Ramón y Cajal found that the neural tissue is organized as a complex net of discrete cells, the neurons. This discovery paved the way for the idea that networks of neurons, communicating with each other via synaptic connections support brain functions. In this framework, Cajal saw plasticity of neural networks as a basis for learning and behavioral plasticity. By the end of the first half of the XXth century, these ideas were converging into the vision of a central role for synaptic plasticity, the plasticity of synaptic connections between neurons. In his book "The organization of behavior" Donald Olding Hebb combined previous ideas by linking plasticity with learning and memory. He formulated a formal rule describing plasticity in his famous quote: "When an axon of cell A is near enough to excite B and repeatedly or persistently takes part in firing it, some growth process or metabolic change

takes place in one or both cells such that A's efficiency, as one of the cells firing B, is increased" (Hebb 1949). A more simplified expression of this idea is attributed to Carla Shatz: "cells that fire together, wire together" (Shatz 1992). This simple formulation however does not capture the idea of directionality that is present in Hebb's postulate; the idea that agrees well with modern understanding of unidirectional signal transmission at a chemical synapse (fig. 1.1).

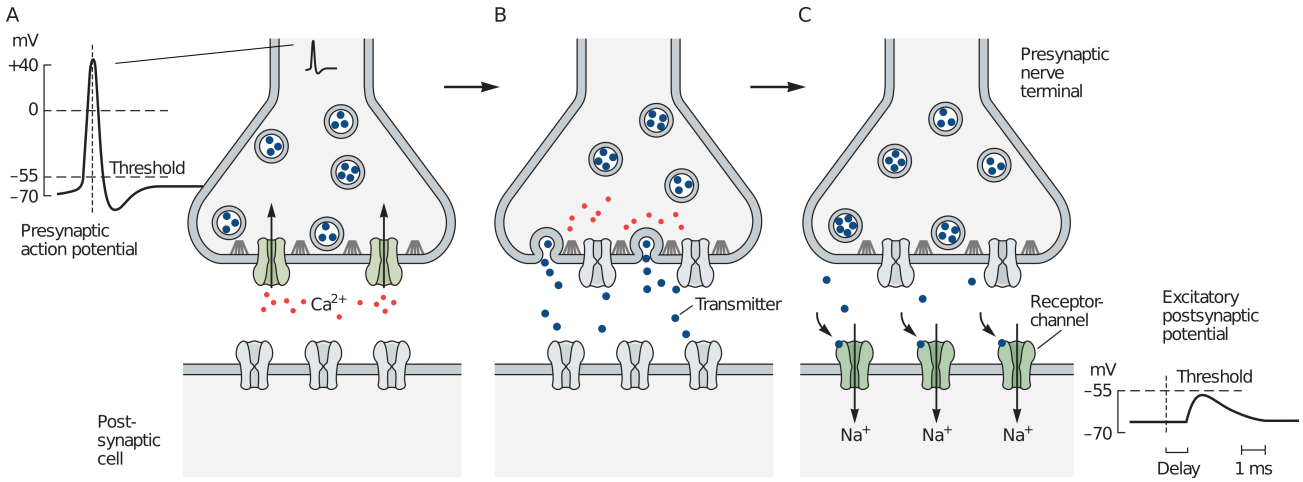

Figure 1.1: Synaptic transmission at chemical synapses involves several steps (see text for description). Modified from Kandel (2013).

The unidirectional signal transmission starts after the electrical activation of a presynaptic neuron (Hebb's cell A). The activation produces a spike of membrane potential, an action potential (AP) (fig. 1.1A). Next, AP propagates without attenuation along the neuron's axon. Upon its arrival at the axonal terminal of the presynaptic neuron, the AP activates voltage-sensitive Ca2+ (calcium) channels (VSCC) in cell's membrane thus allowing calcium to flow into the cell. The AP therefore leads to the release of signaling molecules, neurotransmitter, from the neuron's axonal terminal to the synaptic cleft (Kandel 2013) (fig. 1.1B), the small gap (20-40 nm wide) between the membrane of the presynaptic axon and that of a dendrite of the postsynaptic neuron. In the synaptic cleft, the neurotransmitter binds to receptors at the postsynaptic neuron (Hebb's cell B) (fig. 1.1C); the later leads to a transient postsynaptic current. In the case of excitatory neurotransmission, this current is called excitatory postsynaptic current (EPSC). The EPSC results in a transient increase (depolarization) of membrane potential called the excitatory postsynaptic potential (EPSP)(fig. 1.1C). The EPSP/EPSC further propagates with attenuation from the dendritic synaptic site of its generation toward the soma (the cell body) of the postsynaptic neuron. If many of these EPSPs reach the soma, sum up and their sum reaches a threshold value, a postsynaptic AP is generated. Because of this summation principle, the larger the amplitude of the EPSP at a synapse, the more it contributes to reaching the threshold of AP generation. The amplitude of an individual EPSP/EPSC therefore can be used as a measure of the efficiency of a synapse in triggering postsynaptic AP. The increase of EPSC/EPSP amplitude can be thought of as linked to Hebb's increase of A's efficiency in firing

B.

1.1.2 Classical synaptic plasticity: potentiation and depression

The increase (potentiation) of the amplitude of extracellularly measured EPSP, in response to brief electrical stimulation was known when Hebb published his book (Eccles and McIntyre 1953). Studying the spinal reflex system of cats, Eccles and McIntyre (1953) used 6000 electrical stimuli repeated at 400 Hz to induce the potentiation of electrical potential in response to the stimulation of a dorsal root. However, this type of plasticity persisted only on short time scales spanning from milliseconds to hundreds of seconds. It is problematic to have this short-term synaptic plasticity as a support for learning and memory since memory persists for hours, days, years or even decades. Almost two decades after Hebb's book was published, working with rabbit hippocampus, Bliss and Lømo discovered long-term potentiation (LTP), an increase of the amplitude of EPSPs in response to high-frequency stimulation (HFS, 15 Hz stimulation during 15 s). (fig. 1.2).

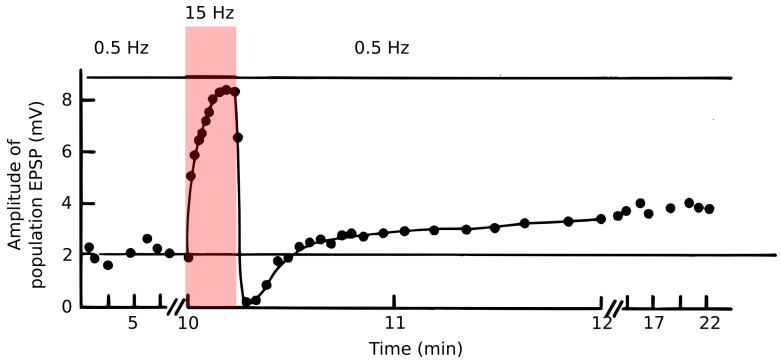

Figure 1.2: Long-term potentiation of population EPSP in respose to HFS (HFS-LTP). In the first 10 min of control recording, test stimuli are delivered at a low frequency of 0.5 Hz to measure the baseline EPSP amplitude. Starting from 10th minute, the HFS is delivered at 15 Hz for 15 s (red shading, total 225 stimuli). After the HFS, 0.5-Hz test stimuli are applied during 12 minutes to measure the amplitude of EPSP. Modified from T. Bliss and Lømo (1973)

This HFS-induced LTP (HFS-LTP) lasted for periods ranging from 30 min to 10 hours (T. Bliss and Lømo 1973). Using stimulation protocol similar to T. Bliss and Lømo (1973) to study plasticity in hippocampus, G. S. Lynch, T. Dunwiddie, and Gribkoff (1977) also found the potentiation of a neuronal input by HFS. G. S. Lynch, T. Dunwiddie, and Gribkoff (1977) studied HFS-induced plasticity in two separate input pathways to neurons of CA1 hippocampal region i.e. HFS was applied to either one of two different subsets of presynaptic neurons. After the application of HFS to the first pathway, the amplitude of potential was increased (LTP). In the second pathway to which HFS was not applied, the amplitude was persistently decreased (long-term depression, LTD). When HFS was instead applied to second pathway while the first

was not stimulated, LTP and LTD were reversed: LTP was observed in the second pathway, and LTD in the first (G. S. Lynch, T. Dunwiddie, and Gribkoff 1977) (fig. 1.3).

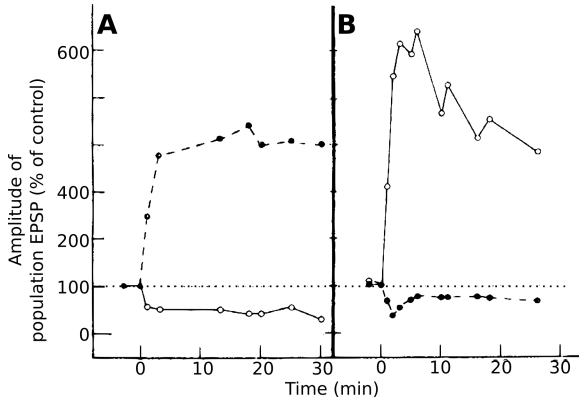

Figure 1.3: HFS results in HFS-LTP in stimulated pathway and LTD in the non-stimulated one; shown by the amplitude plot of the extracellularly measured population spike. Stimulation at 15 Hz during 15 s delivered to the Schaffer (**A**) or commissural (**B**) afferents at time 0. Schaffer responses indicated by solid circles and commissural responses by open circles. Modified from G. S. Lynch, T. Dunwiddie, and Gribkoff (1977)

The LTD persisted on the time scales comparable to LTP. The following year, studying dependence of synaptic responses on the frequency of electrical stimulation, Dunwiddie and Lynch (1978) found an experimental protocol reliably inducing LTD that has become the protocol of choice for the years to come. Low-frequency stimulation (LFS) at 1 Hz lasting for 100 s was reliably inducing LTD (LFS-LTD) in hippocampus. Using this protocol, Barrionuevo, Schottler, and G. Lynch (1980) demonstrated that sequential application of LFS and HFS to the same neuron resulted in a sequence of LFS-depression and HFS-LTP. LFS was reliably inducing LFS-depression (as in Dunwiddie and Lynch (1978)) and reversing the LTP previously induced by HFS (fig. 1.4). Note that depression induced in Barrionuevo, Schottler, and G. Lynch (1980) lasted only about 15 min (not a classical LTD). HFS and LFS differ in their contribution to the generation of postsynaptic APs. HFS generates many EPSPs at high-frequency, thus generates postsynaptic APs with high probability. HFS-LTP therefore is induced when postsynaptic APs are repeated following presynaptic APs. Conversely, LFS leads to rare EPSPs, thus rare postsynaptic APs. Therefore, LFS-LTD is induced when the postsynaptic APs are not correlated with presynaptic ones. The studies discussed above therefore showed that a pathway actively contributing to the activation of postsynaptic cell can be potentiated, in agreement with Hebb's suggestion. Moreover, extending Hebb's vision of plasticity, these studies have also suggested that the potentiation might be reversed or even replaced by depression if the pathway's contribution becomes weak. Synaptic plasticity therefore allows for the bidirectinal modification of synapses. To account for this bidirectionality, Hebb's rule has to be updated. For this purpose, together with Hebb's original formulation, one needs to consider the complementary plasticity rule of Stent (1973): "When the presynaptic axon of cell A repeatedly and persistently fails to excite the postsynaptic cell B while cell B is firing under the influence of other presynaptic axons, metabolic change takes

place in one or both cells such that A's efficiency, as one of the cells firing B, is decreased" (Stent 1973).

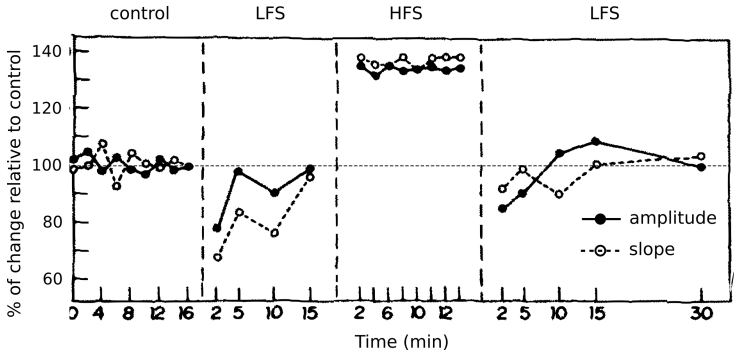

Figure 1.4: Bidirectional plasticity of hippocampal neurons: LFS induces LTD and reverses HFS-induced LTP. Population dendritic responses (extracellularly recorded potentials from the same dendritic zone) are shown for four successive periods (from left to right): control, the period following LFS, the period following subsequent HFS, the period following subsequent LFS. Modified from Barrionuevo, Schottler, and G. Lynch (1980)

1.1.3 Is plasticity necessary and sufficient for learning *in vivo*?

A causal link between synaptic plasticity and learning and memory has been long hypothesized. However, until recently, experimental studies suggesting that synaptic plasticity is implicated in learning and memory did not provide sufficient evidence. Both synaptic plasticity and learning can be affected pharmacologically (see e.g. RG Morris 1989), however, the limitation of the method does not allow precisely targeting a subnet of neurons involved in a particular memory episode. Instead, spatial localization of targeted neurons is imprecisely determined and the pharmacological intervention might have a broad range of unintended effects. Therefore, it is hard to prove that the observed correlation between learning and plasticity reflects causal relationship. Another technique to affect plasticity by using genetically modified organisms (see e.g. Tsien, Huerta, and Tonegawa 1996) suffers similar problems. Even when the spatial localization of affected cells is more or less known, genetic modification might have very broad effects as a result of the activation of compensatory mechanisms during development or during the time following the injection of a virus. Studies utilizing these two approaches found many correlational evidence linking the impairment/enhancement of learning and synaptic plasticity (Martin and R.G.M. Morris 2002). Using multielectrode recording from the hippocampus of behaving rat, Whitlock (2006) found that HFS induces less LTP if LTP was previously induced by learning. However, it is impossible to have a final conclusion based on this data. To finally prove the old idea of the causal link between synaptic plasticity and memory, new more precise experimental techniques might be needed (Neves, Cooke, and T. V. Bliss 2008).

Owing to recently developed experimental approaches such as optogenetics, a more direct support

for the idea became available. Nabavi et al. (2014) used fear conditioning to test the relation between learning and LTD/LTP. They first trained animals to press lever for a reward. Pairing a conditioned stimulus, CS, (here an optogenetic stimulation) with an aversive unconditioned stimuli, US, (electrical shock) resulted in the decrease of lever pressing activity (Fig. 1.5A). Therefore the decrease of lever pressing activity can be considered a conditioned response (CR) to the CS-US pairing. The authors then checked that CS-US pairings indeed gave rise to LTP in the amygdala (both *in vitro* and *in vivo*). Finally, to test how this LTP observed after CS-US learning relates to LFS-LTD and HFS-LTP, they applied in sequence optical stimulation mimicking LFS and HFS protocols to a trained animal. Application of LFS made the animal "forget" the CS-US learned (Fig. 1.5B), whereas subsequent application of HFS restored learned response. The explanation for this can be that LFS induces LTD that cancels LTP induced by learning, whereas HFS induces LTP that restores the LTP removed by LFS. Therefore, Nabavi et al. (2014) provides a strong support for the idea that the LTP and LTD protocols used in vitro indeed support behaviorally-significant learning mechanisms in vivo.

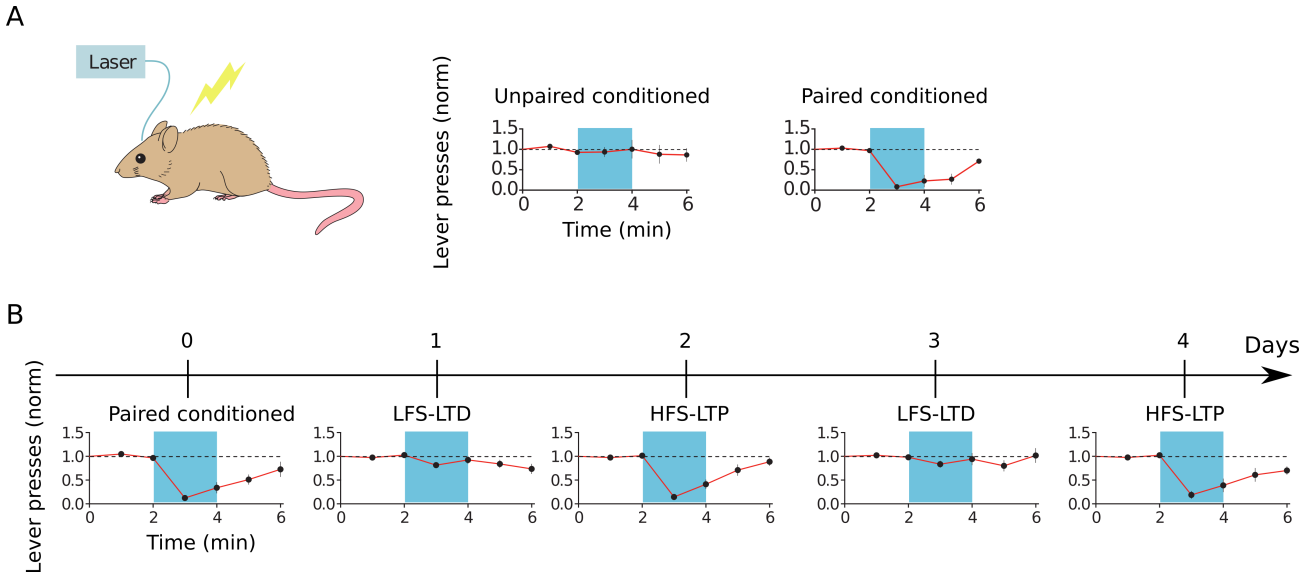

Figure 1.5: *in vivo* experiments; Fear conditioning with optogenetics (see text for details). Modified from Nabavi et al. (2014).

1.1.4 Calcium: a molecule of plasticity

In 1989, based on theoretical considerations, John Lisman (1989) has proposed the idea that bidirectional plasticity (LTD and LTP) can be controlled by the same molecule, calcium. Specifically, the baseline concentration of intracellular calcium corresponds to no plasticity, a high elevation of calcium was thought to cause LTP (Hebb in the words of Lisman), whereas a medium calcium elevation was thought to cause LTD (anti-Hebb in John Lisman (1989)). This calcium control hypothesis of synaptic plasticity was then studied experimentally. Cho et al. (2001) tested this hypothesis using LFS stimulation protocol (200 stimuli at 1 Hz) applied to neurons of perirhinal cortex in slices of rat brain. Their LFS induced LTD when the resting potential of the postsynaptic neuron was from -70 to -40 mV. However, when the resting potential was fixed to -10 mV, this same LFS protocol induced LTP. Using this LFS with -10 mV resting potential, they controlled stimulation-dependent increases of calcium by varying the concentration of intracellular calcium buffer (fig. 1.6). Their results agreed with the prediction of calcium control hypothesis. Indeed, at high concentrations of intracellular calcium buffer, when the concentration of calcium was low, no plasticity was induced. When buffer concentration was decreased that is when calcium concentration was increased to intermediate values, LTD was induced. When buffer concentration was low, calcium concentration was high and LTP was induced. Other groups found experimental support for the calcium control hypothesis using other techniques and plasticity induction paradigms. Cormier, Greenwood, and Connor (2001) used glutamate iontophoresis to directly induce calcium transients in neurons in slices of hippocampal CA1 region. Measuring these transients with calcium optical imaging, they found a relationship between the peak dendritic calcium concentration and synaptic plasticity that agrees with calcium control hypothesis.

To allow the local control of plasticity at synaptic sites at dendritic spines, it is the local calcium concentration in the spines that should be considered in the hypothesis. However, in the studies in support of the calcium control hypothesis, calcium concentration was manipulated more globally: either at the level of a cell, or at the level of dendrites. At this scale, many of the local calcium transients are integrated so that the contributions from single spines overlap and smooth away. In a very recent study, using new plasticity induction paradigm (STDP-like paradigm, see sec. 1.1.6), Tigaret et al. (2016) tested the calcium control hypothesis at the level of single dendritic spines. They found no correlation between the amplitude and integral of calcium transients in spines and the outcome of plasticity. However, they, as well as many others before, have confirmed the involvement of subcellular components linking calcium to plasticity (more about it in the following section, sec. 1.1.5). Therefore, these results do not allow to dismiss the hypothesis. One possible explanation for the absence of correlation between spine calcium concentration and plasticity is that calcium concentration determines plasticity when LFS/HFS

are applied, but not for STDP-like protocols; another explanation is suggested by the possibility of micro- or nano-domains of different calcium concentration inside the single spine (e.g. Higley and Bernardo L. Sabatini 2008; Griffith, Tsaneva-Atanasova, and Mellor 2016). The recent theoretical study of Griffith, Tsaneva-Atanasova, and Mellor (2016) suggests that the change of calcium can be localized to subvolumes around calcium sources without propagating far into the volume of spine. Calcium contained in these local subvolumes, nanodomains, could be actually correlated with plasticity, but not the calcium in the whole spine volume (spine-averaged calcium).

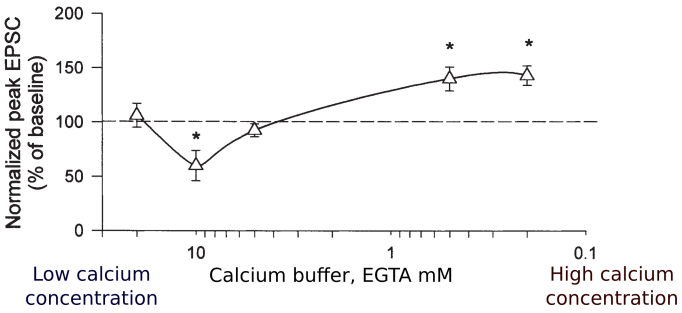

Figure 1.6: Depending on the intracellular calcium concentration: no change, LTD, or LTP can be induced by LFS delivered to the neuron with resting potential -10 mV. *Significant difference from baseline ($p < 0.05$). Modified from Cho et al. (2001).

1.1.5 Plasticity induced by activation timing patterns

The core of both Pavlovian learning and Hebbian learning is the association of coincident events: conditional and unconditional stimuli, and firing of two connected cells respectively. Surprisingly, the question of whether a specific timing between these coincident events is required for plasticity induction was not specifically addressed by the early studies of plasticity. This question had to wait until the 1990s (Debanne, Gahwiler, and Thompson 1994; Markram et al. 1997; Bell et al. 1997; Bi and Poo 1998). To implement Hebbian learning with the association of coincidently active cells, a biological system has to (i) somehow detect coincident events, (ii) communicate coincidence signal to the machinery controlling plasticity at an appropriate synaptic site. These two requirements might seem problematic to satisfy if one considers spatial aspects of unidirectional neuronal signal transmission. The synapses of a neuron are located on its dendrites at sites often distal from the soma. The activation of a single synapse leads to a small postsynaptic current that attenuates while propagating to the soma. To activate a neuron, many of these currents must reach the soma, sum up at the axonal hillock and cross the threshold of AP generation. Therefore the initiation of a postsynaptic AP following presynaptic AP is caused by the total current resulting from delayed summation of many postsynaptic currents. When a postsynaptic AP is initiated, which synapses should be given credit for contributing and

potentiated? If the machinery responsible for synaptic plasticity is localized at the synaptic site, how can it be informed about presynaptic AP's success in evoking postsynaptic AP? In 1997, studying cells from two different brain regions, hippocampus and neocortex, two groups have published similar results suggesting the existence of a signal that communicates the somatic occurrence of the postsynaptic AP back to the synaptic site (Magee and Johnston 1997; Markram et al. 1997). At the time, it was known that action potential not only propagates along the axon without attenuation, but also propagates back into dendrites with attenuation (Kandel 2013). Experimentally, therefore, AP induction at the soma might trigger these back-propagating action potentials (bAPs). Somatic AP can be induced using patch-clamp, whereby a glass micro-pipette with micro-electrode inside is attached to the cell membrane. With patch-clamp, one can inject step-like electrical currents into the cell soma; injected current forces triggering of an AP in the soma; this AP can then back-propagate from the soma into the dendrite. Pairing such bAPs induced by somatic current injection, with coinciding EPSPs triggered by presynaptic activation, resulted in strong calcium influx close to the site of stimulated synapse in slices of rat hippocampus (Magee and Johnston 1997). Both Magee and Johnston (1997) and Markram et al. (1997) found that repeated pairings of postsynaptic bAPs and presynaptically-triggered EPSPs were capable of inducing LTP. Magee and Johnston (1997) found that this LTP depended on intracellular calcium: indeed, LTP was precluded by the pharmacological blockade of two types of calcium channels, VSCC and N-methyl-D-aspartate receptors (NMDARs). NMDARs involvement is worth a notice because of their role in excitatory neurotransmission and peculiar permeability properties. NMDAR together with AMPAR, are synaptic receptors necessary for the major type of excitatory neurotranmission, the glutamatergic neurotransmission. While binding of glutamate is sufficient for AMPAR to become permeable to the influx of ions, NMDAR activation requires more complex conditions. As AMPAR, NMDAR is a channel with a pore gated by glutamate. However, NMDAR pore is blocked in normal conditions by extracellular Mg^{2+} ion (Hille 1992). This Mg^{2+} block of NMDAR is voltage-dependent and can be removed by the depolarization of the postsynaptic membrane potential. Therefore, NMDARs are open when two conditions are satisfied at the same time: i) glutamate is bound to them and ii) cell is depolarized. These properties endow NMDAR with characteristics of the detector of coincidence between postsynaptic depolarization resulting from AP back-propagation, and binding of glutamate resulting from the arrival of presynaptic AP. Magee and Johnston (1997) have confirmed the importance of bAP by demonstrating that the pairing of presynaptic AP with non back-propagating AP is ineffective in inducing LTP. Markram et al. (1997) tested the effects of the time order of coincident EPSPs and APs on synaptic plasticity. In this study, somatic current injection was used to induce 10-15 trains of 5 APs at 10 Hz separated by 4 s; trains were simultaneously induced in two mutually connected cells. (fig. 1.7). Importantly, each AP train in the first cell was triggered 10 ms before the AP train in the second.

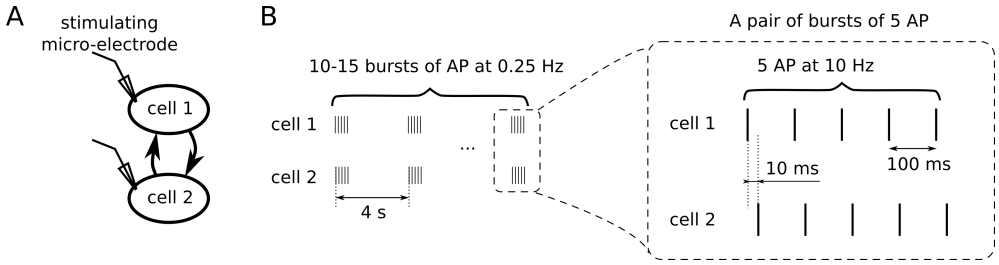

Figure 1.7: Schematic illustration of stimulation protocol of Markram et al. (1997). **A**. Two bidirectionally connected cells were stimulated with intracellular electrodes. **B**. AP-trigering stimuli were delivered to both cells in short bursts of 5 stimili. These bursts were repeated 10-15 times at 0.25 Hz (with 4 s period). Stimulation of cell 2 was 10-ms delayed relatively to cell 1 (zoomed).

Because these two cells were mutually connected, this protocol led to an opposite order of EPSPs and APs in two cells: an AP triggered in the soma of cell 2 systematically occured 10 ms after cell 1 triggered an AP, whereas conversely, each AP in cell 1 was followed after 10 ms by an AP in cell 2 (fig. 1.8A). The repetition of these trains 10 to 15 times every 4 s (thus a total of 50 to 75 AP), led to LTP in the second cell where EPSP-AP delay was 10 ms, and to long-term depression (LTD) of EPSP amplitude in the first cell where EPSP-AP delay was -10 ms (fig. 1.8B). When experiment was repeated with a 100 ms delay instead of 10 ms, no plasticity was induced (fig. 1.8B). By demonstrating the importance of the timing of EPSP-AP coincidence for plasticity, this study supported the hypothesis that bAP might be a coincidence signal for Hebbian plasticity. The LTP they observed was considered Hebbian in the sense of a quasi-causal order of pre- and postsynaptic activations. According to Hebb's vision, a synapse is potentiated if the presynaptic neuron persistently contributes to activation of the postsynaptic one. In the experimental setting of Markram et al. (1997), the presynaptic stimulation alone produces EPSP that is not sufficient for activating postsynaptic neuron. Instead, the postsynaptic neuron is forced to generate AP by somatic current injection. This stimulation however simulates Hebbian causal relationship between pre- and postsynaptic APs by forcing postsynaptic AP shortly after presynaptic AP (and therefore EPSP). Moreover, the results of Markram et al. (1997) contributed to the extension of the Hebb's vision of plasticity by revealing LTD at reversed coincidence timings (as it was earlier proposed by Stent (1973)) and quantifying coincidence timing.

1.1.6 Spike-timing dependent synaptic plasticity (STDP)

Only one year after Markram et al. (1997), Bi and Poo have published a study questioning how a broader range of the coincidence timings affects plasticity (Bi and Poo 1998). To induce synaptic plasticity in cultures of dissociated rat hippocampal neurons, Bi and Poo (1998) used an experimental protocol that was more similar to Markram et al. (1997), than to traditional HFS.

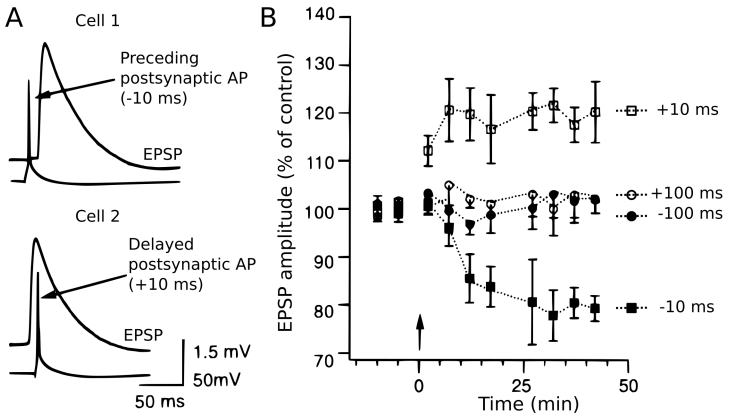

Figure 1.8: **A**. Coincidence interval. A 10-Hz train of 5 APs in cell 1 (only the first AP is shown) was shifted by 10 ms in cell 2. An AP was thus triggered in cell 1 10 ms before an AP in cell 2 in a bidirectionally connected pair of neurons. This resulted in the postsynaptic APs occurring about 10 ms before the onset of the EPSP in cell 1 [solid squares in B] and about 10 ms after the onset of EPSPs in cell 2 [open squares in B]. **B**. Interaction and coincidence intervals. Coincidence interval is represented by data from six bidirectionally coupled neurons. The data when EPSPs and postsynaptic APs were 100 ms apart are also represented. Modified from Markram et al. (1997)

Unlike HFS, their protocol comprised very mild stimulation; current pulses were somatically injected at a low frequency of 1 Hz (compared to the 15 Hz stimulation of T. Bliss and Lømo (1973)). Like in Markram et al. (1997), postsynaptic and presynaptic stimuli were paired with a fixed time-delay between them (spike-timing). The stimulation however was even milder than in Markram et al. (1997); instead of repeating bursts of EPSP-AP pairs, single pairs of EPSP-AP were periodically repeated (see explanation under fig. 1.9).

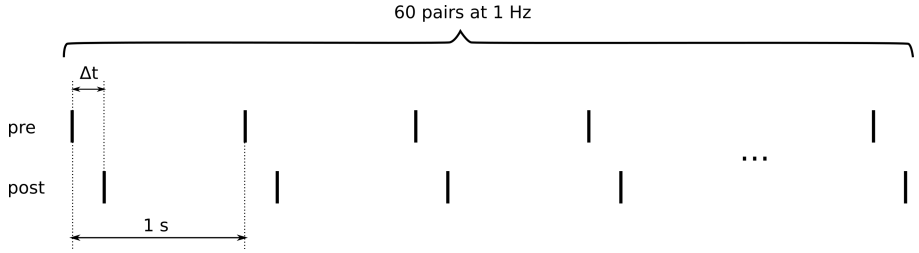

Figure 1.9: Schematic illustration of the stimulation protocol of Bi and Poo (1998). A synapse is activated by stimulation of the presynaptic neuron. With a short delay Δt, postsynaptic neuron is stimulated. This paired stimulation of pre- and postsynaptic neurons is repeated each 1 s (at 1 Hz) for 60 times.

With 60 EPSP-AP pairings delivered at 1 Hz, they were able to induce long-term bidirectional plasticity (both LTP and LTD). The direction of plasticity, LTP or LTD, depended on the sign of the time delay $\Delta t = t_{bAP} - t_{EPSP}$ between EPSP and AP (fig. 1.10 inset shows one EPSP-AP pair with positive and another one with negative delay). To reflect the dependence of induced by this protocol LTD and LTP on timing, I will further refer to them as t-LTD and t-LTP (timing-dependent LTD and LTP) to stress the difference with the timing-independent plasticity induced by other protocols such as HFS-LTP and LFS-LTD. Before the application of the plasticity induction protocol, presynaptic-only test stimuli were applied for 10-30 min at

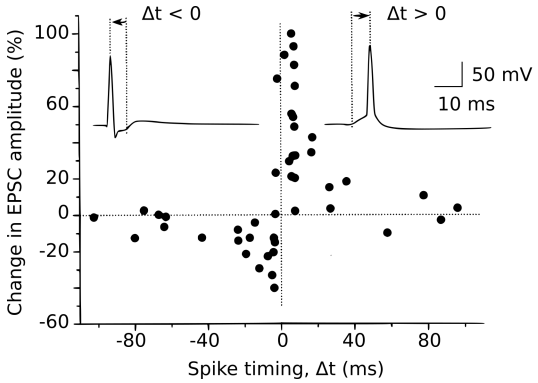

Figure 1.10: Critical window for the induction of synaptic potentiation and depression. The percentage change of the EPSC amplitude 20–30 min after the stimulation protocol (60 stimuli at 1 Hz) is plotted against spike-timing. Spike-timing defined by the time interval (Δt) between the onset of the presynptically triggered EPSP and the peak of the postsynaptic AP during each cycle of repetitive stimulation, as illustrated by the traces above. Modified from Bi and Poo (1998).

a low frequency of 0.03–0.06 Hz to evaluate the baseline value of EPSC amplitude. Baseline evaluation was followed by the induction protocol: 1 min of 60 1-Hz pairings. Next, for another 20-30 min, test stimuli were delivered again to evaluate the resulting change of EPSC amplitude. During this period EPSC amplitudes were gradually increasing or decreasing, and reaching stable values by the end of the period. Therefore, this induction protocol triggered a progressive change in the EPSC amplitude, that reached stable values 20-30 min after the protocol. To quantify plasticity, the difference between average EPSC amplitude at the end and at the beginning of the experiment (before and after plasticity inducing protocol) was divided by the average EPSC amplitude at the beginning. Fig. 1.10 shows the dependence of on spike-timing (Δt). Similarly to Markram et al. (1997), t-LTD was observed for small negative spike-timing (-60<Δt<0 ms), t-LTP was observed for small positive spike-timing (0<Δt<40 ms), while large spike-timing led to no plasticity. Obtaining the data-points for this figure involved a lot of work for Bi and Poo (1998). First, they had to find a pair of connected cells. Many cells have to be discarded as they often die during stimulation and search for a pair of cells has to be repeated. One successful pair of cells that survived an hour-long stimulation gives only one point of the fig. 1.10, since the whole protocol is too long to be applied twice in sequence to the same pair of cells. This hard work turned out fruitful and their results greatly influenced further studies of synaptic plasticity; their experimental protocol became wide-spread for inducing what we now refer to as spike-timing dependent plasticity (STDP). They have moreover given some insight on which subcellular components plasticity relies. In their culture of hippocampal neurons, different sources of calcium were found differently affecting plasticity. When L-type voltage-sensitive calcium channels (L-type VSCC), were blocked pharmacologically, t-LTD at negative Δt was replaced by no plasticity, while t-LTP at postitve Δt was not affected. When NMDARs were blocked, both t-LTD and t-LTP were replaced by no plasticity. t-LTD therefore was VSCC-dependent while t-LTP was both NMDAR- and VSCC-dependent. It is fair to call

the stimulation protocol of Bi and Poo (1998) classical for STDP induction as most of the subsequent STDP studies used it with minor modifications. Typically, across various studies of STDP in different brain regions, only the details of Δt definition are varied; less frequently the number of pairings is varied. The classical STDP protocol of Bi and Poo however could be characterized by three parameters: the timing of AP relatively to EPSP (Δt), the number of pairings, and the frequency of pairing. Following Bi and Poo (1998), up to now, most of STDP studies were concerned about the dependence of plasticity on Δt only. The first glimpse of the dependence of STDP on another parameter of the protocol, frequency, was contained in the early study of Markram et al. (1997). Since then, to our knowledge, no more than three experimental studies on the frequency-dependence of STDP have been published (Markram et al. 1997; P. Sjostrom, G. Turrigiano, and S. Nelson 2001; S. B. Nelson, P. J. Sjostrom, and G. G. Turrigiano 2002). Markram et al. (1997) found that the magnitude of LTP increases with the increase of frequency of the EPSP-AP pairs in slices of rat neocortex. This dependence was further studied by P. Sjostrom, G. Turrigiano, and S. Nelson (2001). Using patch-clamp recordings from thick, tufted L5 (layer 5) neurons in rat visual cortex, P. Sjostrom, G. Turrigiano, and S. Nelson (2001) have characterized the dependence of plasticity on the frequency of pairings (fig. 1.11).

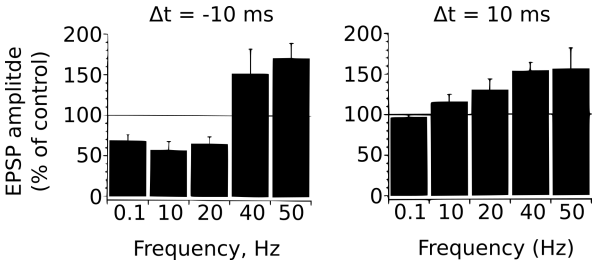

Figure 1.11: The dependence of STDP on the frequency of pairings for $\Delta t = \pm 10$. Modified from P. Sjostrom, G. Turrigiano, and S. Nelson (2001).

They found that the t-LTD at negative spike-timing (Δt = -10 ms) was not dependent on frequency up to 40 Hz. Since at 40 Hz $\Delta t = \pm 10$ ms becomes comparable to the period of pairings, Δt defined as delay between post- and pre-stimuli is no longer equal to spike-timing (defined as delay of a post- relatively to *the nearest* presynaptic stimulus) (for illustration, see fig. 1.12). Therefore, the results at short Δt at 40 Hz should be interpreted with care. For the positive spike-timing, $\Delta t = 10$ ms, the magnitude of t-LTP was found to increase with the increase of frequency from 10 to 40 Hz (similarly to Markram et al. (1997)). Moreover, the change of frequency affected the range of Δt for which t-LTP and t-LTD are induced (fig. 1.13). At frequency 0.1 to 20 Hz, t-LTD was dominant over t-LTP across all examined Δt; whereas only t-LTP or no plasticity were present at high frequencies (40 and 50 Hz). With the increase of frequency from 0.1 to 50 Hz the range of Δt of t-LTD first increased, then decreased, and then t-LTD was completely superseded by t-LTP owing to the expanding range of t-LTP. Therefore,

the main conclusion from P. Sjostrom, G. Turrigiano, and S. Nelson (2001) is that the presence across spike-timings of t-LTP and its amplitude at a given spike-timing increases with frequency, whereas t-LTD is much less affected and tend to be superseded by t-LTP when frequency is increased.

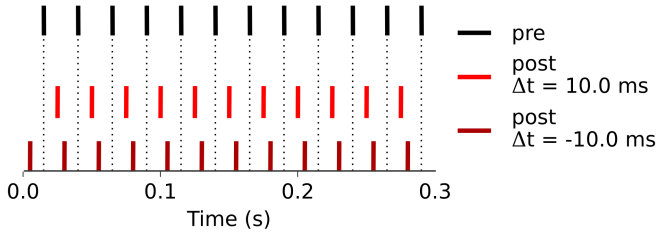

Figure 1.12: Explanation of the loss of timing-dependence at a high-frequency in the protocol of P. Sjostrom, G. Turrigiano, and S. Nelson (2001). At 40 Hz, the period is 25 ms. $\Delta t = \pm$ 10 ms falls roughly in the middle of the period. In these conditions, timing between two nearest post- and presynaptic stimili is ambiguous and no longer defined by Δt

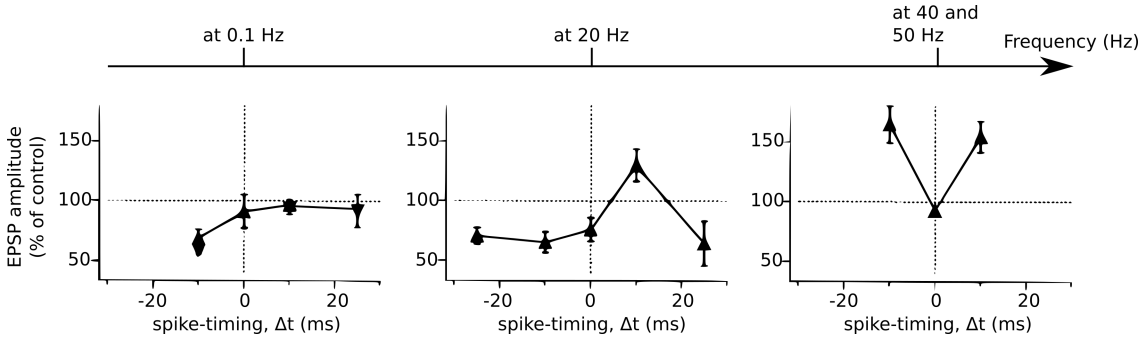

Figure 1.13: The dependence of STDP on both the frequency of pairings and spike-timing. Modified from P. Sjostrom, G. Turrigiano, and S. Nelson (2001). The range of Δt at which t-LTP is present expands with the increase of frequency, whereas t-LTD does not change much. At 40-50 Hz, t-LTP comletely superseeds t-LTD.

1.1.6.1 Diversity of STDP

One year before the seminal study of hippocampal STDP in rats by Bi and Poo (1998), a similarly extensive exploration of timing-dependence of plasticity was carried out in slices of cerebellum-like structure of the electric fish *Gnathonemus petersii* (Bell et al. 1997). Pairing extracellular pre- and delayed intracellular postsynaptic stimulation (360 pre-post pairings at 1 Hz), Bell et al. (1997) found plasticity dependence on timing inversed compared to the one found by Bi and Poo (1998). At negative timings, instead of t-LTD, t-LTP was observed. At positive timings, instead of t-LTP, t-LTD was observed. Being the reverse of Hebbian STDP of Bi and Poo (1998) this plasticity can be called anti-Hebbian. Following studies of STDP in various brain regions and across various experimental conditions revealed that the dependence of STDP on timing (STDP curves) is actually very variable (for review, see Larry F Abbott

and Sacha B Nelson 2000; Caporale and Dan 2008). Fig. 1.14 summarizes the variety of STDP curves across studies.

The STDP can vary even in the same brain region and in the same type of synapses dependent on the stimulation protocol. The classical hippocampal Hebbian STDP of Bi and Poo (1998), that was observed for synapses from excitatory neurons to excitatory neurons is induced by 60 1-Hz pairings of one pre- with one postsynaptic stimuli (fig. 1.14A1). However, the pairing of one presynaptic stimuli with two postsynaptic repeated 70–100 times at 5 Hz induces a plasticity that is noticeably different; it comprises second LTD window at $\Delta t > 0$ (fig. 1.14A2) (Wittenberg and S. S.-. H. Wang 2006).

The STDP observed at synapses from excitatory neurons to inhibitory neurons is in the sharpest contrast to classical STDP (compare fig. 1.14A1 to fig. 1.14B). The difference with classical Hebbian STDP is the most pronounced in the case of anti-Hebbian STDP in cerebellum-like structure that is inversed compared to classical STDP (fig. 1.14B1) (Bell et al. 1997).

For synapses from inhibitory to excitatory neurons, an inhibitory neurotransmitter leads to transient inhibitory postsynaptic current (IPSC); this current leads to a transient decrease of membrane potential (hyperpolarization), an inhibitory postsynaptic potential (IPSP). Because there is no EPSP/EPSC for inhibitory synapses, the plasticity was evaluated by the change of the amplitude of IPSC/IPSP (instead of EPSC/EPSP amplitude). With this, Hebbian STDP with very narrow range of spike-timings (compared to classical STDP) was observed in entorhinal cortex (fig. 1.14C1) (Haas, Nowotny, and Abarbanel 2006). However, in the hippocampus, the STDP for this type of synapses was significantly different: the STDP curve was symmetrical relatively to spike-timing with LTP at small timings at two LTD windows at sides of LTP (fig. 1.14C2).

How can we explain the diversity of STDP? First possibility can be that different signaling pathways are activated in different experimental conditions (including different stimulation conditions). With this, the difference of activated signaling pathways across conditions determines the difference of STDP curves. Second possibility could be that the molecular mechanism of plasticity is the same in all cases, that is the same signaling pathways are differently activated in different conditions; this different activation then leads to different STDP curves. If this explanation is valid then a unified description of various forms of STDP can be developed based on the essential features of the plasticity mechanism. Deciding between these two hypotheses is the central question of this thesis; the present work favors the second possibility and a unified description of plasticity.

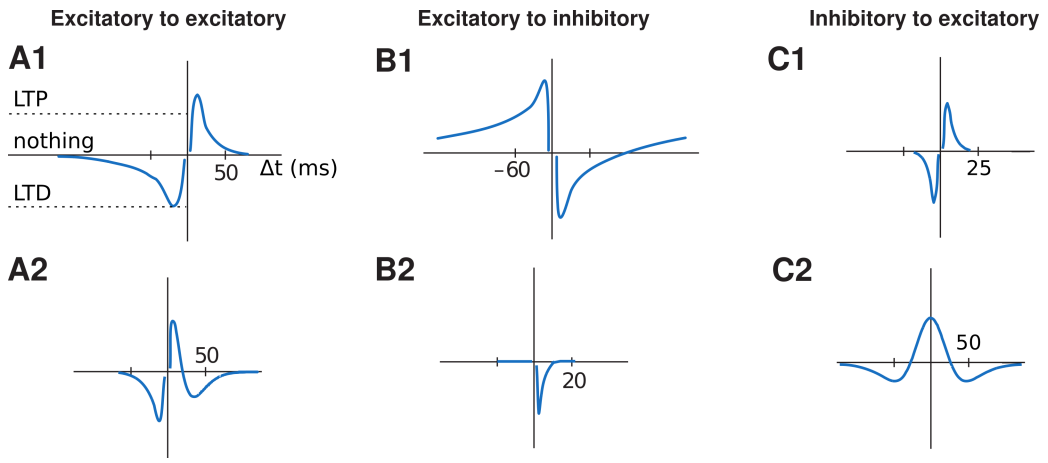

Figure 1.14: Diversity of temporal windows for STDP induction. **A**. Windows for excitatory to excitatory connections. **A1**. in hippocampus: Bi and Poo (1998), Zhang et al. (1998). in dorsal cochlear nucleus: Tzounopoulos et al. (2004). **A2**. in hippocampus: Wittenberg and S. S.-. H. Wang (2006). **B**. Windows for excitatory to inhibitory connections. **B1**. in cerebellum-like structure Bell et al. (1997). **B2**. in dorsal cochlear nucleus: Tzounopoulos et al. (2004). **C**. Windows for inhibitory to excitatory connections. **C1**. in entorhinal cortex: Haas, Nowotny, and Abarbanel (2006). **C2**. in hippocampus: Woodin, Ganguly, and Poo (2003). Temporal axis is in milliseconds. Modified from Caporale and Dan (2008).

1.1.6.2 Evidence of STDP *in vivo*

The first studies of STDP were done *in vitro*, in brain slices or cultures of neurons. However, if STDP is really to be considered not just an artifact of an experimental preparation, but as a support for learning and memory, there has to be evidence of it in intact living brain of an animal. The first evidence of STDP *in vivo* came from the study of the developing visual system of a frog (Zhang et al. 1998). Zhang et al. (1998) stimulated two converging inputs from retina to a tectal neuron of *Xenopus* tadpoles *in vivo*. These two inputs, one subthreshold (leading to EPSP) and another one leading to somatic spike, were pair-stimulated with a fixed delay. The paired stimuli were repeated for 100 s at 1 Hz similarly to Bi and Poo (1998). By varying the time delay between the stimulations of the two inputs, Zhang et al. (1998) obtained STDP-like curve for the EPSP evoked by subthreshold input. This work demonstrated that STDP might govern changes of synaptic connections in the developing brain of an animal and therefore potentially have long lasting impact on the adult brain. In a more recent study, Jacob et al. (2007) studied STDP *in vivo* in the barel cortex of rat. Stimulations of whiskers were paired with postsynaptic APs with a delay. They found an STDP dependence on this delay of similar shape to the one found by Bi and Poo (1998).

In *in vivo* protocols of STDP induction, EPSP is evoked by sensory stimulation (of a whisker in Jacob et al. (2007)). This EPSP has potentially very complex composition involving the activation of many pathways and synapses. This differs noticeably from *in vitro* protocols where presynaptic neurons are stimulated electrically in a more controlled fashion. Thus STDP *in vivo*

induced by sensory stimulation and STDP *in vitro* induced by electrical stimulation cannot be directly compared.

The *in vivo* STDP study by Schulz, Redgrave, and Reynolds (2010) is closer to *in vitro* studies. Schulz, Redgrave, and Reynolds (2010) studied STDP *in vivo* in cortico-striatal synapses of basal ganglia (BG) pairing presynaptic electrial stimulation with postsynaptic electical stimulation. The electical stimulation of the cortex led to the activation of cortical pyramidal cells (presynaptic). This stimulation was paired with postsynaptic AP induced by *in vivo* somatic current injection into a medium-sized spiny neuron of striatum. These pairings were repeated 60 times at low frequency 0.2 Hz. In order for this protocol to actually induce plasticity, the suppliment of a sensory input was required. To this end, each pairing was followed 250 ms later by a light flash to an animal's eye. With this protocol they obtained anti-Hebbian STDP curve: t-LTD for $-5<\Delta t<0$ ms (pre-before-post pairings), t-LTP for $0<\Delta t<5$ ms (post-before-pre pairings). These result however relied on disinhibition of visual pathways to dopamine cells and striatum (by injecting bicuculline to superior colliculus); without this disinhibition no plasticity was induced by the protocol.

These studies support the existence of STDP *in vivo* and suggest that it might play a role in reshaping neural networks and therefore supporting memory and learning (for a review of STDP *in vivo* see Dan and Poo (2006)).

With the current experimental support of STDP *in vivo*, there is still less evidence directly supporting STDP existence *in vivo* than *in vitro*. The conclusions of *in vitro* findings can not always be translated *in vivo*. With this regard, one might criticize the view of STDP as a foundational principle of learning and memory. However, even if the STDP paradigm fails as a foundation of learning *in vivo*, the STDP protocol exposes important aspects of inner workings of mechanisms underling plasticity such as timing-dependence. Timing-dependence might be a basis for learning patterns of correlations in sensory inputs. It is therefore important to continue studying STDP in realistic and artificial conditions to further expose the plasticity mechanisms and refine our concept of plasticity.

1.1.7 STDP of Basal ganglia

1.1.7.1 Basal ganglia

According to a modern hypothesis, the function of basal ganglia (BG) is linked to the learning and memory of skills and habits (Packard and Knowlton 2002; Yin and Knowlton 2006; Graybiel 2008). Traditionally, BG were thought to be related only to movement (Kandel 2013). This view

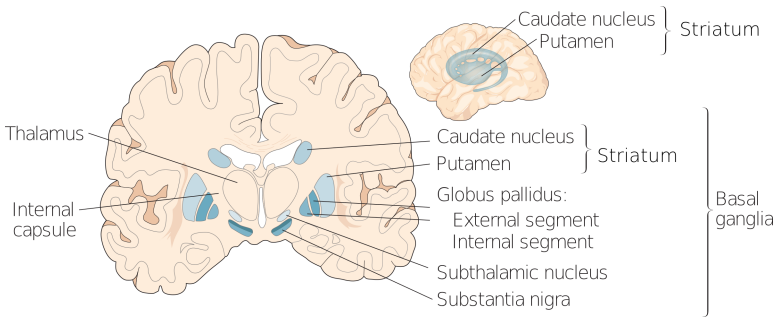

Figure 1.15: The basal ganglia and surrounding structures. Modified from Kandel (2013)

originated from the link between BG defects and pathologies of movement such as Parkinson and Huntington diseases. More modern understanding is that basal ganglia might be also involved in cognition; the later is supported by their link to cognitive diseases such as Tourette syndrome, obsessive-compulsive disorder (OCD) and attention-deficit/hyperactivity disorder (ADHD) (Gazzaniga and Bizzi 2009). In the following, I first describe the anatomy of basal ganglia and then their functional implications.

1.1.7.1.1 Anatomy of basal ganglia

The basal ganglia group a handful of subcortical structures (fig. 1.15):

- **The striatum**, that is divided into the dorsal striatum (consisting of caudate nucleus and putamen) and the ventral striatum (nucleus accumbens and olfactory tubercle, not shown in fig. 1.15),
- **The subthalamic nucleus** (STN),
- **The globus pallidus** internal and external segments (GPi and GPe).
- **The substantia nigra** that further subdivides into two subnuclei: substantia nigra pars reticulata (SNr) and substantia nigra pars compacta (SNc),

Substantia nigra. The SNr is one of the major output structures of BG. The SNc is a very specific structure. Among all brain structures, only the SNc and the adjacent ventral tegmental area contain dopaminergic neurons (cells that release the neurotransmitter dopamine); these cells project their axons to various structures of the BG and elsewhere in the brain. Death of dopaminergic cells is observed in Parkinsonian patients and considered as a cause of movement deficiencies accompanying the disease (Kandel 2013). Dopamine is also considered to be involved in modulating reward-motivated behavior and reinforcement learning (Schultz 2002).

Globus pallidus. The GPi is another major output structure of BG; The GPe is a part of internal BG circuitry (fig. 1.16).

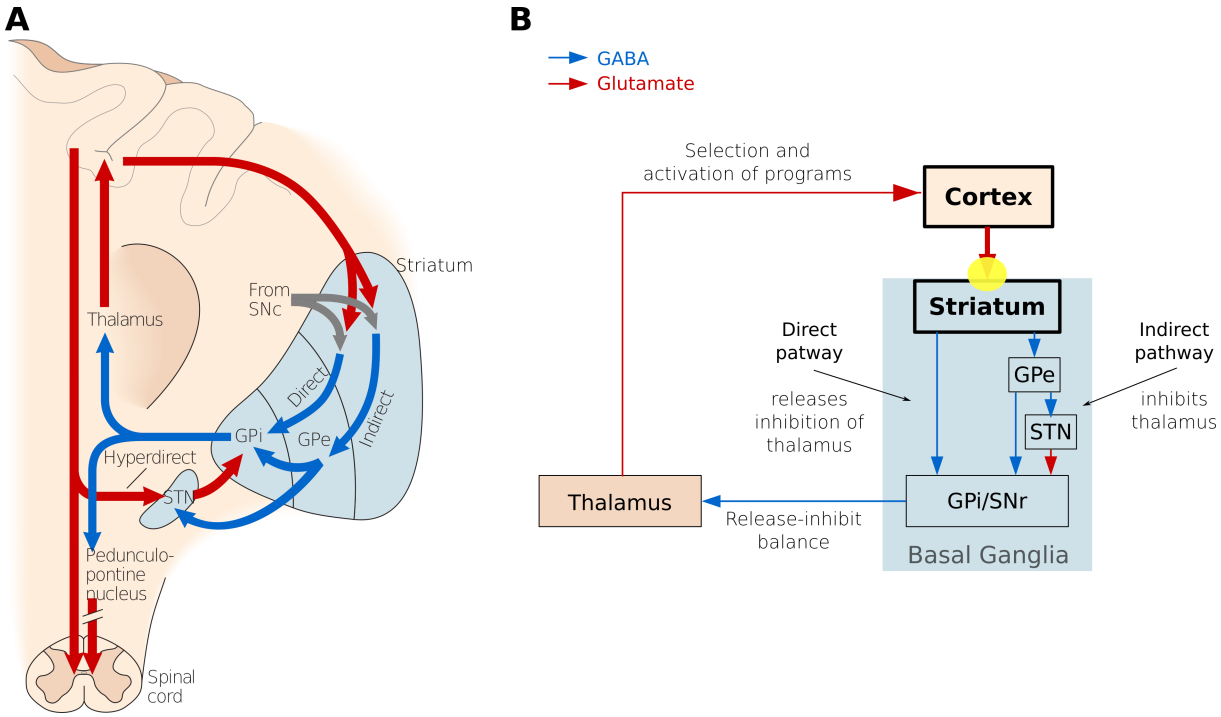

Figure 1.16: The basal ganglia–thalamocortical circuitry. **A**. The circuitry of the basal ganglia includes the striatum, the external and internal segments of the globus pallidus (GPe and GPi, respectively), the substantia nigra pars reticulata (not shown) and pars compacta (SNc), and the subthalamic nucleus (STN). Modified from Kandel (2013). **B**. Simplified scheme of basal ganglia circuitry illustrating the balance of the effects of the activation of direct and indirect pathways. Cortico-striatal synapses shown by yellow-shaded circle. Excitatory connections are shown in red, inhibitory pathways in blue.

Subthalamic nucleus. STN is located between the substantia nigra and the thalamus. It receives its inputs from GPe, cortex, thalamus and brain stem (fig. 1.16). Its output goes to both GPi and GPe, and to SNr. Cortical inputs to STN are called the hyperdirect pathway.

Striatum. The striatum serves as the main input station of basal ganglia; it receives inputs from cerebral cortex, thalamus and brain stem (fig. 1.16). Cortical inputs arriving to striatum are routed through two distinct pathways of BG (fig. 1.16): a *direct* monosynaptic pathway to GPi, and an *indirect* polysynaptic pathway that passes through GPe to both outputs of BG, SNr and GPi (either directly or through STN). Unlike in hippocampus or cortex, where glutamatergic excitatory neurons are the major type of neurons (Gulyás et al. 1999; DeFelipe and Fariñas 1992), in the striatum, most neurons are inhibitory. These include three types of GABAergic neurons (they release the neurotransmitter GABA, γ-aminobutyric acid) (Tepper and Bolam 2004): fast-spiking (FS) interneurons, medium-sized aspiny neurons, and medium-sized spiny neurons (MSNs). MSNs are the major type of striatal neurons and receive most of the excitatory input to striatum from cortex. Because the striatum is the major input nucleus of BG, these cortico-striatal synapses serve as major input synapses of BG. Their input is relayed to the pathways of basal ganglia downstream of MSN (direct and indirect pathways) and further to the outputs of BG. The MSNs of direct and indirect pathway express different dopamine receptor subtypes. In mice, the MSNs of two pathways are segregated: the MSNs of the direct pathway express D1 dopamine receptor (D1R), whereas the MSNs of the indirect pathway express D2 dopamine receptor (D2R) (Gerfen and Surmeier 2011). In addition to FS interneurons, the striatum contains two other types of interneurons differentiated by the neurotransmitter that they release: cholinergic interneurons and (NO)-synthesizing (NOS) interneurons.

1.1.7.1.2 Functions of the basal ganglia

The direct and indirect pathways of BG have opposite effects on the output of BG (fig. 1.16B).

The activation of MSNs belonging to direct pathway imposes inhibition on GPi/SNr. The later releases the inhibition normally imposed on thalamus by GPi/SNr, thus MSN stimulation via the direct pathway ultimately activates the thalamus (by releasing its inhibition).

The activation of the MSNs of the indirect pathway inhibits GPe. This releases inhibition normally imposed by GPe on GPi/SNr. Therefore, the activation of GPi/SNr increases their inhibition of the thalamus. Therefore, stimulation of MSNs from the indirect pathway imposes extra inhibition on thalamus.

The excitatory output from thalamus goes to the cortex where it might modulate various brain functions and be fed back to BG. The later closes the cortex-BG loop. This cortex-BG loop

might create a possibility for a complex iterative processing of information in the BG. Inside the loop, the opposite actions of direct and indirect pathways might take part in deciding stop-or-go about cortical input. One hypothesis is that the balance between the activation of direct and indirect pathways determines release/inhibition of motor programs (fig. 1.16B) (Gazzaniga and Bizzi 2009). This release-inhibit idea might be extended to cognitive level by considering other types of "programs" including skills, habits, thoughts and emotions. The learning of motor/cognitive programs and strategies for release and inhibition thereof might be supported by the synaptic plasticity of BG circuits. In the framework of this idea, the synaptic plasticity of the input synapses between the cortical pyramidal neurons and the MSNs of striatum is especially important. The later is because the synaptic transmission at these input synapses gates all the subsequent processing of cortical input by basal ganglia. It is therefore important to study plasticity of these cortico-striatal synapses.

1.1.7.2 STDP of Basal ganglia

The data accumulated during the last decade shows that synapses from cortex to striatum undergo various forms of plasticity including STDP. STDP at the major input synapses of BG, between cortical pyramidal neurons and MSNs, has been extensively studied (see Elodie Fino and Venance (2010) for review). The STDP of these synapses has peculiar properties: it is anti-Hebbian in normal conditions, but it can become Hebbian if manipulated experimentally.

1.1.7.2.1 anti-Hebbian STDP at cortico-striatal synapses

Using slices of rat brain in which connections from somatosensory cortex to striatum were preserved, Elodie Fino, Glowinski, and Venance (2005) studied plasticity at synapses between cortical layer 5 pyramidal neurons and medium-sized spiny neurons (MSNs) of striatum. To induce plasticity, several major experimental protocols were applied: LFS, HFS and STDP. In all three cases, the somatosensory cortex was stimulated with extracellular electrode. MSNs where recorded intracellularly with patch-clamp. LFS consisted of 600 cortical stimuli at 1 Hz. HFS was delivered at 100 Hz during 1 s (100 cortical stimuli). In agreement with classical LFS and HFS experiments in the hippocampus (described in sec. 1.1.2), LFS induced LFS-LTD whereas HFS induced HFS-LTP. Elodie Fino, Glowinski, and Venance (2005) have applied HFS and LFS protocols sequentially to the same cell during the same experiment (similarly to Barrionuevo, Schottler, and G. Lynch (1980), see sec. 1.1.2). LTP induced by HFS was reversed by the following LFS (to no plasticity). In another experiment, LFS was applied before HFS. In this case, the LTD induced by LFS was reversed to no plasticity by the following HFS. They thus

demonstrated the existence of bidirectional plasticity (both LTP and LTD) at cortico-striatal synapses. Elodie Fino, Glowinski, and Venance (2005) have also applied STDP protocol pairing the extracellular stimulation of the somatosensory cortex with postsynaptic somatic current injection in MSN. With 100 such pairings delivered at 1 Hz, for the first time in striatum, they found anti-Hebbian STDP: t-LTP was observed at negative Δt (postsynaptic stimulation before presynaptic one) and t-LTD at positive Δt; the dependence of plasticity on spike-timing was therefore reversed (t-LTP in place of t-LTD and t-LTD in place of t-LTP) by comparison to the classical Hebbian STDP curve of Bi and Poo (1998) (similarly to what was previously found in cerebellum-like structure of electric fish (Bell et al. 1997), see sec. 1.1.6.1). Note that strong t-LTP for -20<Δt<0 ms, is induced only in a part of experiments, whereas some experiments fail to induce t-LTP. This variability of experimental outcome applies to lesser extent to t-LTD for 10<Δt<30 ms. This variability can be liked to the variability of cell parameters that are important for plasticity (see sec. 2.7.2).

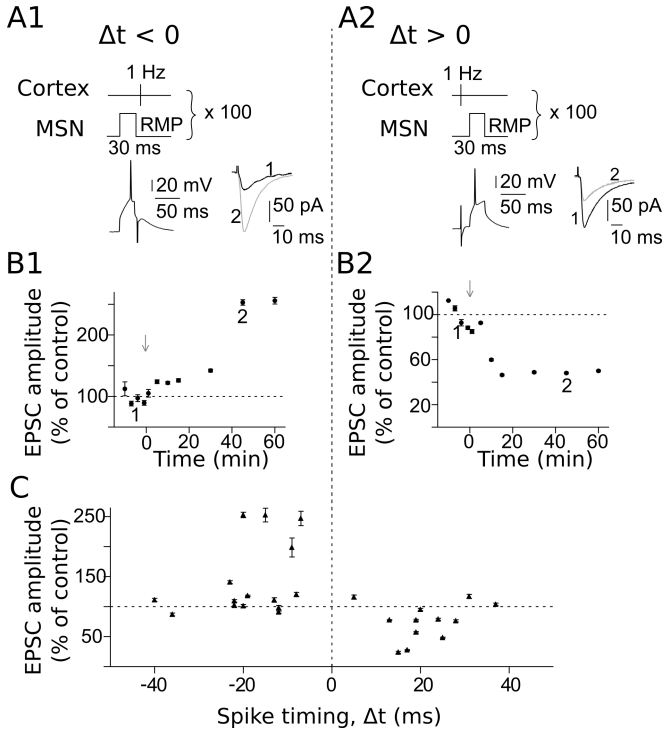

Figure 1.17: Anti-Hebbian STDP at cortico-striatal synapses. **A1**. Schematic illustration of the protocol for pre-before-post pairings ($\Delta t < 0$) (left panel). Single pairing of postsynaptic stimulation of MSN followed by cortical stimulation leads to action potential followed by EPSP in somatic recordings (left panel bottom). The right panel shows EPSC amplitude potentation 45 min after induction protocol (gray trace 2) compared to control (black trace 1). **A2**. Same as **A1** but for post-before-pre pairings ($\Delta t < 0$). **B1**. Change of EPSC amplitude in respose to test stimuli during representative experiment (illustrated at **A1**). **B2**. Same as **B1**, but for experiment as in **A2**. **C**. Spike-timing dependent plasticity curve summarizing all experiments. Modified from Elodie Fino, Glowinski, and Venance (2005).

1.1.7.2.2 Network context of cortico-striatal plasticity

Synaptic transmission between the cortex and MSNs in the striatum might be regulated by other striatal neurons that receive cortical input and project to MSNs. Therefore, because of the local connections to the MSN, the plasticity at synapses between the cortex and these other neurons might have important consequences for the processing of cortical input. Using protocol similar to Elodie Fino, Glowinski, and Venance (2005), 100 pairings of extracellular cortical stimulation with the intracellular stimulation of NOS neurons, Fino et al. (2009) found asymmetric STDP at cortico-NOS synapses: t-LTD for -100<Δt<+30 ms and t-LTP for 30<Δt<65 ms. Elodie Fino, Deniau, and Venance (2008) explored plasticity at synapses between cortex and striatal FS and cholinergic interneurons: the extracellular stimulation of layer 5 of the somatosensory cortex activated MSNs, FS and cholinergic interneurons in the following temporal order: first, FS interneurons, then cholinergic interneurons, and then the MSNs. The synapses to both FS and cholinergic interneurons were found capable of developing bidirectional plasticity (t-LTP and t-LTD) in response to a STDP protocol (100 pairings at 1 Hz). STDP at synapses between cortex and FS interneurons was Hebbian similarly to Bi and Poo (1998). STDP at synapses between cortex and cholinergic interneurons was partially anti-Hebbian: t-LTD at positive Δt, and both t-LTP and t-LTD at negative Δt. At negative Δt, the plasticity (t-LTD or t-LTP) was correlated with the level of excitability of cholinergic interneurons. Striatal STDP therefore varies depending on the specific conditions in each of striatal cell type. The interconnectedness of these cells might lead to a non-trivial interdependence of plasticities simultaneously induced in all cell types.

To find plasticity of a particular cell type not shaded by the influence of another ones, one can exclude influence of some cell types by pharmacological blockade. Blocking GABAergic transmission by $GABA_A$ receptors blocker, Pawlak and Kerr (2008) studied STDP of cortico-striatal synapses in slices of rat brain. To induce plasticity, they used low frequency 0.1 Hz and 60 pairings of EPSP induced by extracellular stimulation of cortical layer 5 and AP induced by postsynaptic current injection. In this setting, in opposition to the anti-Hebbian STDP found by Elodie Fino, Glowinski, and Venance (2005), they found Hebbian STDP. This dramatic difference in results was later explained by the state of GABAergic transmission (Elodie Fino, Paille, et al. 2010; Paille et al. 2013). Using protocol similar to Elodie Fino, Glowinski, and Venance (2005), 100 1-Hz pairings, Elodie Fino, Paille, et al. (2010) showed that blocking all $GABA_A$ receptors in rat brain slice reverses STDP curve from Hebbian to anti-Hebbian when all other conditions were kept the same. It was later shown that it is $GABA_A$ receptors located postsynaptically at MSN that determine Hebbian versus anti-Hebbian STDP (Paille et al. 2013). In normal conditions, therefore, $GABA_A$ signalling contributes to anti-Hebbian plasticity at cortico-striatal synapses. Another finding of Pawlak and Kerr (2008) was the dependence of cortico-striatal STDP on the activation of dopamine receptors. Blocking all D1R (not only in MSNs) resulted in disappearance of both t-LTD and t-LTP. Blocking all the D2R only decreased the extent of t-LTD. Shen et al.

(2008) confirmed the involvement of D1R and D2R into cortico-striatal plasticity. With the block of both $GABA_A$ and $GABA_B$ receptors, Shen et al. (2008) used STDP-like protocol similar to Markram et al. (1997) (see fig. 1.7) and demonstrated the existence of both t-LTP and t-LTD in both populations of MSN: D1-MSN and D2-MSN (MSNs of direct and indirect pathways, see sec. 1.1.7.1.1); t-LTD and t-LTP in D1-MSNs and D2-MSNs were affected by the block of D1R and D2R respectively. Both dopamine receptors, D1R and D2R are therefore involved in bidirectional plasticity induced by STDP and STDP-like protocols in both types of MSNs.

1.1.7.2.3 Molecules involved in cortico-striatal STDP

The cortico-striatal STDP induced by timing-dependent protocols depends on GABAergic and dopaminergic signaling. Understanding these dependencies is therefore important to find out how the mechanism underlying plasticity is modulated by the activity of other cells. However, to understand the plasticity mechanism itself, one has to find on which intracellular molecules it depends.

In the early plasticity studies, it was found that plasticity depends on calcium. This finding suggests that calcium might control plasticity via the activation of signaling downstream calcium. For instance, calcium can bind to calmodulin, this, in turn, can lead to the activation of calcium/calmodulin-dependent protein kinase II (CaMKII). CaMKII is a multi-subunit holoenzyme that has 12 domains, grouped into two clusters of six (Hudmon and Schulman 2002). CaMKII was experimentally found involved in LTP (Citri and Robert C Malenka 2008; Hudmon and Schulman 2002). Indeed, a mutant mice defective in α-CaMKII is deficient in both hippocampal LTP and spatial learning (Silva et al. 1992). Similar deficiencies arise in mutants with selectively blocked autophosphorylation of CaMKII (Giese et al. 1998).

NMDAR and VSCC are two sources of calcium repeatedly appearing important for plasticity in a range of studies (see Citri and Robert C Malenka (2008) for review). The coincidence detection properties of NMDAR led to the idea that NMDAR is responsible for the timing-dependence of STDP. However, in many cases, blocking NMDAR affects only one part of the timing-dependence of plasticity (often only t-LTP). For instance, experimental reports have identified that neocortical t-LTD depends on both NMDAR and cannabinoid receptor type 1 (CB1R) (Sjöström, Gina G. Turrigiano, and Sacha B. Nelson 2003). CB1Rs are located non-postsynaptically (presumably presynaptically) and activated by two endogenous analogs of a molecule responsible for the psychoactive effects of marijuana: tetrahydrocannabinol (THC). These two endogenous analogs of THC, 2-arachidonoylglycerol (2-AG) and anandamide (AEA), are called endocannabinoids. Endocannabinoids are produced postsynaptically and assumed to be transfered out from postsynaptic compartment by an unknown mechanism (Castillo et al.

2012). Upon their exit from the postsynaptic compartment, they reach CB1Rs located on presynaptic neurons or on astrocytes wrapping the synapse (star-shaped glial cells that, among other, provide neurons with mechanical support and nutrients). AEA also has another target with postsynaptic location: transient receptor potential vanilloid type-1 (TRPV1) (Castillo et al. 2012). TRPV1s are non-selective cation ionic channels; that is they are permeable to all kinds of positively charged ions (including Ca^{2+}). Whereas endogenously gated by AEA, they have exogenous agonist capsaicin, a molecule found in hot chili peppers and responsible for the irritating effects of the peppers. The activation of TRPV1 in peripheral nervous system is linked to the sense of pain and temperature (Kandel 2013). In general, in the central nervous system, TRPV1 are known to be involved in LTD (Castillo et al. 2012). AEA and TRPV1 were also implicated in LFS-LTD in amygdala (Puente et al. 2011).

In the somatosensory cortex, t-LTP depends on NMDAR, whereas t-LTD is independent from postsynaptic NMDAR and instead requires group-I metabotropic glutamate receptors (mGluR group-I), VSCC, IP3 receptor-gated stores (Bender 2006) and phospholipase C (PLC) (Nevian and Sakmann 2006). All these molecules belong to a network of molecular interactions part of which are linked to calcium and common downstream targets. Unlike NMDAR and AMPAR which are channels with an ionic pore, mGluR belongs to another class of receptors: the G protein–coupled receptors (GPCRs), that do not have an ionic pore and activate through another mechanism. Upon binding of an agonist (glutamate for mGluRs) to the extracellular part of the GPCR, the receptor undergoes conformational changes that promote binding with trimeric G protein on the intracellular part of the membrane. G proteins are trimers made of α, β and γ subunits. After binding of G protein, α subunit dissociates from $\beta\gamma$-dimer; at the same time, both the dimer ($G_{\beta\gamma}$) and the monomer of α subunit (G_α) dissociate from the receptor (Vilardaga et al. 2010). G_α has three major sub-types: $G_{\alpha q}$, $G_{\alpha s}$, and $G_{\alpha i}$. $G_{\alpha i}$ inhibits the production of cyclic adenosine monophosphate (cAMP) by adenylyl cyclase, thus inhibiting cAMP-activated protein kinase A (PKA). On the opposite, $G_{\alpha s}$ activates adenylyl cyclase thus PKA. $G_{\alpha q}$ activates PLCβ that allows the production of diacylglycerol (DAG) and inositol (1,4,5)-triphosphate (IP3) from phosphatidylinositol (4,5)-bisphosphate (PIP2) (Squire 2008; Berridge, Bootman, and Roderick 2003). IP3 together with intracellular calcium acts on IP3 receptor (IP3R) located on endoplasmatic reticulum (ER); this leads to calcium-induced calcium release (CICR) from ER. mGluRs group I are Gαq GPCRs, therefore, their activation leads to the activation of PLCβ that, through CICR, leads to the increase of intracellular calcium. As calcium was shown to be important for STDP, the molecules involved in this pathway might influence STDP via calcium. Another consequence of PLCβ activation is the production of DAG. DAG is converted to 2-arachidonoylglycerol (2-AG) by diacylglycerol lipase α (DAGLα). Because DAGLα activity is calcium-dependent, 2-AG production may constitute a coincidence detector of pre- and post-activity: 2-AG production needs both PLC to produce the substrate of DAGL,

DAG, and postsynaptic calcium to activate DAGL; PLC can be activated by presynaptic activity via glutamate release and mGluR-I binding. In turn, large postsynaptic calcium transients are triggered by VSCC opening due to postsynaptic spikes and/or NMDAR opening resulting from pre-post activity coincidence. Therefore, the endocannabinoid system seems adequate to support STDP.

The molecular level components involved in plasticity might differ from brain region to brain region, so the identification of the molecules involved in cortico-striatal plasticity, and STDP in particular, requires separate experiments. As in neurons of other brain regions, in striatal MSNs, large calcium transients are evoked by the coincidence between EPSP and bAP (Carter and Bernardo L Sabatini 2004). Carter and Bernardo L Sabatini (2004) found that bAP led to calcium influx via VSCC that was dependent on the level of baseline depolarization. The pairing of bAP with synaptic stimulation boosted calcium influx via NMDAR. Moreover, endocannabinoid system was also shown implicated in cortico-striatal plasticity, e.g.: the activation of TRPV1 was shown to be linked to LFS-LTD (e.g. Grueter, Brasnjo, and Robert C Malenka 2010). Elodie Fino, Paille, et al. (2010) studied the implication of various molecules in anti-Hebbian STDP at cortico-striatal synapses. They used an STDP protocol similar to Elodie Fino, Glowinski, and Venance (2005): 100 1-Hz pairings of extracellular cortical stimulation with somatic current injection in MSN, and coupled it with pharmacology to selectively switch off or inhibit molecules of interest. In agreement with what was previously found in hippocampus, they found that both t-LTD and t-LTP are dependent on postsynaptic calcium. Indeed when the postsynaptic calcium was immobilized by the addition of calcium buffer into the postsynaptic cell, the STDP protocol led to no plasticity whatever Δt.

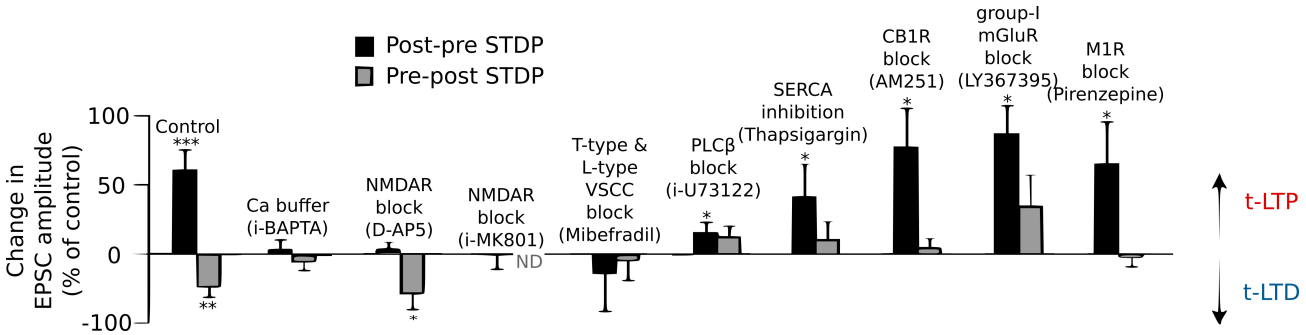

Figure 1.18: Cortico-striatal t-LTP and t-LTD depend on various molecules. The name of a drug used to affect a molecule indicated in bracets. The prefix "i-" before the name of a drug stands for intracellular application of a drug in the postsynaptic neuron (via the patch pipette). Otherwise drug is bath applied to extracellular solution. ND: not determined. $*p < 0.05$, $**p < 0.01$, $***p < 0.001$.

As in many previous STDP studies, t-LTP was found dependent on NMDAR, whereas t-LTD was not (fig. 1.18). t-LTD was found dependent on phospholipase Cβ (PLCβ), on M1 muscarinic GPCR (M1R), and L- and T-type VSCCs. Note that M1R are also $G_{\alpha q}$–coupled GPCR, just like mGluR group-I, so both receptors are expected to activate the same PLCβ. Moroever, blocking

mGluR group-I not only removed t-LTD, but even triggered t-LTP in place of t-LTD.

Furthermore, an important result from Elodie Fino, Paille, et al. (2010) is that VSCC are implicated both in t-LTP and t-LTD in MSNs, as seen from the effect of mibefradil. This is another significant difference with e.g. cortical or hippocampal STDP where the implication of VSCC is often restricted to t-LTD (while the implication of NMDAR is restricted to t-LTP), to the point that some modeling works have assumed that the calcium pool entering via NMDAR controls t-LTP whereas the calcium pool entering though VSCCs controls t-LTD (Karmarkar and Buonomano 2002). Such an assumption is ruled out in the striatum by the results of Elodie Fino, Paille, et al. (2010).

While IP3 leads to CICR from internal calcium stores, including the ER, another mechanism is responsible for the pumping calcium back into ER: sarco/endoplasmatic reticulum Ca2+-ATPases (SERCAs) transfer calcium against calcium concentration gradient into ER. This transfer is done at the expense of ATP degradation (Berridge, Bootman, and Roderick 2003). Therefore, the refill of ER can be blocked by blocking SERCA. Without the refill, ER gets emptied with time. As eventually there would be no calcium to release through IP3R, this effectively blocks CICR. By inhibiting SERCA-pumps, Elodie Fino, Paille, et al. (2010) found that t-LTD was replaced by no plasticity. t-LTD is therefore CICR-(and calcium-) dependent.

Inhibition of DAGLα (not shown in fig. 1.18) as well as blocking of the 2-AG receptors CB1R precluded t-LTD, but not t-LTP. These experiments confirm the importance of the pathway for t-LTD and suggest the following mechanism: activation by mGluR group-I (and/or M1 receptors) activates PLCβ, thus generating DAG and IP3. The former gives rise to 2-AG and CB1R signaling whereas the latter triggers CICR which amplifies Ca transients. The activation of CB1R therefore might serve as an entry point for downstream plasticity mechanisms responsible for t-LTD. In this putative mechanism, the dependence of t-LTD on the various molecules upstream CB1R is fully explained by their participation to CB1R activation. A scheme summarizing the experiments is shown on fig. 1.19.

1.1.7.2.4 Endocannabinoid-dependent STDP of cortico-striatal synapses induced by a low number of pairings

Typical STDP protocol consists of prolonged stimulations that comprise 60-100 pairings. Depending on the frequency of pairings, the stimulation alone can last from 1 minute (60 pairing at 1 Hz) to almost 17 minutes (100 pairings at 0.1 Hz). These number of pairings correspond to a rather long-duration stimulation. From everyday life experience, it seems that learning might occur on a much shorter time scale with a single and brief exposure to a stimuli (e.g. learning an

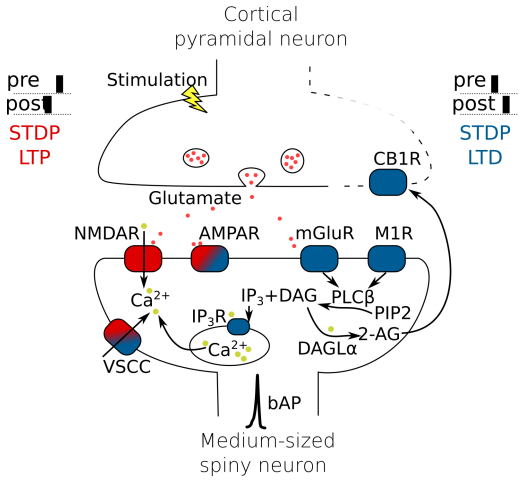

Figure 1.19: Summary of cortico-striatal t-LTP and t-LTD dependence on subcellular components. Green full circles symbolize Ca or Ca-dependent steps. Replotted from Elodie Fino and Venance (2010).

association between touching fire and pain from single trial). This kind of learning was reported in a range of studies (e.g. Rutishauser, Mamelak, and Schuman 2006; Schwartz et al. 2002). In order for STDP to support such learning, STDP should be present for short time scales, or equivalently, for small number of pre-post pairings in experimental protocols. By analogy with experimental protocol single-trial learning can be compared to a single stimulation with a low number of stimuli. When striatal neurons are monitored over episodes of learning, a fraction of them shows brief transient responses during the learning of novel instruction (Schultz, Tremblay, and Hollerman 2003). This brief activation might be controlling learning-related synaptic plasticity.

Using slices of rat and mice brains preserving cortico-striatal connections, Cui, Paille, et al. (2015) studied the dependence of cortico-striatal STDP on the number of pairings of the protocol (reduced compared to Elodie Fino, Glowinski, and Venance (2005)). They observed that the t-LTD at $\Delta t>0$ progressively disappears when the number of pairings decreases from 100 downto 1 (fig. 1.20). t-LTP at $\Delta t<0$ however shows more complex dependence on the number of pairings. With the decrease of the number of pairings t-LTP disappears faster than t-LTD (about 50 pairings). However, if the number of pairings decreases further, a form of t-LTP reappears between 5 and 20 pairings.

Unlike the t-LTP triggered by 50 pairings or more, that depends on the activation of NMDAR (see above) but not eCB, the t-LTP induced by 5-10 pairings was found eCB-dependent but not NMDAR-dependent (fig. 1.21). Indeeed, Cui, Paille, et al. (2015) showed that this t-LTP triggered by 5-10 pairings depends on eCB both through the activation of CB1R and transient receptor potential vanilloid type-1 (TRPV1).

The existence of a t-LTP relying on the endocannabinoid system challenges the traditional vision

of endocannabinoid system as a system supporting only LTD (Citri and Robert C Malenka 2008; Robert C. Malenka and Mark F. Bear 2004). The major difficulty it raises is to understand how a unique signaling system – the eCB system – can trigger both LTP and LTD. And what quantity along the signaling pathway controls the orientation of the synapse toward LTD or its functional inverse LTP? Note that similar questions have been raised for calcium and LTP and LTD in the hippocampus for many years. The calcium-control hypothesis, that states that postsynaptic calcium levels and/or time courses decide the outcome of plasticity (LTP or LTD) has been the topics of many experimental (see e.g. Tigaret et al. 2016) and modeling studies (Shouval, Mark F Bear, and Leon N Cooper 2002; Shouval, Castellani, et al. 2002; Graupner and Brunel 2012). However, how eCB controls STDP outcome in the striatum remains to be deciphered.

To understand theoretically the basis of this new plasticity and its dependence on the parameters of plasticity induction protocol and subcellular conditions, one has to put together the interactions between the molecules implicated in this plasticity. The resulting molecular networks can become complex enough to preclude simple qualitative analysis. To circumvent this limitation, I employed mathematical modeling and computer simulation of these molecular networks. In the next section, I will review the modeling efforts in Computational Neuroscience with a special focus on the modeling of subcellular dynamics and synaptic plasticity.

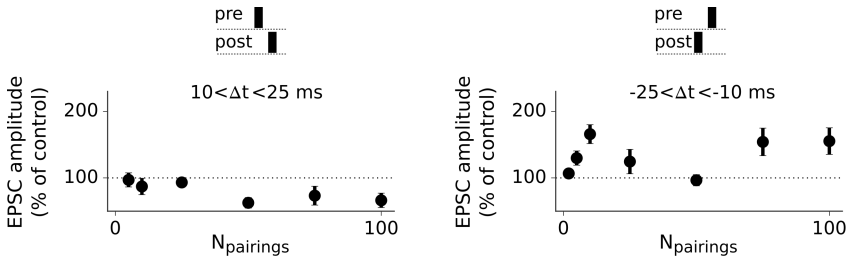

Figure 1.20: The dependence of cortico-striatal t-LTP and t-LTD on the number of pairings ($N_{pairings}$). Replotted from data by Cui, Paille, et al. (2015)

1.2 Modeling synaptic plasticity

1.2.1 Synaptic weight

Before discussing modeling, let me define the key concept of the mathematical studies of synaptic plasticity, the synaptic weight.

As we have seen in sec. 1.1, multiple measures can be used to evaluate plasticity experimentally. For instance, one can measure intracellularly or extracellularly the change of the amplitude or the

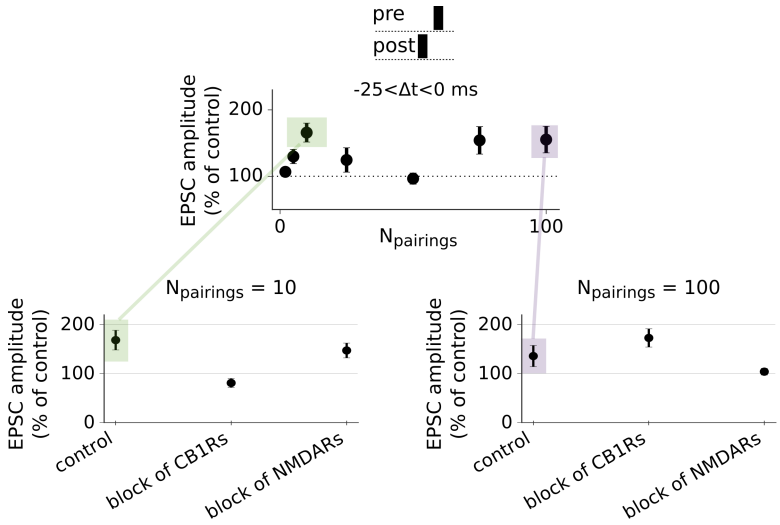

Figure 1.21: t-LTP induced by 100 pairings is NMDAR-dependent whereas t-LTP induced by 10 pairings is eCB-dependent. Plotted from data by Cui, Paille, et al. (2015)

slope of currents or potentials in response to a protocol inducing plasticity. To quantify induced plasticity, one then computes the ratio of the chosen quantity before and after the application of a plasticity induction protocol. This ratio is often referred to as the synaptic weight change in Computational Neuroscience literature and defined as the relative change of EPSC amplitude. In abstract terms, it is a very simple quantity: a synapse is depressed if the change in weight is less than 1 and potentiated if it is greater than 1. I denote this abstract synaptic weight as W. In the following, I will also often refer to a particular experimental definition of the synaptic weight (denoted W_{total}): W_{total} is the average EPSC amplitude in the last 10 minutes of the plasticity evaluating phase of the experimental protocol (after the end of the plasticity induction phase), divided by the average EPSC amplitude before the plasticity induction phase during the baseline phase.

1.2.2 Modeling neurons and networks

1.2.2.1 Electrical properties of neurons

The early effort to understand quantitatively the excitation of a nerve was at the time of Cajal and Pavlov. In 1907, Louis Lapicque proposed to model the electrical excitation of nerves by representing cellular membrane by equivalent electrical circuit with capacitor and resistance (for the English translation of the original French text see Brunel and van Rossum (2007)). Electrical excitation of a nerve (AP generation) was assumed when capacitor charges up to a threshold voltage. This simple model, now called leaky integrate-and-fire, is still actively used in simulations of neural networks because of its efficiency from computational standpoint. Almost

fifty years later, the major development in modeling of single neurons happened with the work of Hodgkin and Huxley (1952). Using joint experimental-theoretical approach, they have developed the equivalent electrical circuit description of a neuron membrane (fig. 1.22). The total tonic current through the surface of membrane (I) was divided to components: sodium (I_{Na}) and potassium currents (I_K), and small leakage current (I_L) made of chloride and other ions.

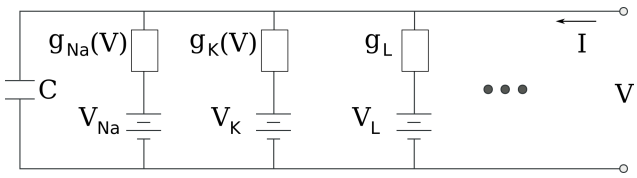

Figure 1.22: Equivalent electrical circuit representing membrane used by Hodgkin and Huxley (1952). g_x and V_x are conductances and reversal potentials for various current components. Taken from https://de.wikipedia.org/wiki/Datei:Hodgkin-huxley-circuit.svg

According to Ohm's law for equivalent circuit the transmembrane current can be computed as:

$$I = C\frac{\mathrm{d}V}{\mathrm{d}t} + g_K(V)(V - V_K) + g_{Na}(V)(V - V_{Na}) + g_L(V - V_L) \tag{1.1}$$

where g_x and V_x are conductances and reversal potentials (for which a current component changes its direction) for various current components (x=Na,K,L); C is membrane capacitance; V is membrane potential. The difficult part of the study was to determine the dependence of sodium and potassium conductances on the membrane potential. This part required extensive experimental work employing the state-of-the-art experimental techniques at the time (patch-clamp intracellular recording). The conductances of current components were described with a system of ordinary differential equations (ODE). The parameters of these equations were then fitted to the experimental data obtained by patch-clamp recordings from giant squid neuron. After fitting, their model quantitatively reproduced the generation of an action potential. This work brought Hodgkin and Huxley Nobel Prize in Physiology or Medicine in 1963. This model became the golden-standard in the modeling of the electrical excitation of neurons. The extensions of Hodgkin-Huxley model in use today can include great diversity of extra components of the total transmembrane current. These extra components are now attributed to various ionic channels (e.g. VSCCs are the source of calcium current component, see sec. 1.1).

Hodgkin and Huxley used Ohm's law approximation that is not always valid. To model an ionic current through a semi-permeable membrane two approaches can be utilized (Sterratt 2011; Hille 1992):

- **Ohm's law** provides an approximation for the case when the movement of ions is mostly determined by electric force, that is diffusion is small because concentrations of ions are

not too different at both sides of the membrane):

$$I_x = g_x(V - V_x) \tag{1.2}$$

The conductance g_x can be a function of various factors. The reversal potential V_x is determined by the concentrations of the ion x at both sides of the membrane.

- **Goldman-Hodgkin-Katz (GHK)** equation that describes more general case when the movement of ions is determined by both diffusion and electric force, when concentrations of an ion are noticeably different on two sides of the membrane:

$$I_x = P_x z_x^2 \frac{VF^2}{RT} \frac{[\mathrm{x}]_i - [\mathrm{x}]_o \exp(-z_x VF/RT)}{1 - \exp(-z_x VF/RT)} \tag{1.3}$$

where P_x is permeability that can be a function of various factors, z_x is valence of ion x, $[\mathrm{x}]_i$ and $[\mathrm{x}]_o$ are concentrations of ions x inside and outside of the cell respectively, F is Faraday constant, R is universal gas constant, T is absolute temperature

The reversal potential of a current made of ions x (obtained from GHK when $I_x = 0$) is given by the so-called Nernst potential:

$$V_x = \frac{RT}{z_x F} \ln\left(\frac{[\mathrm{x}]_o}{[\mathrm{x}]_i}\right)$$

The same V_x is used in Ohm's law approximation.

1.2.2.2 Models of networks and simple synapses

The Hodgkin-Huxley model was a success of bottom-up approach. It was validated experimentally so that it can be used to derive simpler models preserving key dynamical features of the original model (Izhikevich 2007). These simplified models can be then used for simulations at the level of neural networks.

In parallel to the bottom-up ascent from biophysics to an abstraction, top-down approach was used by other groups to produce theories of artificial neural networks. McCulloch and Pitts (1943) studied networks of artificial neurons using the formalism of symbolic logic. The notion of synaptic weight and plasticity was not yet present in this study.

In the second half of 1950s, after Hebb's book was published, Rochester et al. (1956) used IBM 704, a state-of-the-art computer at the time, to test Hebb's theory by simulating neural networks with plastic connections. They found that pure Hebbian rule (allows potentiation only) is not sufficient for the formation of cell assemblies predicted by Hebb. Without additional assumptions, pure Hebbian rule caused synaptic weight to grow without bound (Rochester et al. 1956).

The next influential development was Franc Rosenblatt's perceptron (Rosenblatt 1958). The perceptron is a network of artificial binary neurons with feedforward connectivity inspired by that of retina (layers of neurons with no connections inside a layer and all-to-all connectivity between layers). The synapses to the output layer were endowed with modifiable synaptic weights (called "values" by Rosenblatt). Given a set of weights and an input, the only one output neuron gets activated (by design of the model). This property allows to use Perceptron for the classification of input patterns. The id of the activated output neuron can be taken as the id of the class to which an input belongs. Perceptron's learning is a biologically implausible model of learning. However, this model unlike more complex and more biologically plausible models finds practical applications in pattern recognition and classification. This model led to the development of a whole class of biologically implausible, but practically useful models of artificial neural networks or its modern incarnation "Deep Learning" (LeCun, Bengio, and Hinton 2015). To understand how learning is actually implemented in the brain, new models have to be developed. A new kind of model of an artificial neural network was proposed by Hopfield (1982). The network consisted of binary neurons with all-to-all connectivity. The synaptic weights were allowed to be bidirectionally modified: to depress and potentate or vanish. Hopfield showed that such networks were capable of storing and retrieving patterns of activity of neurons ("memories"). From the perspective of Dynamical Systems, "memories" were stored in the form of attractors in the state space of the model. To store a pattern of activity in Hopfield networks, synaptic weights have to be decreased for synapses connecting neurons that do not fire together in the pattern, and increased if neurons either fire together or quiescent together. This rule is reminiscent of that of Hebb. However, this learning is applied not to ongoing activity patterns, but rather to a desired one. It is the synapses connecting the neurons that *would* fire in correlated fashion with the target pattern that are reinforced rather than those between neurons whose firing is *actually* correlated. Synapses are therefore changed not by local synaptic machinery, but rather by external intervention that is designed to obtain a desired pattern. The rule therefore does not explain learning of patterns via synaptic modification, but rather gives recipe to adjust all synapses to store patterns. In order to have higher-level properties of neural networks truly emerging from elementary synaptic and neuronal dynamics, synaptic weights should not be set up by an artificial procedure. Instead, they should be set by local learning rules controlled by events at the scale of single synapses and neurons. To study the development of selective response of cells in visual cortex to visual stimulus, Bienenstock, L N Cooper, and Munro (1982) proposed a new model of synaptic plasticity. Their learning rule is now called BCM (short for Bienenstock, Cooper, Munro). Here the learning rule was local and applied to ongoing activity. Similarly to Hebbian learning rule, the change of synapse was dictated by coactivaiton of pre- and postsynaptic neurons. The synaptic weight was modified in proportion to the product of presynaptic activity and a nonlinear function of postsynaptic activity. The

addition of this nonlinear function was the major innovation that allowed to stabilize Hebbian learning (correcting its tendency to increase synaptic weights in an unbounded fashion). As a result of BCM plasticity rule, a neuron can develop selective response to one of the input patterns presented in a random sequence (Bienenstock, L N Cooper, and Munro 1982). This work demonstrated that local simple plasticity rule can lead to a form of self-organization: the development of neuronal selectivity to a stimulus whereas without plasticity the neuron shows no preference for any stimuli. These early models suggest that the plasticity of synaptic weights might allow neurons and neural networks to perform various non-trivial functions (selective filtering of stimuli, associative retrieval of stored patterns, classification of patterns). However these models did not consider explicitly coincidence timing requirements of plasticity. Moreover, the question of how the plasticity is actually implemented in living cells was not addressed.

1.2.3 Modeling synaptic plasticity

1.2.3.1 Phenomenological models of timing-dependent plasticity

Gerstner et al. (1996) proposed a synaptic learning rule based on timing between pre- and postsynaptic spikes (here "spikes" means the abstract representation of APs). In Kempter, Gerstner, and Van Hemmen (1999), a presynaptic spike occurring before postsynaptic one led to an increase of synaptic weight, whereas postsynaptic spike occurring before presynaptic one led to a decrease of synaptic weight. This weight update rule was described by a function of spike-timing that was remarkably similar to the STDP curve obtained experimentally in hippocampal slices by Bi and Poo (1998). With this plasticity rule, Kempter, Gerstner, and Van Hemmen (1999) modeled 50 excitatory input synapses of a single neuron receiving Poisson trains as its inputs. The plasticity of synapses led to the normalization of average synaptic weight: when weights were initially high, the average value of weights decreased after learning, whereas when initial values were low, the average values of weights increased to the same steady-state value. When the inputs were split in two groups: a group of inputs correlated with the output (postsynaptic spikes) and a group of uncorrelated ones, learning specifically increased the weights of the synapses receiving correlated inputs, and decreased the weights of those receiving uncorrelated inputs.

Song, Miller, and L. F. Abbott (2000) proposed a plasticity rule and a model similar to that of Kempter, Gerstner, and Van Hemmen (1999). The spike-timing dependence of this rule provided a simple approximation of the spike-timing dependence of the plasticity observed experimentally in hippocampus by Bi and Poo (1998), Zhang et al. (1998). Song, Miller, and L. F. Abbott (2000) gave the phenomenon of STDP its name. Unlike Kempter, Gerstner, and Van Hemmen

(1999), the model of Song, Miller, and L. F. Abbott (2000) included inhibitory inputs and a larger total quantity of inputs (200 inhibitory and 1000 excitatory inputs). These inputs drove an integrate-and-fire neuron through STDP-modified synapses. When inputs were independent Poisson trains, the steady-state distribution of synaptic weights was bimodal: most of the weights had values around the lower and the upper bounds. When inputs had various degrees of correlation between each other, the weights in groups of inputs with higher correlation took higher steady-state values. The form of STDP studied by Song, Miller, and L. F. Abbott (2000) and Kempter, Gerstner, and Van Hemmen (1999) therefore introduced a competition between synapses based on the degree of correlation between pre- and postsynaptic spiking. Song and L. F. Abbott (2001) aimed to test if this type of STDP can account for the development of stimulus-selectivity in neurons. In their model, a random recurrent network of neurons received a randomly presented input via feedforward synapses endowed with STDP. When STDP came to an equilibrium, each neuron of the recurrent network had developed selective response to an input pattern. These studies demonstrated that a simple timing-dependent rule for the modification of synaptic weight can introduce correlation-based competition between synapses and lead to the formation of stimulus-selectivity. It is hard however to draw conclusions from these studies on how the learning of temporal correlations is actually implemented in living-cells. A major simplification used in these models is that the outcome of an experiment (STDP curve of Bi and Poo (1998)) is taken as the fixed update rule for synaptic weight. It was experimentally shown that the STDP outcome is actually dependent on experimental conditions and the parameters of the stimulation (e.g. frequency, see sec. 1.1.6.1). It is therefore evident that the actual plasticity update rule should be more complex than a simple fit to one of its outcomes observed in a very specific condition (i.e. a typical experimental protocol with an artificially regular stimulation pattern of 60-100 pairings at 1 Hz). To understand theoretically the actual plasticity rule in terms of its dependence on subcellular components, several pieces of knowledge have to fit together. First, we have to have experimental data on which of these components are important for plasticity. Second, we have to have models for these components and their interactions. Third, we have to have a link between the dynamics of these interacting components and plasticity. In the following, I first describe the models of subcellular components involved in plasitcity and then state-of-the-art models of plasticity.

1.2.3.2 Subcellular building blocks for mechanistic models of synaptic plasticity

1.2.3.2.1 Memory inside the cell

In order for subcellular mechanisms to maintain a potentiated or depressed state of a synapse, there should be a way to store information about the synapse state at the subcellular level.

Crick (1984) proposed that even in the presence of molecular turnover, a persistent molecular "memory" can be implemented by a molecule, for which, two stable states exist. Following year, JE Lisman (1985) proposed a model of simple molecular system capable of storing one bit of information (e.g. about potentiated vs non-potentiated state of a synapse) as a result of its bistability. The core component of this system is an autophosphorylating kinase (K_1 and $K_1{}^*$ at fig. 1.23), that, when phosphorylated ($K_1{}^*$ form) becomes capable of phosphorylating its non-phosphorylated form (K_1). Upon coupling with a phosphatase that removes the phosphorylation, it becomes possible to achieve bistability: either (i) most of the molecules of the kinase end up phosphorylated or (ii) all molecules remain not phosphorylated. This is achieved as a result of the positive feedback loop: phosphorylation of the kinase leads to even greater phosphorylation. If its initial phosphorylation level is low then phosphatase activity wins over and all molecules of the kinase ends up unphosphorylated. On the contrary, if the initial phosphorylation level is high enough, autophosphorylation wins over phosphatase activity. If the state of phosphorylation of the kinase can be controlled by an external stimulus (e.g. a stimulus that activates another kinase K_2 that also contributes to the phosphorylation of K_1), then the final binary state of this system (phosphoryalted/non-phosphorylated) can be controlled by this stimulus. This system acts like a flip-flop device and is capable of storing one bit of information (if synapse is potentiated or not).

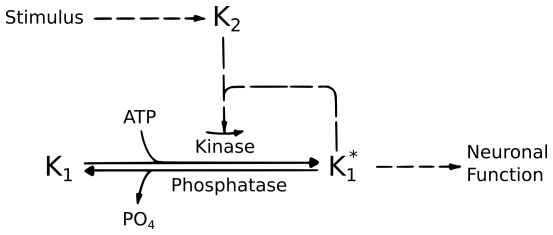

Figure 1.23: Reactions in a bistable switch. The switch itself is constructed from two proteins: kinase-1, which can exist in either an inactive state (K_1) or an active state ($K1*$), and a phosphatase. The transition between inactive and active states is due to a phosphorylation reaction that can be catalyzed by active kinase-1 or by the kinase-2 activated during neuronal stimulation.

1.2.3.2.2 Kinetic formalism

A simple way to represent a chemical reaction is to draw a scheme showing reactants on the left part of the scheme and products on the right:

$$\mathrm{A} + \mathrm{B} \underset{\mathrm{k}_b}{\overset{\mathrm{k}_f}{\rightleftharpoons}} \mathrm{A}' + \mathrm{B}' \tag{1.4}$$

where A, B are concentrations of reactants and A', B' are concentrations of products. In general a reaction can go in both directions with the rate of the forward reaction given by the constant k_f, and the rate of backward reaction by the constant k_b. If reactants come close together in

space and/or collide, one might expect reaction eq. 1.4 to occur with some probability (for simplicity taken constant and proportional to a rate constant). The chance of reaction occurring therefore might be determined by the probability of a collision and the probability of the reaction to occur upon a collision. If the medium where the reaction occurs is perfectly mixed, that is the concentration of the reactants is uniformly identical in the whole volume of the medium, then the probability of a collision might be considered constant and proportional to the product of the concentrations of reactants. Indeed the probability for a molecule of a reactant to occupy a position in a infinitesimal subvolume is proportional to the concentration of the reactant and assumed independent from the probability of other reactant to occupy the same spot. Under this perfect-mixing hypothesis, the probability of the forward reaction and backward reaction is therefore proportional to $k_f AB$ and $k_b A'B'$ respectively. The appropriate choice of units for rate constants allows to take $k_f AB$ and $k_b A'B'$ as rates of forward and backward reactions respectively. The later statement expresses the law of mass action (rate/probability of reaction is proportional to masses/concentrations of reactants). The change of the concentration of reactants/products over time can be modeled with ordinary differential equations (ODE) as:

$$\begin{aligned} \frac{dA}{dt} &= \frac{dB}{dt} = k_b A'B' - k_f AB \\ \frac{dA'}{dt} &= \frac{dB'}{dt} = -k_b A'B' + k_f AB \end{aligned} \tag{1.5}$$

If the assumption of perfect mixing is satisfied, the system of ODE eq. 1.5 can be used to describe any chemical reaction in a complex molecular network (U S Bhalla and Iyengar 1999). For instance, if reaction scheme eq. 1.4 is applied twice: for the first reaction, A=E, B=S, A′=ES, B=0, for the second, A=ES, B=0, A′=E, B′=P, then these two reactions can be compressed into well known enzyme-substrate biochemical reaction:

$$\mathrm{E} + \mathrm{S} \underset{\mathrm{k_2}}{\overset{\mathrm{k_1}}{\rightleftharpoons}} \mathrm{ES} \xrightarrow{\mathrm{k_3}} \mathrm{E} + \mathrm{P} \tag{1.6}$$

$$\begin{aligned} \frac{d[E]}{dt} &= -k_1[E][S] + k_2[ES] + k_3[ES] \\ \frac{d[S]}{dt} &= -k_1[E][S] + k_2[ES] \\ \frac{d[ES]}{dt} &= k_1[E][S] - k_2[ES] - k_3[ES] \\ \frac{d[P]}{dt} &= k_3[ES] \end{aligned} \tag{1.7}$$

where [E], [S], [ES] and [P] are concentrations of enzyme, substrate, enzyme-substrate complex

and product respectively.

If one assumes that [ES] changes are small at the time scale of product formation ($\frac{d[ES]}{dt} \approx 0$):

$$\frac{d[P]}{dt} = \frac{k_3[E]_0[S]}{K_M + [S]}. \tag{1.8}$$

where $K_M = (k_2 + k_3)/k_1$ and the constant $[E]_0 = [ES] + [E]$ is the total enzyme concentration.

The activation of a receptor can also be described using the same formalism (Destexhe, Z F Mainen, and T J Sejnowski 1994; Alain Destexhe, Z. Mainen, and T. Sejnowski 1995; Alain Destexhe, Zachary F Mainen, and Terrence J Sejnowski 1998). When the agonist (A) binds to a receptor in closed state (x_C), the receptor undergoes conformational changes and enters activated/open state (x_O). The agonist can then unbind allowing the receptor to return to a closed state. Optionally, one can consider additional states of the receptor to account for e.g. desensitization/inactivation (x_I). fig. 1.24 shows a simple three state scheme of a receptor activation and desensitization:

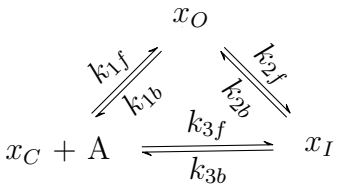

Figure 1.24: General three-state kinetic scheme

One can choose units for rate constants ($k_{xb}, k_{xf}, x = 1, 2, 3$) to consider fractions of receptors in a particular state (or probabilities of states) instead of actual concentrations. With this approach, one obtains $x_C + x_O + x_I = 1$ (receptor is in one of the states with certainty; this is equivalent to a statement that the total concentration of receptors in all states is constant).

The corresponding system of ODEs therefore reads:

$$\begin{aligned} \frac{dx_O}{dt} &= k_{1f}x_C A + k_{2b}x_I - (k_{1b} + k_{2f})x_O \\ \frac{dx_I}{dt} &= k_{2f}x_O + k_{3f}x_C A - (k_{2b} + k_{3b})x_I \\ x_C &= 1 - x_O - x_I \end{aligned} \tag{1.9}$$

1.2.3.3 Calcium-controlled plasticity

A good theory compresses a variety of experimental data into a concise model that contains all the particular experimental cases. As we have seen in sec. 1.1, various experimental protocols can be used to induce plasticity. What if these various experimentally observed forms of plasticity

express the same fundamental mechanisms? In such a case, we can hope for a unified description that accounts for all experimental protocols. In the beginning of 2000s, an influential attempt at such a description was made (Shouval, Mark F Bear, and Leon N Cooper 2002; Shouval, Castellani, et al. 2002). This attempt was build around the older idea of calcium control hypothesis of John Lisman (1989). Shouval, Mark F Bear, and Leon N Cooper (2002) noticed that the calcium-dependence of plasticity is the recurrent finding across many experimental reports (sec. 1.1.4). They therefore proposed to describe time-evolution of synaptic weight (W) by a calcium-dependent function:

$$\frac{dW}{dt} = \frac{1}{\tau(C)}\left(\Omega(C) - W\right) \tag{1.10}$$

where C is postsynaptic calcium concentration, $\Omega(C)$ and $\tau(C)$ are taken to match experimental observations. $\Omega(C)$ expresses mathematically the dependence of plasticity on calcium concentration as observed by Cho et al. (2001) and others (see fig. 1.6 in sec. 1.1.4). They assumed that low calcium concentration leads to no-plasticity, medium leads to synaptic depression and high calcium concentration leads to synaptic potentiation (see $\Omega(C)$ plot on fig. 1.25). Moreover, they assumed that the time of relaxation $\tau(C)$ in eq. 1.10 is also calcium dependent; so that the synaptic weight changes faster when calcium concentration is higher (see $\tau(C)$ plot on fig. 1.25). To express this hypothesis they used:

$$\begin{aligned} \Omega(C) &= A + \mathrm{sig}(C - \alpha_2, \beta_2) - A\mathrm{sig}(C - \alpha_1, \beta_1) \\ \mathrm{sig}(x, \beta) &= \exp(\beta x)/(1 + \exp(\beta x)) \\ \tau(C) &= \frac{P_1}{P_2 + C^{P_3}} + P_4 \end{aligned} \tag{1.11}$$

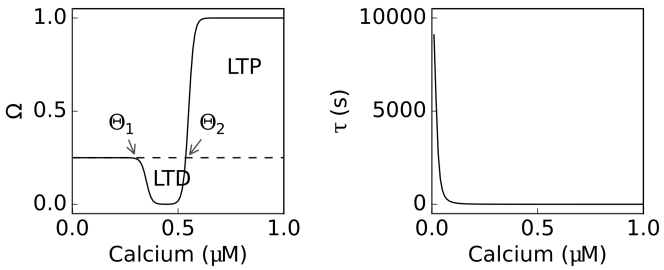

Figure 1.25: Functions used by Shouval, Mark F Bear, and Leon N Cooper (2002) to express calcium-control hypothesis (left panel compare to fig. 1.6). The parameters of eq. 1.11: A=0.25, $\alpha_1 = 0.35$, $\alpha_2 = 0.55$, $\beta_1 = 80$, $\beta_2 = 80$, $P_1 = 0.1$ sec, $P_2 = P_1 10^{\breve{}4}$, $P_3 = 3$ and $P_4 = 1$ sec. Replotted from Shouval, Mark F Bear, and Leon N Cooper (2002)

To obtain calcium input for this model, Shouval, Mark F Bear, and Leon N Cooper (2002) used a simplifying assumption that calcium only comes through NMDAR and has simple linear decay term. With their simple model, Shouval, Mark F Bear, and Leon N Cooper (2002) qualitatively

reproduced the dependence of plasticity on the frequency of presynaptic stimulation. Moreover, using classical STDP protocol with 100 1-Hz pairings, Shouval, Mark F Bear, and Leon N Cooper (2002) achieved partial agreement with the experimental data on the hippocampal STDP by Bi and Poo (1998) (compare blue trace on fig. 1.26 and fig. 1.10).

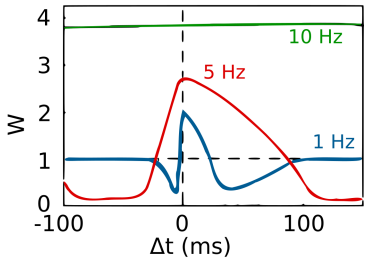

Figure 1.26: STDP curve obtained as a result of the application of simulated STDP protocol with 100 pre-post pairings to the simple model of Shouval, Mark F Bear, and Leon N Cooper (2002) at 1 Hz (blue), 5 Hz (red) and 10 Hz (green). Modified from Shouval, Mark F Bear, and Leon N Cooper (2002)

One consequence of their model was the appearance of the second t-LTD window for $45<\Delta t<90$ ms that was larger than the first t-LTD window for small negative Δt. Such STDP was indeed observed in hippocampus with stimulation at 5 Hz (compare to fig. 1.14A2). Furthermore, the model captured the tendency of STDP, observed in neurons of visual cortex by P. Sjostrom, G. Turrigiano, and S. Nelson (2001), to shift toward t-LTP when the frequency of stimulation is increased (compare fig. 1.26 against fig. 1.11 and fig. 1.13). However, whereas this model captures some of the aspects of plasticity, it neither explains the biochemical mechanisms behind calcium-dependence of plasticity nor it provides us with a realistic form of this dependence.

Finding these mechanisms is complicated by the fact that neurons contain multiple molecules interacting with one another in complex biochemical networks. To find out the molecules crucial for plasticity, a useful approach is the approach of systems biology: modeling and analysis of interactions between species of complex molecular networks (Kotaleski and Blackwell 2010). Many models of this kind have calcium or CaMKII as their output (for review see Manninen et al. (2010)). Regarding CaMKII based models, the major development was the work of Graupner and Brunel (2007). This study effectively combined the idea of calcium-control of plasticity of Shouval, Mark F Bear, and Leon N Cooper (2002) with the idea of molecular "memory" of JE Lisman (1985). For Lisman's unspecified autophosphorylating kinase, they considered CaMKII. Similarly to Lisman's unspecified kinase, CaMKII is controlled by kinase-phosphatase system. Graupner and Brunel (2007) linked this kinase-phosphatase system to calcium input by modeling molecular network in between the two. Calcium input in their model plays the same role as "external stimulus" played in Lisman's model: it controls the kinase-phosphatase system and eventually the final (UP or DOWN) state of autophosphorylating kinase (CaMKII).

Calcium binding to calmodulin produces a calcium/calmodulin complex (CaM) that then can

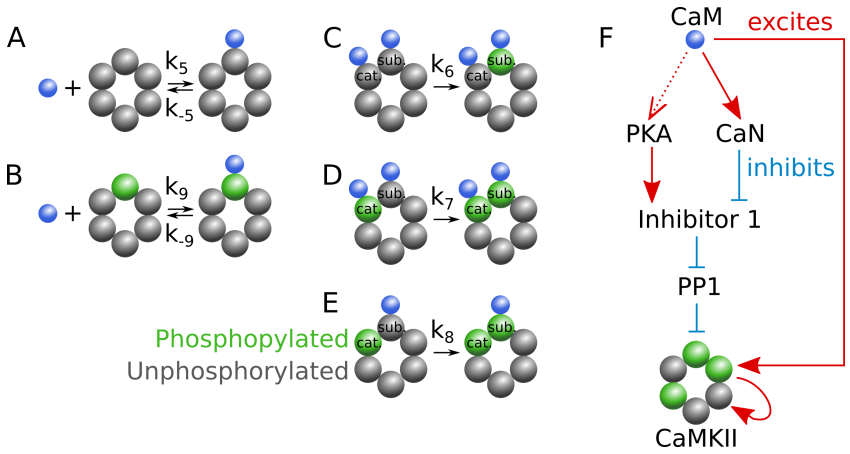

Figure 1.27: CaMKII activation by the calcium/calmodulin complex (CaM, blue balls). The CaMKII holoenzyme consists of a ring of six subunits, each of which can be either dephosphorylated (gray balls) or phosphorylated (green balls). **A,B**. Binding: the calcium/calmodulin complex can bind to a dephosphorylated (**A**) or a phosphorylated subunit (**B**) with forward/backward reaction rates k_5/k_{-5} and k_9/k_{-9} respectively. **C–E**. Intersubunit phosphorylation steps. **C-D**. Initiation step: when two calmodulins are bound to two neighbor subunits (referred to as substrate "sub" and the catalyst, "cat"), the "cat" subunit can phosphorylate the "sub" subunit (green) with constant k_6 (**C**) or with constant k_7 if the "cat" subunit is phosphorylated (**D**). **E**. Once phosphorylated, the "cat" subunit remains active even after calmodulin dissociation thus phosphorylating the "sub" subunit with constant k_8. **F**. The signaling cascade controlling CaMKII activity. Red arrows indicate activation relationship. The red arrow on the right corresponds to activation of CaMKII by CaM (through reactions **A** and **B**), the red circular arrow on the right-bottom corresponds to the activation of CaMKII through autophosphorylation reactions (**C-E**). CaMKII subunits can be dephosphorylated (desactivated) by protein phosphatase 1 (PP1) (blue lines indicate inhibition). In turn PP1 is inhibited by the phosphorylated form of so-called "inhibitor 1", I1. I1 phosphorylation (and activation as inhibitor) is contributed by PKA and its dephosphorylation triggered by Calcineurin (CaN). Therefore, PKA activates (disinhibits) CaMKII whereas CaN desactivates it. Finally because CaN is activated by CaM, CaM indirectly deactivates CaMKII via CaN but activates it directly via direct interaction. PKA activity depends on cAMP that is produced from ATP by adenylyl cyclase. Graupner and Brunel (2007) hypothesized that cAMP production is initiated by CaM. This hypothesis makes PKA activity indirectly dependent on CaM. Modified from Graupner and Brunel (2007).

phosphorylate a subunit of CaMKII (fig. 1.27A,B). A phosphorylated subunit of CaMKII can serve as a catalyst for further intramolecular CaMKII phosphorylation (fig. 1.27C-E). Dephosphorylation of a phosphorylated CaMKII subunit is due to protein phosphatase 1 (PP1) (fig. 1.27F). The objective of the model by Graupner and Brunel (2007) was to generate a detailed model of the entire biochemical network implicated in CaMKII phospohorylation. As Graupner and Brunel (2007) aimed to model STDP of hippocampal neurons, they considered hippocampus specific pathways controlling PP1 and therefore dephosphorylation of CaMKII. In hippocampus, PP1 is inhibited by phosphorylated inhibitor 1 (I1) protein. In Graupner and Brunel (2007), dephosphorylation I1 is controlled by CaM-dependent calcineurin (CaN). The phosphorylation of I1 is controlled by PKA. For the PKA activation, Graupner and Brunel (2007) made a hypothesis that hippocampal PKA activation indirectly depends on CaM, which is not strongly supported by experimental data.

1.2.3.3.1 Essential equations of Graupner and Brunel (2007) model

Calmodulin/calcium complex (CaM) (fig. 1.27) is produced when calmodulin (CM) binds calcium (C) in cooperative manner (the affinity for calcium increases if other calcium molecules are already bound):

$$\mathrm{CM} + 4\mathrm{C} \overset{\mathrm{K_1}}{\rightleftharpoons} \mathrm{CM(C)_1} + 3\mathrm{C} \overset{\mathrm{K_2}}{\rightleftharpoons} \mathrm{CM(C)_2} + 2\mathrm{C} \overset{\mathrm{K_3}}{\rightleftharpoons}$$
$$\overset{\mathrm{K_3}}{\rightleftharpoons} \mathrm{CM(C)_3} + \mathrm{C} \overset{\mathrm{K_4}}{\rightleftharpoons} \mathrm{CM(C)_4}$$

Here and in the following $K_i = k_{-i}/k_i$ is the dissociation constant, k_i and k_{-i} are forward and backward reaction rates respectively.

Because calmodulin binding to calcium is fast, these reactions quickly reach equilibrium. Thus even when calcium changes, equilibrium approximation can provide a reasonable estimate of the concentration of the complex. With this approximation, the concentration of calcium/calmodulin complex with four calcium ions bound (CaM) can be computed as:

$$CaM = [CM(C)_4] = \frac{CaMT}{1 + \sum_{i=1}^{4}(C^i \cdot \prod_{j=5-i}^{4} K_j)}, \tag{1.12}$$

where $CaMT$ is total calmodulin concentration.

Note that it is assumed for simplicity that only those calmodulins with four calcium ions bound (CaM) can activate CaMKII. For simplicity, Graupner and Brunel (2007) considered that

CaM binding to CaMKII subunits (fig. 1.27) is also in equilibrium. With this approximation, instead of writing ODEs for each possible CaMKII phosphorylation pattern, one can write simple expressions for the concentrations of products through concentrations of reactants. This allows to derive simple formulas for the probabilities that CaM binds to phosphorylated (γ) and dephosphorylated (γ^*) subunit of CaMKII:

$$\begin{aligned} \gamma &= CaM/(CaM + K_5) \\ \gamma^* &= CaM/(CaM + K_9) \end{aligned} \tag{1.13}$$

The dephosphorylation of a phosphorylated subunit was assumed independent of whether CaM is bound to it or not. It is modeled according to enzyme-substrate reaction eq. 1.6 (with PP1 as the enzyme, and a subunit of CaMKII as the substrate). The approximation according to eq. 1.8 allowed to estimate the rate of subunit dephosphorylation (k_{10}) as:

$$k_{10} = k_{12} PP1/(K_M + CaMKII^*) \tag{1.14}$$

where K_M is Michaelis constant; k_{12} is the maximal dephosphorylation rate; $PP1$ is the concentration of PP1; $CaMKII^*$ is the total concentration of phosphorylated subunits of CaMKII computed accross all possible states of phosphorylation of CaMKII:

$$CaMKII^* = \sum_{i=0}^{13} m_i y_i, \tag{1.15}$$

where m_i is the number of the phosphorylated subunits of CaMKII in state i and y_i is the concentration of CaMKII in state i.

The approximations eq. 1.13 and eq. 1.14 allow to write simple production and degradation terms for the system of ODEs describing the concentrations of CaMKII molecules with different numbers of phosphorylated subunits (rewritten from that of Graupner and Brunel (2007)):

$$
\begin{aligned}
\sigma_i^j &= \sum_{k=i}^{j} y_k \\
y_0 &= y_{000000} = 2CaMKII_0 - \sigma_1^{13} \\
\frac{dy_1}{dt} &= \frac{dy_{100000}}{dt} = 6k_6\gamma^2 y_0 - (4k_6\gamma^2 + k_7\gamma + k_{10})y_1 + 2k_{10}\sigma_2^4 \\
\frac{dy_2}{dt} &= \frac{dy_{110000}}{dt} = (k_7\gamma + k_6\gamma^2)y_1 - (3k_6\gamma^2 + k_7\gamma + 2k_{10})y_2 + k_{10}(y_5 + \sigma_5^7) \\
\frac{dy_3}{dt} &= \frac{dy_{101000}}{dt} = 2k_6\gamma^2 y_1 - 2(k_7\gamma + k_6\gamma^2 + k_{10})y_3 + k_{10}(\sigma_5^7 + 3y_8) \\
\frac{dy_4}{dt} &= \frac{dy_{100100}}{dt} = k_6\gamma^2 y_1 - 2(k_7\gamma + k_6\gamma^2 + k_{10})y_4 + k_{10}(y_6 + y_7) \\
\frac{dy_5}{dt} &= \frac{dy_{111000}}{dt} = k_7\gamma(\sigma_2^3 - y_5) + k_6\gamma^2(y_2 - 2y_5) + k_{10}(2y_9 + y_{10} - 3y_5) \\
\frac{dy_6}{dt} &= \frac{dy_{110100}}{dt} = k_6\gamma^2(\sigma_2^3 - y_6) + k_7\gamma(2y_4 - 2y_6) + k_{10}(-3y_6 + \sigma_9^{11} + y_{11}) \\
\frac{dy_7}{dt} &= \frac{dy_{110010}}{dt} = k_6\gamma^2(y_2 + 2y_4 - y_7) + k_7\gamma(y_3 - 2y_7) + k_{10}(-3y_7 + \sigma_9^{11} + y_{11}) \\
\frac{dy_8}{dt} &= \frac{dy_{101010}}{dt} = k_6\gamma^2 y_3 - 3k_7\gamma y_8 + k_{10}(y_{10} - 3y_8) \\
\frac{dy_9}{dt} &= \frac{dy_{111100}}{dt} = k_7\gamma(\sigma_5^7 - y_9) + k_6\gamma^2(y_5 - y_9) + k_{10}(-4y_9 + 2y_{12}) \\
\frac{dy_{10}}{dt} &= \frac{dy_{111010}}{dt} = k_6\gamma^2 y_5 + k_6\gamma^2 y_6 + k_7\gamma(y_7 + 3y_8 - 2y_{10}) + k_{10}(2y_{12} - 4y_{10}) \\
\frac{dy_{11}}{dt} &= \frac{dy_{110110}}{dt} = k_7\gamma(y_6 - 2y_{11}) + k_6\gamma^2 y_7 + k_{10}(y_{12} - 4y_{11}) \\
\frac{dy_{12}}{dt} &= \frac{dy_{111110}}{dt} = k_6\gamma^2 y_9 + k_7\gamma(2\sigma_9^{11} - y_9 - y_{12}) + k_{10}(6y_{13} - 5y_{12}) \\
\frac{dy_{13}}{dt} &= \frac{dy_{111111}}{dt} = k_7\gamma y_{12} - 6k_{10}y_{13}
\end{aligned}
\tag{1.16}
$$

$CaMKII_0$ denotes the total concentration of CaMKII (made of two clusters of six subunits), $2CaMKII_0$ therefore stands for the concentration of six-subunit clusters. y_i denotes the concentration of six-subunit clusters in a state of phosphorylation i. The index of i denotes the various distinguishable combinations of phosphorylated (denoted by 1) and dephosphorylated (denoted by 0) subunits in six subunit ring of CaMKII. For instance, $y_5 = y_{111000}$, $y_6 = y_{110100}$, $y_7 = y_{110010}$, and $y_8 = y_{101010}$, all have three phosphorylated subunits (the same level of activation): $m_5 = m_6 = m_7 = m_8 = 3$. In terms of symmetry, however, these four cannot be equated. Graupner and Brunel (2007) assumed that PKA activation depends on CaM. Although its validity is not very clear, this assumption allowed them to describe the effects of both PKA and CaN on I1 in a unified manner: both PKA-dependent phosphorylation and CaN-dependent

dephoshorylation rates of I1 were modeled with simple Hill functions of CaM:

$$\nu_x(CaM) = k_x^0 + \frac{k_x}{1 + (K_x/CaM)^{n_x}} \tag{1.17}$$

where $x = CaN, PKA$, k_x^0 is CaM-independent base activity. Finally, they describe the interaction between PP1 and I1:

$$\begin{aligned} \frac{dI1}{dt} &= \frac{dPP1}{dt} - \nu_{CaN} I1 + \nu_{PKA} I1_0 \\ \frac{dPP1}{dt} &= -k_{11} I1 \cdot PP1 + k_{-11}(PP1_0 - PP1) \end{aligned} \tag{1.18}$$

where $PP1_0$ and $I1_0$ are total PP1 and I1 concentrations. Note that their $k_{\pm 13}$ is $k_{\pm 11}$ here.

1.2.3.3.2 Graupner and Brunel (2007) model emulates STDP

In the Graupner and Brunel (2007) model the concentration of phosphorylated subunits of CaMKII ($CaMKII^*$) can be bistable for a range of calcium concentration that actually defines two regions of bistability (shaded areas on fig. 1.28).

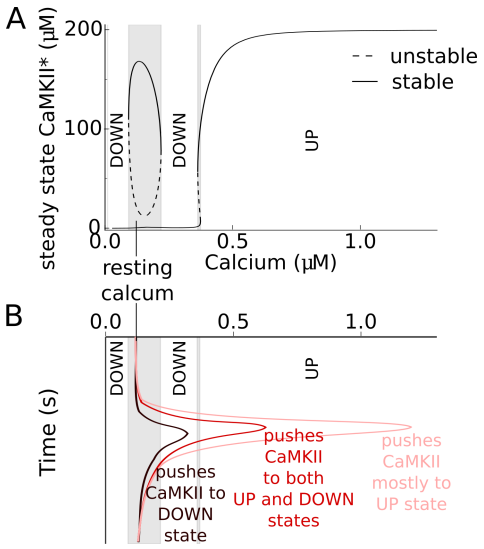

Figure 1.28: **A**. Bifurcation diagram (BD) for phosphorylated CaMKII when calcium concentration is considered as a parameter. **B**. Calcium transients can pass through different regions at BD thus pushing $CaMKII$ to UP or DOWN state depending on the instantaneous calcium concentration. For details, see text. Figure at panel A is obtained with the source code of Graupner and Brunel (2007) https://senselab.med.yale.edu/modeldb/ShowModel.cshtml?model=114452.

This model can be exposed to sequences of postsynaptic calcium transients evoked in STDP protocols. As a result of such simulated STDP protocols, with each calcium transient, calcium raises from its resting state to its peak value, and passes through various regions on bifurcation

diagram at fig. 1.28B.

Repeated calcium transients of high amplitude push CaMKII towards high phosphorylation state (UP), while repeated calcium transients of small amplitude push CaMKII towards low phosphorylation state (DOWN). When calcium returns to its resting value at which both UP and DOWN states are possible (for which $CaMKII^*$ is bistable), the outcome of the protocol (UP or DOWN state) is determined by the state of CaMKII. Accumulation of large numbers of high amplitude calcium transients during the protocol can push CaMKII into basin of attraction of UP state, so that when calcium is back at its resting state, CaMKII ends up the UP state. Because the resting "basal" calcium concentration (roughly 0.1 μM) lies in the leftmost bistable region (gray in fig. 1.28), a given synapse at rest can either be in the UP state or in the DOWN state.

A major issue with this model (as with almost all molecular-level models of synaptic plasticity) is that it displays only two stable states (UP and DOWN) so it cannot be directly used to reproduce the usual 3 states of STDP: no plasticity, LTP and LTD. To circumvent this issue, the authors assume that, before the beginning of the STDP protocol, half of the synapses are initially in the UP state, and half in the DOWN state. If a calcium transient evoked by the protocol is too small and calcium remains well in the leftmost bistable domain (much lower than the black trace at fig. 1.28), each synapse remains on its branch of steady state (UP or DOWN), and the global effect is no change in synaptic weight. If now the calcium transient becomes larger than the end of the leftmost bistable region but remains smaller than the rightmost bistable region (black trace at fig. 1.28), the only stable steady state becomes the DOWN state so half of the synapses (those that were initially UP) undergo a UP-to-DOWN transition. At the level of the synapse population, this yields an effective LTD. If now the calcium transient is noticeably larger than the rightmost bistable region (light red trace), the UP synapses remain in their UP state, but those that were initially DOWN switch to the UP state, thus mimicking an effective LTP.

Therefore, depending on the amplitude of calcium transients, the concentration of phosphorylated CaMKII ($CaMKII^*$) can end up in either UP or DOWN state. This is reminiscent of the calcium-control hypothesis of Shouval, Mark F Bear, and Leon N Cooper (2002):

- small amplitude calcium transients produce nothing;
- medium calcium transients produce transition from UP to DOWN states thus LTD;
- high calcium transients produce transitions from DOWN state to UP thus LTP.

Moreover, when the population of synapses was exposed to the classical STDP protocol of Bi and Poo (1998) (60 1-Hz paired pre-then-post or post-then-pre stimuli), the calcium transients (with suitable parameters) reached intermediate amplitude for small negative (post-than-pre) but were

much amplified for small positive (pre-than-post) thus emulating the typical Hebbian-STDP curve for hippocampus, similar to the experimental results of Bi and Poo (1998) (fig. 1.29).

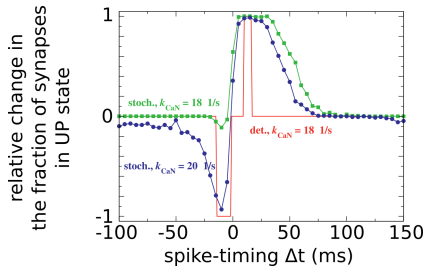

Figure 1.29: Emulation of STDP based on CaMKII bistability. The relative change in the fraction of synapses in UP state is taken as analogous to synaptic weight. Deterministic stimulation protocol produces the dependence on spike-timing of the relative change in the fraction of synapses in UP state (red line) of similar shape to the STDP-curve of Bi and Poo (1998). To achieve a smooth curve better matching to Bi and Poo (1998), stochastic stimulation (green and blue lines with symbols) and adjustment of a parameter were required (blue line). Stochastic stimulation results (where the maximal conductance of NMDAR and VSCC are randomly chosen upon each pre- and postsynaptic spike respectively) are shown for $k_{CaN} = 18$ 1/s (green line with squares, same value as in deterministic case) and $k_{CaN} = 20$ 1/s (blue line with circles). Modified from Graupner and Brunel (2007).

Despite of its success in describing hippocampal Hebbian STDP the model of Graupner and Brunel (2007) cannot be used to describe anti-Hebbian STDP at cortico-striatal synapses because:

1) the model does not account for endocannabinoid system. In Graupner and Brunel (2007), both t-LTD and t-LTP are NMDAR-CaMKII-dependent, whereas at cortico-striatal synapses t-LTD is endocannabinoid dependent. Furthermore, the form of t-LTP at cortico-striatal synapses expressed for low number of stimuli depends on both endocannabinoids and TRPV1 activation.
2) the model does not consider several calcium sources found important for plasticity at cortico-striatal synapses and their specific roles. T-type VSCC (along with L-type important for both t-LTP and t-LTD at cortico-striatal synapses), TRPV1 (important for t-LTP) and CICR (t-LTD) are absent in Graupner and Brunel (2007). While their model does include NMDAR, its role is different from that at cortico-striatal synapses where t-LTP is only NMDAR dependent.

1.3 Summary

The efficiency of interneuronal signal transmission changes in the process of synaptic plasticity. A form of synaptic plasticity dependent on temporal patterns of activations (spikes) of connected neurons, spike-timing dependent plasticity (STDP), depends on the various components of subcellular networks of biochemical reactions. The overall shape of STDP as well as the implicated biochemical signaling pathways involved in STDP vary across the brain regions.

In basal ganglia, at synapses from cortical pyramidal neurons (presynaptic) to medium-sized spiny neurons of striatum (postsynaptic), two molecular components appear to be crucial for synaptic plasticity: CaMKII, downstream of the postsynaptic signaling pathway starting from calcium, and presynaptic CB1R activation, downstream of the postsynaptic signaling pathways starting from calcium and GPCR-mediated synthesis of endocannabinoids (eCB). A model aiming at reproducing these major features of cortico-striatal STDP has to include major sources of calcium: VSCC, NMDAR, TRPV1, CICR, and pathways leading to the production of endocannabinoids: 2-AG and AEA. Moreover, such a model has to provide the link between the plasticity and CaMKII and CB1R activation. Finding this link for CB1R is crucial to understand eCB-t-LTP, the new form of endocannabinoind-dependent STDP observed at cortico-striatal synapses for short durations of stimulation with low number of stimuli. More generally, such a model would provide valuable hints of how endocannabinoids can support bidirectional STDP (both depression and potentiation). To develop a mathematical model of cortico-stratal STDP, in the following chapter, I will start from adapting the Graupner and Brunel (2007) model of hippocampal NMDAR-CaMKII-dependent STDP to cortico-striatal synapses. This model requires that calcium input is precisely detailed. I therefore modelled the major sources of calcium that were found important for cortico-striatal STDP (NMDAR, L- and T-type VSCC, TRPV1, and CICR). To study the endocannabinoid-dependent plasticity (eCB-t-LTD and especially the new eCB-t-LTP), I modelled the activation of cannabinoid receptor type 1 (CB1R) by postsynaptically produced endocannabinoids. I then exposed the model containing all these striatum specific components to the stimulation protocol that induces STDP in experiments.

Chapter 2

A mathematical model of cortico-striatal STDP

2.1 In a nut shell

I developped a model that couples the model of Graupner and Brunel (2007) with calcium sources important for cortico-striatal STDP (NMDAR, L- and T-type VSCC, TRPV1, and CICR) and endocannabinoid signaling. This model is first calibrated to reproduce the NMDAR-dependence of anti-Hebbian STDP at cortico-striatal synapses. In this calibrated model, activation of the endocannabinoid system depends on the parameters of the STDP stimulation protocol. Moreover, the spike timing-dependence of CB1R activation in the model is related to the spike timing-dependence of eCB-dependent plasticity in experiments. To describe this relation, I introduced a phenomenological hypothesis of endocannabinoid-control of plasticity: a low activation of CB1R leads to no plasticity, a medium activation of CB1R leads to LTD, medium-to-high activation of CB1R leads to no plasticity, whereas a high activation of CB1R leads to LTP. With this phenomenological hypothesis, the model qualitatively reproduces both eCB-t-LTD and the recently discovered form of plasticity, eCB-t-LTP. I then used the model to provide model-based predictions that were confirmed in the lab of our experimental collaborators (Laurent Venance Lab, CIRB, Collège-de-France, Paris, France), thereby validating the model. Using the validated model, I studied the dependence of plasticity on the patterns of neuronal activation beyond the typical artificially regular STDP protocol. Furthermore, I extended the validated model to study modulation of cortico-striatal STDP by glutamate clearance from the synaptic cleft and by dopamine.

2.2 Towards the model

2.2.1 CaMKII-dependent plasticity at cortico-striatal synapses

The model of Graupner and Brunel (2007) provided a connection between calcium, CaMKII and STDP in hippocampal synapses. In other brain regions, however, the molecular mechanisms of plasticity can be different from that found in hippocampus.

An important molecule in Graupner and Brunel (2007), inhibitor 1 (PPP1R1A) is the major isoform in hippocampal neurons, but not in striatal MSN. MSN are indeed enriched with another isoform called, dopamine and cAMP-regulated phosphoprotein Mr 32,000 (DARPP-32 or PPP1R1B). DARPP-32 is therefore known to control plasticity in MSNs instead of I1 (Yger and Girault 2011). Moreover, since DARPP-32 is also connected to dopamine signaling, it represents a crosstalk between Ca-NMDAR signaling and dopamine signaling. However, the mechanisms by which DARPP-32 are implicated in Ca-NMDAR signaling are the same as I1. Similarly to I1 in hippocampus, DARPP-32 phosphorylation on threonine 34 (Thr-34) inhibits PP1 (Yger and Girault 2011) and therefore activates phosphorylation of CaMKII and synaptic plasticity. Just like I1, DARPP-32 phosphorylation on Thr-34 is controlled by the calcineurin PKA couple. However, compared to hippocampal neurons, activation of PKA by calcium in MSN is more established. At basal calcium, PKA in MSN is inhibited by DARPP-32 phosphorylation on its Thr-75 site. Dephosphorylation of DARPP-32 Thr-75 site is controlled by PP2A so that PP2A activation leads to PKA activation by disinhibition. Hippocampal neurons usually express high levels of the B56 subunit of PP2A that is not activated by calcium. However MSNs express large amounts of the B72 regulatory subunit of PP2A in place of B56. This striatum-specific regulatory subunit provides B72-PP2A with calcium-activation properties (Ahn et al. 2007). Therefore, calcium elevations in MSNs are expected to activate PP2A thus PKA. Modeling studies therefore suggested that dopamine and calcium cooperate to phosphorylate DARPP-32 (Nair, Upinder S. Bhalla, and Kotaleski 2016; Gutierrez-Arenas, Eriksson, and Kotaleski 2014; Lindskog et al. 2006; Nakano et al. 2010; Fernandez et al. 2005). Because this phosphorylation leads to CaMKII-activation and can trigger CaMKII-dependent synaptic plasticity through inhibition of PP1, the calcium-dopamine synergy supports theories of reinforcement learning where the dopamine signal is considered as a signal controlling calcium-dependent plasticity (Dayan and Balleine 2002). Note that dopamine signaling in the postsynaptic neurons (the MSN) is out of the focus of the current work. I however use the above data as a support that PKA is indeed activated by calcium in MSNs.

The original model of Graupner and Brunel (2007) that was developed for hippocampus used $n_{PKA} = 8$ as cooperativity exponent for PKA activation by Ca (eq. 1.17), and two regions of

bistability (fig. 1.28). In the striatum, experimental data suggests lower value for n_{PKA} (Ahn et al. 2007). I therefore lowered the value of n_{PKA} to 3. With this modification of the model and readjustment of its parameters, the model still exhibits the first region of bistability (the one that includes basal Ca concentration) but has lost the second one (compare fig. 2.1 with fig. 1.28). In the MSN, NMDAR is known to control t-LTP but, to our knowledge, NMDAR-dependence for t-LTD has never been described. A bifurcation diagram with a single bistability zone for NMDAR-dependent STDP thus appears sufficient.

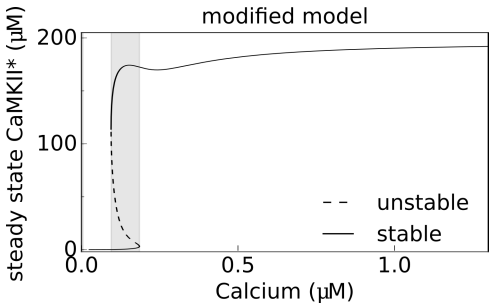

Figure 2.1: Bifurcation diagram (BD) for phosphorylated CaMKII when calcium concentration is considered as a parameter. Parameters modified from that of the original model: n_{PKA} lowered from 8 to 3, CaM_0=0.07052 μM, k_{CaN0}=0.05, k_{CaN} = 20.5, Kd_{PKA}=0.159, k_{PKA0}=0.0025, k_{PKA}=4.67

2.2.2 Spatial constrains

Due to the small volume of a dendritic spine, molecules can be present in small amounts. Therefore, the resulting fluctuations of concentrations can render inapplicable the approximation of perfect mixing described in sec. 1.2.3.2.2. The stochastic reaction-diffusion simulations of Oliveira, Kim, and Blackwell (2012) suggest that the colocalization of PKA and adenylate cyclase (AC) can amplify the phosphorylation of DARPP-32 on Thr-34. However, the overall shape of the transients of DARPP-32 phosphorylated on Thr-34 in response to a pulse of dopamine is similar to the case with no colocalization (see fig. 4C of Oliveira, Kim, and Blackwell (2012)). Therefore perfect mixing appears to be still effectively valid approximation. Moreover, spatially detailed stochastic model would require a greater number of parameters, some of which are often difficult to constrain experimentally: diffusion coefficients for mobile molecules, degree of clustering/colocalization among immobile ones. Therefore, for the sake of simplicity, in this thesis, I will use the assumption of perfect mixing.

2.2.3 Calcium sources

To provide calcium-dependent models of plasticity with calcium input one needs to model the major sources of cytosolic calcium. In doing so, one has to consider that the concentration of

calcium is significantly higher outside the cell than inside the cell. Because of this, the movement of calcium ions is set by both diffusion and electrical force. Therefore, the GHK description should be preferred over Ohm's law (see sec. 1.2.2.1). The later statement is true if perfect mixing is assumed. However, a possibility of a local violation of this perfect mixing assumption should be considered unless proven otherwise. In this case, locally in a subvolume of a dendritic spine, the concentration of calcium might be comparable to that outside the cell.

In sec. 1.1, VSCC and NMDAR were presented as the two major sources of postsynaptic calcium involved in synaptic plasticity. However, other sources can also play a role. As we have seen in sec. 1.1.7.2.3, that at cortico-striatal synapses, t-LTD is dependent on CICR from internal calcium stores. Moreover, eCB-t-LTP at these synapses depends on the activation of TRPV1 that are also calcium permeable. A component of calcium current might be contributed by calcium permeable AMPAR (Carter and Bernardo L Sabatini (2004)). Carter and Bernardo L Sabatini (2004), however demonstrated that in the conditions relevant for STDP, when presynaptic stimulation is paired with postsynaptic depolarization, the NMDAR contribution to calcium dominates over that of AMPAR. Thus, for the sake of simplicity, I ignored calcium influx through AMPAR. Hence, for the modeling of the cortico-striatal STDP, I included four sources of calcium: NMDAR, VSCC, CICR and TRPV1.

2.2.3.1 NMDAR

When open, NMDAR are permeable to Na^+, K^+ and to lesser extent to Ca^{2+} ions. The total current is well described by Ohm's law approximation (sec. 1.2.2.1) (e.g. Koch (1999)). A simple way to model the calcium component of the total current is by approximating it by a fraction of total current (Ohm's law approximation). Alternatively, one can model calcium current component according to GHK. Assuming that the concentration of Mg^{2+} is fixed in the given environment, one has to focus on the variations of membrane potential and the concentration of glutamate in the synaptic cleft. In this case, NMDAR conductance (g_{NMDAR}) can be described with (Alain Destexhe, Zachary F Mainen, and Terrence J Sejnowski 1998):

$$\begin{aligned} g_{NMDAR} &= g^{max}_{NMDAR} P^{open}_{NMDAR} \\ P^{open}_{NMDAR} &= B(V) O_{NMDAR} \end{aligned} \tag{2.1}$$

where g^{max}_{NMDAR} is the maximal conductance, O_{NMDAR} is the fraction of NMDAR in the open state when no Mg^{2+} is present in extracellular medium (O_{NMDAR} can be interpreted as the probability of NMDAR to be in open state). P^{open}_{NMDAR} is the fraction/probability of NMDAR in open state when Mg^{2+} is present in extracellular medium.

P^{open}_{NMDAR} multiplied by a constant factor can be used to compute permeability instead of conductance (if GHK is used instead of Ohm's law). For simplicity, I used the simplest kinetic model of NMDAR with only two states: open and closed (obtained by eliminating the state x_I in fig. 1.24, or fixing $x_I = 0$ in eq. 1.9). The non-linear function $B(V)$ describing magnesium block is given by (Jahr and Stevens 1990):

$$B(V) = \frac{1}{1 + [Mg^{2+}] \exp(-0.062V)/3.57} \tag{2.2}$$

2.2.3.2 VSCC

Because calcium concentration outside of the cell at rest is much higher than that inside, to describe calcium current, GHK description is to be preferred over the simpler Ohm's law. Thus one has to have an estimation of calcium concentration inside of a spine and outside of a cell. One also has to describe the dependence of permeability on membrane potential (voltage). Based on the dependence of steady state current on membrane potential, VSCCs are subdivided to several types (Hille 1992; Koch 1999). I considered the models of L- and T-type VSCC because both were found involved in cortico-striatal STDP (sec. 1.1.7.2.3).

Ca^{2+} L-type v1.3 channels in striatal neurons can be described by (Wolf et al. 2005):

$$\begin{aligned}
P_{CaLv1.3} &= p_{CaLv1.3} \cdot (m_{CaLv1.3})^2 \cdot h_{CaLv1.3} \\
\frac{dh_{CaLv1.3}}{dt} &= \frac{h^{\infty}_{CaLv1.3}(V) - h_{CaLv1.3}}{\tau^h_{CaLv1.3}/q^h_{CaLv1.3}} \\
\frac{dm_{CaLv1.3}}{dt} &= \frac{m^{\infty}_{CaLv1.3}(V) - m_{CaLv1.3}}{\tau^m_{CaLv1.3}(V)/q^m_{CaLv1.3}} \\
m^{\infty}_{CaLv1.3}(V) &= \frac{1}{1 + \exp(\frac{V - m^{half}_{CaLv1.3}}{m^{slope}_{CaLv1.3}})} \\
h^{\infty}_{CaLv1.3}(V) &= \frac{1}{1 + \exp(\frac{V - h^{half}_{CaLv1.3}}{h^{slope}_{CaLv1.3}})} \\
m^{\alpha}_{CaLv1.3}(V) &= \frac{c^{\alpha}_{CaLv1.3}(V - V_{CaLv1.3})}{\exp(\frac{V - V_{CaLv1.3}}{k^{\alpha}_{CaLv1.3}}) - 1} \\
m^{\beta}_{CaLv1.3}(V) &= c^{\beta}_{CaLv1.3} \exp(V/k^{\beta}_{CaLv1.3}) \\
\tau^m_{CaLv1.3}(V) &= \frac{1}{m^{\alpha}_{CaLv1.3}(V) + m^{\beta}_{CaLv1.3}(V)}
\end{aligned} \tag{2.3}$$

Here $P_{CaLv1.3}$ and $p_{CaLv1.3}$ are permeability and its maximum value respectively, $m_{CaLv1.3}$ and $h_{CaLv1.3}$ gating variables describing the voltage-dependent kinetics of the channel, V is membrane potential. $x^y_{CaLv1.3}$ where $x = q, c, k, h, m$, $y = h, m, half, slope, \beta, \alpha$ and $\tau^h_{CaLv1.3}$ are parameters

chosen to match experiments. A more detailed description of all parameters can be found (Appendix B).

Ca^{2+} T-type channels were not included in base version of the model (their inclusion is does not alter our key results, but increases complexity); they were only modeled in simulations comparing GHK vs. Ohm's law (for details see Appendix A.4.1, and Appendix C.1).

2.2.3.3 CICR

As a result of CICR, the concentration of intracellular calcium can oscillate. A simple two-variable model of IP3R-mediated calcium oscillations was developed by Li and Rinzel (1994). However in the famous Li and Rinzel (1994) model, IP3 concentration was considered constant (a parameter). This is hardly suitable in our case, since we need to account for the kinetics of DAG and IP3 that will give rise to 2-AG production and CICR, respectively. De Pittà et al. (2009) extended the model of Li and Rinzel (1994) to account for glutamate binding to mGluR and the kinetics of IP3 and DAG. De Pittà et al. (2009) aimed at modeling astrocytes; however, the same CICR related pathways are present in neurons. Therefore, I appled the model to neurons. The equations of De Pittà et al. (2009) read:

$$
\begin{aligned}
\frac{dIP3}{dt} &= \nu_{prod} - \nu_{degr} \\
\frac{dh_{CICR}}{dt} &= a_2 d_2 \frac{IP3 + d_1}{IP3 + d_3}(1 - h_{CICR}) - a_2 C \cdot h_{CICR} \\
\nu_{prod} &= \nu_{glu} + \nu_{PLC_\delta} \\
\nu_{glu} &= \nu_\beta \mathrm{Hill}(G, K_R + K_P \mathrm{Hill}(C, K_\pi, 1), 1) \\
\nu_{PLC_\delta} &= \frac{\nu_\delta}{1 + IP3/\kappa_d} \mathrm{Hill}(C, K_\delta, 2) \\
\nu_{degr} &= \nu_{3K} + r_{5P} IP3 \\
\nu_{3K} &= \widetilde{\nu}_{3K} CaMKII^* \cdot \mathrm{Hill}(IP3, K_3, n_3) \\
J_{IP3R} &= r_C (m_\infty n_\infty h)^3 (C_{ER} - C) \\
m_\infty &= \mathrm{Hill}(IP3, d_1, 1) \\
n_\infty &= \mathrm{Hill}(C, d_5, 1) \\
J_{SERCA} &= \nu_{ER} \mathrm{Hill}(C, k_{ER}, 2) \\
J_{leak} &= r_l (C_{ER} - C)
\end{aligned}
\tag{2.4}
$$

with the Hill function defined as

$$
\mathrm{Hill}(x, K, n) = \frac{x^n}{x^n + K^n}. \tag{2.5}
$$

C and C_{ER} are calcium concentrations in the cytosol and inside the ER respectively. C and C_{ER} are altered by the calcium fluxes from and to ER. J_{IP3R} is the calcium flux through IP3R (it flows out of ER); J_{SERCA} is the calcium flux caused by SERCA pumps (it flows into ER, opposite to J_{IP3R}); J_{leak} is the calcium leak flux out of ER. J_{IP3R} is caused by the activation of IP3R (with maximal permeability r_C) by both calcium and IP3. IP3 (and DAG) production (with the rate ν_{prod}) is due to calcium-activated PLC_δ (with the rate ν_{PLC_δ}) and GPCR-mediated activation of PLCβ (with glutamate-dependent rate ν_{glu}). ν_{glu} compresses the pathway starting from the activation of mGluR and leading to the activation of PLCβ. Glutamate (G) binding to mGluR leads to dissociation of α subunit from G protein. $G_{\alpha q}$ activates PLCβ that allows the production of diacylglycerol (DAG) and inositol (1,4,5)-triphosphate (IP3) from phosphatidylinositol (4,5)-bisphosphate (PIP2). These steps are summarized as a single glutamate-dependent rate of IP3/DAG production, ν_{glu} (linearity of mGluR activation to PLCβ activation is assumed). For the description of other parameters, see Appendix B. For full description of this model, see De Pittà et al. (2009).

The rate of IP3 degradation, ν_{degr} is determined by the activity of IP3 3-kinase (IP3-3K) (with rate ν_{3K}) and inositol polyphosphate 5-phosphatase (with maximal rate r_{5P}). To describe the phosphorylation of IP3-3K catalyzed by phosphorylated CaMKII, De Pittà et al. (2009) used the following approximation to describe $CaMKII^*$:

$$CaMKII^* \propto \text{Hill}(C, K_D, 4) \tag{2.6}$$

If one uses the forth order Hill function on the right-hand side of eq. 2.6 in place of $CaMKII^*$ in eq. 2.4 then $\widetilde{\nu}_{3K}$ can be interpreted as a constant that lumps together a constant converting the Hill function to actual $CaMKII^*$ and a constant related to IP3 dependence of IP3-3K. This is however a very simple model of $CaMKII^*$ compared to that of Graupner and Brunel (2007). Therefore, to interface the model of De Pittà et al. (2009) with that of Graupner and Brunel (2007), I computed the concentration of active CaMKII according to the model of Graupner and Brunel (2007) (eq. 1.15) and then I used it in eq. 2.4 instead of approximation used by De Pittà et al. (2009) (eq. 2.6). I changed the value and units of $\widetilde{\nu}_{3K}$ to account for the fact that $CaMKII^*$ in Graupner and Brunel (2007) represents actual concentration of phosphorylted CaMKII subunits (not a fraction as in De Pittà et al. (2009)).

2.2.3.4 TRPV1

TRPV1 conductance/permeability depends on the concentration of eCB agonist AEA and voltage (Castillo et al. 2012; Matta and Ahern 2007). Matta and Ahern (2007) have proposed a model of TRPV1 that reproduced: the dependence on voltage, temperature and agonist/antagonist

modulation of TRPV1. According to this model the probability of TRPV1 to be in its open state (P^{open}_{TRPV1}) can be modeled as:

$$\begin{aligned} P^{open}_{TRPV1} &= \frac{1}{1+\frac{1+J+K+Q+JK+JQ+KQ+JKQ}{L(1+JD+KC+QP+JKCD+JQDP+KQCP+JKQDCP)}} \\ Q &= \frac{AEA}{KD} \\ J &= J_0 \exp(\frac{zFV}{RT}) \\ K &= \exp(-(\Delta H - T\Delta S)/RT) \end{aligned} \tag{2.7}$$

where L, J_0, D, C, P are constants fitted to reproduce experiments; ΔS and ΔH change in entropy and enthalpy respectively; z is valence of ions flowing through TRPV1 (2 for Ca^{2+}); F is Faraday constant; R is universal gas constant; T is absolute temperature; AEA is anandamide concentration. One can use P^{open}_{TRPV1} to compute either permeability (if GHK is used) or conductance (if Ohm's law is used). I used Ohm's law and therefore computed conductance.

2.2.3.5 Postsynaptic production of endocannabinoids

2-AG production is thought to occur in the postsynaptic neuron where it is initiated by DAG production via mGluR- and M1R-activated PLCβ. DAG-Lipase α (DAGLα) then produces 2-AG from DAG. DAG is co-produced together with IP3 by PLCβ and PLCδ (thus follows the same production dynamics as IP3) and is consumed by DAGLα (yielding 2-AG) and DAG kinase (DAGK, yielding phosphatidic acid):

$$\frac{dDAG}{dt} = \nu_{prod}(C, IP3, G) - \frac{r_{DGL} \cdot DAGL_0 \cdot \varphi_{DAGL} \cdot DAG}{DAG + K_{DAGL}} - r_{DAGK} \cdot DAG \tag{2.8}$$

where $\nu_{prod}(C,\ IP3,\ G)$ is the term that describes IP3 production dynamics in De Pittà et al. (2009) (see eq. 2.4); $IP3$ is IP_3 concentration; φ_{DAGL} represents the fraction of activated DAGLα and $DAGL_0$ its total (activated + not activated) concentration (see below), r_{DGL} its maximal rate and K_{DAGL} its Michaelis constant for DAG; r_{DAGK} is the degradation rate by DAGK (that I assume linear for simplicity). 2-AG dynamics is obtained as the balance between postsynaptic synthesis (by DAGLα) and presynaptic degradation (by MAG-Lipase) (Piomelli 2003) upon retrograde transfer:

$$\frac{d2AG}{dt} = \frac{r_{DGL} \cdot \varphi_{DAGL} \cdot DAG}{DAG + K_{DAGL}} - r_{MAGL} 2AG \tag{2.9}$$

where $2AG$ is 2-AG concentration, r_{MAGL} lumps together both enzyme degradation by MAG-Lipase and 2-AG spillover out of the synapse.

How DAGLα is activated *in vivo* is unknown, except for the calcium-dependence of its activation. I therefore assumed a simple activation by calcium. Hence, DAGLα dynamics is modeled here by:

$$\frac{d\varphi_{DAGL}}{dt} = r_K C^{n_K} \cdot (1 - \varphi_{DAGL}) - r_P \cdot \varphi_{DAGL} \tag{2.10}$$

where n_K, r_K, r_P are constants.

In vitro experiments suggest that DAGLα activation could be triggered by phosphorylation by a kinase (Rosenberger, Farooqui, and Horrocks 2007). Therefore, an alternative, more complex, model of DAGLα activation could be that DAGLα is activated by a calcium-dependent kinase. If calcium-dependent deactivation of DAGLα by a phosphatase is also assumed, an alternative model of φ_{DAGL} can be described with:

$$\begin{aligned}\frac{d\varphi_{DAGL}}{dt} = &\left(r_{K0} + r_K \frac{C^{n_K}}{K_K^{n_K} + C^{n_K}}\right)(1 - \varphi_{DAGL}) \\ &- \left(r_{P0} + r_P \frac{C^{n_P}}{K_P^{n_P} + C^{n_P}}\right)\varphi_{DAGL}\end{aligned} \tag{2.11}$$

where K_x, n_x, r_x, for which x is K or P (for Kinase and Phosphatase respectively), are constants. Implementing this mechanism in our model does not appreciably alter the results presented below.

Finally, to model AEA synthesis, I considered the well-documented 2-step pathway (Starowicz, Nigam, and Di Marzo 2007):

$$PE + PC \overset{AT}{\rightarrow} NAPE \overset{PLD}{\rightarrow} AEA$$

with PE: phosphatidylethanolamine, PC: phosphatidylcholine, AT: N-acetyltransferase, NAPE: N-Arachidonyl-Phosphatidyl-ethanolamine and PLD: NAPE-selective phospholipase D. Note that alternative synthesis pathways might exist, but because their relevance to neurons and MSNs is not clear yet (Starowicz, Nigam, and Di Marzo 2007), I did not consider them here. NAPE synthesis was modeled under the assumptions that i) PC and PE are in excess amounts and ii) half-maximal activation of AT is obtained at Ca^{2+} concentrations (around 0.2 to 0.5 mM, see Hansen et al. (1998)) that are well above the largest baseline calcium level in the model (allows to approximate AT-dependent rate by a linear function of calcium). Under those assumptions,

$$\frac{dNAPE}{dt} = \upsilon_{AT} C - r_{PLD} \frac{NAPE}{K_{PLD} + NAPE}$$

where ν_{AT}=$r_{AT}[PE][PC]/K_{act}$ with r_{AT} the maximal rate of AT and K_{act} its calcium activation constant. r_{PLD} and K_{PLD} represent PLD enzyme activity and its Michaelis-Menten constant,

respectively. Likewise, the second step (AEA production) was modeled as

$$\frac{dAEA}{dt} = r_{PLD}\frac{NAPE}{K_{PLD} + NAPE} - r_{FAAH}\frac{AEA}{K_{FAAH} + AEA}$$

where the latter summand represents AEA degradation by FAAH; r_{FAAH} and K_{FAAH} represent FAAH enzyme activity and its Michaelis-Menten constant, respectively. Now, AEA synthesis is expected to proceed at a much faster rate than NAPE synthesis, so that NAPE is found at very low levels in cells (Hillard and Campbell 1997). The corresponding quasi-steady state assumption on NAPE concentration ($dNAPE/dt \approx 0$) then simplifies the expression of AEA dynamics to a single equation:

$$\frac{dAEA}{dt} = \nu_{AT}C - r_{FAAH}\frac{AEA}{K_{FAAH} + AEA} \tag{2.12}$$

2.2.3.6 CB1R activation and desensitization

I modelled CB1Rs activation with a simple three-state kinetic model: activated / open (x_{CB1R}), desensitized (d_{CB1R}) and inactivated (i_{CB1R}):

$$\begin{aligned}
\frac{dx_{CB1R}}{dt} &= \alpha_{CB1R} \cdot eCB \cdot i_{CB1R} - (\beta_{CB1R} + \gamma_{CB1R})x_{CB1R} \\
\frac{dd_{CB1R}}{dt} &= -\epsilon_{CB1R}d_{CB1R} + \gamma_{CB1R}x_{CB1R} \\
x_{CB1R} + d_{CB1R} + i_{CB1R} &= 1
\end{aligned} \tag{2.13}$$

where $eCB = 2AG + 0.10AEA$ accounts for the fact that AEA is also a partial agonist of CB1R (Freund, Katona, and Piomelli 2003). I assumed here that AEA is 10-times less efficient than 2-AG; α_{CB1R}, β_{CB1R}, γ_{CB1R} and ε_{CB1R} are the rate constants for the transitions between states. This model is a particular case of kinetic scheme fig. 1.24 with $x_C = i_{CB1R}$, $x_O = x_{CB1R}$, $x_I = d_{CB1R}$, $k_{1f} = \alpha_{CB1R}$, $k_{1b} = \beta_{CB1R}$, $k_{2f} = \gamma_{CB1R}$, $k_{2b} = 0$, $k_{3f} = 0$, $k_{3b} = \varepsilon_{CB1R}$.

I considered that the activation of presynaptic CB1R results in the activation of its downstream signaling (y_{CB1R}):

$$y_{CB1R} = k_{CB1R} \cdot x_{CB1R} + C_1 \tag{2.14}$$

y_{CB1R} describes the total endocannabinoid dependent activation of the presynaptic signaling involved in plasticity and will be referred to as "CB1R activation" below; C_1 is a constant that accounts for presynaptic plasticity modulation by e.g. tonic dopamine (see chapter sec. 2.10.1)

2.3 Putting it all together

By now, we have separate models of the subcellular components involved in cortico-striatal STDP. However, to simulate STDP protocols and their pre- and post-stimulations, these components should be connected to each other and linked to membrane voltage dynamics. To this end, we have to model: i) glutamate release caused by presynaptic extracellular cortical stimulation and ii) voltage change of postsynaptic membrane as a result of bAP caused by postsynaptic current injection. To model the response to electrical stimulation, we have to model electrical currents through the postsynaptic membrane. We also have to link electrical currents to calcium fluxes, calcium fluxes to calcium concentration, calcium concentration to calcium-CaMKII-dependent plasticity and endocannabinoid signaling.

2.3.1 Postsynaptic membrane

I modeled postsynaptic element as a single isopotential compartment with a passive electric response given by:

$$\begin{aligned} C_m\frac{dV}{dt} &= -g_L(V-V_L) - I_{AMPAR}(V) - I_{GABA_AR}(V) - I_{NMDAR}(V,G(t)) \\ &\quad - I_{VSCC}(V) - I_{TRPV1}(V,AEA) - I_{act}(t) \\ I_{VSCC}(V) &= I_{CaLv1.3}(V) + I_{CaT}(V) \end{aligned} \tag{2.15}$$

where V is membrane potential; I_{leak} is the leak current; g_L and V_L are leak conductance and reversal potential respectively; I_{AMPAR}, I_{GABA_AR}, I_{NMDAR}, I_{VSCC} and I_{TRPV1} are through AMPAR, $GABA_AR$, NMDAR, VSCC and TRPV1 respectively; $I_{CaLv1.3}$ and I_{CaT} are the currents through L-type v1.3 and T-type VSCC respectively (permeabilities modeled according to eq. 2.3 and eq. A.1); both of these currents are modeled according to GHK (eq. 1.3); I_{AMPAR}, I_{GABA_AR}, I_{NMDAR} and I_{TRPV1} are modeled according to Ohm's law (eq. 1.2) (see sec. 1.2.2.1); I_{act} is the action current accompanying the postsynaptic (somatic) stimulation (back-propagating action potential on top of a step-like depolarization); G is the glutamate concentration in the synaptic cleft and AEA denotes anandamide concentration. To compute corresponding conductances, the fractions of open NMDAR, AMPAR and $GABA_AR$ are modeled according to (Alain Destexhe, Z. Mainen, and T. Sejnowski 1995) with two-state kinetic models and 1.0 mM Mg^{2+} (fig. 1.24 and eq. 1.9 without x_I state). NMDAR conductance is modeled with eqns. 2.1, 2.2. $GABA_AR$ and AMPAR conductances modeled with $g_x = g_x^{max}O_x$ where x=$GABA_A$,AMPAR, O_x is the probability of open state, g_x^{max} is maximal conductance.

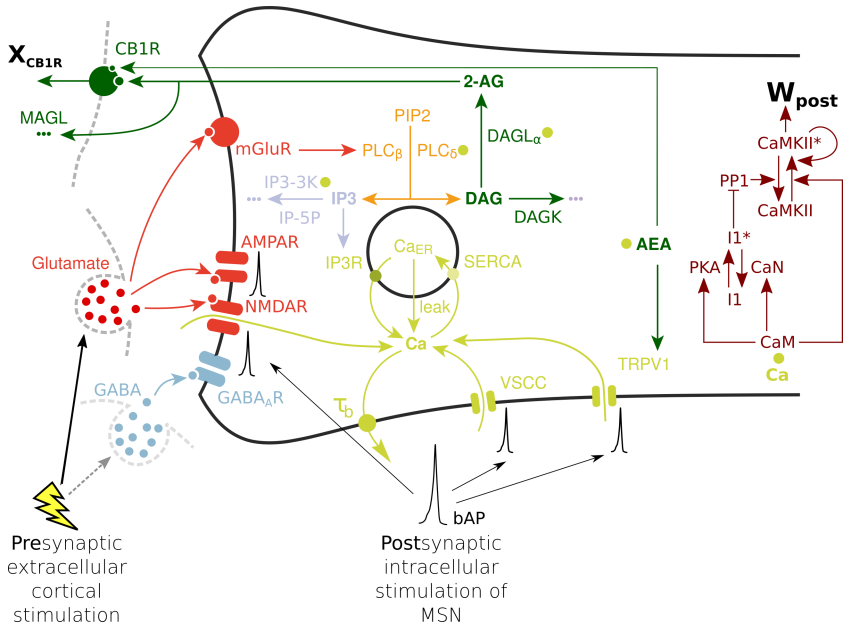

Figure 2.2: Our model includes calcium sources important for cortico-striatal STDP (calcium related components shown in light green). Glutamate related components are shown in red. Binding of glutamate to AMPARs, NMDARs and mGluR group-I leads to their activation. AMPAR and NMDAR activation triggers EPSCs and EPSPs. Calcium current through NMDAR alters intracellular calcium concentration. VSCC and TRPV1 also contribute to intracellular calcium dynamics. TRPV1 current is dependent on cytosolic calcium concentration via calcium-dependent synthesis of AEA (endocannabinoid related components shown in green). Another contribution to the calcium concentration comes from CICR. Calcium is released from ER to cytosol via two mechanisms: i) passive leak, ii) release through IP3R that is coactivated by calcium and IP3. Light purple shows IP3-mediated activation of IP3R and IP3-degradation pathways. IP3/DAG production pathway is shown in orange. This pathway requires PLCβ actviation that in turn activates in GPCR-mediated manner. mGluR group-I, GPCR activated upon binding of glutamate, is therefore controlling CICR. SERCA pumps oppose CICR by pumping calcium from the cytosol back into ER. Passive leaks of calcium are also considered. Cytosolic calcium resulting from interplay of aforementioned processes provides input for the model of CaMKII phosphorylation of Graupner and Brunel (2007) (dark red on the right part of the figure). The concentration of phosphorylated CaMKII subunits ($CaMKII^*$) sets the value of the postsynaptic weight W_{post}. GABA related components are shown in light blue. Note that because all electrical currents (through AMPAR, NMDAR, GABA, VSCC, TRPV1) affect membrane potential and at the same time depend on membrane potential, changes of currents affect each other globally through membrane potential. The mGluR and calcium mediated activation of PLCβ induces the production of 2-AG and AEA. 2-AG, and to a lower extent AEA, activates CB1R (x_{CB1R} is the fraction of non-desensitized CB1R), which then modulates the presynaptic weight, W_{pre}. Total synaptic weight W_{total} combines post- and presynaptic components: W_{post} and W_{pre}.

The total ionic current through TRPV1 was modeled as

$$I_{TRPV1}(V, AEA) = g_{TRPV1} \cdot V \cdot P^{open}_{TRPV1}(V, AEA) \tag{2.16}$$

where g_{TPRV1} is maximal conductance of TRPV1. The mathematical expression for the probability of TRPV1 to be open was taken from (Matta and Ahern 2007) (see eq. 2.7).

2.3.2 Subcellular dynamics

To model the dynamics of the cytoplasmic concentration of calcium, C, I computed calcium fluxes in three ways:

- for the currents computed according to GHK (I_x when x=Cav1.3, CaT), I transform a current (I_x) into a calcium flux (J_x) by multiplying it by a constant factor (ξ_x):

$$J_x = \xi_x I_x \tag{2.17}$$

- for the currents composed of several components (I_x when x=NMDAR, TRPV1) and computed according to the Ohm's law, I considered two possibilities when computing calcium flux resulting from the calcium component of the current:
  - either, calcium flux was computed according to eq. 2.17; calcium current component assumed to have the same shape as the total current (calcium current component obeys Ohm's law as well as total current),
  - or, calcium flux computed with GHK equation (eq. 1.3) modified to describe flux instead of current. Permeability replaced by a constant, $\widetilde{P_x}$, lumping the permeability (P_x) and the constant converting current to flux (ξ_x):

$$J_x = \widetilde{P_x} z_x^2 \frac{VF^2}{RT} \frac{[\mathrm{x}]_i - [\mathrm{x}]_o \exp(-z_x VF/RT)}{1 - \exp(-z_x VF/RT)} \tag{2.18}$$

    In the base version of the model, Ohm's law approximation was used. GHK approximation was only used in the model aiming to explain Hebbian/anti-Hebbian STDP switch based on the on/off state of postsynaptic $GABA_A$Rs (see Appendix C.1).

I moreover take into account the dynamics resulting from calcium exchange with internal calcium stores (Calcium-Induced Calcium Release, CICR). The equation for cytosolic calcium therefore reads:

$$
\begin{aligned}
T_C(C)\frac{dC}{dt} &= J_{ER} + J_{ch} - \frac{C - C_b}{\tau_{C_b}} \\
J_{ER} &= J_{IP_3R} - J_{SERCA} + J_{leak} \\
J_{ch} &= J_{NMDAR} + J_{VSCC} + J_{TRPV1}
\end{aligned}
\tag{2.19}
$$

where J_{NMDAR}, J_{VSCC}, J_{TRPV1} are calcium fluxes modeled as described above; J_{IP3R}, J_{SERCA}, J_{leak} are fluxes that describe CICR according to the model of (De Pittà et al. 2009) (eq. 2.4;eq. 2.6). In eq. 2.19, C_b is the basal cytosolic calcium level resulting from equilibration with calcium diffusion out of the cell and τ_{C_b} is the corresponding time scale. The presence of endogenous calcium buffer B (considered in quasi-equilibrium with cytosolic calcium at each time point) results in a calcium-dependent time scaling factor (see sec. A.5):

$$
T_x(x) = 1 + \frac{B_T}{K_{dB}(1 + x/K_{dB})^2} \tag{2.20}
$$

where B_T and K_{dB} are constants and $x = C$ or C_{ER}. C_{ER}, the calcium concentration in the endoplasmatic reticulum (ER) is given by

$$
T_{C_{ER}}(C_{ER})\frac{dC_{ER}}{dt} = -\rho_{ER}(J_{IP_3R} - J_{SERCA} + J_{leak}) \tag{2.21}
$$

where ρ_{ER} is the ER to cytoplasm volume ratio.

C provides input to the modified model of CaMKII phosphorylation (sec. 2.2.1).

2.3.3 Stimuli

After each presynaptic spike at time t^i_{pre} I modelled the time course of glutamate (G) as a single exponential decay with peak value G_{max}, baseline value G_0 and clearance rate τ_G:

$$
G(t) = G_0 + G_{max} \sum_i \exp\left(-\frac{t - t^i_{pre}}{\tau_G}\right) H(t - t^i_{pre}) \tag{2.22}
$$

where *H(x)* is the Heaviside function *H(x)*=1 if $x \geq 0$, 0 otherwise.

In several instances, delayed GABA release from FS interneurons following presynaptic cortical stimulation was simulated with

$$GABA(t) = GABA_0 + GABA_{max} \sum_i \exp\left(-\frac{t - t^i_{pre} - \Delta_{GABA}}{\tau_{GABA}}\right) H(t - t^i_{pre} - \Delta_{GABA}) \quad (2.23)$$

where Δ_{GABA} describes the delay of synaptic transmission from cortex to FS interneurons, $GABA_0$ is baseline GABA concentration from which GABA is elevated to its peak value $GABA_{max}$ following presynaptic stimulus at t^i_{pre}; τ_{GABA} decay time constant of single GABA elevation. To model postsynaptic action current back-propagating from the soma, I used a sum of a DC component arising from the step-depolarization and a spike-induced transient that decays exponentially:

$$\begin{aligned} I_{act}(t) &= -DC_{max} \sum_i R(t, t^i_{post}, DC_{dur}) \\ &\quad - AP_{max} \sum_i H(t - \delta - t^i_{post}) \exp\left(\frac{t - \delta - t^i_{post}}{\tau_{bAP}}\right), \\ R(t, t_0, L) &= H(t - t_0) - H(t - t_0 - L), \end{aligned} \quad (2.24)$$

where DC_{max} and DC_{dur} are the amplitude and the duration of step-current; AP_{max} is the amplitude of the action current producing bAP, δ is the delay between the outset of the step depolarization and that of the bAP; τ_{bAP} is the time scale for bAP decay. The time difference between the onset of EPSC and peak depolarization of bAP is given by

$$\Delta t = t^i_{post} + \delta - t^i_{pre} \quad (2.25)$$

2.4 Anti-Hebbian t-LTP with Graupner and Brunel (2007)

With Ohm's law approximation for calcium fluxes (for details about why it was chosen and alternative possibilities, see Appendix C.1), simulated STDP protocol with a large number (60-100) of 1-Hz pairings switches CaMKII from an initial DOWN state (no plasticity) to its UP state (t-LTP) for Δt=-15 ms, whereas it remains in the DOWN state for Δt=+15 ms (fig. 2.5). Thus the model emulates the timing-dependence of cortico-striatal anti-Hebbian NMDAR-dependent t-LTP. To explain how this emerges from the model, let us take a closer look at spike-timing dependence of calcium.

Fig. 2.3 shows the contributions of individual sources to a calcium transient for Δt=-15 (fig. 2.3A)

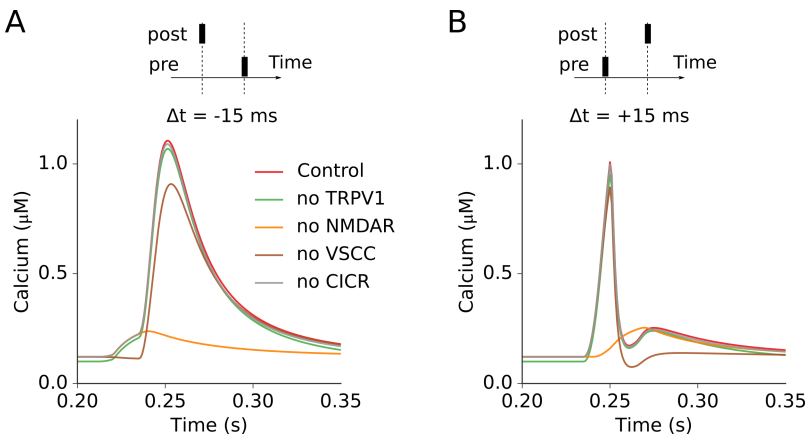

Figure 2.3: Decomposition of a calcium transient into its constituents for Δt = -15 ms (**A**) and 15 ms (**B**). One of the calcium sources is switched off and the calcium output of the model to single paired stimulus is reported.

and 15 ms (fig. 2.3B). For both Δt, NMDARs provide the major contribution to cytosolic calcium and VSCCs the second one. Thanks to the nonlinearity of the NMDAR flux-voltage curve and high-amplitude voltage transient described above, the calcium flux through NMDAR is transiently outwards for Δt=15 ms. This outward direction is because NMDARs are open (glutamate is present in synaptic cleft) when bAP reaches its peak, i.e. for voltages above NMDAR's reversal potential 0 mV, for which, the NMDAR current is outward. As a result, calcium transient is larger (has both larger width and maximum amplitude) for Δt=-15 compared to Δt=+15 ms. The difference of calcium transients between pre-post and post-pre is less pronounced for Δt's with larger absolute values ($|\Delta t| \geq 30$) (Fig. 2.4B). For large $|\Delta t|$, the coincidence of pre- and post- stimuli is impaired. As a consequence, the amplification of calcium transient due to the coincidence vanishes and no plasticity is observed at large $|\Delta t|$, in agreement with experimental data. The above difference in the amplitude and width of calcium transients at small $|\Delta t|$ then propagates downstream of calcium along the signaling pathway: larger calcium transients cause larger CaM transients (compare fig. 2.4C1 and C2). The later in turn results in larger $CaMKII^*$ transients for small post-then-pre Δt compared to small pre-then-post ones (compare fig. 2.4C1 and C2). As a result of repeated stimulations, $CaMKII^*$ transients build up with each post-pre pairing with Δt = -15 ms (fig. 2.5A) but they are not large enough to build up with pre-post pairings (fig. 2.5B). When the number of pairings (N_{pairings}) is large enough (more than 50), the $CaMKII^*$ transients with Δt = -15 ms have built up enough to enter the basin of attraction of the UP state. So when the stimulation ceases, $CaMKII^*$ remains in the UP state even long after the end of the stimulation protocol. As we associate UP state of CaMKII with LTP and DOWN with no plasticity, this means that large number of post-pre pairings with Δt=-15 ms lead to a t-LTP state that persists after the simulation (memory) whereas pre-post pairings trigger no plasticity.

The results of this subsection depend on the transient outflux of calcium via NMDAR for

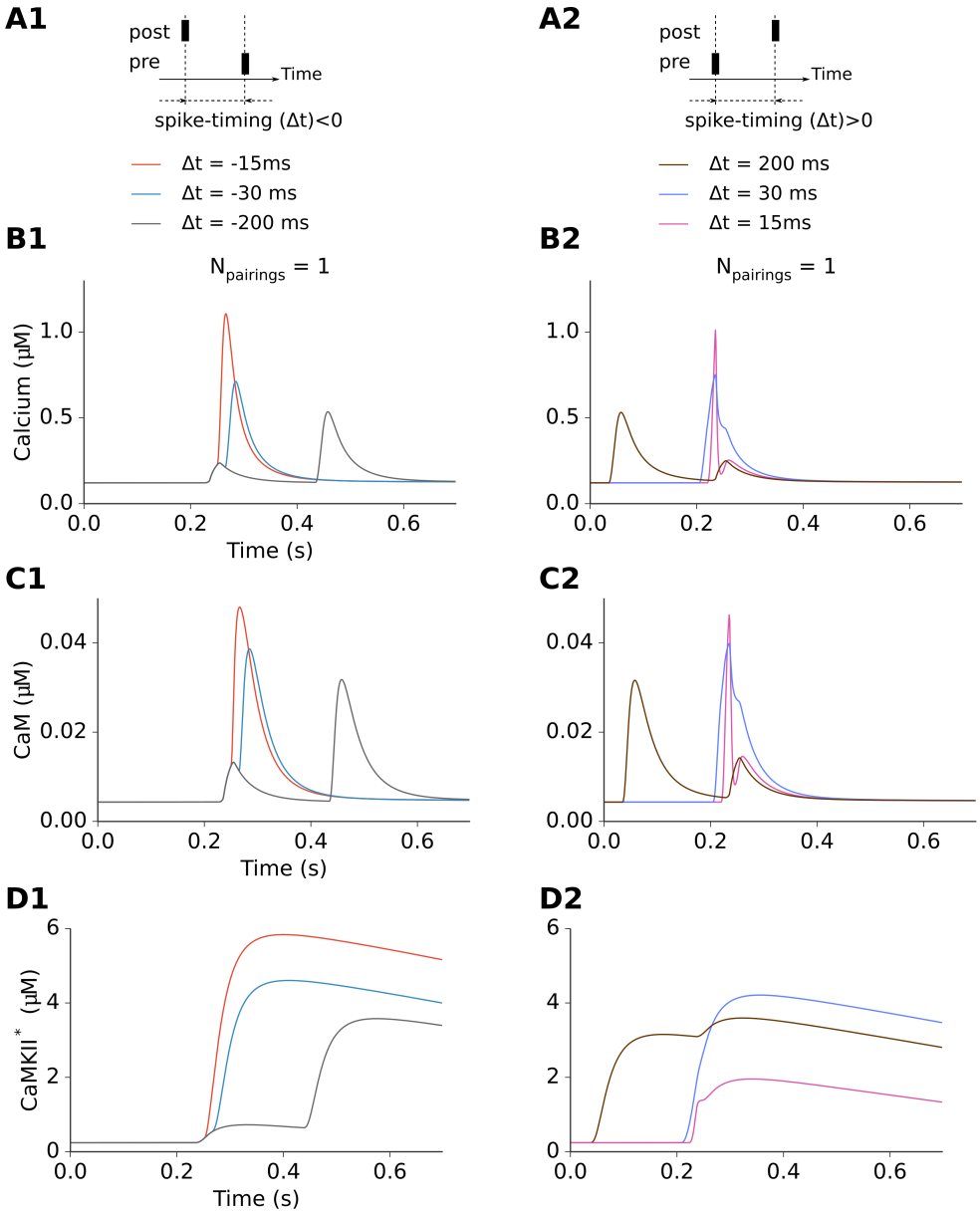

Figure 2.4: Transients of calcium (**B**), CaM (**C**) and phosphorylated CaMKII ($CaMKII^*$) (**D**) depending on spike timing. A single pre-before-post pairing with Δt=-15 ms (**A1**) leads to a larger calcium transient than a single post-before-pre pairing with Δt=+15 ms (**A2**) (compare **B1** and **B2**). Larger calcium transient (**B1**) leads to a larger CaM transient (compare **C1** and **C2**) and to a larger $CaMKII^*$ transient (compare **D1** and **D2**).

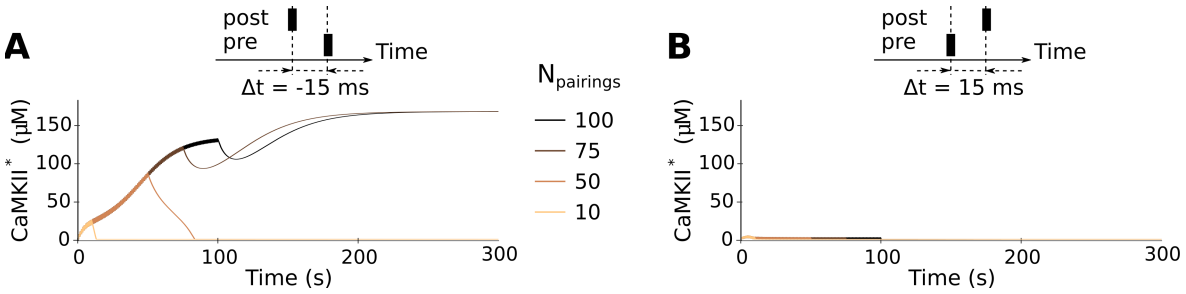

Figure 2.5: The model reproduces NMDAR-t-LTP with large numbers of pairings. The oncentration of phosphorylated (active) CaMKII depends on the number of pairings, N_{pairings}. With spike-timing Δt=-15 (**A**) and +15 (**B**) ms, 1 Hz pairings were delivered to the model with CaMKII initially in its DOWN state (low phosphorylation). The model reproduces NMDAR-t-LTP of basal ganglia: t-LTP for post-before-pre pairings (**A**), nothing for pre-before-post pairings (**B**).

pre-before-post pairing; that is the results depend on the validity of Ohm's law approximation for NMDAR (and TRPV1) calcium current. In order for this approximation to be valid, calcium concentration should be not too different on both sides of the membrane. In recent modeling study, Griffith, Tsaneva-Atanasova, and Mellor (2016) simulated calcium diffusion in a spine in response to EPSP-bAP pairing. The calcium concentration in the nanodomain around NMDAR was more than 20 times larger than the concentration of calcium averaged over spine volume (see their Fig.1C). In their model, during EPSP-bAP pairing, high calcium concentrations were contained in nanodomains around NMDARs and VSCCs (their Fig.1B). Therefore, the calcium concentration in such a nanodomain can be closer that outside the cell than to spine average; thus rendering Ohm's law approximation applicable. I took these results as a support for our model. We currently lack experimental data to directly support the idea that nanodomain calcium concentration is comparable to that outside the cell.

I have also evaluated a possibility of an alternative explanation of anti-Hebbian STDP. This was based on the model featuring postsynaptic $GABA_AR$ activation and NMDAR and TRPV1 calcium currents modeled with GHK. This alternative model however did not provide a reasonable explanation for Anti-Hebbian STDP. More calcium for post-before-pre than for pre-before-post pairings without GABA can be switched to less calcium for post-before-pre than for pre-before-post; however, Hebbian STDP, can be only switched to LTD or no plasticity for pre-before-post and LTD for post-before-pre because calcium amplitudes are decreased in the model with GABA. Hebbian $\rightarrow$ anti-Hebbian switch can be achieved if one either decreases plasticity thresholds with GABA signaling, or increases calcium currents (by increasing ξ_x and permeabilities, see eq. 2.17;eq. 2.18). This however is not supported experimentally. In Paille et al. (2013), it was proposed that by shifting the balance of NMDAR and VSCC calcium fluxes, depolarizing GABA current might provide an explanation for Hebbian-anti-Hebbian switch. The depolarizing effect of GABA could be present at distal synapses if bAP attenuation is strong enough (with depolarization from bAP, membrane potential should stay below the reversal potential of GABA,

-60 mV). Indeed, the recent work of Jędrzejewska-Szmek et al. (2016) suggests that the reversal of the polarity of STDP due to GABA might occur only at distal synapses (their fig. 6C). Our model however does not account for spatial effects and assumes little or no attenuation of bAP. Therefore, to obtain calcium-dependence on Δt corresponding to anti-Hebbian STDP, I used the simpler model without GABA and with Ohm's law approximation for NMDAR and TRPV1 currents (I thus favored nanodomain hypothesis). For details, see Appendix C.1.

However, regardless of the way anti-Hebbian STDP is achieved, what matters for the calcium-controlled plasticity is calcium transients themselves; the way they were generated is of less crucial importance for our work. Thus, even if the part of the model generating calcium transients may turn out disputable, our modeling of plasticity downstream calcium transients can be still correct.

2.5 Introducing endocannabinoid-dependent plasticity to the model

The data of Cui, Paille, et al. (2015) and Fino, Paille, Cui, et al. (2010) (figs. 1.20, 1.21, 1.19) can be summarized in the following table:

Table 2.1: Short summary of the experimental data by Cui, Paille, et al. (2015) and Fino, Paille, Cui, et al. (2010)

$N_{pairings}$	pre-post	post-pre	Long delay (> 30-40 ms)
10	no plasticity	eCB-t-LTP	no plasticity
100	eCB-t-LTD	NMDAR-t-LTP	no plasticity

With the model described so far, NMDAR-CaMKII-dependent plasticity allows to account for NMDAR-t-LTP and its dependence on the number of post-pre pairings. In the following, I will introduce both eCB-t-LTD and eCB-t-LTP (sec. 1.1.7.2.4).

Fig. 2.6 illustrates the model output regarding endocannabinoid signaling. The CB1 receptor is mostly activated by 2-AG, whose production is DAGLα-dependent and therefore calcium-dependent. As we have seen before, calcium transients are wider and of higher amplitude for post-pre pairings with small negative Δt than for pre-post pairings with small positive Δt, and higher for smaller $|\Delta t|$ than for large. As a consequence, the fraction of calcium-activated DAGLα is significant only for small values of $|\Delta t|$ (<25 ms) and larger for post-pre than for pre-post pairings (fig. 2.6B). Therefore, the differences in calcium transients also propagate downstream

to DAGLα activation. The differences of DAGLα activation propagate to 2-AG and ultimately to CB1R activation. At the end of the pathway, the calcium transients resulting from repeated pairings (fig. 2.6A) give rise to CB1R transients that depend on Δt too (fig. 2.6C). Therefore the above dependence of the calcium transients on Δt, are conserved along the eCB pathway and ultimately create a spiking-dependence in CB1R activation transients. But the presence of the signaling pathway in addition to periplasmic calcium channels has an effect that goes beyond the propagation of the timing dependence of calcium transients. Indeed, within a wide parameter range, the amplitude of the calcium peaks triggered by each paired stimulation has a very specific envelope (fig. 2.6A): for the first 10–20 pairings, the amplitude of calcium peaks increases, then it decreases until it reaches constant amplitude after 50 pairings. During those first 10–20 pairings, repeated activation of mGluRs progressively increases the quantity of IP3 in the cytoplasm, which contributes an extra influx of calcium to the cytosol, from the endoplasmic reticulum. This boost of cytoplasmic calcium however progressively disappears when N_{pairings} increases above 30-40 pairings because of the depletion of calcium in the endoplasmic reticulum. This dependence of the amplitude of the successive calcium peaks on N_{pairings} (first increase, then decrease) is transmitted to the amplitude of eCB transients and, ultimately, to CB1R activation (y_{CB1R}). The envelope is even more marked at the level of CB1R activation because of CB1R desensitization that amplifies the decay above 20 pairings (fig. 2.6C).

For all Δt, the amplitude of the CB1R activation (y_{CB1R}) peaks first increases for the first 10–20 pairings, then decreases to converge to constant amplitude. As a result, y_{CB1R} reaches large values only for short post-pre pairings (Δt around -15 ms) while even short pre-post pairings ($0 < \Delta t < 10$ ms) do not give rise to such large amplitude peaks.

This peculiar dynamics of y_{CB1R} brings a plausible explanation to the bidirectional features of eCB-dependent plasticity. To express the difference between the presynaptic eCB-dependent and postsynaptic NMDAR-CaMKII-dependent plasticity mechanisms, I will consider separately two components of synaptic weight: a postsynaptic weight W_{post} (proportional to the fraction of active CaMKII, $CaMKII^*$) and a presynaptic weight W_{pre} (to be related to eCB). In the experiments, eCB-t-LTP is observed for small N_{pairings} and small negative Δt, i.e. where the peaks of y_{CB1R} in our model exhibit the highest amplitudes across various (N_{pairings}, Δt) pairs. On the other hand, eCB-t-LTD or no plasticity is observed in the experiments in conditions where the peaks of y_{CB1R} in the model are of moderate or low amplitude, respectively. Therefore, a potential mecanism emerges whereby W_{pre} would depend on the magnitude of y_{CB1R} so that whenever y_{CB1R} reaches moderate amounts – i.e. when it is located between two threshold values, Θ_{LTD}^{start} and Θ_{LTD}^{stop} - W_{pre} drops (LTD); whereas W_{pre} rises (LTP) if y_{CB1R} is larger than a third threshold, Θ_{LTP}^{start} (see the dashed lines in fig. 2.6C1,C2 and summary in fig. 2.63D. W_{pre} remains unchanged outside those ranges, i.e. if $y_{CB1R} < \Theta_{LTD}^{start}$ or if $\Theta_{LTD}^{stop} < y_{CB1R} < \Theta_{LTP}^{start}$.

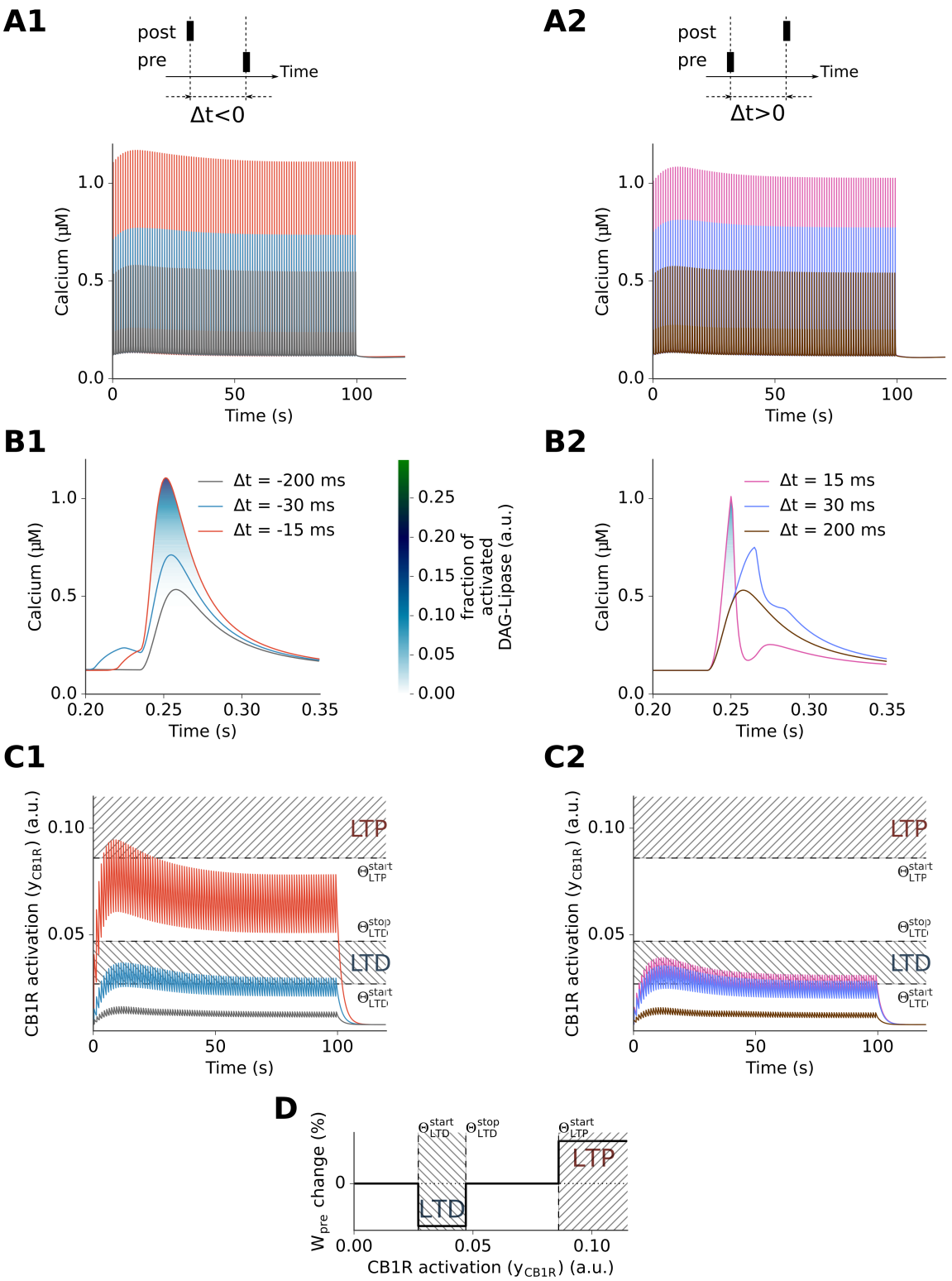

Figure 2.6: Spike-timing dependence in the endocannabinoid-signaling part of the model. **A-C.** Cytoplasmic calcium and CB1R activation for post-pre (first column) or pre-post pairings (second column). **D**. Schematic of our phenomenological model for eCB plasticity.

Combining this mechanism with the shape of y_{CB1R} evolution upon N_{pairings} indeed explains the main characteristics of corticostriatal STDP:

1. With short pre-post pairings (10<Δt<40 ms), y_{CB1R} reaches the LTD range (between Θ_{LTD}^{start} and Θ_{LTD}^{stop} (fig. 2.6C2) during most of the 100 pairings: each pairing thus reduces W_{pre}. Since pre-post pairings do not alter CaMKII-dependent W_{post} (fig. 2.5B), the net result is a reduction of W_{total}, i.e. the expression of eCB-t-LTD.

2. For few (5 to 30) post-pre-pairings, the amplitude of successive y_{CB1R} peaks overcomes Θ_{LTP}^{start} for 5 to 30 post-pre-pairings, resulting in an increase of W_{pre} sufficient for LTP. Since more than 50 post-pre pairings are needed to alter W_{post} (fig. 2.5A), the change of W_{total} is due to W_{pre} alone; the induced t-LTP is thus eCB-t-LTP (fig. 2.6C1).

3. Above 30 post-pre pairings, the amplitude of y_{CB1R} transients gets back below Θ_{LTP}^{start} so that the above W_{pre} increase is no more triggered, thus explaining why eCB-t-LTP is not expressed for $N_{\text{pairings}} > 30$. However, when N_{pairings}>50, the accumuation of active CaMKII described above (fig. 2.5) increases W_{post}, which triggers a sharp rise of W_{total}, reflecting NMDAR-t-LTP.

In conclusion, the mechanism proposed to account for eCB-STDP is the following: eCB-t-LTD requires moderate levels of CB1R activation, which can be reached with pre-post pairings.

eCB-t-LTP demands higher levels of CB1R activation that are reached only with 5–30 post-pre pairings, where every component of the model contributes maximally to CB1R activation (maximal cytosolic calcium influx from NMDAR, VSCC, TRPV1 and maximal calcium efflux from internal stores, combined with a small CB1R desensitization).

Beyond 30 post-pre pairings, calcium efflux from the internal calcium stores decreases while in parallel CB1R desensitization increases. CB1R activation becomes insufficient to maintain the elevation of the synaptic weight, so that eCB-t-LTP vanishes.

In the next section, I will formally express these mechanisms.

2.6 Formal introduction of synaptic plasticity and synaptic weights

As explained above, I quantify the total synaptic weight, W_{total} as the product of a presynaptic and a postsynaptic components:

$$W_{total} = W_{pre} W_{post}. \tag{2.26}$$

A detailed biophysical modeling of the CB1R-dependent plasticity hypothesis described above is not feasible due in particular to the current lack of experimental data on the presynaptic signaling pathways relating eCB signaling to plasticity. Therefore, I chose to use a simple phenomenological mechanism. Essentially, I adapted the mechanism developed to describe the control of plasticity by calcium concentrations in Shouval, Mark F Bear, and Leon N Cooper (2002), assuming instead that it is the amount of CB1R activation that controls the presynaptic weight:

$$\Omega(y_{CB1R}) = \begin{cases} 1 - A_{LTD} & \text{if } \Theta_{LTD}^{start} < y_{CB1R} < \Theta_{LTD}^{stop} \\ 1 + A_{LTP} & \text{if } \Theta_{LTP}^{start} < y_{CB1R} \\ 1 & \text{otherwise} \end{cases} \tag{2.27}$$

where the function Ω sets the direction of plasticity: LTD, LTP or no plasticity, y_{CB1R} is defined by eq. 2.14 (sec. 2.2.3.6); the Θ's are the threshold levels of y_{CB1R} determining plasticity induction; A_{LTD} and A_{LTP} are parameters determining the rate of LTD and LTP induction respectively. I also define "W_{pre} change" (appears on fig. 2.6) as $\Omega(y_{CB1R})$-1. The dynamics of the presynaptic weight W_{pre} is then given by:

$$\begin{aligned} \frac{dW_{pre}}{dt} &= \frac{\Omega(y_{CB1R}) - W_{pre}}{\tau_{W_{pre}}(z_{CB1R})} = \frac{\Omega(k_{CB1R}x_{CB1R} + C_1) - W_{pre}}{\tau_{W_{pre}}(k_{CB1R}x_{CB1R} + C_2)}, \\ \tau_{W_{pre}}(z_{CB1R}) &= \frac{P_1}{P_2^{P_3} + {z_{CB1R}}^{P_3}} + P_4, \end{aligned} \tag{2.28}$$

$\tau_{W_{pre}}$ describes the time scale of presynaptic plasticity changes; $z_{CB1R} = k_{CB1R} \cdot x_{CB1R} + C_2$ describes the effects of CB1R activation dependent presynaptic signaling on $\tau_{W_{pre}}$; C_2 is a constant that accounts for the modulation of plasticity time scales; P_1–P_4 are constants chosen to yield rapid changes of W_{pre} for large $2AG$ values and very slow changes at very low $2AG$. This was chosen as a simple/parsimonious system to implement memory of the synaptic change, i.e. to ensure that the changes of W_{pre} triggered during the pairing protocol will persist after the protocol end. To account for experimental observation that the presynaptic weight ranges from about 50 to 300%, W_{pre} was clipped to 3.0 (hard bound).

For W_{post}, I refer to the NMDAR signaling pathway. The molecular steps along this pathway are well characterized from glutamate to CaMKII activation but the downstream molecular mechanisms, leading from CaMKII activation to changes of the synaptic weights are still unclear, especially in MSNs. Therefore, I adopt the hypothesis, already used in (Graupner and Brunel 2007) and others before, that the long-term (steady state) increase of W_{post} is proportional to the fraction of activated (phosphorylated) CaMKII. I assume that W_{post} increases linearly with the

concentration of phosphorylated CaMKII subunits ($CaMKII^*$). Since the largest postsynaptic LTP observed experimentally was about 450%, I set:

$$W_{post} = 1 + 3.5\frac{CaMKII^*}{CaMKII^*_{max}} \tag{2.29}$$

The system of ODE eqns. 2.4, 2.8, 2.9, 2.10, 2.12, 2.13, 2.15, 2.16, 2.19, 2.20, 2.21, 2.22, 2.24, 2.25, 2.26, 2.27, 2.28, 2.29 is integrated numerically (see Apendix A) until the synaptic weights reach stable values (typically observed for t $\approx$ 15 min after the end of the stimulation protocol). I use the final value of the pre- and postsynaptic weights to compute the total synaptic weight change due to the stimulation protocol. Note that I also take into account that the experimental precision on the spike-timing delay (δt) is around 2 to 5 ms. To emulate this, the simulation results were averaged (blurred) over this time window using convolution of W_{pre} and W_{post} with a normalized Gaussian function with zero mean and s.d. = 3 ms.

2.7 Fitting model to data

The work that I am going to present next is a product of collaboration with experimental lab. We used joint experimental-modeling approach to tackle the validity of the model and guide experiments based on the model's predictions. On the experimental part, the work was done in the Electrophysiology lab of Laurent Venance (CIRB, Collège-de-France, Paris) where striatal eCB-t-LTP was first discovered. Most of the data on eCB-STDP (including that needed for the validation of the model's predictions) was acquired by Yihui Cui, Hao Xu, and Vincent Paille.

2.7.1 The model fits the data

I then tested whether the model is able to reproduce the experimental data on cortico-striatal STDP outcome when both Δt and N_{pairings} are varied. The values of a large part of the parameters implicated in intracellular dynamics, eCB dynamics or electrophysiology in the model are restricted by previous experimental measurements (see Appendix B). To estimate the values of the parameters for which we lack previous experimental constraints, I used the experimental data shown in fig. 2.7 and in Cui, Paille, et al. (2015), that is, I optimized those parameter values so that the model emulates the synaptic weight changes triggered by STDP protocols with various spike timings Δt and numbers of paired stimulations N_{pairings} (data points at fig. 2.7). For more details on fitting, see Appendix A. The changes of the total synaptic weight for the whole range of Δt and N_{pairings} are illustrated in fig. 2.7A by the model-generated color-coded

map.

In agreement with the experiments, the outcome of plasticity in the model can be split along three domains:

- a first LTP domain for -3<Δt<-25 ms and 3<N_{pairings}<40,
- a second LTP domain for -10<Δt<-25 ms and N_{pairings}>50, and
- a LTD domain for 10<Δt<25 ms and N_{pairings}>20.

Note that the model correctly accounts for the presence of a plasticity gap for 40–60 post-pre pairings that isolates the two LTP domains in agreement with experimental observations (Cui, Paille, et al. 2015) and that the expression of plasticity does not change when N_{pairings}>100 (fig. 2.8A). To compare model and experimental data on a quantitative basis, fig. 2.7A2,A3 also show the average weight change for -25<Δt<-10 ms or 10<Δt<25 ms. Even quantitatively, modeling results (full lines) are in agreement with the experimental data (full circles). Likewise, fig. 2.7A4,A5 show the weight change for STDP protocols with 10 or 100 pairings and Δt ranging from -40 to 40 ms, i.e. cross-sections of the color-coded map along the vertical dashed lines. Again, model (full lines) matches experiments (full circles). Quantitative agreement is found for the amplitude and the sign of plasticity, as well as for the dependence of plasticity on spike timing. To our knowledge, this model is the first mathematical model able to account for the outcome of the plasticity when both Δt and N_{pairings} are varied. I ran simulations of model variants where parts of the signaling pathways were removed (*in silico* knock-out). In the NMDAR signaling knockout, I removed the whole signaling pathway downstream of NMDAR, i.e. calmodulin and CaMKII. Since W_{post} relies entirely on CaMKII activation, the NMDAR signaling knockout corresponds to a situation where the contribution of W_{post} is absent and only W_{pre} contributes to W_{total}. As expected, the post-pre NDMAR-dependent LTP is absent in this NMDAR signaling knockout model, but pre-post t-LTD and post-pre t-LTP (observed with low numbers of pairings: 5<N_{pairings}<35) are preserved (fig. 2.7B). Comparison with experimental data where NMDAR was blocked confirms the match between model and experiments (fig. 2.7B). Simulations of the CB1R *in silico* knockout model, where CB1R activation remains null whatever eCB levels are shown in fig. 2.7C. Because W_{pre} depends on CB1R activation, the CB1R *in silico* knockout model actually reflects the case were only W_{post} contributes to W_{total}. In this case, the only remaining plasticity domain is the LTP expressed for post-pre pairings (N_{pairings}>50). Again, averaging over -25<Δt<-10 ms and 10<Δt<25 ms with 10 or 100 pairings evidences the match of the model with experimental data in which CB1R was inhibited with AM251 (fig. 2.7C).

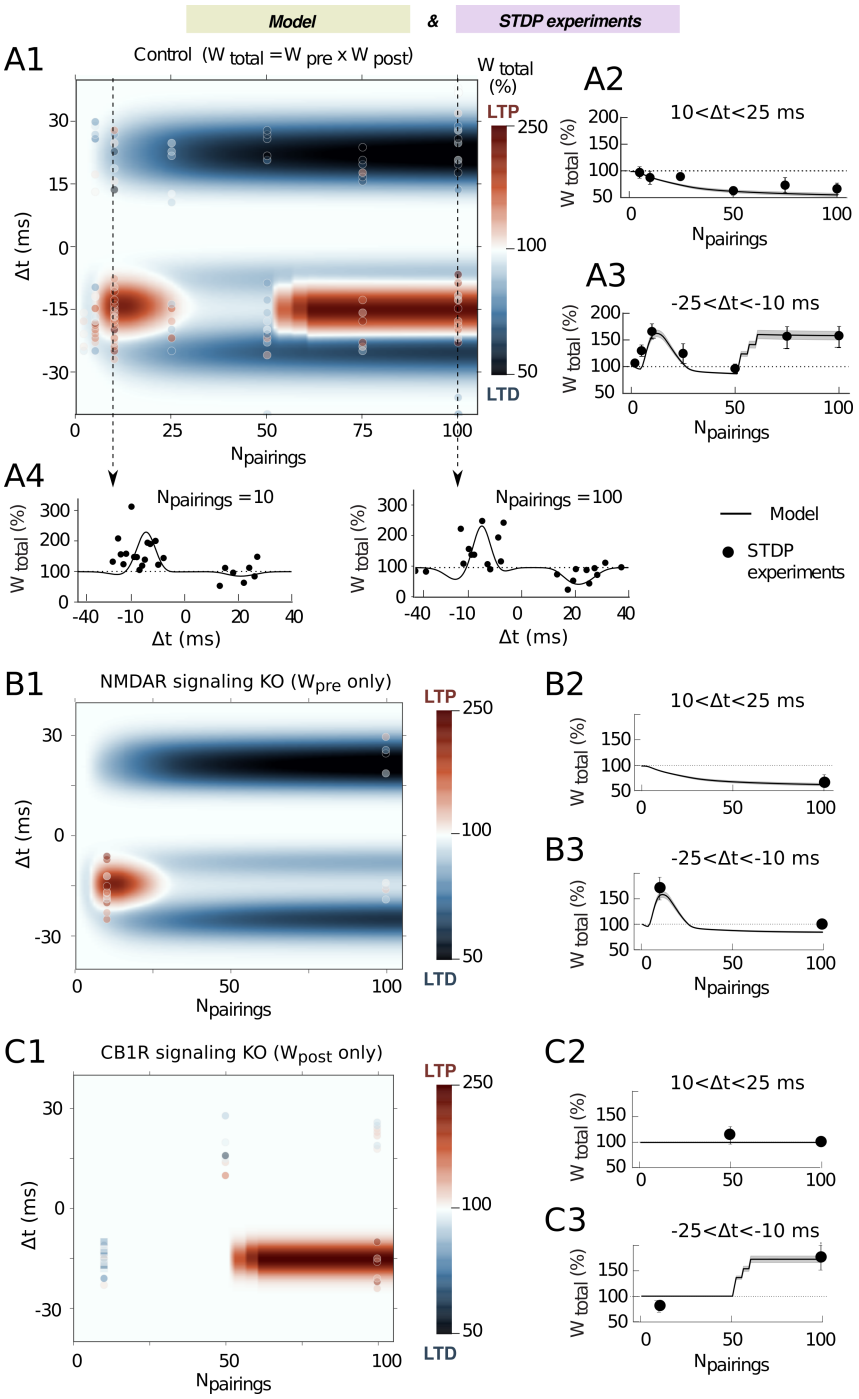

Figure 2.7: The mathematical model matches the experimental data. **A**. Changes of the total synaptic weight W_{total} (LTP and LTD) when N_{pairings} and Δt vary. **A1**. Color-coded changes of W_{total} in the (N_{pairings}, Δt) space. The color bar indicates the color code. The background map shows the simulation results whereas the color-coded points (same color-code as the simulations) are experimental results. The average changes with N_{pairings} of W_{total} integrated over short positive or short negative Δt are shown in (**A2**) and (**A3**), respectively. Cross-sections of the two-dimensional map (**A1**) along the N_{pairings}-axis are shown as changes of W_{total} with Δt, for N_{pairings}=10 (**A4**) or 100 (**A5**) pairings at 1 Hz. In (**A2-A5**), full black lines represent the simulation results whereas the full black circles show experimental results. **B,C**. Corresponding results obtained with variants of the mathematical model where NMDAR-signaling (**B**) or eCB-signaling (**C**) were knocked-out *in silico*. The 2D maps (**B1, C1**) use the same color code and symbols as (**A1**). The average changes of W_{total} over short positive or short negative spike timings Δt (**B2,C2**) and (**B3,C3**), respectively, use the same symbols as (**A1-2**).

2.7.2 Robustness of the model

I then analyzed how much the model outcome was sensitive to variations of the parameters.

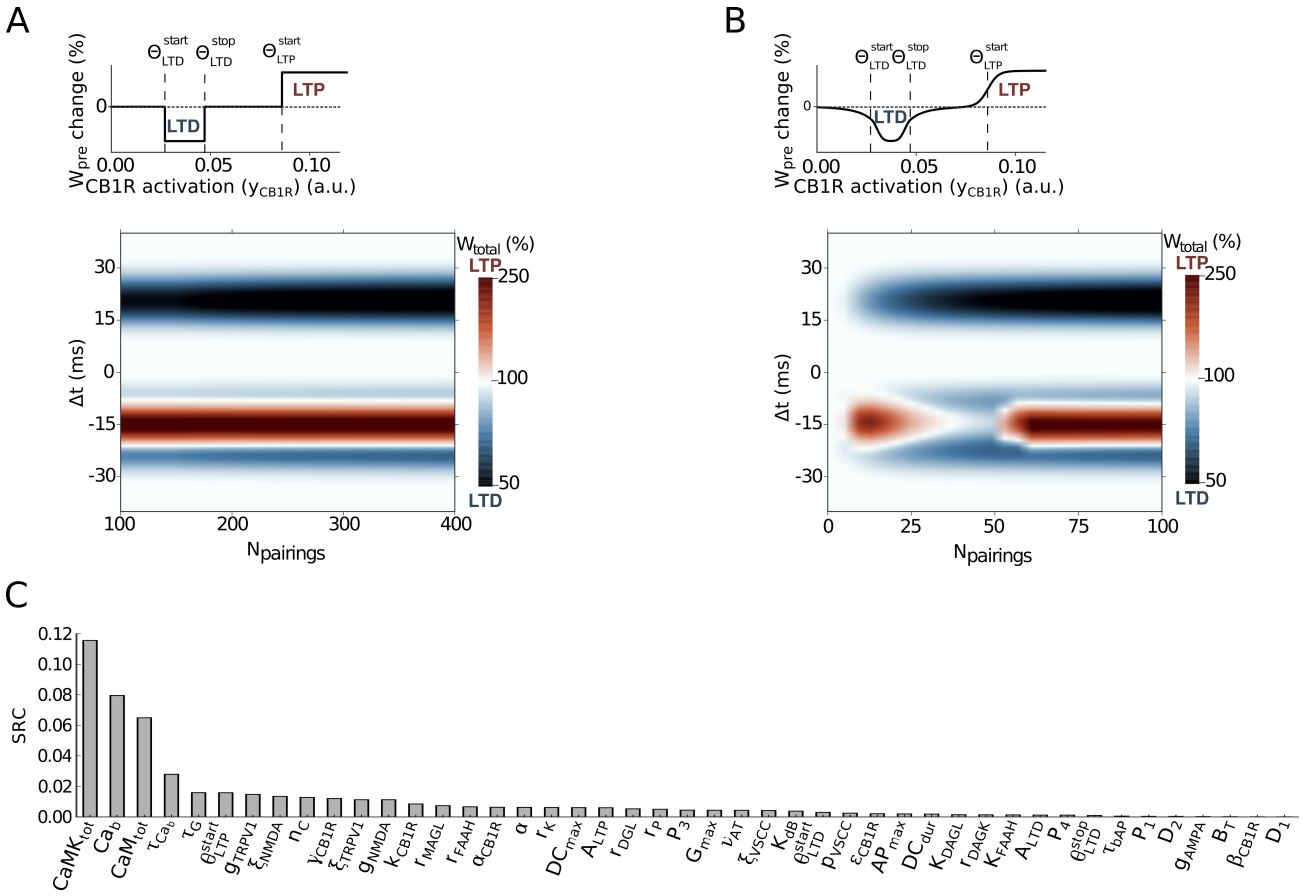

Figure 2.8: Robustness of the model. **A**. Output of the model for more than 100 pairings and (upper panel) the sharp threshold mechanism for eCB-plasticity given by (eq. 2.27). **B**. Output of the model when the sharp eCB plasticity is replaced by a smooth function given by eq. 2.30 with k_s=2 (upper panel). **C**. Sensitivity analysis of the model parameters. The parameters are ranked according to their standardized linear-regression coefficient (SRC, see Appendix A) that measures the sensitivity of the model output to variations of the parameter.

First, I changed the sharp thresholds for eCB-dependent plasticity for smooth thresholds. The sharp thresholding mechanism described by the function Ω above (eq. 2.27) was opted for its simplicity in the absence of further supporting information. Smooth thresholding mechanisms can be used instead with no major alteration of the main results. This can be demonstrated by replacing the function Ω (eq. 2.27) in eq. 2.28 by a smooth equivalent function whose graph is

depicted in fig. 2.8B:

$$\begin{aligned}
\Omega(y_{CB1R}) &= 1 + A_{LTD}\left(\mathrm{Hill}(y_{CB1R} - y_0, k_\omega(y_{CB1R}), 2) - 1\right) + \frac{A_{LTP}}{1 + \exp\left(\frac{\Theta_{LTP}^{start} - y_{CB1R}}{0.0013 k_s}\right)} \\
k_\omega(y_{CB1R}) &= 0.004 k_s + 0.01 k_s \left(1 - \frac{|y_{CB1R} - y_0|}{y_0 - \Theta_{LTD}^{start}}\right)^2 R(y_{CB1R}, \Theta_{LTD}^{start}, \Theta_{LTD}^{stop} - \Theta_{LTD}^{start}) \\
y_0 &= 0.5(\Theta_{LTD}^{stop} + \Theta_{LTD}^{start})
\end{aligned} \tag{2.30}$$

where the function R is rectangle function defined in eq. 2.24; k_s is a constant that determines the degree of smoothness (larger k_s corresponds to smoother Ω).

In spite of the smooth thresholds (even when smoothing is very substantial, $k_s = 3$), the model output is very similar to that obtained with sharp thresholds (compare the color map of fig. 2.8B with that of fig. 2.7A1). Therefore, our choice of a sharp thresholding for eCB-dependent plasticity is not crucial for the model output.

I further undertook sensitivity analysis of the model (explained in Appendix A). As expected, the most sensitive parameters were those related to reactions that are known from pharmacological experiments to be indeed crucial to STDP (fig. 2.8C): the total amount of calmodulin or CaMKII, post-synaptic calcium buffering (Elodie Fino, Paille, et al. 2010; Cui, Paille, et al. 2015), TRPV1 and NMDA channels (Elodie Fino, Paille, et al. 2010; Cui, Paille, et al. 2015), DAG-Lipase activity (Cui, Paille, et al. 2015) or FAAH and MAG-Lipase activity (see below). The model was also found sensitive to the dynamics of CB1R desensitization, in agreement with the importance of CB1R desensitization in the decay of eCB-LTP above 15–20 post-pre stimulations. The model was also sensitive to the value of the threshold for eCB-LTP induction (whether smooth or sharp). I suspect that this could explain the dispersion of the amplitudes of eCB-t-LTP (fig. 2.7A4). More surprising is the sensitivity of the model to the dynamics of glutamate in the synaptic cleft (decay rate τ_G). Alterations of the dynamics of glutamate release and uptake can thus be expected to play an important role in the control of STDP at the cortico-striatal synapse. This aspect is further studied in sec. 2.10.2.

2.8 Model predicts new data

In the Laurent Venance's Lab (CIRB, Collège-de-France, Paris, France), our collaborators tested several predictions of the model. In many cases, they found a good match between experiments and model's predictions. In the following, I will present the results of modeling against the corresponding new experimental data from Laurent Venance's lab.

2.8.1 Frequency-dependence of plasticity

In addition to spike timing and number of pairings, STDP is also known to depend on the pairing frequency. All the above results were obtained at 1 Hz. I tested the frequency dependence of eCB-LTP, i.e. the plasticity induced by a low number of pairings. fig. 2.9A shows the prediction of the model for N_{pairings}=10. When frequency increases above 1 Hz, the eCB-t-LTP triggered by post-pre stimulations (Δt<0) persists and is even observed for an increasingly large Δt range. The model also predicts the expression of another t-LTP, triggered by 10 pre-post stimulations (Δt>0) for frequency larger than 2 Hz. To test the validity of these model predictions, our experimental collaborators explored 10 STDP pairings for 0.1, 2.5 and 4 Hz (besides 1 Hz). 10 post-pre pairings at 0.1 Hz were able to induce t-LTP (133 ± 14, n=10, p=0.0386) (fig. 2.9B), which was not significantly different from eCB-t-LTP induced with 10 pairings at 1 Hz (p=0.1538) (fig. 2.9C). This result is not predicted by the model, for which the t-LTP induced by 10 post-pre pairings vanishes quickly below 1 Hz. At frequencies >1 Hz, they observed t-LTP for 10 post-pre pairings at 2.5 Hz (161 ± 15, n=23, p=0.0004) and 4 Hz (165 ± 14, n=22, p=0.0001), but also for pre-post pairings at 2.5 Hz (130 ± 14, n=12, p=0.0490 for Δt<+50 ms; 119 ± 9, n=20, p=0.060 for Δt<+100 ms) and 4 Hz (139 ± 13, n=10, p=0.0150). Moreover, the Δt range for t-LTP induction was considerably enlarged for post-pre pairings: from -30<Δt<0 ms at 1 Hz to -100<Δt<0 ms at 2.5 or 4 Hz. Note that for pre-post pairings, t-LTP could be observed for Δt<+50 ms (fig. 2.9D and E). Therefore, when the frequency of the pairings was increased to 2.5 or 4 Hz, experimental results show a very good match with the prediction of the model: first a symmetric Hebbian plasticity, i.e. the induction of t-LTP not only for post-pre but also for pre-post pairings, and, secondly an enlargement of the range of Δt in which plasticity was observed.

I then investigated the signaling pathways involved in those two t-LTP (fig. 2.10A). In experiments, our collaborators (Cui, Prokin, et al. 2016) observed that for 2.5 and 4 Hz STDP, post-pre t-LTP was not prevented with AM251 (CB1R blocker) (150 ± 11, n=6, p=0.0069) or with D-AP5 (NMDAR blocker) (135 ± 12, n=11, p=0.013) but was precluded with a mixture of both AM251 and D-AP5 (96 ± 3, n=9, p=01800). Similarly, for pre-post pairings at 2.5 and 4 Hz, t-LTP was still observed with AM251 (149 ± 15, n=7, p=0.0178) but was prevented with D-AP5 (134 ± 27, n=5, p=0.2684) or a mixture of AM251 and D-AP5 (88 ± 11, n=3, p=0.4090). The mathematical model with N_{pairings}=10 does not show such a mixed NMDAR- and eCB-LTP (both t-LTP are purely eCB-dependent). Remarkably, however, the t-LTP in the model becomes mixed for N_{pairings}>12. For 15 pairings (at 4 Hz), for instance (fig. 2.10B), the post-pre LTP in the model depends both on CB1R and NMDAR. Therefore, model predictions confirmed by experiments suggest that at frequencies above 1 Hz, the t-LTP triggered by 10–15 post-pre or pre-post pairings becomes both eCB and NMDAR-dependent.

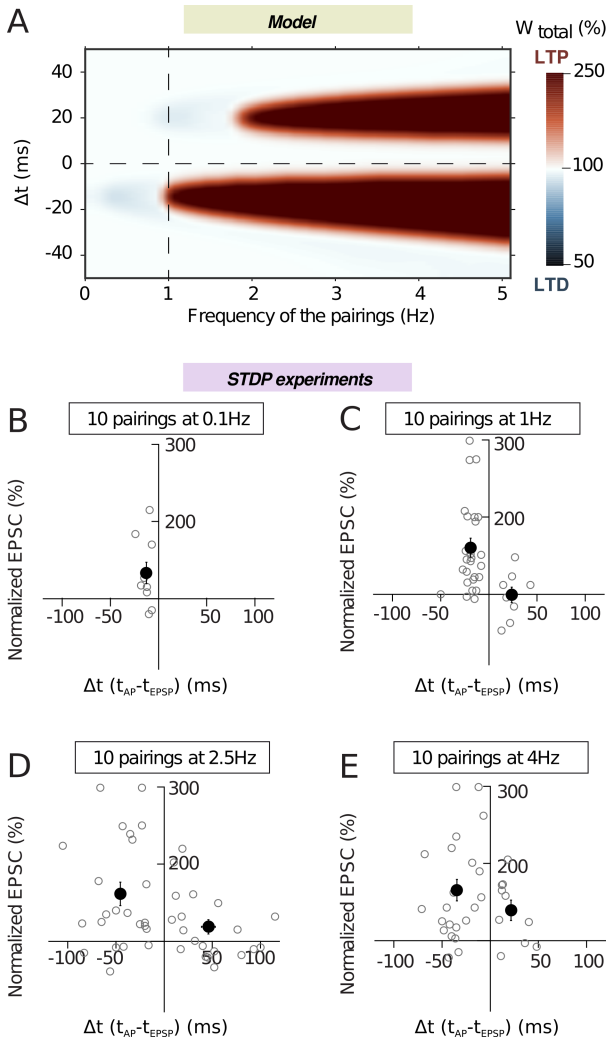

Figure 2.9: Model predicts the frequency dependence of eCB-t-LTP. **A**. Color-coded changes of W_{total} in the (Δt, frequency) parameter space for 10 pairings. Except the pairing frequency, all parameters are the same as in fig. 2.7. **B-E**. Graphs summarizing the recent experimental data from our collaborators (Cui, Prokin, et al. 2016): STDP occurs for 10 pairings at 0.1 Hz (**B**), 1 Hz (**C**), 2.5 Hz (**D**) and 4 Hz (**E**); each grey empty circle represent the synaptic efficacy changes 45–50 min after pairings protocols for a single neuron; the black circles represent the averages of plasticity.

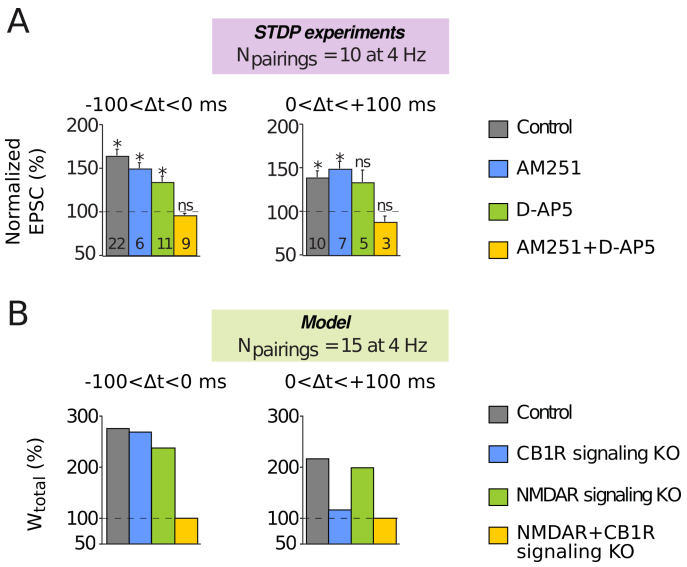

Figure 2.10: Both CB1R and NMDAR are involved in symmetric hebbian plasticity induced with 10 pairings at 4 Hz. **A**. Data from our collaborators (Cui, Prokin, et al. 2016). Summary bar graphs illustrate that symmetric Hebbian plasticity (t-LTP) induced with post-pre and pre-post were not prevented by AM251 (CB1R blocker) or D-AP5 (NMDAR blocker) (except for pre-post pairings) but were precluded by the application of both antagonists AM251+D-AP5; Error bars represent SEM. *p<0.05. ns: not significant. **B**. The mathematical model predicts similar behavior for $N_{\text{pairings}} = 15$ (at 4 Hz). Except the pairing frequency, all parameters are the same as in fig. 2.7 (values given in Appendix B).

2.8.2 MAG-Lipase regulates 2-AG and therefore eCB-STDP

To substantiate the causal role of the amplitude of 2-AG transients in activating CB1R and therefore bidirectional eCB-plasticity, one can boost the endogenous levels of 2-AG during STDP protocols. Indeed, if the amplitude of CB1R activation controls the expression of eCB-STDP, the outcome of a given STDP protocol should change if one modifies the amount of CB1R activated by this very same STDP protocol. For this purpose, I inhibited MAG-lipase (MAGL), the major enzyme responsible for 2-AG degradation (Piomelli 2003), to increase the endogenous level of 2-AG.

I utilized the model to select three scenarios in which it should be possible *in silico*, by inhibiting MAGL, to 1) increase the magnitude of an existing eCB-t-LTP, 2) induce an eCB-t-LTP for a protocol that normally induces neither eCB-t-LTP nor NMDAR-t-LTP (i.e. 50 post-pre pairings; fig. 2.7A and Cui, Paille, et al. (2015)) and 3) convert an eCB-LTD (induced with 100 presynaptic stimulations without postsynaptic simulations) into eCB-LTP.

First, I tested the possibility to increase the eCB-t-LTP magnitude by inhibiting MAGL. For this purpose, I chose the minimal pairing protocol for which eCB-t-LTP is detected, that is five post-pre pairings (fig. 2.11) (fig. 2.7A3 and fig. 1.20).

Five pairings appears the lowest number of pairings needed to induce significant eCB-t-LTP as

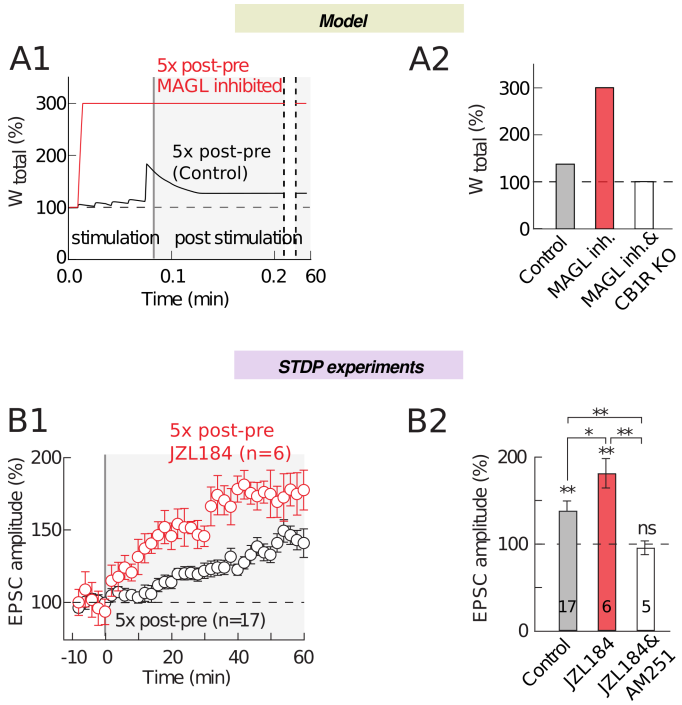

Figure 2.11: MAGL inhibition increases eCB-t-LTP magnitude induced by 5 pairings. **A**. Model prediction for eCB-LTP amplitude induced by $N_{pairings}$=5 post-pre pairings with Δt=-15 ms. **A1**. MAGL and DAG-Kinase inhibition (red line) were simulated by fixing the value of the maximal rates of each enzyme to 0 and 5%, respectively, of their default values listed in Appendix B (control model, black line). **A2**. Summary bar graph of the t-LTP amplitude predicted by the model for N_{pairings}=5 post-pre pairings, Δt=-15 ms. **B**. Summary of experimental data from Laurent Venance's lab. t-LTP induced by 5 post-pre pairings in control conditions and with JZL184 treatment (MAGL inhibitor). **B2**. Summary bar graph illustrates that t-LTP magnitude was increased by MAGL inhibition (JZL184) while prevented by CB1R inhibition (JZL184+AM251).

illustrated by the average STDP ($134 \pm 13\%$, p=0.0190, n=17) (fig. 2.11B); The model faithfully predicted eCB-t-LTP for such number of pairings (fig. 2.7A and fig. 2.11A). In the model, I introduced noncompetitive inhibition of the MAGL by decreasing its maximal rate r_{MAGL}. Simulation of the model with 5 post-pre pairings under MAGL inhibition predicts that such an inhibition increases the net level of 2-AG produced during the protocol and the amplitude of eCB-LTP (fig. 2.11A). As predicted by the model, inhibition of the MAGL with JZL184 significantly increased the magnitude of eCB-t-LTP ($182 \pm 17\%$, p=0.0048, n=6; p=0.0294 when compared to 5 post-pre pairings in control conditions) (fig. 2.11B). Our collaborators confirmed that this amplification was CB1R-mediated since no plasticity was observed when CB1R were blocked by AM251 ($96 \pm 8\%$, p=0.6123, n=5) (fig. 2.11B).

Second, I tested the possibility to induce eCB-t-LTP by inhibiting MAGL. Indeed, the model predicts that MAGL inhibition may turn a STDP protocol that yields no plastic change in control conditions into eCB-t-LTP. For this purpose, I chose a STDP pairing for which I detected no plasticity in control conditions: i.e. the "plasticity gap" around 50 post-pre pairings (fig. 2.7A3) (the zone between 40 and 60 pre-post pairings that separates the two LTP domains). *In silico*, the control STDP protocol (50 pairings with Δt=-15 ms) does not trigger any plasticity but when MAG lipase is inhibited, eCB-t-LTP emerges (fig. 2.12A). Experimentally, as previously reported (Cui, Paille, et al. 2015), STDP protocols with 50 post-pre pairings failed to induce any plasticity in control conditions as illustrated by the average STDP ($101 \pm 7\%$, p=0.9030, n=13) (fig. 2.12B). As predicted by the model, it was found that 50 post-pre pairings under inhibition of MAGL with JZL184 induced t-LTP ($139 \pm 15\%$, p=0.0248, n=9) (fig. 2.12B). This t-LTP was eCB-mediated since suppressed by AM251 ($93 \pm 4\%$, p=0.3365, n=5) (fig. 2.12B2). Therefore, by acting on the 2-AG levels, we were able to trigger eCB-t-LTP for an activity pattern, which does not generate LTP in control conditions.

The third model prediction is that amplifying 2-AG production during STDP may even eliminate the need for a coincidence between presynaptic and postsynaptic activity to express eCB-LTP. *In silico*, pre-post pairing coincidence is needed for the model to express plasticity. Indeed, a protocol with 100 presynaptic stimulations only (i.e. in the absence of postsynaptic stimulation), does not change W_{total} in the model (fig. 2.13A). However, if I decrease the maximal rates of MAGL and DAG kinase activity (the major source of DAG consumption in the model), I obtain a robust eCB-t-LTP, even in the absence of any postsynaptic stimulation. Experimentally, 100 presynaptic stimulations (without postsynaptic pairing) induced LTD ($76 \pm 9\%$, p=0.0337, n=8), which was CB1R-mediated since prevented with AM251 ($102 \pm 7\%$, p=0.8108, n=4) (fig. 2.13B1); note that this LTD was not predicted by the model. In agreement with the model, when 2-AG levels were amplified by MAGL inhibition with JZL184, 100 pre-synaptic stimulations triggered LTP ($143 \pm 17\%$, p=0.0299, n=11) instead of LTD in control conditions (fig. 2.13B2). This t-LTP

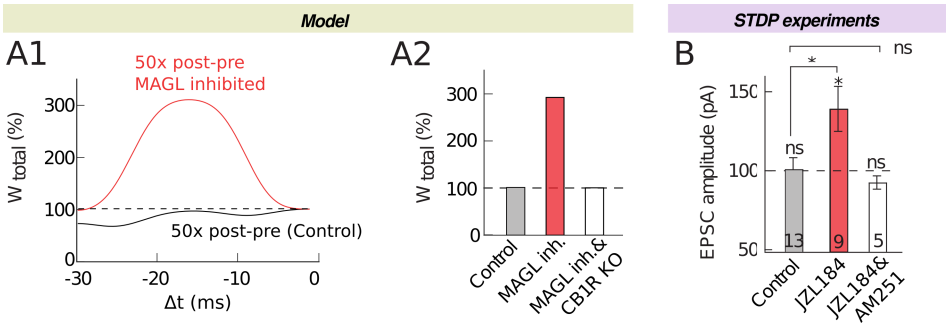

Figure 2.12: MAGL inhibition unveils eCB-t-LTP expression with 50 pairings. **A**. Model prediction for the plasticity induced by N_{pairings}=50 post-pre pairings. **A1**. In control (full black line), the synaptic weight is unchanged by 50 post-pre pairings for 0>Δt>-25 ms. Amplified eCB production due to MAGL inhibition (full red line), uncovers a large-amplitude t-LTP. In the model, MAGL inhibition was emulated by setting its maximal rate to 40% of its default value Appendix B. **A2**. Summary bar graph of the t-LTP amplitude predicted by the model for N_{pairings}=50 post-pre pairings at Δt =-15 ms. **B**. 50 post-pre pairings induced t-LTP with MAGL inhibition but not in control. **B1**. Summary of synaptic weight along time induced by 50 post-pre pairings in control conditions and with JZL184 treatment. **B2**. Summary bar graph illustrates that MAGL inhibition allowed t-LTP to be expressed, which was CB1R-mediated since prevented by AM251. *p<0.05. ns: non-significant.

was eCB-mediated since it was prevented when JZL184 was co-applied with AM251 ($93 \pm 4\%$, p=0.1509, n=5) (fig. 2.13C2).

To summarize, manipulating the activity of the MAGL was sufficient to 1) control the magnitude of eCB-t-LTP, 2) induce eCB-t-LTP or 3) even to reverse eCB-LTD into eCB-t-LTP. These experimental validations of the model predictions thus support our model hypothesis that 2-AG levels control eCB plasticity in a bidirectional way, with large 2-AG levels yielding eCB-t-LTP and lower levels eCB-t-LTD.

2.9 Beyond STDP. Spike-pattern-dependent plasticity

A typical STDP protocol of repeated paired electrical stimulation is fully characterized by:

1) the delay between each post- and presynaptic stimulations within a pairing, Δt;
2) the frequency at which each pairing (1) is repeated;
3) the number of pairings (1) delivered at a frequency (2), N_{pairings}.

Across both experimental and theoretical STDP related studies, most of the attention is given to the dependence of plasticity on Δt. The dependence of STDP on the frequency is rarely considered (to my knowledge, no more than three experimental studies). The dependence of STDP on the N_{pairings} below 60 was only recently addressed (Cui, Paille, et al. 2015).

Besides being artificially regular, most of the STDP protocols consist in varying spike-timing only. Thus the STDP results observed experimentally are likely just scratching the surface of

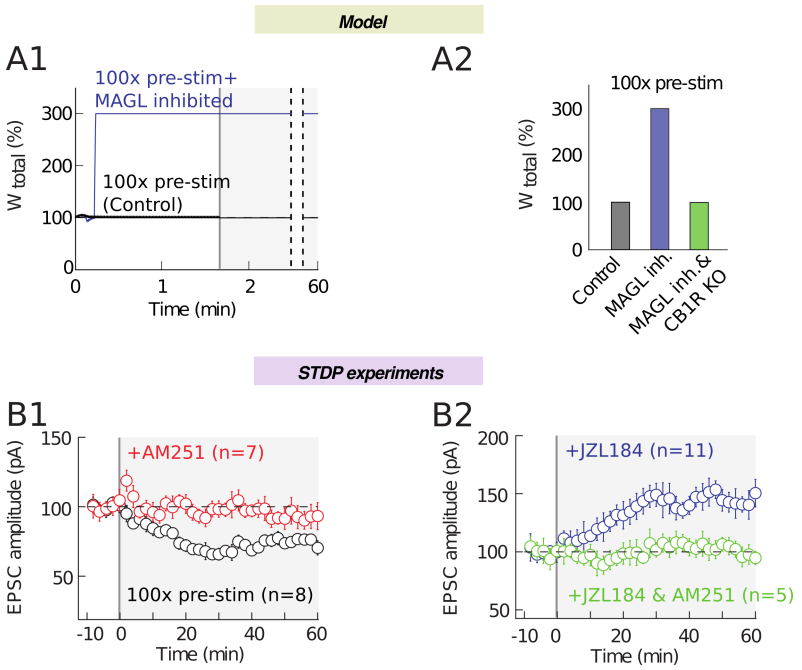

Figure 2.13: MAGL inhibition shifts eCB-LTD into eCB-LTP, induced by 100 presynaptic stimulations. **A**. Model prediction for the changes in synaptic weight induced by 100 presynaptic stimulations. **A1**. MAGL and DAG-Kinase inhibition were obtained by fixing the value of the maximal rates of each enzyme to 0 and 5%, respectively, of their default values listed in Appendix B. **A2**. Summary bar graph of the LTP amplitude predicted by the model for 100 presynaptic stimulations in the absence of postsynaptic stimulations. **B1**. Summary of LTD induced with 100 presynaptic stimulations. This 2-AG-mediated LTD was prevented by AM251 (n=7). **B1**. MAGL inhibition by JZL184 shifts eCB-LTD, induced by 100 presynaptic stimulations, into eCB-t-LTP. *p<0.05. ns: non-significant.

the plasticity mechanisms: exposing plasticity outcome in a very specific artificial conditions (and likely not physiologically relevant ones). Neurons *in vivo* receive patterned inputs far more complex than sequences of artificially regular 60-10 periodic spike trains with a fixed delay between them. These inputs are nonstationary (frequency changes over time, sometimes abruptly) and can depend on both the environment and the brain state. The input can therefore contain many spikes in one period of time and none in another.

To understand how learning is actually implemented in the brain at the level of single cells, that is how a plasticity rule acting at the level of single synapse can support unsupervised learning of statistical regularities in the incoming patterns, one has to consider learning rules that can accommodate for the features of the input: in terms of STDP protocol, all its three parameters (Δt, N_{pairings}, frequency) should be varied either independently (due to a mix of many small unrelated inputs and intrinsic noise) or in a coordinated manner (reflecting patterns of the world).

Having extensively validated our detailed model against the experimental data, we can examine plasticity outcomes when the model is exposed to more realistic inputs beyond classical STDP protocols. Starting from classical STDP protocol, I first studied the simple cases of the dependence of plasticity outcome on each parameter of the protocol independently. I then proceeded to study more complex cases when parameters are varied in a correlated fashion. In the previous section, I have studied plasticity dependence on both Δt and N_{pairings} when frequency was fixed, and the dependence on Δt and frequency when N_{pairings} was fixed. In the following, I will first examine how plasticity varies when N_{pairings} and frequency change, at a fixed Δt. For a given pair (N_{pairings}, frequency), I will search for different families of STDP curves. I will then focus on the plasticity evoked by more realistic spike-patterns, whereby all the parameters, Δt, N_{pairings} and frequency are varied simultaneously over time.

2.9.1 The dependence of STDP on the frequency and the number of pairings

To illustrate the dependence of plasticity on N_{pairings} and frequency, I selected two values of Δt=-15 ms (close to the maximum of t-LTP for 10 and 100 1-Hz pairings, see fig. 2.7) and Δt=+20 ms (close to the maximum of t-LTD for 10 and 100 1-Hz pairings, see fig. 2.7). For these two Δt, fig. 2.14 shows how W_{total} depends on both frequency and N_{pairings}. For both Δt, the border of the LTP region has hyperbolic-like shape. This property is preserved across a wide range of Δt's for which the region of LTP found (not shown). Consider a protocol with a given (N_{pairings}, frequency) pair. If this protocol does not induce LTP (e.g. with N_{pairings}<10 and frequency<1 Hz, i.e. both below magenta triangle at fig. 2.14), then according to fig. 2.14,

increasing N_{pairings} or frequency will eventually end up triggering LTP. Note however that fig. 2.14 evidences threshold values for N_{pairings} and frequency, below which the two parameters (N_{pairings} and frequency) must be simultaneously increased to get LTP. For Δt=-15 ms (fig. 2.14A), LTP expression needs frequencies>0.5 Hz and N_{pairings}>2, while for Δt=+20 ms (fig. 2.14B), LTP will not be induced if frequencies<1.2 Hz or N_{pairings}<3. For instance, with Δt=+20 ms and 1-Hz protocol, it is impossible to induce LTP whatever N_{pairings}.

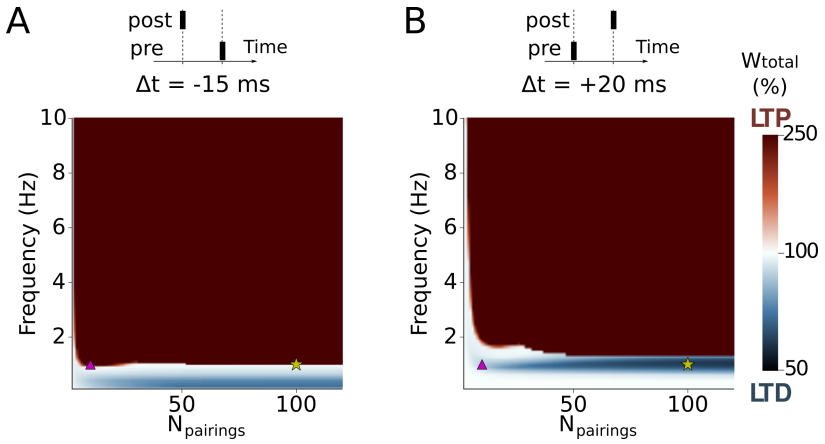

Figure 2.14: Dependence of STDP on both the frequency and the number of pairings (N_{pairings}) for Δt=-15 ms (**A**) and Δt=+20 ms (**B**). Red color corresponds to t-LTP, blue to t-LTD. Protocols with frequency and below 10 pairings at 1 Hz (magenta triangle) do not induce induce t-LTP. If the frequency is too low (below 0.5 Hz for Δt=-15 ms and 1.2 Hz for Δt=+20), it is impossible to induce LTP whatever the number of pairings. To induce LTP, both N_{pairings} and frequency should be sufficiently large. eCB-t-LTD (dark blue) is expressed only at low frequencies for sufficiently large N_{pairings} (**B**). The yellow stars locate a typical STDP protocol (100 paitings at 1 Hz).

To understand why the increase of N_{pairings} and that of frequency play similar roles in promoting LTP, let us consider the time-evolution of the variables controlling plasticity: $CaMKII^*$ and y_{CB1R} (CB1R activation) (fig. 2.15). Pairings evoke calcium transients. A transient of calcium evokes a transient of $CaMKII^*$ (or y_{CB1R}). These transients have a decay time that is larger than that of calcium transient. Let us consider two consecutive calcium transients. If by the time the second calcium transient arrives, the increase of $CaMKII^*$ (or y_{CB1R}) evoked by the first calcium transient has not decayed to its resting value, then the new peak adds up on top of the previous one (from the first transient). If transients are repeated, $CaMKII^*$ (or y_{CB1R}) builds up with each calcium transient (with each pairing) (fig. 2.15A,B). The blue traces on fig. 2.15A,B show the build up for the 1-Hz protocols with increasing N_{pairings}. If this build up is sustained long enough (blue traces with N_{pairings}>50 at fig. 2.15A1), then, by the end of the stimulation protocol, plasticity is induced (the plasticity outcome is denoted by bold text at fig. 2.15). Another way to strengthen this build up is to increase frequency (orange and red traces). This reduces the time between transients, thus, the time a transient has to decay before another transient arrives. Therefore, repeated transients build up faster (compare orange and blue traces at fig. 2.15A1).

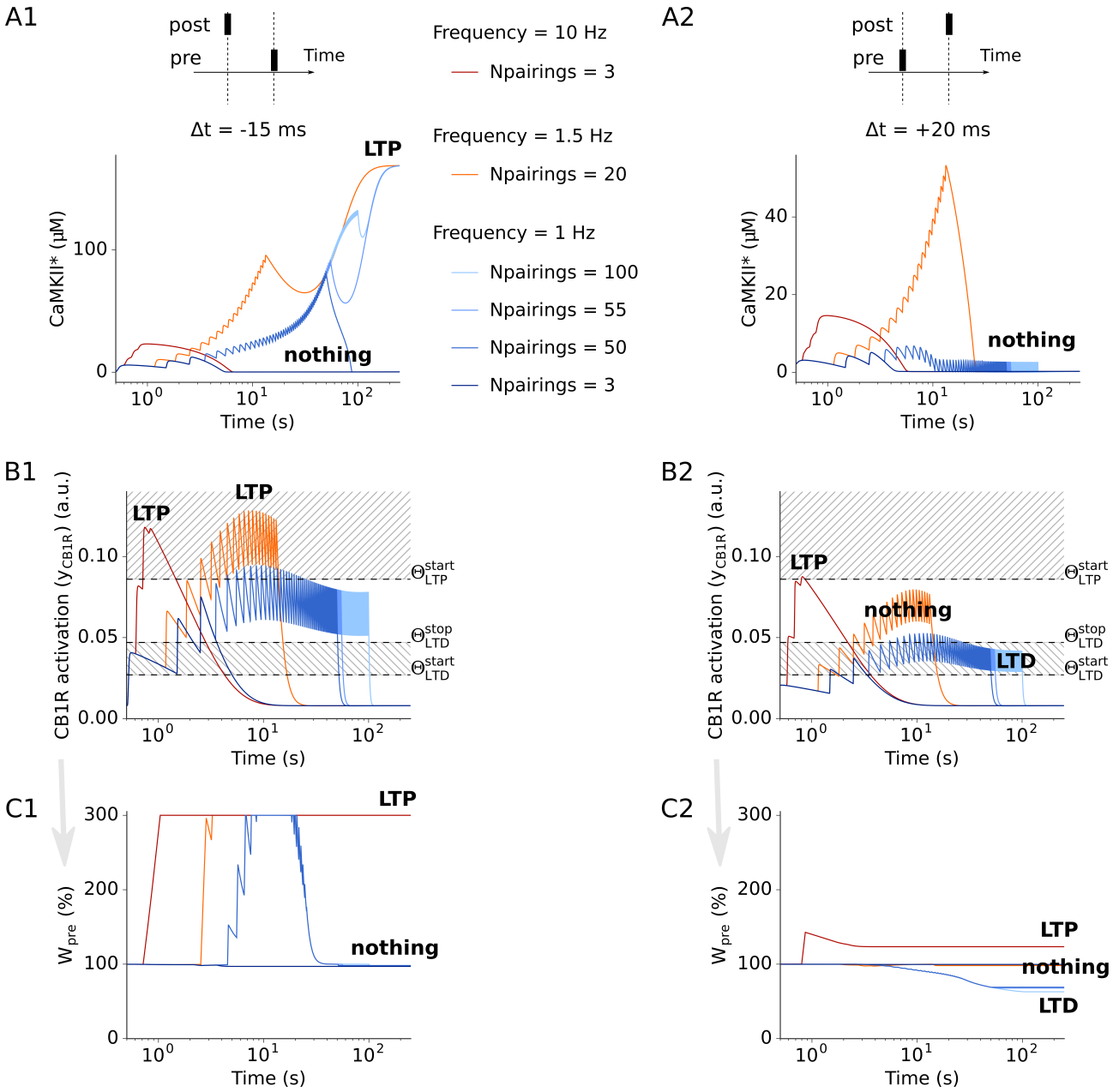

Figure 2.15: Illustration of the similar role played by the frequency and N_{pairings} in t-LTP induction. **A**. Transients of $CaMKII^*$ evoked by protocols with various combinations of N_{pairings} and frequency for Δt=-15 ms (**A1**) and +20 ms (**A2**). **A2**. The same protocols as (**A1**) but for Δt=20 ms do not induce NMDAR-CaMKII-t-LTP. **B**. Transients of CB1R activation (y_{CB1R}) evoked by protocols with various N_{pairings} and frequency for Δt=-15 ms (**B1**) or 20 ms (**B2**). **C**. Resulting dynamics of W_{pre}. For details, see text.

The partitioning of the (N_{pairings}, frequency) plane into LTP and LTD regions depends on spike-timing. In other words, each point on the (N_{pairings}, frequency) plane corresponds to a potentially STDP curve. I then studied how the shape of the spike-timing dependence of pre- and postsynaptic components of STDP curve depends on the location in the (N_{pairings}, frequency) plane. To this end, I computed W_{pre} and W_{post} for protocols with different values of (Δt, N_{pairings}, frequency) and clustered the resulting STDP curve into regions of similar shapes. I discretized the 2D parameter plane (N_{pairings}, frequency) as a Cartesian grid of $\mathrm{M_N x M_f}$ points. $\mathrm{M_N}$ and $\mathrm{M_f}$ are the number of points of N_{pairings} and frequency respectively, $\mathrm{M{=}M_N M_f}$ is the total number of points on 2D grid. To reflect equal importance of W_{pre} and W_{post}, I concatenate vectors with coordinates $W_{pre_j} = W_{pre}(\Delta t_j)$ and $W_{post_j} = W_{post}(\Delta t_j)$:

$$\mathbf{W} = (W_{pre_1}, ..., W_{pre_N}, W_{post_1}, ...W_{post_N}) \in \mathbb{R}^{2N}, \tag{2.31}$$

where j is the index numerating points on chosen grid of Δt, N is the number of points at which Δt was discretized. $\mathbf{W}$ depends on both N_{pairings}, frequency and combines W_{pre} and W_{post} without data loss (components can be always retrieved back) and without giving preference to either one (both taken with the same scaling).

I first examine the deviation of STDP curves from the STDP curve with 100 1-Hz pairings. To this end, I compute mean squared displacement of $\mathbf{W}_i$ from $\mathbf{W}_r$ where r corresponds to $(N_{\text{pairings}_r}, \text{frequency}_r) = (100, 1)$:

$$\text{MSD}_{\mathbf{W}} = \frac{1}{M}\sum_{i=1}^{M}(\mathbf{W}_i - \mathbf{W}_r)^2$$

The dependence of $\text{MSD}_{\mathbf{W}}$ on N_{pairings} and frequency is shown at fig. 2.16. STDP curves with similar $\text{MSD}_{\mathbf{W}}$ tend to be clustered on (N_{pairings_i}, frequency_i)-plane.

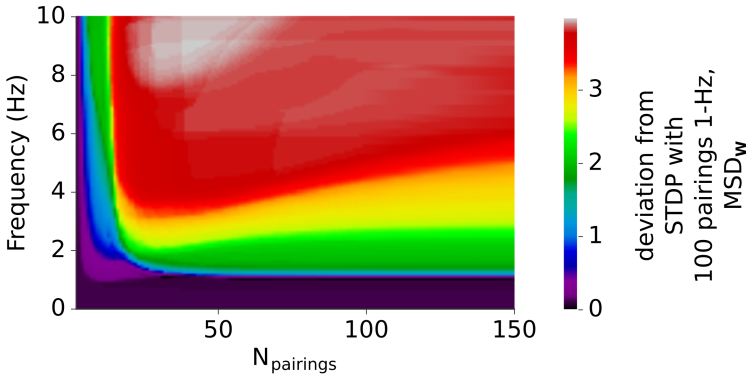

Figure 2.16: Color-coded mean squared displacement (MSD) of STDP curves from the STDP curve for 100 1-Hz pairings. MSD is similar for proximal values of frequency and the number of pairings; that is STDP curves similarly distant from the STDP curve for 100 paitings at 1 Hz, tend to be clustered on (N_{pairings_i}, frequency_i)-plane.

Visual analysis of fig. 2.16 suggests there are about 11 clusters of distances from the reference STDP curve.

I then checked if the STDP curves with similar $MSD_{\mathbf{W}}$ belong to classes of similar STDP curves. I used $\mathbf{W}_i$ to reveal the characteristic types of STDP curves using K-Means clustering algorithm applied to $\mathbf{W}_i$. This algorithm first randomly assigns $\mathbf{W}_i$ data points to K clusters. Second, centroid (mean) is computed for each cluster. Third, every point is reassigned to the cluster whose centroid is closest to that point. Next, the second and the third steps are repeated until a there is no further change in the assignment of the data points (for short description and implementation details see sklearn website http://scikit-learn.org/stable/modules/clustering.html). I set the number of clusters K to 11, close to 10 as suggested by the number of clusters at fig. 2.16. K=11 is selected for the illustration purposes, a lower value of K leads to visually different STDP curves included in the same cluster, while higher values make algorithm too sensitive to small differences in STDP curves so that globally similar STDP curves are attributed to different clusters. The resulting partitioning of the STDP curves into K=11 regions of similar shapes is shown in fig. 2.17. The shape of the typical STDP for every region is very variable (see inset plots on fig. 2.17). This variability of STDP in the model agrees with *in vitro* experiments presented in sec. 1.1.7.2.1. *In vivo*, neurons generate and receive trains of AP that are far from the regular ones used in STDP protocols. Thus, the question arises: are the STDP protocols used in experiments adequate for deciphering how plasticity actually operates *in vivo*. *In vivo*, the parameters of spike-trains (the spike-timing, the frequency and the number of pairings) all change with time at the same time. This corresponds to the parameters' values jumping across various regions with various plasticity outcomes. Even a small variation of the parameters can allow the parameters to explore several different STDP clusters (when the mean values of parameters are close to borders between clusters). Therefore, based on the knowledge of how plasticity operates under artificial conditions, it is not obvious how one can predict the plasticity outcome with *in vivo*-like spiking patterns. Therefore, to understand the functional implication of plasticity *in vivo*, it is important to study it under more realistic patterns of pre- and postynaptic spiking. For a modeling study, one would need a model that like the one presented here, can account for the variability of STDP curves when stimulation changes. Many of the phenomenological models of STDP take single fixed STDP curve as a fixed update rule for synaptic weight (e.g. a fit to an STDP curve of Bi and Poo (1998)). Whereas such single STDP curve is obtained for a very specific experimental stimulation conditions (e.g. 60 1-Hz pairings in Bi and Poo (1998)), models that take it as weight update rule are often exposed to spiking patterns outside the range for which they were fitted (e.g. Kempter, Gerstner, and Van Hemmen 1999; Song, Miller, and L. F. Abbott 2000; Song and L. F. Abbott 2001). This approach can provide insights on how simple timing-dependent rules can affect e.g. the dynamics of networks. However, to provide the full description of STDP, a model has to account for the

variability of STDP curves.

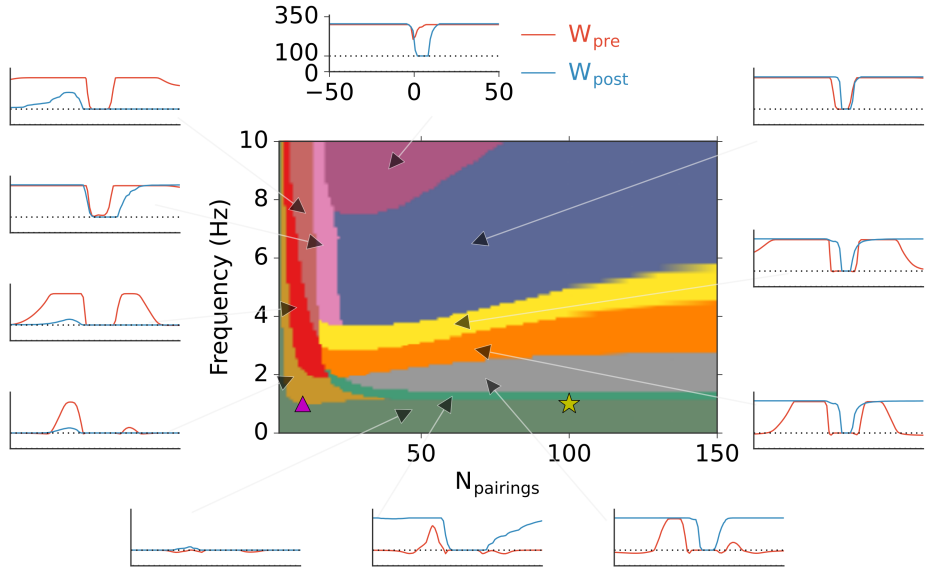

Figure 2.17: Spike-timing dependence of pre- and postsynaptic components depends on the frequency and the number of pairings. Colored regions in the center show 11 clusters of STDP curves with similar shapes found by K-Means clustering. Arrows point to medians of all STDP curves in a cluster. Insets (origins of arrows) show the average (across all STDP curves in a cluster) dependence of W_{pre} (red line) and W_{post} (blue line) on spike-timing, Δt. STDP is actually very variable even inside clusters of similar STDP. Yellow star and magenta triangle show protocols with 100 and 10 1-Hz pairings respectively.

2.9.2 Irregular spiking

2.9.2.1 Spike-timing jitter

I start the study of the plasticity under more realistic spike-patterns by introducing stochasticity in the form of a slight deviation from typical STDP protocol. The first motivation for this is to evaluate the robustness of the results presented above. The second motivation is to have a toggle on the continuum of possible spiking patterns from completely artificial to more realistic ones, that can be used to evaluate the position of spiking patterns of a typical experimental STDP protocol on this artificial to realistic axis. Fulfilling the second motivation would allow us to evaluate how much currently used experimental protocols can tell us about the actual implementation of learning.

In the experiments reproduced with the model, spike-timing is not expected to be as precise as it is in the model. Because the step current of long duration (30 ms compared to 2 ms of single AP) is used for intracellular stimulation, postsynaptic potential is slowly approaching threshold of AP generation. Typically an AP is generated close to the end of the step current. However, depending on the state of postsynaptic potential, the threshold of AP generation can be reached

earlier. Thus the actual postsynaptic timing ${t^i_{post}}^{(actual)} = {t^i_{post}}^{(desired)} - \eta \pm \eta$, where η=$\delta/2$=3/2 ms, and ${t^i_{post}}^{(desired)}$ is t^i_{post} (postsynaptic timing in eq. 2.25).
Because the timings postsynaptic spikes are variable with time, the spike-timing (Δt) varies as well. To account for this, I introduce uniformly distributed jitter into postsynaptic timing (and therefore Δt). The probability-density of the jitter is given by:

$$f(\Delta t_{jitter}) = \begin{cases} \frac{1}{2\Delta t^{max}_{jitter}} & \text{if } |\Delta t_{jitter}| < \Delta t^{max}_{jitter}, \\ 0 & \text{otherwise} \end{cases} \tag{2.32}$$

New postsynaptic timings become:

$$t^i_{post} = {t^i_{post}}^{(old)} + \Delta t^i_{jitter},$$

where Δt_{jitter} is postsynaptic jitter sampled from density eq. 2.32. The equation for the new Δt's is then reads:

$$\Delta t^i = t^i_{post} + \delta - t^i_{pre} = \Delta t^{(old)} + \Delta t^i_{jitter}, \tag{2.33}$$

where $\Delta t^{(old)} = {t^i_{post}}^{(old)} + \delta - {t^i_{pre}}^{(old)}$.

Fig. 2.18 shows an example of how regular STDP protocol (fig. 2.18A) is transformed by applying jitter to it (fig. 2.18B). Jitter affects both Δt and periodicity (frequency) of a postsynaptic spike train.

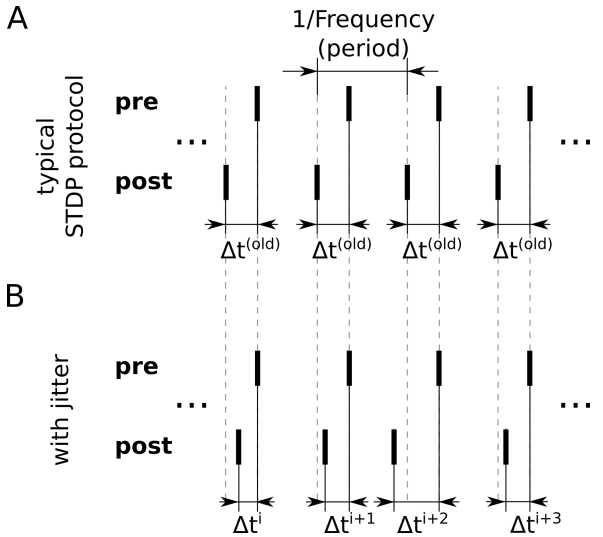

Figure 2.18: **A**. Schematic illustration of typical STDP protocol when frequency and Δt are constant. **B**. Jitter of the Δt applied to the STDP protocol in **A** produces a protocol in which both Δt and frequency of the postsynaptic spike train are varied with each new pairing i.

I first modeled jitter with various Δt^{max}_{jitter} the typical STDP stimulation protocol with 100 pairings at 1 Hz (fig. 2.19).

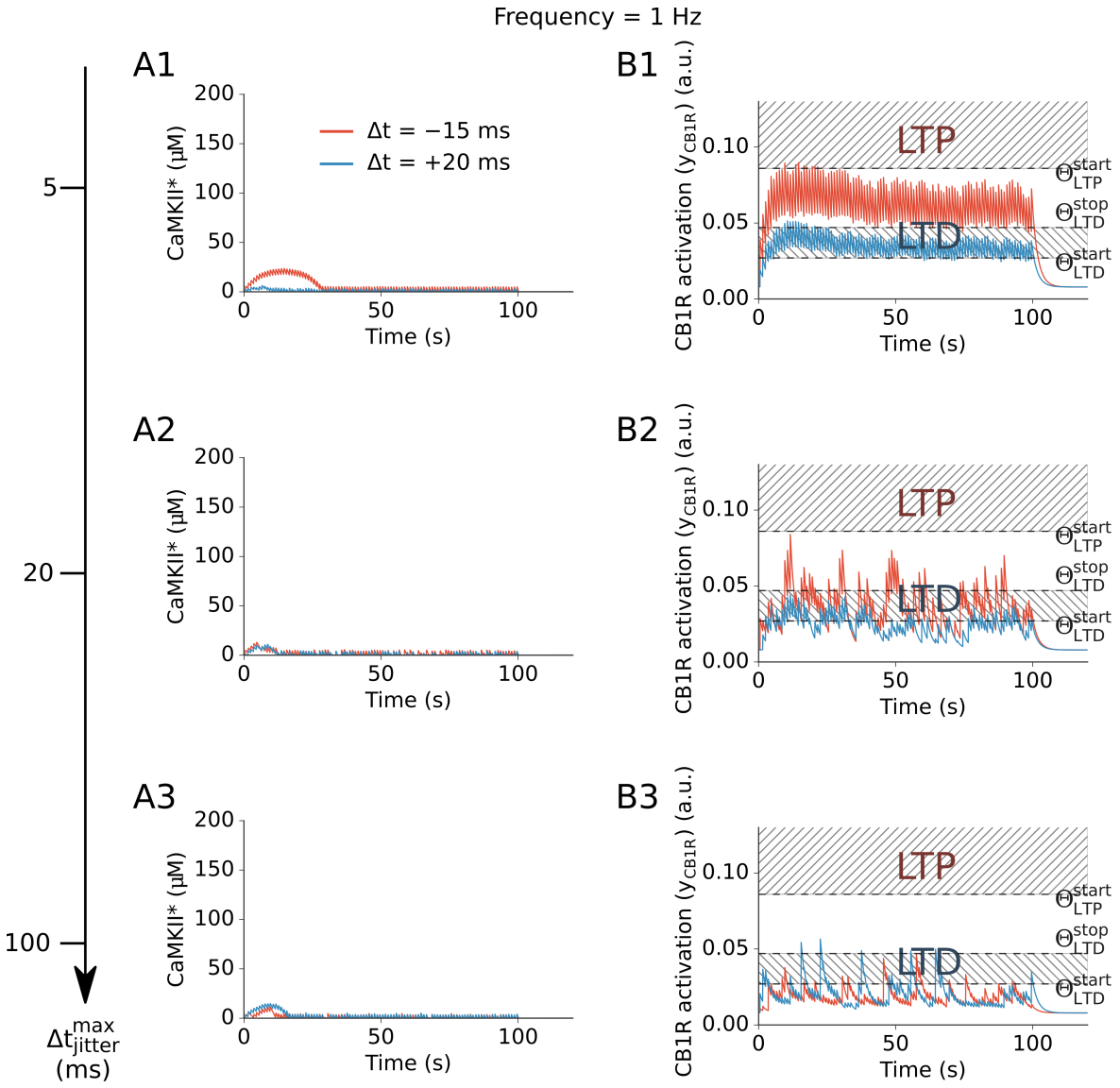

Figure 2.19: eCB-STDP is more robust to jitter than CaMKII-STDP with paired stimuli at 1 Hz. Transients of $CaMKII^*$ (**A**) and CB1R activation (y_{CB1R}) (**B**) evoked by 100 1-Hz pairings for Δt=-15 ms (red) and +20 ms (blue) for increasing Δt^{max}_{jitter} (**1-3**).

Jitter with $\Delta t^{max}_{jitter} > 3$ ms is sufficient to prevent the occurrence of NMDAR-CaMKII-t-LTP (CaMKII end up in DOWN state, see fig. 2.19A). However, eCB-t-LTP for small N_{pairings} can occur up to Δt^{max}_{jitter}=5 ms (CB1R activation, y_{CB1R} reaches values above LTP threshold, Θ^{start}_{LTP}, see fig. 2.19B1-2). Therefore, at 1-Hz, eCB-t-LTP is more robust than NMDAR-CaMKII-t-LTP. eCB-t-LTD is even more robust and can occur even for Δt^{max}_{jitter} up to 100 ms (y_{CB1R} takes values between Θ^{start}_{LTD} and Θ^{stop}_{LTD}). This prediction is confirmed experimentally by our collaborators (fig. 2.20). In their experiments, eCB-t-LTP with 10 pairings at 1 Hz (brown full circles) can be induced with larger jitter than NMDAR-CaMKII-t-LTP with 100 1-Hz pairings (grey full circles). This result qualitatively reproduces the dependence of these two forms of plasticity on jitter in the model (brown and black solid lines respectively).

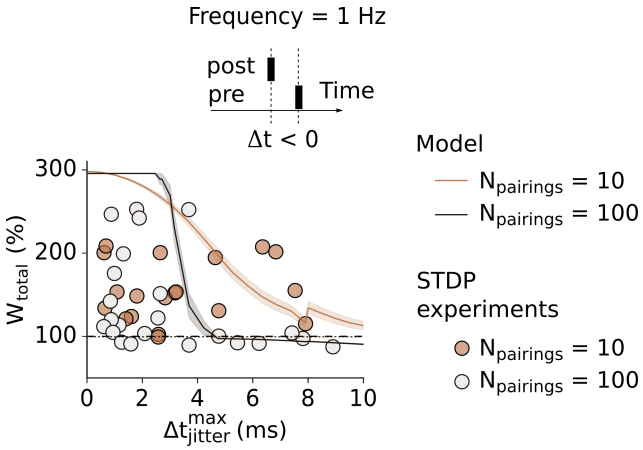

Figure 2.20: Experiments confirm model's prediction that eCB-t-LTP is more robust to jitter than NMDAR-CaMKII-t-LTP. Full circles correspond to experimental data points with the protocol with 10 (brown-filled) and 100 (gray-filled) pairings. Data from Laurent Venance's lab (Cui et al., unpublished). -30<Δt<0 ms in experiments and Δt=-15 ms in the model. Solid line shows average over 30 runs of the model, shaded area around the lines shows standard error of mean.

To explain why at 1 Hz eCB-t-LTP is more robust than NMDAR-CaMKII-t-LTP, I examine the dependence of peak of $CaMKII^*$ and y_{CB1R} transients on spike-timing (fig. 2.21). At 1-Hz, the NMDAR-CaMKII-t-LTP is induced only for short negative Δt's that correspond to peaks of $CaMKII^*$ transients with maximal amplitude. Many successive $CaMKII^*$ transients of high amplitude (N_{pairings}>50) are required for NMDAR-CaMKII-t-LTP. The protocol with Δt=-15 ms, corresponds to the maximal peak $CaMKII^*$ transient evoked by a single pairing (center of red shaded region at fig. 2.21). Jitter with Δt^{max}_{jitter} samples Δt from the range around the maximum of $CaMKII^*$ peak amplitude (-15-Δt^{max}_{jitter}, -15+Δt^{max}_{jitter}) (part of the black curve in red shaded region on fig. 2.21A). Larger Δt^{max}_{jitter} corresponds to wider range of sampled Δt around the maximum, thus to values of $CaMKII^*$ lower than the maximum (fig. 2.21A1-4). With this sampling, many of the repeated pairings fail to deliver $CaMKII^*$ transients with maximal amplitude. Consequently, the build up of $CaMKII^*$ after many pairings is insufficient to induce LTP.

In the protocol without jitter, with Δt=+20 ms (blue dashed line at fig. 2.21), the peak amplitude of a $CaMKII^*$ transient is lower than that with $|\Delta t|$>50 ms. With jitter and Δt=+20 ms, large Δt^{max}_{jitter}=100 ms would lead to sampling more of large Δt (part of the curve in blue shaded region at fig. 2.21A3), thus to higher peaks of $CaMKII^*$ than that for the protocol with the same Δt=+20 ms and no jitter. Most of these larger peaks, however, are lower than maximum and do not build up high enough for LTP (fig. 2.19A4).

In fig. 2.21, the elevation of the maximum y_{CB1R} peak (for Δt=-15 ms) compared to its baseline values (for $|\Delta t| > 50$ ms) is higher than that of $CaMKII^*$ (compare the black curve in fig. 2.21A and B). Because of this, a random sampling of peaks from a wide range of Δt from the curve on fig. 2.21A,B would give higher variance of y_{CB1R} peaks than of $CaMKII^*$ peaks. This means that for Δt=-15 ms, with the increase of jitter (the range of sampled Δt's), the change of the sampled peaks (decrease) will be more pronounced for y_{CB1R} than for $CaMKII^*$, i.e. the quantity of points located in red shaded region *and* close to the maximum of the black curves is smaller for y_{CB1R} than for $CaMKII^*$ (fig. 2.21A3,B3). Even for moderate jitter, many sampled y_{CB1R} peaks have low amplitude compared to maximum (fig. 2.21B1,2). However, peaks of close to maximum amplitude contribute substantially to the build up of y_{CB1R} (see e.g. fig. 2.19B2). This large contribution of single y_{CB1R} peak was required in the model to achieve high build up of y_{CB1R} with low N_{pairings} around 10; that is required to reproduce eCB-t-LTP. On the contrary, the contribution of each single peak of $CaMKII^*$ had to be kept small because the NMDAR-CaMKII-t-LTP is observed only for N_{pairings}>50. The difference of amplitude of single peaks explains higher robustness of y_{CB1R} to jitter than that of $CaMKII^*$ for the protocol with 1-Hz stimulation: even if some of the y_{CB1R} peaks are low, the highest peaks will still support high build up; on the contrary, if each peak has to be close to its maximum to induce plasticity, with jitter many peaks fail to contribute substantially to the build up, and the build up is prevented.

The differences of peaks induced by stimulation with Δt=-15 ms and Δt=+20 ms are caused by the particular shape of the dependence of $CaMKII^*$ (and y_{CB1R}) peaks on Δt. Therefore, the effect of increasing jitter is determined by the shape of the dependence of the peak amplitude of a $CaMKII^*$ (and y_{CB1R}) transient on spike-timing.

Jitter with $\Delta t^{max}_{jitter} \gg 2\Delta t$ ($\gg 30$ in example at fig. 2.21) renders positive and negative Δt's almost indistinguishable (see fig. 2.21A3,B3). If Δt^{max}_{jitter} increases even more (and becomes comparable to 1/frequency), the periodicity of spike-trains becomes noticeably impaired. When $\Delta t^{max}_{jitter} \simeq 0.5$/frequency, the periods (inter-spike intervals) of spike-trains become poorly defined (the variance of the period is comparable to its mean, i.e. the period varies from about 0 to 2/frequency).

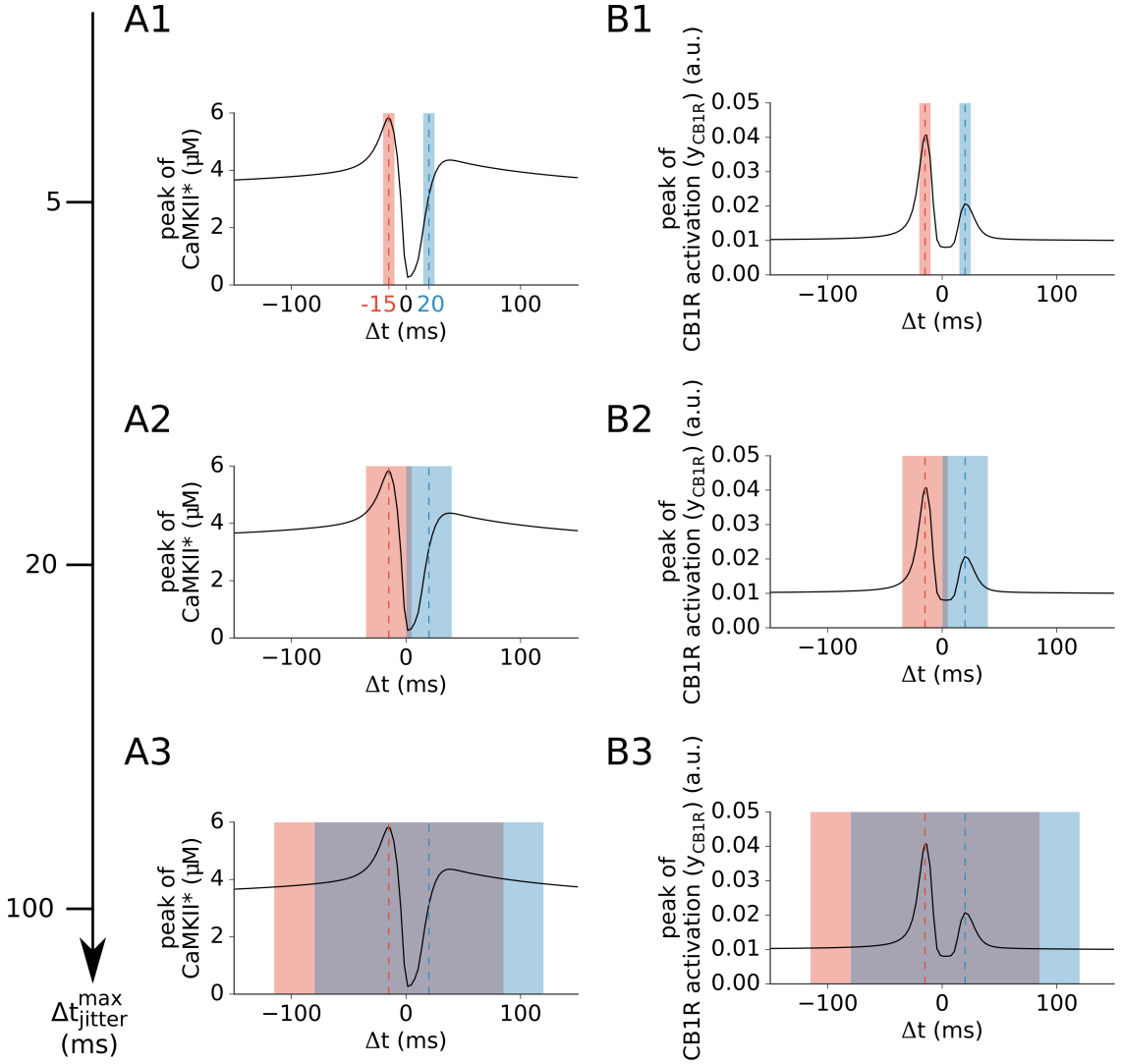

Figure 2.21: The explanation of the effect of jitter on the variables controlling the plasticity outcome. The amplitude of $CaMKII^*$ (**A**) and CB1R activation y_{CB1R} (**B**) transient in response to a single pairing depends on spike-timing, Δt, that in turn depends on maximum jitter Δt^{max}_{jitter} (shown with shading). Δt=-15 (+20) ms is marked by red (blue) dashed line.

The effect of jitter on plasticity however changes with frequency (compare fig. 2.19 and fig. 2.22). With 100 pairings at frequencies>1Hz and no jitter, CaMKII-t-LTP induction is no more restricted to short negative Δt around -15 ms, but also induced for large Δt (see STDP curves in clusters above yellow star at fig. 2.17A). This means that even for large Δt, peaks of $CaMKII^*$ are sufficient for high build up of $CaMKII^*$. Therefore, when more of large Δt's are sampled with the increase of jitter, NMDAR-CaMKII-t-LTP persists. Moreover, for short positive Δt, if jitter becomes sufficiently high, most of the sampled peaks have higher amplitude than without jitter (compare peak amplitudes in blue regions at fig. 2.21A1 and fig. 2.21A3); therefore, NMDAR-CaMKII-t-LTP, that is absent with Δt=+20 ms without jitter, can be induced with the increase of jitter to Δt^{max}_{jitter}=100 ms (fig. 2.22A4). Thus, at larger frequencies, the persistence of NMDAR-CaMKII-t-LTP at high Δt^{max}_{jitter} is explained by the increased amplitude of peaks of $CaMKII^*$ at large Δt. This is not the case for eCB-plasticity: unlike for $CaMKII^*$, the y_{CB1R} peaks at large Δt are much smaller than at short Δt (fig. 2.21A,B), thus the small increase of frequency that is sufficient to promote NMDAR-CaMKII-t-LTP at large Δt does not promote eCB-plasticity. Therefore, eCB-STDP dependence on Δt^{max}_{jitter} is similar for the protocols with 1 and 1.25 Hz (compare fig. 2.19B and fig. 2.22B). Hence at higher frequencies, NMDAR-CaMKII-t-LTP is present for wider range of Δt and more robust to jitter than eCB-t-LTP.

With Δt^{max}_{jitter} larger than 50 ms, positive and negative Δt become essentially indistinguishable (see fig. 2.21A3,B3). In this case, one expects to obtain a symmetric STDP curve with timing-dependence that flattens out with further increase of jitter ($\Delta t \ll \Delta t^{max}_{jitter}$ because the sampled Δt's are too much spread around the Δt mean). In our model, the timing-dependent part of the amplitude of $CaMKII^*$ and y_{CB1R} is restricted to $|\Delta t|$<50 ms. This suggests that spike-timing based learning can only play a significant role for Δt^{max}_{jitter}<50 ms. To verify this, I examined the dependence of the spike-timing dependence of plasticity on Δt^{max}_{jitter} for protocols with 10 or 100 pairings at 1 or 1.25 Hz (fig. 2.23, red color corresponds to LTP and blue LTD). Indeed, when jitter is high, Δt^{max}_{jitter}>50 ms, the spike-timing dependence of W_{total} disappears (all points along a vertical line have similar color) in all four cases presented at fig. 2.23. Unlike for the case when jitter is low, it is impossible to induce LTP by tuning Δt of the noisy input (pre) to that of the noisy output (post). To induce LTP, an efficient strategy is the same as in deterministic case with no jitter (see sec. 2.9.1), that is to increase the frequency and the number of pairings (fig. 2.23B2). Let us now examine the case of moderate jitter 15<Δt^{max}_{jitter}<50 ms and 1Hz; with enough jitter, the timing-dependence of STDP flattens (e.g. Δt^{max}_{jitter}=20 ms at fig. 2.23A1). For moderate Δt^{max}_{jitter}, the timing-dependence can be restored by increasing the frequency (compare the extent along Δt^{max}_{jitter}-axis of blue and red domains at fig. 2.23A1 and at fig. 2.23B1).

For low jitter (Δt^{max}_{jitter}<3 ms) that is inherent to experimental conditions, the outcome of our model is robust. For higher jitter at a low frequency, our model correctly predicts the outcome of

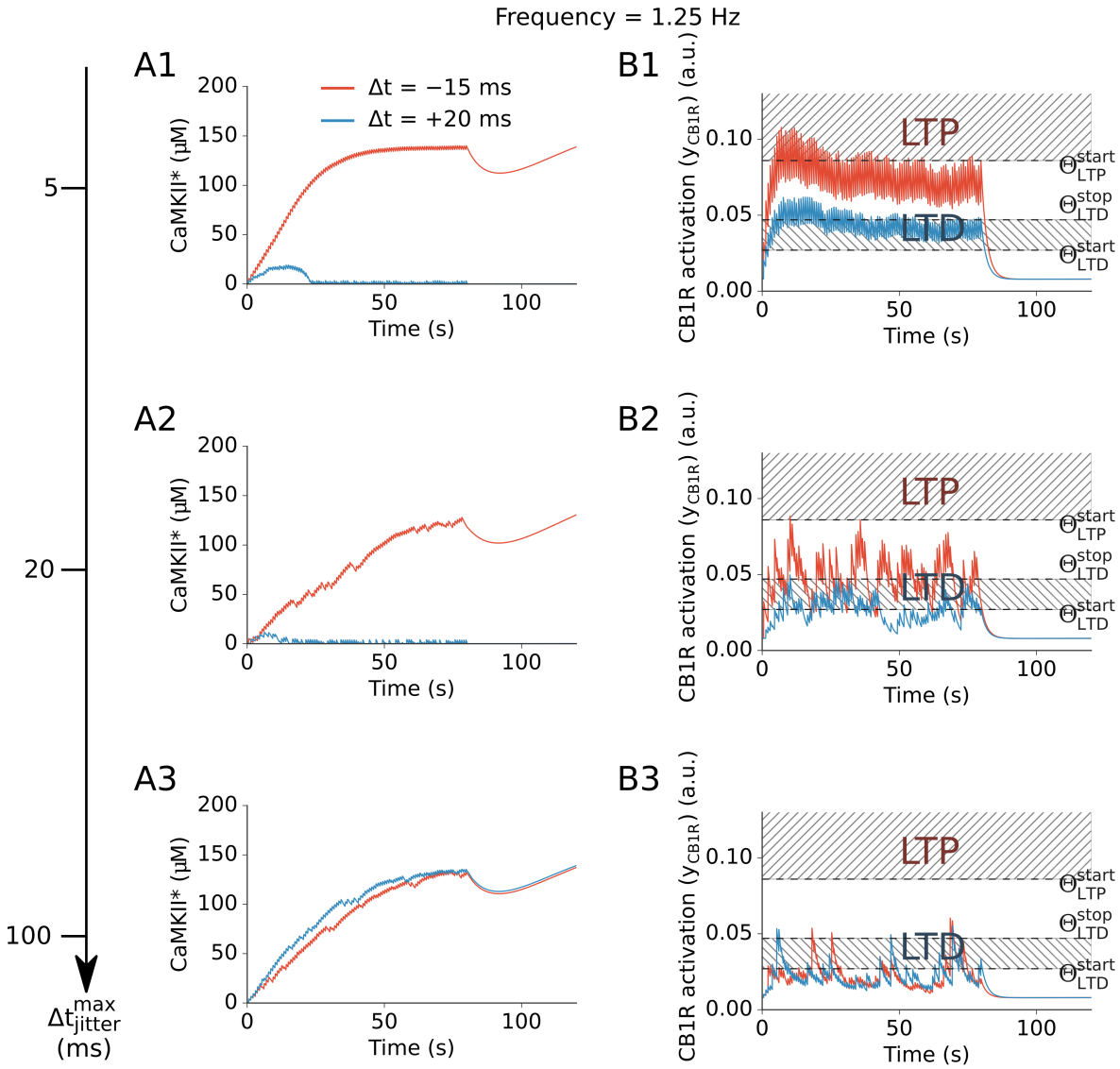

Figure 2.22: eCB-STDP is less robust to jitter than CaMKII-STDP with paired stimuli at 1.25 Hz. With 100 pairings at frequencies>1Hz, NMDAR-CaMKII-t-LTP is induced for large Δt, but not for short ones (see clusters above yellow star at fig. 2.17A). High jitter samples more of large Δt thus leads to t-LTP.

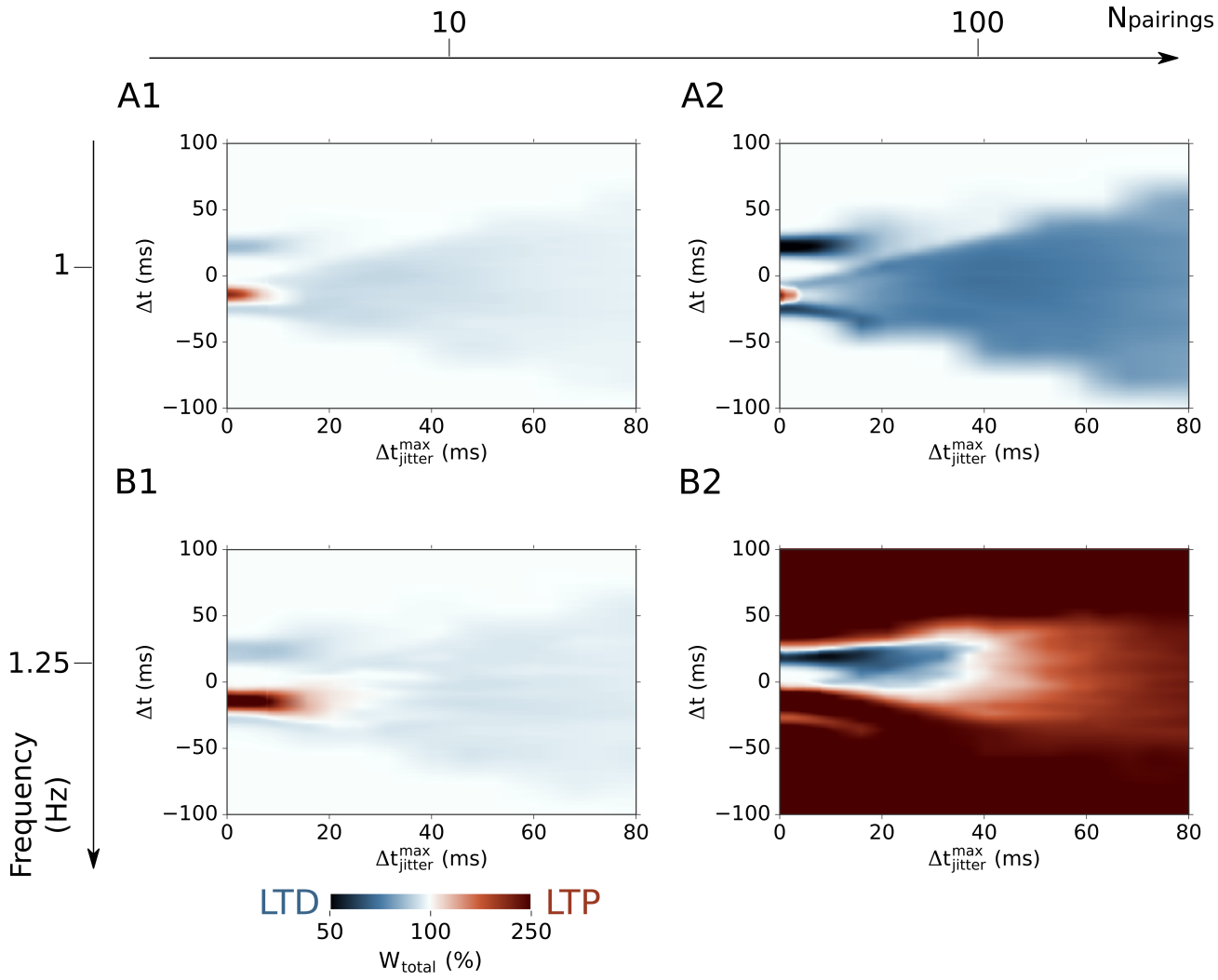

Figure 2.23: The dependence of mean STDP on both spike-timing (Δt) and jitter (Δt_{jitter}). Color codes W_{total} averaged over 30 runs of the model for each pair of Δt and Δt_{jitter}. **A**. Protocols with the frequency of 1 Hz with 10 (**A1**) and 100 (**A2**) pairings. **B**. As **A**, but for the larger frequency of 1.25 Hz with 10 (**B1**) and 100 (**B2**) pairings.

experiments where jitter of various degrees is intentionally introduced into spike-timing: eCB-t-LTP is more robust than NMDAR-t-LTP at low frequency (1 Hz). However, even slight increase of frequency in the model can reverse this pattern of robustness: NMDAR-t-LTP becomes instead more robust than eCB-t-LTP. Simulations suggest that at low frequency, spike-timing based learning (both LTP and LTD) is supported by eCB-plasticity rather than NMDAR-CaMKII-plasticity. Our model also suggests that in order for timing-dependent plasticity to be functional *in vivo*, most of the inter-spike intervals for both pre- and postsynaptic neurons should be larger than 50 ms. If this was found in an experimental *in vivo* learning paradigm, this would suggest that the observed type of learning might rely on spike-timing dependent plasticity.

2.10 Modulation of STDP

2.10.1 Modulation of STDP by dopamine

Dopamine signaling plays an important role in multiple neurological diseases and in reinforcement learning (Schultz 2002; Kandel 2013). However, we currently do not understand the precise mechanisms of dopamine modulation of plasticity at synapses from cortical neurons to MSN. Therefore, implementing the detailed dopamine signaling in MSN is an important future direction of the present work. This would require the modeling of dopamine and cAMP-regulated phosphoprotein 32 kDa (DARPP-32) and signaling pathways coupling it to other postsynaptic components of the model. Modulation by dopamine might potentially have very broad effects by affecting multiple subcellular components and their interactions. These include endocannabinoid signaling and eCB-LTD (Mathur and Lovinger 2012; Giuffrida et al. 1999; Kreitzer 2005). However, whether dopamine modulates the recently discovered eCB-LTP is not known. The model of eCB-LTP, and, more generally, of bidirectional eCB plasticity, is the major contribution of the present work. Our joint modeling-experimental approach highlights that in addition to NMDAR-CaMKII-dependent plasticity, eCB-dependent plasticity has several interesting properties that can make it a good candidate mechanism to support learning:

- eCB-dependent plasticity is robust when the synapse is exposed to slightly irregular spiking at low frequencies.
- Moreover, eCB-plasticity can be expressed using short-duration stimuli. Thus, eCB-dependent plasticity seems suitable to support fast learning *in vivo* (such as single trial learning).

For these reasons, to understand learning in basal ganglia, the modulation of bidirectional eCB-plasticity might be at least as important as that of NMDAR-CaMKII-plasticity. Postsynaptic

dopamine signaling can potentially modulate eCB-plasticity via the modulation of the pathways of postsynaptic eCB synthesis. However, a more direct dopamine control of this plasticity might be achieved by the modulation of presynaptic pathways downstream of CB1R. Indeed, presynaptic cortical neurons of cortico-striatal synapses are known to express D2-type dopamine receptors (D2R) (H. Wang and Pickel 2002; Bamford et al. 2004). Our experimental collaborators confirmed that eCB-t-LTP can indeed be controlled by dopamine acting on presynaptic D2Rs (see below). To account for these new experiments with the model, in the absence of quantitative data on presynaptic signaling pathways, I have introduced modulation of presynaptic plasticity by tonic dopamine in a simplest possible way, that is I assume that linear combination of D2R activation by dopamine and CB1R activation by endocannabinoids controls presynaptic plasticity. This choice is supported by the fact that both D2R and CB1R are GPCR of the same type ($G_{i/o}$), that is they likely share the same signaling downstream of G-protein.

2.10.1.1 A brief summary of new experimental results

In the lab of Laurent Venance, our collaborators investigated the regulation of eCB-STDP by dopamine using experimental techniques including: Electrophysiology, Pharmacology, Lesioning, Opto-Genetics. The detailed description of their experiments is given in Appendix C.3. In the following, I will briefly summarize their key results.

They showed that eCB-t-LTD (induced with a large number of pairings) is affected by the block of D1R or D2R or both (see tbl. 2.2). Note that our collaborators did not examine the location of these D1 and D2 receptors.

They also found that the form of plasticity, eCB-t-LTP (induced with a low number of pairings), requires activation of D2R (see tbl. 2.2). These D2Rs were found located presynaptically (for the detailed description, see Appendix C.3).

Table 2.2: Summary of experiments on the involvement of various types of dopamine receptors in endocannabinoid-dependent plasticity

Condition	10 post-pre	100 pre-post
Control	eCB-t-LTP	eCB-t-LTD
D1R & D2R blocked	t-LTD	t-LTP
D1R blocked	eCB-t-LTP	no plasticity
D2R blocked	t-LTD	t-LTP

Altogether their experiments indicate that eCB-t-LTP induced by a low number of post-pre pairings depends on presynaptic D2R, but does not depend on D1R, whereas eCB-t-LTD induced

by 100 pre-post pairings is mediated by both D1R and D2R with unknown location.

2.10.1.2 Investigation of the interaction between dopamine and eCB-t-LTP with the model

In eqns. 2.27, 2.28, I used linear functions (y_{CB1R} and z_{CB1R}) of the CB1R open probability (x_{CB1R}) to describe the activation of CB1R downstream signaling. This description can be extended to account for the presynaptic D2R signaling. Both D2R and CB1R are GPCR with $G_{i/o}$ downstream signaling. If we hypothesize that D2R is co-localized with CB1R in the presynaptic neurons, D2R and CB1R can be sharing the same $G_{i/o}$ downstream signaling. With this, the previous assumption of CB1R control of plasticity can be generalized: instead of CB1R, $G_{i/o}$ can be postulated controlling presynaptic plasticity. This new model would indeed be more general because it can be reduced to the previous model when the changes of $G_{i/o}$ activation are determined only by the changes of CB1R activation (when other factors provide constant contributions). To describe the $G_{i/o}$ control of plasticity, in the absence of specific experimental data, I combine CB1R activation and D2R activation linearly (as was done previously). Instead of CB1R activation only (variables y_{CB1R} and z_{CB1R}), I consider the activation of $G_{i/o}$ signaling that combines both CB1R and D2R activation. Variables y_G (instead of y_{CB1R}) and z_G (instead of z_{CB1R}) are postulated to control W_{pre} and $\tau_{W_{pre}}$ respectively:

$$\begin{aligned} y_G &= k_{CB1R} \cdot x_{CB1R} + \gamma_1 \cdot DA + C_1, \\ z_G &= k_{CB1R} \cdot x_{CB1R} + \gamma_2 \cdot DA + C_2, \end{aligned} \tag{2.34}$$

where DA is the concentration of (tonic) dopamine, γ_1 and γ_2 quantify the effect of D2R activation on Ω and $\tau_{W_{pre}}$ respectively, and C_1 and C_2 summarize the effects of other $G_{i/o}$-GPCR pathways (beyond CB1R and D2R) on Ω and $\tau_{W_{pre}}$ respectively. I then replaced y_{CB1R} and z_{CB1R} by y_G and z_G in the equation for Ω and $\tau_{W_{pre}}$ (eq. 2.27).

With the model modified according to eq. 2.34 (fig. 2.24A), without changing parameters outside of the presynaptic plasticity mechanism, I reproduced the data on plasticity dependence on dopamine acting on presynaptic D2 (tbl. 2.2, fig. C.4;fig. C.6). To this end, I decreased k_{CB1R} from 3000 to 2400 to reflect the decreased relative contribution of CB1R to $G_{i/o}$ signaling when the contribution of dopamine is added. I have manually adjusted parameters to preserve key results of the model (compare colormap at fig. 2.7 to fig. 2.24B):

$\Theta^{stop}_{LTD} = 0.053$ (changed from 0.047), $\Theta^{start}_{LTP} = 0.085$ (from 0.086), $A_{LTD} = 1.82$ (from 0.65), $A_{LTP} = 24$ (from 13.54), $k_{CB1R} = 2400$ (from 3000), $C_1 = 1.26 \cdot 10^{-2}$ (from $0.7 \cdot 10^{-2}$), $C_2 = 0.42 \cdot 10^{-3}$ (from $0.7 \cdot 10^{-3}$). New parameters added: $DA = 0.01\mu$M, $\gamma_1 = 0.84 \cdot k_{DA}$,

$\gamma_2 = 0.028 \cdot k_{DA}$.

The efficiency of D2 receptor, k_{DA}, equals to 1.0, sets the D2R activation in control conditions. Lower (higher) values of k_{DA} correspond to the decrease (increase) of D2R activation.

Fig. 2.24C illustrates the changes undergone by the two eCB-controlled domains when the level of presynaptic D2R signaling decreases progressively from 100% to 0% of its control value (k_{DA} decreases from 1.0 to 0.0). The bottom row shows that eCB-t-LTP ($3<N_{\text{pairings}}<30$ and $-10>\Delta t>-25$ms) is drastically altered by a reduction of presynaptic D2R signaling: the amplitude of eCB-t-LTP first decreases, then eCB-t-LTP is replaced by eCB-t-LTD. This model behavior matches the experimental results reported above (tbl. 2.2, fig. C.4A and fig. C.6A). The top row illustrates how eCB-t-LTD (sub-domain exemplified for $N_{\text{pairings}}>70$ and $+10<\Delta t<+25$ ms) is not affected by the decrease of presynaptic D2R signaling in the model. This model prediction was not yet verified experimentally. It cannot be compared against experimental results presented above (tbl. 2.2, fig. C.4) showing that t-LTD induced by 100 pairings is replaced by t-LTP when D2Rs are blocked. This is because the current version of the model can only account for the presynaptic D2R signaling, whereas the location of D2R involved in STDP induced by 100 pairings was not yet experimentally determined. It is as well not known if t-LTP induced by 100 pairings with the nonspecific block of D2R relies on pre- or postsynaptic pathways.

In control conditions (fig. 2.24D, red line), the combination of the effect of CB1R activation by eCBs (released upon the STDP stimulation protocol) and that of D2R by (tonic) dopamine, build up to yield y_G levels (red) that overcome the LTP threshold (Θ_{LTP}^{start}), thus resulting in the observed LTP. However, with D2R activation blocked (fig. 2.24D, blue line), the contribution of D2R to y_G disappears and y_G cannot reach Θ_{LTP}^{start} anymore, thus effectively preventing the expression of eCB-t-LTP. Nevertheless, y_G still crosses the LTD range (between Θ_{LTD}^{start} and Θ_{LTD}^{stop}) with LTD accumulating in proportion to the time spent in this range. As a result, eCB-t-LTD is expressed instead of eCB-t-LTP. This is in agreement with the aforementioned experimental data (tbl. 2.2, fig. C.4A and fig. C.6A) in which the prolonged inhibition or deletion of D2R switched eCB-t-LTP into t-LTD. Therefore, according to the model, the switch from eCB-t-LTP to eCB-t-LTD observed when presynaptic D2R are blocked is due to the reduction of the synergistic effect of D2R on the presynaptic $G_{\alpha i/o}$-GPCR pathway that needs to be present in addition to the activation of the presynaptic $G_{i/o}$-GPCR pathway by CB1R to reach the activation threshold for the expression of eCB-t-LTP. Thus, the presynaptic cortical D2R not only allow the expression of eCB-t-LTP, they even control the polarity (LTP vs LTD) of the plasticity induced by a low numbers of pairings.

Whereas the above exploration of the model considered reduced activation of the dopaminergic system, hyperdopaminergy in the striatum is as well of interest since it is often observed in drug

addiction (Volkow et al. 2009). I then used the mathematical model to explore the effects of increased dopamine levels on the STDP. Fig. 2.24A shows model prediction when the level of tonic dopamine is increased threefold with respect to the control case of Fig. 2.24B. The induction of eCB-t-LTP is hardly altered by hyperdopaminergy. The main modification is that eCB-t-LTP can be induced by larger N_{pairings} so the eCB-t-LTP domain fuses with the NMDAR-CaMKII-t-LTP domain. In contrast, hyperdopaminergy has a drastic effect on eCB-t-LTD in the model: the whole eCB-t-LTD domain actually disappears so pre-post pairings fail to induce any plasticity whatever N_{pairings} or Δt. With large D2R activation, for the range of Δt previously corresponding to eCB-t-LTD domain, baseline y_G remains located above Θ_{LTD}^{stop}, but below Θ_{LTP}^{start}, which is too large to induce LTD but too small to trigger LTP. Therefore, the prediction of our mathematical model is that hyperdopaminergy (via activation of presynaptic cortical D2R), besides preventing the induction of eCB-t-LTD, should considerably extend the domain of expression of eCB-t-LTP. These predictions however have not yet been tested experimentally.

2.10.2 Modulation of STDP by glutamate uptake

Glutamatergic neurotransmission is the major type of excitatory synaptic transmission in the brain. Upon its release from a presynaptic neuron to synaptic cleft, glutamate binds to glutamate receptors on a postsynaptic dendritic spine; this enables activation of the receptors. Therefore, the activation of the postsynaptic glutamate receptors can be impacted by the dynamics of glutamate in the synaptic cleft. For instance, glutamate dissociation from AMPAR determines the decay phase of EPSC (Clements et al. 1992). Prolonged exposure to glutamate leads to AMPAR desensitization and consequent decrease of EPSC amplitudes (Goubard, Elodie Fino, and Venance 2011). Among many potential consequences of altered excitatory synaptic transmission, synaptic plasticity might become no longer inducible or, on the contrary, become inducible abnormally easy. From engineering perspective, a process as sensitive as glutamate dynamics would better be tightly regulated to avoid instabilities. Indeed, cells implement several mechanisms to control the dynamics of glutamate. First, the AMPAR glutamate receptors quickly desensitize when exposed to glutamate, thus over-activation is prevented (M. V. Jones and Westbrook 1996). Second, the excess glutamate is removed from the synaptic cleft by glutamate transporters on neurons and astrocytes (Danbolt 2001; Rothstein et al. 1994).

When the major type of astrocytic glutamate transporters (fig. 2.25), EAAT2 (excitatory amino acid carrier 2, so-called GLT-1) is blocked pharmacologically, the characteristics of EPSC could be potentially altered (see scheme of glutamate transmission at fig. 2.26).

Our experimental collaborators in the lab of Laurent Venance have studied how the clearance of glutamate by astrocytic glutamate transporters EAAT2 affects cortico-striatal STDP combining

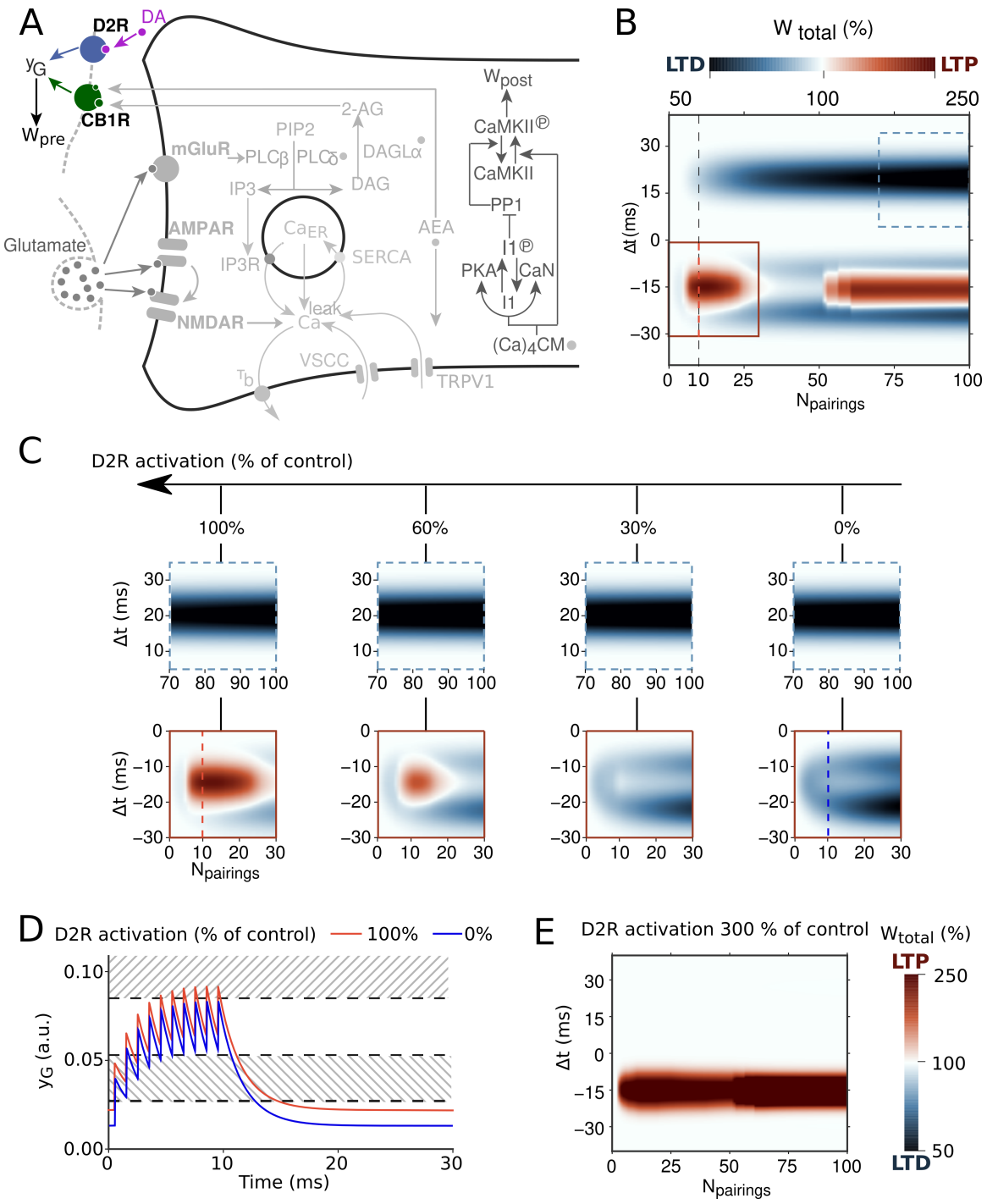

Figure 2.24: **A**. Scheme of the model extended with presynaptic D2R signaling (based on the original model in fig. 2.2). **B**. Model prediction for changes of the total synaptic weight W_{total} (LTP and LTD) triggered by STDP protocols with varying N_{pairings} and Δt (at 1Hz frequency). The color bar gives the color code. The eCB-t-LTP domain ($3<N_{\text{pairings}}<40$, $-10<\Delta t<-25$ ms) and the eCB-t-LTD domain ($N_{\text{pairings}}>70$, $+10<\Delta t<+25$ ms) are boxed with blue dashed or red full lines, respectively. **C**. Progressive alterations of the eCB-t-LTD (top row) or eCB-t-LTP (bottom row) domains when the activation of presynaptic dopamine receptors D2R is progressively reduced from 100% to 0% of the control shown in (**B**). **D**. Temporal evolution of the variable y_G, that summarizes presynaptic $G_{\alpha i/o}$-GPCR activation during an STDP protocol consisting of 10 pairings at 1Hz and Δt=-15ms. In the model, LTD is triggered when y_G is in a range defined by the thresholds Θ_{LTD}^{start} and Θ_{LTD}^{stop} whereas LTD is triggered when $y_G>\Theta_{LTP}^{start}$. D2R activation was 100% (red full line) or 0% (blue full line). **E**. Model prediction for changes of W_{total} upon hyperdopaminergy, i.e. with a threefold increase of tonic dopamine compared to the control case shown in (**B**). All other parameters were as in (**B**).

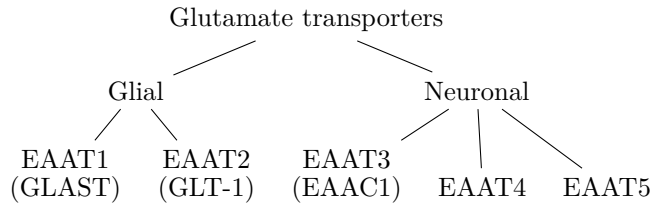

Figure 2.25: Classification of Excitatory Amino-Acid Transporters (EAATs).

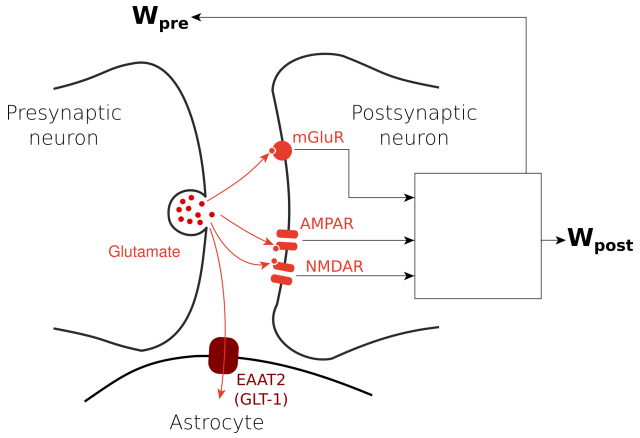

Figure 2.26: Glutamate concentration in synaptic cleft is regulated by the astrocytic glutamate uptake by EAAT2 (dark red). Alteration of this process could alter synaptic plasticity controlled by the glutamate dependent pathways (red).

Pharmacology and Electrophysiology techniques. The experimental results in this subsection are the product of the Ph.D. project of Silvana Valtcheva.

2.10.2.1 Blocking glutamate uptake by EAAT2 causes AMPAR-mediated depolarization

Valtcheva and Venance (2016) found that EAAT2 block by dihydrokainic acid (DHK) applied during 5 min leads to pronounced depolarization of membrane potential of MSNs. This depolarization was fully reversed after 15-min washout of DHK (fig. 2.27A1). The depolarization was almost fully prevented by the block of AMPAR, but not NMDAR (see fig. 2.27B1).

A plausible interpretation of these data is that the depolarization is due to tonic AMPAR current induced by extra glutamate not cleared from the synaptic cleft. The AMPAR-mediated depolarization of the resting potential can have large influence on the induction of plasticity. Indeed, the depolarization affects voltage-dependent conductances. Our collaborators therefore tested if plasticity can be induced by this depolarization alone. Without application of any stimulation protocol, depolarization during 5 min of DHK application followed by 15 min of DHK washout led to no plasticity (data not shown). Potentially, however, the depolarization can have pronounced effects on plasticity induction when a stimulation protocol is applied together with

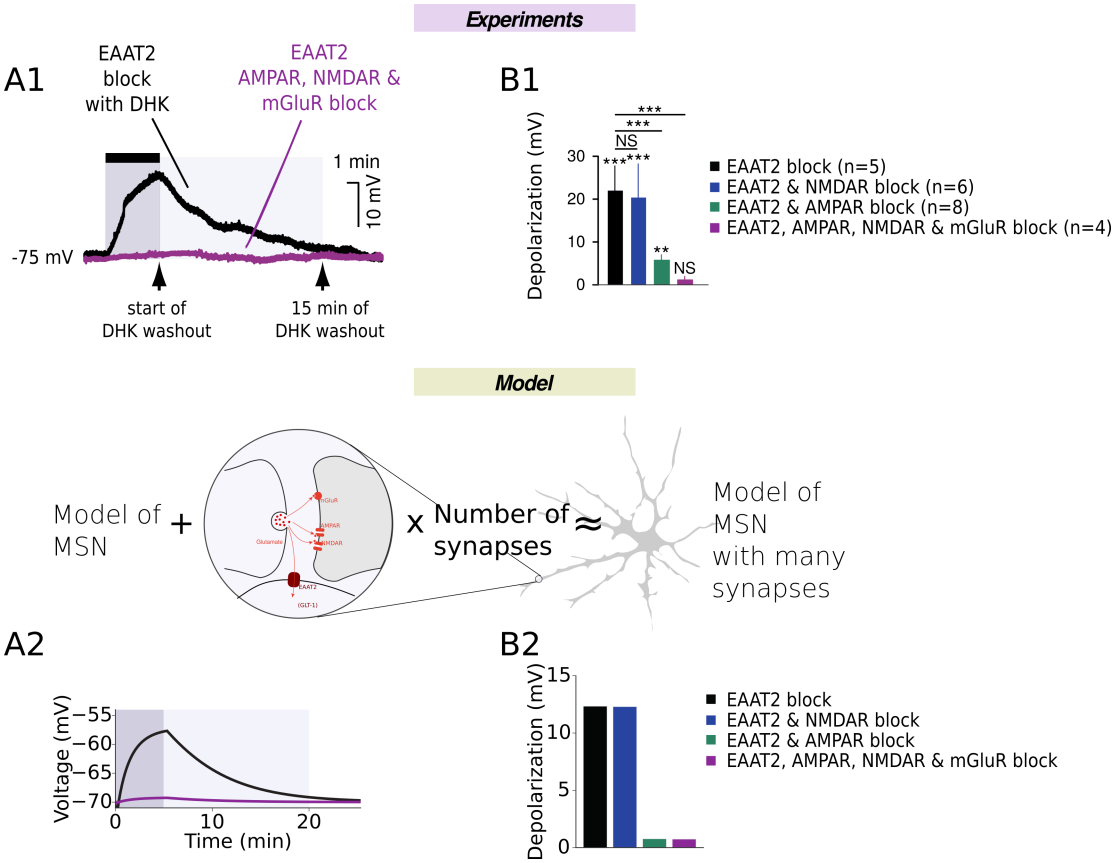

Figure 2.27: Blocking EAAT2 leads to depolarization of membrane potential of MSNs in both experiment (**1**) and model (**2**). **A1**. EAAT2 block with dihydrokainic acid (DHK) induces depolarization. Current-clamp recording of MSN showed that a brief application of DHK (300 μM during 5 min) induced significant depolarization. This DHK-induced depolarization was reversed 15 min after the begining of DHK washout. **B1**. DHK-induced depolarization (black bar) was prevented by the block of AMPAR current (green bar), but not NMDAR one (blue bar). With the block of all glutamate transmission, AMPAR, NMDAR and mGluR, extra depolarization vanished. Drugs used: D-AP5 to block NMDARs (50μM, n=6), CNQX to block AMPARs (20 μM, n=8) and MCPG to block mGluR type-I (500μM). **A2**. Model of single synapse with conductances scaled by the factor 1500 reproduces depolarization when the level of synaptic glutamate is first exponentially increased during 5 min (simulating action of DHK) and then exponentially decreased (with time constant three times smaller than that of increase) during 15 min (simulating washout of DHK). In the model, NMDAR, AMPA and mGluR blocks were simulated by setting g_{NMDAR}, g_{AMPA} and ν_β to 5% of their value in EAAT2 block condition (see text). Plots A1 and B2 modified from Valtcheva and Venance (2016). MSN image modified from http://www.neuroscience.ubc.ca/images/MSN.jpg.

the block of EAAT2. I therefore aimed to simulate the depolarizing effect of EAAT2 blockade with the model. EAAT2 blockade is expected to yield abnormally high concentrations of extracellular glutamate. In such conditions, AMPARs are known to desensitize rapidly (Goubard, Elodie Fino, and Venance 2011). Therefore, to account for AMPAR desensitization, I replaced simple two state model of AMPAR with three state model (fig. 1.24). Specifically, fig. 1.24 was taken with $k_{1f} = \alpha_{AMPA}$, $k_{1b} = \beta_{AMPA}$, $k_{2f} = \gamma_{AMPA}$, $k_{2b} = 0$, $k_{3f} = 0$, $k_{3b} = \varepsilon_{AMPA}$ (for numerical values of parameters see Appendix B). Parameters of this new model were chosen to preserve the same EPSC amplitudes in response to presynaptic stimuli at 1 Hz. This model however cannot be directly used to account for the AMPAR-mediated depolarization. It has a single electrical compartment interfaced with a network of chemical reactions in a dendritic spine that is linked to plasticity (see sec. 2.3). The model can be interpreted as cell consisting of a soma and a single spine with a synapse. In normal conditions, this simple approach in modeling electrical signaling is reasonable because the model is fitted to somatic recordings. Another reason is that we do not have the data on STDP curves measured at the level of MSNs dendrites (these dendrites are too thin to allow for dendritic patch-clamp recordings). Whereas this rough simplification of electrical signaling provides sufficient input to simulate chemical signaling and plasticity at a representative spine, it is not sufficient to account for AMPAR-current contributed by all synapses. To model the current contributed by all synapses when EAAT2 are blocked, the simplest modification of the model is to scale synaptic currents by the estimated number of activated glutamatergic synapses into an MSN. According to different sources, the number of cortico-striatal synapses ($N_{synapses}$) varies from 5000 to 10000 per cell (Kincaid, Zheng, and Wilson 1998). Moreover, the number of synapses activated by single cortical stimulus is not known. I used a modest estimate on it: $N_{synapses}$=1500. I have scaled synaptic conductances: $g_x^{(new)} = g_x^{(old)} \cdot N_{synapses}$ where $x = AMPA, NMDA$. I then exposed the model to slow glutamate transient designed to mimic baseline glutamate elevation caused the block of EAAT2 during 5 min followed by the decay of glutamate concentration (G) caused by 15-min washout of EAAT2 blocker.

$$G(t) = \begin{cases} G_m(1 - \exp(-t/\tau_{G1})) & \text{if } t < \tau_{G1} \\ 0.95 \cdot G_m \exp(1 - t/\tau_{G2}) & \text{if } t \geq \tau_{G2} \end{cases}$$

where τ_{G1}=5 min, τ_{G2}=15 min. Constant G_m was selected to simulate voltage transient at (fig. 2.27A1) and to yield maximal membrane potential around -55 mV as observed experimentally. With G_m=0.05 μM, the model faithfully reproduces slow voltage transient and its pharmacology (compare fig. 2.27A1 and B1, and A2 and B2). I will use this value in the next subsection to compare the model to STDP experiments.

2.10.2.2 STDP is dramatically altered by the block of EAAT2

During the block of EAAT2s, Valtcheva and Venance (2016) applied STDP induction protocol with 100 pairings at 1 Hz. First, baseline EPSC amplitudes were recorded for 10 min. Then EAAT2 antagonist DHK was applied during 5 min. After that, the membrane potential closely approached its maximal value (see fig. 2.27A1). At this moment, STDP protocol was applied followed by the start of DHK washout. Synaptic efficacy changes were evaluated 60 minutes after the end of STDP protocol (in the last 10 min of the recording). With this protocol, only t-LTD was induced with short -70<Δt<+70 ms, but only t-LTP was induced with large $|\Delta t| > 70$ ms (fig. 2.28A).

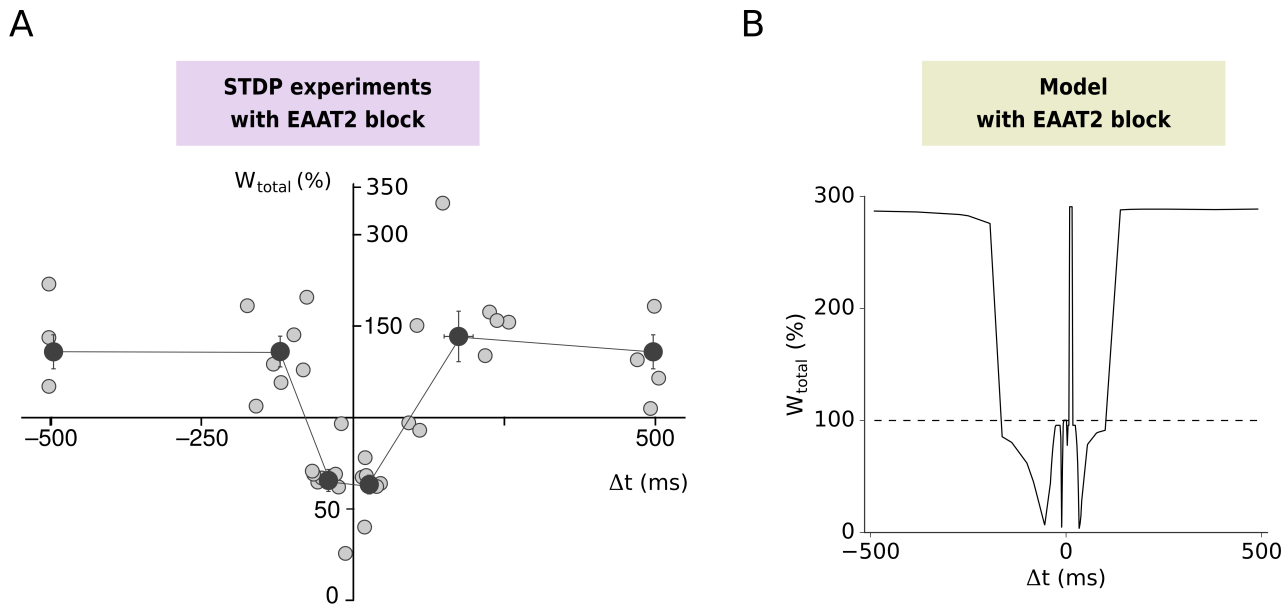

Figure 2.28: EAAT2 blockade dramatically alters STDP: only t-LTD is induced with short Δt, only t-LTP is induced with large Δt. **A**. Experimental STDP curve obtained with the blockade of EAAT2 (Modified from figure 1j in Valtcheva and Venance (2016)). t-LTP is observed for large $|\Delta t|$>70 ms, t-LTD is observed for short $|\Delta t|$<70 ms. **B**. Same as **A** but obtained with adjusted model (see text).

Thus, STDP curve became quasi-symmetric: positive and negative Δt with the similar absolute value yield similar plasticity outcomes. For large Δt, this is similar to STDP curves observed with the model without EAAT2 block when the frequency is high (see STDP curve in purple and magenta clusters in fig. 2.17). Valtcheva and Venance (2016) have tested which subcellular components are involved in this new STDP. According to Valtcheva and Venance (2016), t-LTP at large Δt depends on NMDAR signaling. t-LTD at short Δt does not depend on NMDAR, on mGluR nor on endocannabinoid signaling.

As stated above, the single compartment isopotential model with a single synapse cannot be used to simulate depolarization caused by AMPAR currents from many synapses. However, the reverse statement is also true, the isopotential model with electrical signaling scaled to

simulate many synapses cannot be used to generate input to chemical signaling at a single spine. I therefore, use the original model (single synapse) with the following modifications:

1) AMPAR desensitization kinetics was modeled the same as with the scaled model (see subsection above).
2) I changed the glutamate baseline to the value G_m estimated with the scaled model while simulating EAAT2 block (in subsection above).
3) I changed resting membrane potential V_L from -70 to -55 mV mimicking depolarization induced by EAAT2 block. This accounts for extra current contributed by synapses not modeled explicitly. I have verified that this modification alone does not induce any plasticity in agreement with experiments (not shown). Note that this was the key modification for reproducing the data on fig. 2.28A.
4) To simulate involvement of extrasynaptic NMDAR (see Valtcheva and Venance (2016)), NMDAR with GluN2B subunit, I have added an extra NMDAR current modeled with eq. 2.1 where all indexes "NMDA" replaced with "GluN2B" and parameters kept to the same values. This equivalent to increasing only the conductance of NMDAR. Note that kinetics of NMDAR-GluN2B was exactly the same as NMDAR kinetics (same as in control model). With a fixed conductance, slower kinetics for NMDAR-GluN2B did not alter the outcome of plasticity with EAAT2 block. Therefore, according to the model, what counts for this plasticity outcome is the increase of NMDAR calcium current, not its kinetics.
5) I assumed that elevated glutamate also results in increased spiking of FS interneurons. I have therefore added GABA release (eq. 2.23) and the activation of $GABA_AR$ (two state kinetic model).

After the adjustment of parameters of GABA and endocannabinoid signaling, and the increase conductance of NMDAR (to simulate NMDAR-GluN2B activation) (see Appendix B), the modified model qualitatively reproduces the shape of STDP curve under the block of EAAT2 (compare fig. 2.28A and B).

To explain how STDP curve changes its shape from that in control conditions to that with EAAT2 block, I will consider timing-dependence of the amplitude of single transient of $CaMKII^*$ and presynaptic $G_{i/o}$ activation (y_G) (fig. 2.29). For generality, I will be referring to presynaptic $G_{i/o}$ spike-timing dependent plasticity, G-t-LTP and G-t-LTD, rather than just eCB-t-LTP and eCB-t-LTD. Consider the range of protocols with various Δt and fixed frequency and N_{pairings}. In each of these protocols, a pairing evokes transients of $CaMKII^*$ and y_G. If pairings are repeated the transients build up: the peak values are higher after each transient. If by the end of the protocol transients build up high enough, plasticity is induced. For each Δt, I compared the amplitudes of $CaMKII^*$ (fig. 2.29A) and y_G (fig. 2.29B) transients evoked by single pairings in control (black line) and with the block of EAAT2 (blue line). For most Δt, these amplitudes are

higher with EAAT2 block than in control. With repeated pairings, these higher amplitudes build up to higher final value. Therefore, for $|\Delta t|$>50 ms, for which, the build up was high in control, but not sufficient for plasticity, the extra build up with EAAT2 block leads to the crossing the threshold for plasticity induction (NMDAR-t-LTP for large Δt). This is similar to the case when the build up is increased by other means, e.g. by the slight increase of stimulation frequency. Compare the frequency dependence of STDP in control shown in fig. 2.30A and when EAAT2 block is simulated fig. 2.30B. With EAAT2 block, one thus can expect that with spike-timing jitter, STDP outcome should be similar to that in control when frequency is increased. Indeed, as it was shown in sec. 2.9.2.1, in control conditions, the increase of jitter results in sampling more of large $|\Delta t|$ (for which CaMKII-t-LTP is induced). Fig. 2.31A shows experimental results when large uniform jitter with $\Delta t_{\text{jitter}} = 500$ ms was applied to STDP protocol with Δt_{STDP}=0 ms with 100 pairings at 1 Hz. This essentially random protocol was applied in control conditions (fig. 2.31A1) and with the block of EAAT2 (fig. 2.31A2). Model reproduces both of these experimental results (fig. 2.31B).

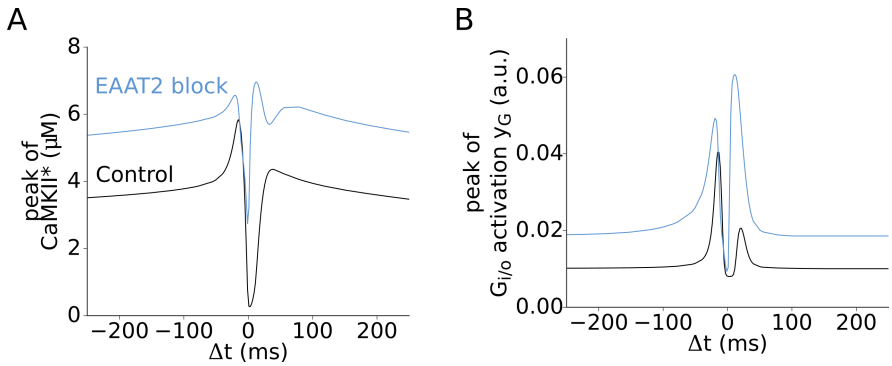

Figure 2.29: The amplitudes of $CaMKII^*$ (**A**) and y_G (**B**) transients in response to a single pairing depending on Δt in control (black) and with EAAT2 block (light blue).

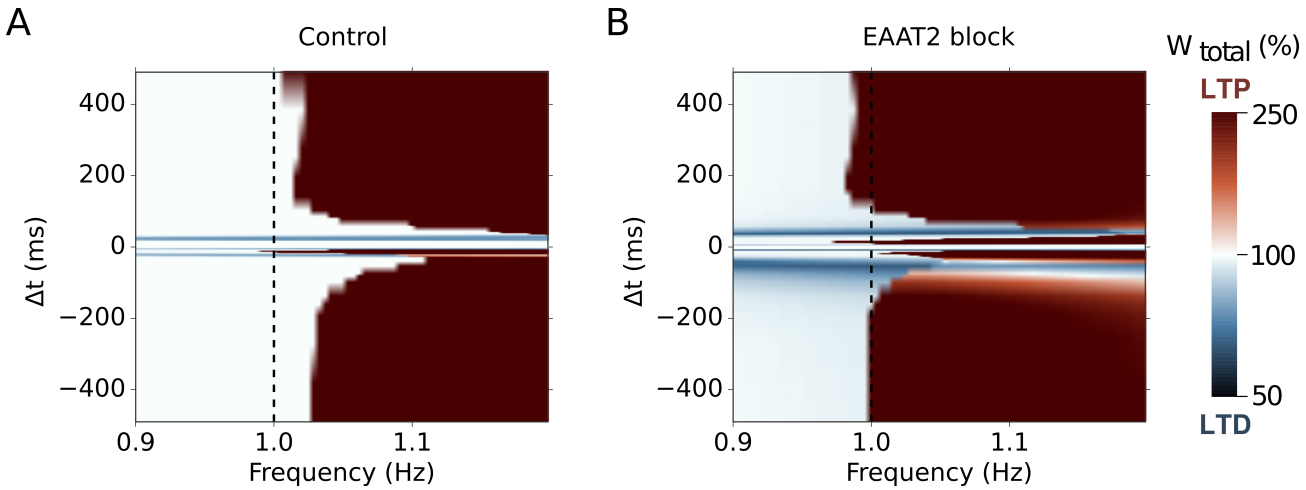

Figure 2.30: Frequency-dependence of STDP in control (**A**) and with EAAT2 block (**B**) for the simulated stimulation protocol with 100 pairings.

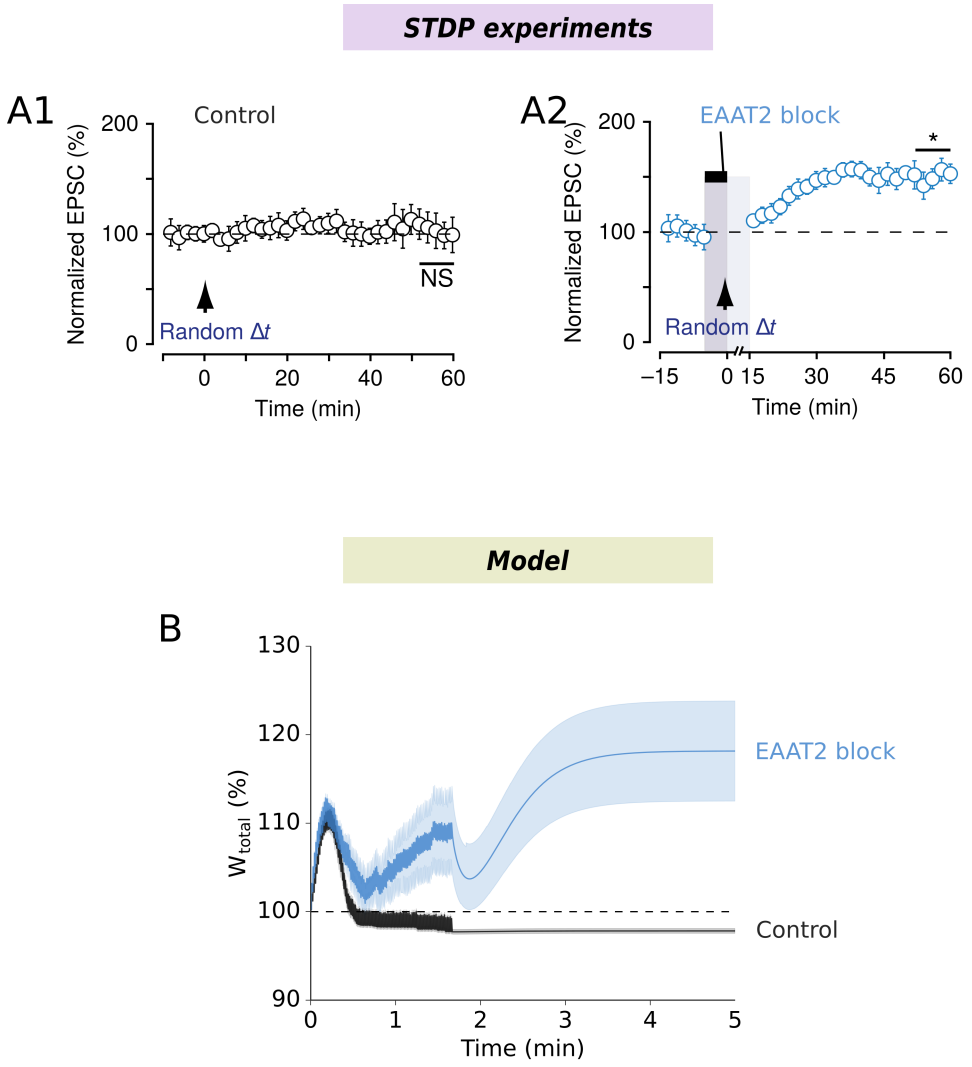

Figure 2.31: Changes of synaptic weight in time when the STDP protocol with 100 pairings at 1 Hz with jitter applied to postsynaptic spiking. $\Delta t_{jiiter}^{max} = 500$ ms, reference Δt=0 ms (the actual spike timing is not defined, see sec. 2.9.2.1). **A**. Experimental data of 60 min of STDP protocol, stimulation is applied during 100 s shown by arrow (Modified from Valtcheva and Venance (2016)). **A1**. In control. **A2**. With EAAT2 block. **B**. The model simulated experiments in **A1** (black solid line), and **A2** (light blue solid line).

Chapter 3

Discussion

3.1 Comparison to STDP models

The work in this thesis fits the tradition of reductionist thinking that at the level of single neurons, learning is supported by synaptic plasticity that is in turn supported by biochemical reactions at the subcellular level. One can model one of these levels and use the model to explain the hierarchically higher phenomena. Depending on the chosen level, computational models of plasticity and in particular STDP can be divided in two groups. Models in the first group aim at predicting the consequences of STDP on e.g. neuronal receptive fields, network dynamics (Song and L. F. Abbott 2001; Clopath et al. 2010; Costa et al. 2015) or feature extraction (Sprekeler, Michaelis, and Wiskott 2007; Bellec et al. 2016). In those models, the function describing the changes of synaptic weight with spike timing is usually given as hypothesis of the model. Within the second group, modeling starts from the level of biochemical reactions, i.e. signaling pathways implicated in plasticity. This modeling aims at understanding how the function describing weight changes with spike timing emerges from those signaling pathways (see e.g. Graupner and Brunel (2010) for a review). In a number of models in this second group, intracellular signaling is restricted to cytoplasmic calcium variation, thus implementing calcium-control hypothesis (Shouval, Mark F Bear, and Leon N Cooper 2002; Shouval, Castellani, et al. 2002). The mathematical models that consider signaling downstream of calcium usually account for a single intracellular signaling pathway (i.e. a single coincidence detector), most often NMDAR-CaMKII (Rubin 2005; Graupner and Brunel 2007; Urakubo et al. 2008). Noticeable exceptions are for instance Karmarkar and Buonomano (2002) and Paille et al. (2013), where the calcium pool entering via NMDAR controls t-LTP whereas the calcium pool entering though VSCCs controls t-LTD, thus implementing two coincidence detectors. However those models do not consider the signaling pathways beyond calcium entry through NMDAR and VSCC. In the

model developed here, calcium entering through NMDARs and VSCCs fills the same calcium pool. However, the model implements a second coincidence detector via a pathway starting from postsynaptic mGluR5 activation and leading to the activation of presynaptic cannabinoid receptors type 1 (CB1Rs) by postsynaptically produced endocannabinoids (eCBs). To my knowledge, this is the first model to incorporate two detailed signaling pathways to account for STDP: NMDAR-CaMKII (with calmodulin, PKA, CaN and PP1) for t-LTP and the eCB system for t-LTD and t-LTP. In the model, the eCB system comprises mGluR5, PLCβ, DAGL, MAGL, DAG-Kinase, calcium-induced calcium release (IP3R channels, SERCA pumps), IP3 dynamics (PLCδ, PI3K), VSCC, TRPV1 and CB1R. Owing to this very fine grained description, the model was able to account for STDP outcomes under various pharmacological interventions when all three parameters of STDP stimulation protocol were varied, that is, not only spike timing Δt, but also N_{pairings} and frequency. This capacity has allowed the exploration of a novel form of plasticity, endocannabinoid and spike timing dependent long-term potentiation, eCB-t-LTP, induced by a low number of post-pre pairings at 1 Hz (Cui, Paille, et al. 2015; Cui, Prokin, et al. 2016).

3.2 Assumptions and limitations

3.2.1 Postsynaptic plasticity

The model of postsynaptic hippocampal CaMKII-dependent plasticity of Graupner and Brunel (2007) was adapted to describe cortico-striatal synapses and it is thus inherits some limitations of that model. Compared to hippocampus, in striatum, CaMKII-dependent plasticity is supported by striatum-specific signaling pathways. Because of this, some assumptions of Graupner and Brunel (2007) can be more applicable to cortico-striatal synapses than to hippocampal ones, whereas the validity of other assumptions can be disputable for cortico-striatal synapses. The activation of PKA by calcium is more established in striatum than in hippocampus, thus the assumption of calcium-dependence of PKA activation could be more applicable to cortico-striatal synapses than to hippocampal synapses. On the other hand, I1 that is present in hippocampus and controls CaMKII in Graupner and Brunel (2007), is absent in MSNs. Another isofrom, DARPP-32 is expressed instead of I1. I kept the equations describing I1, assuming that DARPP-32 participates in CaMKII-plasticity similarly to I1 in hippocampus. To verify or falsify this assumption, a detailed modeling of DARPP-32 and related pathways would be required.

After modification to describe cortico-straital synapses, the model of NMDAR-CaMKII-dependent plasticity of Graupner and Brunel (2007) reproduced anti-Hebbian NMDAR-CaMKII-dependent t-LTP. This result however relayed on the assumption that calcium concentration in nanodomain

around NMDAR is much higher than the average concentration in the spine (this is supported by the recent modeling work of Griffith, Tsaneva-Atanasova, and Mellor (2016)). More generally, our result relied on the assumption that pre-before-post pairings produce smaller calcium transients than post-before-pre pairings. Regarding the calcium-controlled plasticity, knowing calcium transients is sufficient to determine the outcome of plasticity; the question of how these transients were generated is of less crucial importance for plasticity outcome. Thus, even if the part of the model generating calcium transients may turn out disputable, our modeling of plasticity downstream calcium transients can be still correct.

3.2.2 Presynaptic plasticity

To reproduce eCB-t-LTD and the new form of plasticity eCB-t-LTP, I had to extend the model with endocannabinoid signaling. I added pathways from postsynaptic eCB synthesis to presynaptic CB1 endocannabinoid receptor (CB1R) activation. To describe the relation between CB1R activation in the model and eCB plasticity observed experimentally, I introduced the hypothesis of endocannabinoid control of plasticity similar to the calcium control hypothesis used by others before. I have assumed that similarly to calcium control of both LTD and LTP in calcium control hypothesis, the activation of CB1R downstream signaling controls both eCB-LTD and eCB-LTP. I have further assumed that the total outcome of plasticity is given by the combination of pre- and postsynaptic plasticity: for simplicity, the total synaptic weight is taken as a product of pre- and postsynaptic weight. This choice proved sufficient for the model to reproduce key experimental findings on cortico-striatal plasticity (fig. 2.7) and to predict new experiments (figs. 2.9, 2.10, 2.11, 2.12, 2.13, 2.14, 2.20). We however do not know how this presynaptic plasticity mechanism is actually implemented. To answer this, new quantitative data on presynaptic plasticity mechanisms would be required.

3.2.3 Presynaptic plasticity modulation by D2R activation by tonic dopamine

To reproduce the dependence of eCB-t-LTP induced by a low number of pairings on dopamine acting on presynaptic D2R, I assumed that the two $G_{i/o}$-GPCR pathways, D2R and CB1R, co-localize in the presynaptic neurons. Based on this assumption, I have postulated that the effects of CB1R and D2R on presynaptic plasticity add up linearly. With this and without the modification of parameters outside of presynaptic plasticity mechanism, the model qualitatively reproduced the effects of the pharmacological block of presynaptic D2R. Rephrased in more general terms, the assumption postulates that the dependence of plasticity change on the

activation of CB1R signaling is controlled by the activation of D2R signaling. To find out if (and how) such mechanism is implemented, more quantitative data on presynaptic dopamine signaling would be needed.

3.2.4 Presynaptic plasticity modulation by EAAT2 block

To simulate the block of astrocytic glutamate transporters, EAAT2, I assumed that the major effect of this block is a depolarization of postsynaptic resting membrane potential. Our collaborators aimed to test if reversal of this depolarization can reverse STDP to its form in EAAT2 block conditions. By shifting the baseline voltage back to its resting value by injecting a constant postsynaptic current, they observed no change of plasticity in disagreement with the model. However, the recordings and current injection were performed at a soma. Whereas the reversal of depolarization at soma can be confirmed by somatic recordings, the reversal of depolarization in dendrites and especially their distal parts can not be measured (because of the very thin dendrites of MSN). Current injected at soma is diluted while flowing into the dendrites. Thus, the somatic current poorly controls the voltage in the dendrites, a well known issue of so-called poor space-clamp (Williams and Mitchell 2008). This can account for no difference between the two conditions. Therefore, these data do not discredit the modeling result that the effects of EAAT2 block are mostly explained by the depolarization of membrane potential. To invalidate or confirm this explanation, another experiment can be performed in the future. Membrane potential can be manipulated by changing the concentrations of ions in the extracellular solution. In this case, it is guaranteed that resting potential is uniformly set everywhere and in all cells.

Compared to the control, in the model with EAAT2 block, I have increased eCB-LTP threshold. This is supported by the following argument. When EAAT2s blocker is bath applied, the concentration of glutamate increases at all synapses. Therefore, the tonic AMPAR current is expected to be present not only in MSNs, but in all other neurons with glutamatergic synapses; these include presynaptic cortical afferents. Similarly to its effects in MSNs, tonic AMPAR current can be expected to cause depolarization in these neurons. Depolarization increases calcium current via VSCC at axonal terminals of cortical afferents. The extra calcium can increase presynaptic calcineurin activation. According to the data of our collaborators, eCB-t-LTD relies on calcineurin activation (see figure 10 and supplementary figure 1 in Cui, Prokin, et al. (2016)). This can shift LTD-LTP balance toward LTD, or equivalently, LTP becomes harder to induce. This later was simulated with the increase of LTP threshold.

3.3 Parameters, fitting and predictions

The base version of resulting model contained 36 Ordinary Differential Equations (ODE) and about 130 parameters among which about 50 were poorly constrained experimentally i.e. "free" parameters. A common view that with so many parameters a model can be fitted to produce almost any output is expressed by the quote attributed to John von Neumann (Dyson 2004):

> "With four parameters I can fit an elephant, and with five I can make him wiggle his trunk."

This joke expresses tradition in physics in describing the fundamental laws of nature with simple models with the minimal number of parameters. In general, however, fitting any data regardless of the equations of the model cannot be achieved even with a high number of parameters. A simple example is fitting a weighted sum of increasing functions to a decreasing function. With positive weights (parameters), no matter how many terms in the sum are taken and whatever parameters, one can never fit a decreasing function. This simple example illustrates two types of constraints: i) structure of the model and ii) the bounds on its parameters. Whereas the approach minimizing the number of parameters is sensible when one describes a simple system or a complex system that is reduced to its average behavior, it is not sufficient when it is desired to simulate the details of the dynamics of a complex system. First intuition is that in an ideal case, all the parameter values should be fixed by experiments. As it is often unfeasible in practice, one can try to constrain as many parameters as possible, and then, fit the remaining ones to obtain a desired outcome of the model. However, this strategy can be more harmful for the ability of a model to predict new data, than the alternative strategy, where all model parameters are collectively fitted to an experimental outcome of interest, independently of direct experimental measurements of individual parameter values (Gutenkunst et al. 2007; Machta et al. 2013). The later is true if the model's outcome of interest has sloppy parameter sensitivities; that is the outcome is sensitive only to a handful of parameters combinations (stiff directions in parameter space), whereas other parameter combinations can range widely with little effect on the outcome (sloppy directions in parameter space). This pattern of parameter sensitivities is considered as a key feature of systems biology models (Gutenkunst et al. 2007). Our model shows sloppy-like behavior with regard to 50 "free" parameters (fig. 2.8). Indeed, the model's outcome is highly sensitive to only 4-10 parameters out of 50. With sloppy sensitivities, constraining sloppy combinations of parameters that weakly impact a model's outcome constrains the region of parameter space, and therefore, the range of available outcomes after fitting. When remaining parameters are fitted, the movement along stiff directions is restricted by previously constrained parameter combinations that are not relevant for the outcome. Therefore, the resulting fit is likely to be worse than the one obtained from fitting all the parameters at the same time. On

the other hand, with the collective fit for sloppy models, most of the parameters are expected to be not identifiable. However, the predictions can be still valid. The ability to predict new data not incorporated into the model during fitting can be used to check if overfitting took place. The fitted sloppy model should be evaluated not based on the match between its parameters to experiments, but by its ability to predict new data not used during fitting. With this regard, our model performed well in reproducing much of extra experimental data. With the same parameter set as used for fitting data in fig. 2.7, the model has qualitatively reproduced frequency-dependence of plasticity (figs. 2.9, 2.10) and various experiments on MAG-Lipase inhibition (figs. 2.11, 2.12, 2.13). Moreover, the model qualitatively reproduced STDP outcomes with jitter applied to spike-timing (fig. 2.20). Further, without modifying of parameters outside of presynaptic plasticity mechanism, the model has reproduced the experiments on the modulation of plasticity by dopamine acting on the presynaptic D2 receptor (fig. 2.24). Moreover, with restricted modification of parameters, the model reproduced the effects of the blockade of astrocytic glutamate transporters EAAT2 on STDP (fig. 2.28). The overall conclusion is that the model was proven credible not only in its ability to reproduce experimental data, but also in its ability to predict variety of data not used during fitting.

3.4 Modulation of plasticity and its key components

Owing to the assumption that effects of CB1R and tonic D2R activation on plasticity add up, eCB-LTP is expressed if the sum of the CB1R and tonic D2R activation is high enough (above LTP threshold). In other words, with increased D2R activation by dopamine (tonic), a lower activation of CB1R can suffice to induce plasticity by the pairing protocol. Equivalently, the effective threshold for plasticity induction is decreased by the increase of presynaptic D2R activation.

The change of plasticity by the simulated block of EAAT2 can be explained by changes of several crucial components of the model. The simulated EAAT2 block led to changes of the spike-timing dependence of $CaMKII^*$ and y_G transients evoked by a single pairing. The shape of this dependence was only slightly affected, whereas for most of the spike-timings, the amplitudes of these transients have been increased. With repeated pairings, these transients with larger amplitudes build up to larger values (compared to control) by the end of the protocol. These larger values become sufficient to cross the thresholds for plasticity induction for large spike-timings.

Taken together these findings suggests that the modulation of plasticity is due to the modulation of the build up and the thresholds. With this regard, the key features of the model are:

i) The spike-timing dependence of $CaMKII^*$ and y_G transients evoked by a single pairing (the dependence of build up on spike-timing).

ii) Thresholds for plasticity induction (how much of the build up is needed for plasticity induction).

iii) Decay time-course of $CaMKII^*$ and y_G transients ($\frac{1}{\text{Decay time}}$ is about the minimal frequency needed for the build up).

iv) Envelope of the peaks of repeated $CaMKII^*$ and y_G transients (determines the dependence of the build up and therefore plasticity on the number of pairings when the frequency is fixed); If the envelope is raising-then-decaying-then-steady, t-LTP at a small number of pairings can be observed (around the maximum of the envelope).

The importance of these four points is supported by the sensitivity analysis (fig. 2.8). Indeed, the parameters that are the most crucial for plasticity are:

- the total amount of CaMKII and CaM (postsynaptic LTP threshold),
- baseline calcium (both $CaMKII^*$ and y_G),
- calcium and glutamate dynamics time constants and CB1R activation rates (decay times of both $CaMKII^*$ and y_G),
- presynaptic LTP threshold,
- composition of calcium sources (dependence on spike-timing).

To develop a reduced version of our model while keeping its crucial properties, one can limit the subset of considered parameters to the plasticity thresholds and the parameters crucial for spike-timing dependence and time-course of $CaMKII^*$ and y_G.

3.5 Variability of plasticity and plasticity in *in vivo*-like conditions

In agreement with experiments, I found that spike timing dependence of plasticity is actually very variable when both the number of stimuli and their frequency are varied. This suggests, that some of the differences reported in experimental literature might be explained by the used stimulation protocols. This also supports the possibility of a unified description of various forms of plasticity based on a model of a similar kind to the one developed here. As the dependence on the spike-timing is just one aspect of plasticity, focusing on a more general problem of plasticity and its dependence on spiking *patterns* (with varied spike-timing, frequency and the number of pairings) might provide us with a better understanding of the learning at the level of single cells. In a sensory system, spiking patterns experienced by a synapse should reflect statistical

regularities of the natural world. Does the plasticity implement learning of these regularities or the prediction of incoming sequences of spiking patterns? Can we develop an unsupervised local learning rules for pattern recognition and feature extraction that are similar to the ones implemented in the brain? To answer such questions, one would need a model that, like the one developed here, can account for plasticity changes when the synapse is exposed to *in vivo*-like spiking patterns.

3.6 Future directions

Dopamine signaling plays an important role in multiple neurological diseases and in reinforcement learning (Schultz 2002; Kandel 2013). However, we currently do not understand the precise mechanisms of dopamine modulation of plasticity at synapses from cortical neurons to MSN. Therefore, implementing the detailed dopamine signaling in MSN is an important future direction of the present work. This would require the modeling of DARPP-32 and signaling pathways coupling it to other postsynaptic components of the model. Modulation by dopamine might potentially have very broad effects by affecting multiple subcellular components and their interactions. These include endocannabinoid signaling (Mathur and Lovinger 2012; Giuffrida et al. 1999; Kreitzer 2005), dopamine-calcium interactions (Nair, Upinder S. Bhalla, and Kotaleski 2016; Gutierrez-Arenas, Eriksson, and Kotaleski 2014; Lindskog et al. 2006; Nakano et al. 2010; Fernandez et al. 2005) and ARPP-21 signaling (Nair, Upinder S. Bhalla, and Kotaleski 2016). Another future direction can be in evaluating the model's performance at learning patterns. First, this can include recordings of spontaneous spiking patterns *in vivo* and during learning related behavior, when input-output spikes should be respectively correlated and not correlated. These patterns can then be used with our model to decipher how behaviorally relevant patterns are processed by the synaptic plasticity; that is answering what is the input-output transformation that is promoted by the learning at the level of single synapses (what is extracted from input patterns by single-synapse learning). While these data are not available, a simpler scenario can be implemented. One can consider the model of a single neuron driven by multiple inputs via synapses endowed with our model of plasticity. The stream of inputs can be designed to have random parts and repeated motifs with the same statistics as that of the random parts. What are the conditions for the plasticity to learn these non random sequences and represent them in the output spiking? Answering this question with a detailed and validated model might give guidance for studies of how pharmacological interventions can affect not only the plasticity expression in simple cases, but also how they can affect the function of plasticity in learning. Having this understanding with the detailed model might allow for the reduction of this model to produce an unsupervised learning rule qualitatively similar to the one implemented in the

brain. Moreover, the reduction of the model can allow its analytical treatment. Furthermore, the reduced model will be faster to simulate and therefore more suitable for the simulations evaluating the effects of plasticity at the network level. It might become possible to use the reduced model for new unsupervised learning algorithms with artificial neural networks. Unlike learning procedures currently used for supervised learning in artificial networks, such as gradient descent, unsupervised learning rule based on our model would be local to a synapse. For this reason, it would be easier to implement it in hardware compared to e.g. gradient descent.

Appendices

Appendix A

Extra methods

A.1 Parameters

The values of a large part of the parameters implicated in intracellular dynamics, eCB dynamics or electrophysiology in the model are restricted by previous experimental measurements (see sec. B). To estimate the values of the parameters for which we lack previous experimental constraints, I used the experimental data shown in fig. 2.7 and in Cui, Paille, et al. (2015), that is, I optimized those parameter values so that the model emulates the synaptic weight changes triggered by STDP protocols with various spike timings Δt and numbers of paired stimulations N_{pairings}. For each set of parameters, I have computed W_{total} for (Δt, N_{pairings}, frequency) corresponding to experimental data points at fig. 2.7. I then defined mean squared displacement of W_{total} in model from that in experiments ($\text{MSD}_{\text{mod}}^{\text{exp}}$). The automated parameter optimization to minimize this $\text{MSD}_{\text{mod}}^{\text{exp}}$ was implemented using various algorithms included in PyGMO python module (primarily Differential Evolution and Particle Swarm Optimization). A complimentary approach was to hand-tune the parameters from the set found with PyGMO to better match to experiments.

A.2 Model implementation

The version of the model described in Cui, Prokin, et al. (2016) is freely available online:
https://github.com/iprokin/Cx-Str-STDP
or
https://senselab.med.yale.edu/modeldb/ShowModel.cshtml?model=187605.

Simulation control, plotting, and data manipulation were implemented in python. Computationally heavy part of solving ODE is implemented in FORTRAN.

I used the following tools to implement the model:

- gfortran (GNU Fortran compiler, part of GCC) for fast numerical integration, and
- python2.7 for simulation control and data manipulation and visualization, including:
  - pandas, NumPy, SciPy, scikit-learn for data analysis and manipulation (*Pandas: Python Data Analysis Library* 2012; E. Jones, Oliphant, Peterson, et al. 2001; Pedregosa et al. 2011),
  - fork of python's multiprocessing library included in pathos module (McKerns and Aivazis 2010) for parallel computing,
  - PyGMO for numerical optimization (a powerful library developed by ESA, http://esa.github.io/pygmo/),
  - matplotlib and pandas for plotting (Hunter 2007),
- f2py (part of NumPy python module) to interface FORTRAN code with python.

I implemented Ordinary Differential Equations (ODEs) of the model in FORTRAN95. To numerically integrate the ODEs, I used the original FORTRAN77 implementation of the LSODA solver from the ODEPACK library https://people.sc.fsu.edu/~jburkardt/f77_src/odepack/odepack.html (the same solver that is used in SciPy). I first compiled ODEPACK as shared library. This library was then used to compile FORTRAN module for python2.7 with f2py and gfortran. At both stages of compilation, I have used maximum compiler optimization level "-Ofast" that produces fastest running code. I verified that this setting does not alter the results of the integration; lower optimization levels "-O3", "-O2" produced equivalent results. The absolute and relative tolerances of LSODA were both equal to 10^{-7}. Initial conditions were set to the steady-state of each variable in the absence of stimulation (ODEs were integrated for 100-300 s of modelled time). Numerical integration proceeded until the synaptic weights reach stable values (typically observed around t $\approx$ 5 min after the end of the stimulation protocol), and I kept the final value of the pre- and postsynaptic weights to compute the total synaptic weight change due to the stimulation protocol. To assure that LSODA solver does not skip a pairing as a result of the variable time-step, the solver was supplied with an array of singularity points, the points where the components of vector-function representing Right-Hand Side (RHS) of ODE system has discontinuities; in our case, the points when pre- and post- stimuli were delivered to the model. As an alternative to solvers from ODEPACK, I implemented Euler method in FORTRAN95. I verified that the results of integration do not depend on the choice of the method. LSODA was used to obtain all results presented in this thesis, except for fig. C.1 where Euler method was used. This choice was made to mitigate the tendency of LSODA to increase integration step size and interpolate solution between steps when the RHS vector-function changes slow. This

problem arises when calcium is modeled with Ohm's law to compute steady state (slow changes). When using this approximation, calcium has to have hard lower limit 0 (at fig. C.1, note sharp slope change of steady state calcium concentration at about 25 mV). This creates a singularity point with timing that is not known in advance. In steady-state computation, variables change slowly. Consequently, LSODA increases step size and therefore it skips the singularity point and interpolates calcium to negative values. Hence, simpler Euler method is a better choice in this particular case. This problem however does not arise in simulated STDP protocols because voltage goes above 25 mV only at pairings; for pairings, singularity points are supplied to the solver, therefore the integration is carried out correctly.

A.3 Sensitivity analysis

I quantified the model sensitivity to variations of the M=50 parameters p_k, $k = 1 \dots \mathrm{M}$ whose values are not experimentally constrained, "free parameters", listed in fig. 2.8C. To this end, I generated N=2500 random parameter vectors $\mathbf{p}^j = \left\{p_k^j\right\}$ $j = 1 \dots \mathrm{N}$ by randomly sampling each component p_k independently from an uniform distribution ranging from 0.1 to 1.9 of its best-fit value $\mathrm{p_{ref,k}}$ given in sec. B. I partitioned the (Δt, N_{pairings})-plane of fig. 2.7A1 (below) as a grid of N points and measured the mean squared distance D for each vector $\mathbf{p}^j$ as:

$$D(\mathbf{p}^j) = \sqrt{\frac{1}{2N}\sum_{i=1}^{N}\left[\left(W_{\mathrm{pre}}(i|\mathbf{p}^j) - W_{\mathrm{pre}}(i|\mathbf{p}_{\mathrm{ref}})\right)^2 + \left(W_{\mathrm{post}}(i|\mathbf{p}^j) - W_{\mathrm{post}}(i|\mathbf{p}_{\mathrm{ref}})\right)^2\right]}$$

where $W_{\mathrm{pre}}\,(i|\mathbf{p}^j)$ denotes the value of the presynaptic weight at point i of the (Δt, N_{pairings})-grid when the values of the free parameters are given by the vector $\mathbf{p}^{\mathrm{j}}$, and $\mathbf{p}_{\mathrm{ref}}$ denotes the best-fit values. I then fitted the resulting points with linear regression

$$D(\mathbf{p}) = \mathbf{p}^{\mathrm{T}}\mathbf{b} + b_0$$

using ordinary least squares. Here $\mathbf{b} = (b_1,\dots,b_M)$ is the vector of regression coefficients and b_0 a constant. Note that I did not adapt the parameters of numerical integration of the model to each set of randomly chosen parameters. Parameters that led to integration failure were thus not taken into account. These rejections did not compromise uniformity of the distribution. I then computed for each parameter p_k its standardized linear-regression coefficient (SRC)

$$SRC_k = b_k\frac{Var\,(p_k)}{Var\,(D)}$$

where $Var(p_k) = 0.27{p_{\mathrm{ref},k}}^2$. SRC_k is a measure of sensitivity of parameter k (Saltelli et al. 2002): when p_k varies away from its best-fit value, the distance between the resulting model output and the reference output of fig. 2.7A1 is proportional to SRC_k.

A.4 Extra components of the model

A.4.1 VSCC T-type

Ca^{2+} T-type channels can be described by (Wolf et al. 2005):

$$\begin{aligned} P_{CaT} &= p_{CaT} \cdot (m_{CaT})^3 \cdot h_{CaT} \\ \frac{dh_{CaT}}{dt} &= \frac{h^{\infty}_{CaT}(V) - h_{CaT}}{\tau^h_{CaT}(V)/q^h_{CaT}} \\ \frac{dm_{CaT}}{dt} &= \frac{m^{\infty}_{CaT}(V) - m_{CaT}}{\tau^m_{CaT}(V)/q^m_{CaT}} \\ m^{\infty}_{CaT}(V) &= \frac{1}{1+\exp(\frac{V-m^{half}_{CaT}}{m^{slope}_{CaT}})} \\ h^{\infty}_{CaT}(V) &= \frac{1}{1+\exp(\frac{V-h^{half}_{CaT}}{h^{slope}_{CaT}})} \end{aligned} \tag{A.1}$$

Here P_{CaT} and p_{CaT} are permeability and its maximum value respectively, m_{CaT} and h_{CaT} gating variables describing the voltage-dependent kinetics of the channel, V is membrane potential. x^y_{CaT} where $x = q, h, m$, $y = h, m, half, slope$ are parameters chosen to match experiments. A more detailed description of all parameters can be found (sec. B). The functions $\tau^h_{CaT}(V)$ and $\tau^h_{CaT}(V)$ were obtained by linear interpolation from the experimental data of McRory et al. (2001); see the model of Wolf et al. (2005) and the data of McRory et al. (2001) (their fig. 6B,E).

Table A.1: Experimentally determined voltage-dependence of kinetic parameters of T-type calcium channel (data taken from the source code of the model of Wolf et al. (2005) from https://senselab.med.yale.edu/modeldb/showModel.cshtml?model=112834&file=/nacb_msp/cat.mod)

V (mV)	τ^h_{CaT} (ms)	τ^h_{CaT} (ms)
-65	382	20.2
-60	208	20.2
-55	162	13.1
-50	129	8.7
-45	119	6.8
-40	107	5.6

V (mV)	τ^h_{CaT} (ms)	τ^h_{CaT} (ms)
-35	107	4.4
-30	107	3.8
-25	108	3.6
-20	109	3.3
-15	109	3.6
-10	110	3.6
-5	110	3.3
...	...	...
10	110	3.3

A.5 Fast calcium buffering approximation

Calcium (C) binding to endogenous buffer (B) leads to formation of calcium-buffer complex (CaB). This can be described with

$$\mathrm{C} + \mathrm{B} \underset{\mathrm{k_-}}{\overset{\mathrm{k_+}}{\rightleftharpoons}} \mathrm{CaB}$$

Corresponding system of ODE reads:

$$\begin{aligned} &\frac{d[Ca]}{dt} = R + J, \\ &\frac{d[CaB]}{dt} = -R, \\ &\frac{d[Ca]}{dt} + \frac{d[CaB]}{dt} = J, \\ &R = k_-[CaB] - k_+[C \cdot B], \end{aligned} \tag{A.2}$$

where k_x are reaction rates and J accounts for total calcium flux.

Equilibrium approximation (fast buffering) $R = 0$ implies that

$$B = K_{dB}[CaB]/C, \tag{A.3}$$

where $K_{dB} = k_-/k_+$.

Total concentration of buffer (B_T constant) is

$$CaB + B = B_T.$$

This equation together with eq. A.3 gives

$$CaB = B_T/(1 + K_{dB}/C).$$

Taking derivative gives:

$$\frac{dCaB}{dt} = \frac{B_T}{K_{dB}(1 + C/K_{dB})^2}\frac{dCa}{dt}.$$

Plugging this $\frac{dCaB}{dt}$ in the third equation of system eq. A.2 gives

$$T_C(C)\frac{d[Ca]}{dt} = J,$$
$$T_x(x) = 1 + \frac{B_T}{K_{dB}(1 + x/K_{dB})^2}.$$

Expanding total calcium flux $J = J_{ER} + J_{ch} - \frac{C-C_b}{\tau_{C_b}}$ gives eq. 2.19.

Appendix B

Parameters

In the tables B.1 and B.2 below, groups of parameters corresponding to various components of the model are separated with alternating color. “Name in code” shows name of a parameter in “pars” dictionary in python code and inside “pars” structure in FORTRAN code. If a group of parameters includes parameter “on”, its value controls if this component is enabled (when 1) or disabled (when 0). In the later case, values of all other parameters in group are irrelevant. After a table, list of reference for parameters values is given.

Table B.1: Parameter values in control conditions

Description	Name	Name in code	Values	Units	Reference
AMPAR opening rate constant	α_{AMPAR}	AMPA, Alpha	1.02	$1/(\mu M \cdot s)$	Adapted from Alain Destexhe, Z. Mainen, and T. Sejnowski 1995
AMPAR closing rate constant	β_{AMPAR}	AMPA, Beta	190	1/s	Adapted from Alain Destexhe, Z. Mainen, and T. Sejnowski 1995
AMPAR closing rate constant	ϵ_{AMPAR}	AMPA, Epsilon	0	1/s	Adapted from Alain Destexhe, Z. Mainen, and T. Sejnowski 1995
AMPAR desensitization rate constant	γ_{AMPAR}	AMPA, Gamma	0	1/s	Adapted from Alain Destexhe, Z. Mainen, and T. Sejnowski 1995
AMPAR maximal conductance	g_{AMPA}	AMPA, gAMPA	5.1	nS	Estimated from experimental data
Controls if AMPAR is enabled	—	AMPA, on	1	—	—
CB1R opening rate constant	α_{CB1R}	CB1R, Alpha	0.240195	$1/(\mu M \cdot s)$	Estimated from experimental data
CB1R closing rate constant	β_{CB1R}	CB1R, Beta	11.0719	1/s	Estimated from experimental data
CB1R closing rate constant	ϵ_{CB1R}	CB1R, Epsilon	0.0477957	1/s	Estimated from experimental data
CB1R desensitization rate constant	γ_{CB1R}	CB1R, Gamma	416.379	1/s	Estimated from experimental data
Controls if CB1R with desensitization is enabled	—	CB1R, on	1	—	—
IP3R binding rate (inactivation)	a_2	CICR, a2	0.5	$\mu M/s$	Adapted from De Pittà et al. 2009
IP3R affinity for IP3	d_1	CICR, d1	0.13	μM	De Pittà et al. 2009
IP3R dissociation constant (inactivation)	d_2	CICR, d2	3.049	μM	Adapted from De Pittà et al. 2009
IP3R affinity for IP3	d_3	CICR, d3	0.9434	μM	De Pittà et al. 2009
IP3R affinity for Ca	d_5	CICR, d5	0.12	μM	Adapted from De Pittà et al. 2009
SERCA pump affinity for Ca	K_{ER}	CICR, ker	0.05	μM	De Pittà et al. 2009

Continued on next page

Table B.1: Parameter values in control conditions

Description	Name	Name in code	Values	Units	Reference
Maximal IP3R rate	r_c	CICR, rc	4	1/s	Adapted from De Pittà et al. 2009
ER-to-cytosol volume ratio	ρ_{ER}	CICR, rhoER	0.3	—	Adapted from De Pittà et al. 2009
Ca leak from the ER	r_l	CICR, rl	0.1	1/s	De Pittà et al. 2009
Maximal SERCA pump rate	ν_{ER}	CICR, ver	8	μM/s	Adapted from De Pittà et al. 2009
Total endogeneous Ca buffer	B_T	CaBuff, BT	4.5	μM	—
Basal cytoplasmic Ca concentration	Ca_b	CaBuff, Cab	0.1	μM	Bernardo L. Sabatini, Oertner, and Svoboda 2002; Jackson and Redman 2003
Endogeneous Ca buffer affinity for Ca	K_{dB}	CaBuff, KdB	0.5	μM	Jackson and Redman 2003; Nägerl et al. 2000
Time scale for Ca exit	τ_{Ca_b}	CaBuff, tauCab	0.007	s	—
Tonic synaptic dopamine	DA	DA, DA	0.01	μM	—
Dopamine effect on rate of eCB plasticity	$C1/DA$	DA, gamma1DA	0.7	$1/\mu$M	Estimated from experimental data
Dopamine effect on time scale of eCB plasticity	$C2/DA$	DA, gamma2DA	0.07	$1/\mu$M	Estimated from experimental data
DAGL α affinity for DAG	K_{DAGL}	DGLandDAG, KDGL	30	μM	Okamoto et al. 2004
Maximal DAG kinase activity	r_{DAGK}	DGLandDAG, kDAGK	2	μM/s	Set for rapid turnover dynamics
Maximal MAG lipase activity	r_{MAGL}	DGLandDAG, kMAGL	0.5	μM/s	Set for rapid turnover dynamics
Maximal DAGL α rate	r_{DGL}	DGLandDAG, rDGL	20000	μM/s	Set for rapid turnover dynamics
Controls if CB1R with desensitization is used to compute W_{pre}	—	ECb, CB1R_on	1	—	—
FAAH Michaelis-Menten constant	K_{FAAH}	ECb, KFAAH	1	μM	Okamoto et al. 2004
The constant determining the rate of LTD induction	A_{LTD}	ECb, LTDMax	0.65	—	Estimated from experimental data
The lower limit of LTD induction	θ_{LTD}^{start}	ECb, LTDstart	0.027	—	Estimated from experimental data

Continued on next page

Table B.1: Parameter values in control conditions

Description	Name	Name in code	Values	Units	Reference
The upper limit of LTD induction	θ_{LTD}^{stop}	ECb, LTDstop	0.047	—	Estimated from experimental data
The constant determining the rate of LTP induction	A_{LTP}	ECb, LTPMax	13.5425	—	Estimated from experimental data
The lower limit of LTP induction	θ_{LTP}^{start}	ECb, LTPstart	0.086	—	Estimated from experimental data
presynaptic plasticity time scale	P_1	ECb, P1	1e-09	s	Set to yield rapid (slow) changes of W_{pre} for high (low) 2-AG values
presynaptic plasticity time scale	P_2	ECb, P2	1e-05	s	Set to yield rapid (slow) changes of W_{pre} for high (low) 2-AG values
presynaptic plasticity time scale	P_3	ECb, P3	7	—	Set to yield rapid (slow) changes of W_{pre} for high (low) 2-AG values
presynaptic plasticity time scale	P_4	ECb, P4	2	s	Set to yield rapid (slow) changes of W_{pre} for high (low) 2-AG values
Fraction of AEA contributing to CB1R activation	α	ECb, alphaAEACB1	0.1	—	Set for lower activation of CB1R by AEA compared to 2-AG
Scaling factor for endocannabinoid contribution to plasticity	k_{CB1R}	ECb, kCB1R	3000	$1/\mu$M	Estimated from experimental data
Controls if eCB plasticity is enabled	—	ECb, on	1	—	—
N-acetyltransferase activity	ν_{AT}	ECb, vATAEA	0.2	1/s	half-maximal activation of AT is obtained at Ca2+ concentrations that are well above the calcium levels in the model (around 0.2 to 0.5 mM)
FAAH enzyme activity	r_{FAAH}	ECb, vFAAH	4	μM/s	Estimated from experimental data

Continued on next page

Table B.1: Parameter values in control conditions

Description	Name	Name in code	Values	Units	Reference
Base half-half-width of LTD window	—	ECb_smooth, K	0.0007	—	Defined via k_s in eq. 2.30 to have single smoothness parameter
Flatness of LTD window tip	—	ECb_smooth, kadd	0	—	Defined via k_s in eq. 2.30 to have single smoothness parameter
Exponent controlling flatness of LTD window tip	—	ECb_smooth, kn	1	—	Fixed in eq. 2.30
Enlargement of LTD window compared to sharp thresholds	—	ECb_smooth, kw	10	—	Set to fit smooth LTD window width
Exponent of LTD window	—	ECb_smooth, n	2	—	Fixed in eq. 2.30
Controls if smooth Ω-function is used (eq. 2.30)	—	ECb_smooth, on	0	—	—
Smoothness of LTP threshold	—	ECb_smooth, tau	0.0001	—	Defined via k_s in eq. 2.30 to have single smoothness parameter
$GABA_AR$ opening rate constant	—	GABAA, Alpha	5	$1/(\mu M \cdot s)$	Adapted from Alain Destexhe, Z. Mainen, and T. Sejnowski 1995
NMDAR NR2B closing rate constant	—	GABAA, Beta	180	1/s	Adapted from Alain Destexhe, Z. Mainen, and T. Sejnowski 1995
Reversal potential $GABA_AR$	—	GABAA, EGABAA	-60	mV	Directly measured in experiments
Conductance of $GABA_AR$	—	GABAA, gGABAA	10	nS	Estimated from experimental data
Controls if GABAA is enabled	—	GABAA, on	0	—	—
GABA baseline concentration in the cleft	$GABA_0$	GABA_release, BaseLevel	0	μM	Estimated from experimental data
GABA peak concentration in the cleft	$GABA_{max}$	GABA_release, GABAmax	1000	μM	Estimated from experimental data
Cortex-to-FS synaptic delay	Δ_{GABA}	GABA_release, delay	0.003	s	Estimated from experimental data
Controls if GABA release is simulated	—	GABA_release, on	0	—	—

Continued on next page

Table B.1: Parameter values in control conditions

Description	Name	Name in code	Values	Units	Reference
If steady rise-then-fall is used	—	GABA_release, steadyrise_on	0	—	—
GABA decay time constant in the cleft	τ_{GABA}	GABA_release, tauGABA	0.005	s	Estimated from experimental data
Glutamate baseline concentration in the cleft	G_0	Glu_release, BaseLevel	0	μM	Estimated from our experimental data
Glutamate peak concentration in the cleft	G_{max}	Glu_release, Glumax	2000	μM	Estimated from our experimental data
If steady rise-then-fall is used	—	Glu_release, steadyrise_on	0	—	Used only to simulate change of resting potential under the block of EAAT2
Glutamate decay time constant in the cleft	τ_G	Glu_release, tauGlu	0.005	s	Estimated from our experimental data
PI3K affinity for IP3	K_3	IP3, k3	1	μM	De Pittà et al. 2009
PLCδ product inhibition	κ_d	IP3, kappad	1.5	μM	De Pittà et al. 2009
PI3K Ca-activation constant	K_D	IP3, kd	1.5	μM	Adapted from De Pittà et al. 2009
PLCδ Ca-activation	K_δ	IP3, kdelta	0.1	μM	De Pittà et al. 2009
regulation by PLCβ termination signal	K_P	IP3, kp	10	μM	De Pittà et al. 2009
PKC Ca-activation constant	K_π	IP3, kpi	0.6	μM	De Pittà et al. 2009
Glu affinity to mGluR	K_R	IP3, kr	1.3	μM	De Pittà et al. 2009
Hill exponent of IP3-dependent IP3-3K activation	n_3	IP3, n3	1	—	Adapted from De Pittà et al. 2009
Controls if De Pitta's approximation is used for CaMKII-IP3 interaction	—	IP3, old_IP3_on	False	—	—
5P-IP maximal rate	r_{5P}	IP3, r5p	0.2	1/s	Adapted from De Pittà et al. 2009
PI3K maximal rate	$\widetilde{\nu}_{3K}$	IP3, v3k	0.001	μM/s	Set to agree with the model of CaMKII phosphorilation
PLCβ maximal rate	ν_β	IP3, vbeta	0.8	μM/s	Adapted from De Pittà et al. 2009
PLCδ maximal rate	ν_δ	IP3, vdelta	0.02	μM/s	De Pittà et al. 2009

Continued on next page

Table B.1: Parameter values in control conditions

Description	Name	Name in code	Values	Units	Reference
Coefficient converting NMDAR current to calcium fluxes	ξ_{NMDA}	I_to_Ca_flux, NMDA	70	μM/pCol	set to match Ca2+ amplitudes Bernardo L. Sabatini, Oertner, and Svoboda 2002
Controls if NMDA is computed with GHK	—	I_to_Ca_flux, NMDA_by_GHK	0	—	Set for anti-Hebbian STDP
Coefficient converting TRPV1 current to calcium fluxes	ξ_{TRPV1}	I_to_Ca_flux, TRPV1	310	μM/pCol	set to match Ca2+ amplitudes Bernardo L. Sabatini, Oertner, and Svoboda 2002
Controls if TRPV1 is computed with GHK	—	I_to_Ca_flux, TRPV1_by_GHK	0	—	Set for anti-Hebbian STDP
Coefficient converting VSCC current to calcium fluxes	ξ_{VSCC}	I_to_Ca_flux, VDCC	84	μM/pCol	set to match Ca2+ amplitudes Carter and Bernardo L Sabatini 2004
Ca-activation constant for K	K_K	KandP_on_DAGLP, KmK	3	μM	Estimated from experimental data
Ca-activation constant for phosphatase P	K_P	KandP_on_DAGLP, KmP	0.053	μM	Estimated from experimental data
Hill number for K activation	n_K	KandP_on_DAGLP, nK	6	—	Estimated from experimental data
Hill number for P activation	n_P	KandP_on_DAGLP, nP	3	—	Estimated from experimental data
Base level of kinase K activity, eq. 2.11	r_{K0}	KandP_on_DAGLP, r0K	0	1/s	Estimated from experimental data
Base level of phosphatase P activity, eq. 2.11	r_{P0}	KandP_on_DAGLP, r0P	0	1/s	Estimated from experimental data
Maximal rate of kinase K	r_K	KandP_on_DAGLP, rK	50	μM/s	Estimated from experimental data
Maximal rate of phosphatase P	r_P	KandP_on_DAGLP, rP	380	μM/s	Estimated from experimental data
Controls if simple model for ϕ_{DAGL} is used	—	KandP_on_DAGLP, simple_DAGLP_on	1	—	—

Continued on next page

Table B.1: Parameter values in control conditions

Description	Name	Name in code	Values	Units	Reference
NMDAR opening rate constant	α_{NMDAR}	NMDA, Alpha	0.072	$1/(\mu M \cdot s)$	Adapted from Alain Destexhe, Z. Mainen, and T. Sejnowski 1995
NMDAR closing rate constant	β_{NMDAR}	NMDA, Beta	100	1/s	Increased from Alain Destexhe, Z. Mainen, and T. Sejnowski 1995
Magnesium concentration	$[Mg^{2+}]$	NMDA, Mg	1	mM	Directly measured in experiments
NMDAR maximal conductance	g_{NMDA}	NMDA, gNMDA	1.53	nS	Estimated from experimental data
Controls if NMDAR is enabled	—	NMDA, on	1	—	—
Permeability of NMDAR to Ca2+	—	NMDA, p_ca	2.08324e-46	μL/s	—
NMDAR NR2B opening rate constant	$\alpha_{NMDA-NR2B}$	NMDA_NR2B, Alpha	0.072	$1/(\mu M \cdot s)$	Same as for NMDAR
NMDAR NR2B closing rate constant	$\beta_{NMDA-NR2B}$	NMDA_NR2B, Beta	100	1/s	Same as for NMDAR
Extracellular Mg2+ concentration	$[Mg^{2+}]$	NMDA_NR2B, Mg	1	mM	Directly measured in experiments
Conductance of NMDAR NR2B	g_{NMDA}	NMDA_NR2B, gNMDA	0.28	nS	Estimated from experimental data
Controls if NMDAR NR2B is enabled	—	NMDA_NR2B, on	0	—	—
Permeability of NMDAR NR2B to Ca2+	—	NMDA_NR2B, p_ca	2.08324e-46	μL/s	Estimated from experimental data
the voltage sensor to channel gating coupling constant	C	TRPV1, C	23367	—	Matta and Ahern 2007
the temperature sensor to channel gating coupling constant	D	TRPV1, D	1100	—	Matta and Ahern 2007
Change in enthalpy	ΔH	TRPV1, DH	205000	kJ/mol	Matta and Ahern 2007
Change in entropy	ΔS	TRPV1, DS	615	J/(mol K)	Matta and Ahern 2007
Equilibrium constant of voltage sensor at 0 mV	J_0	TRPV1, J0	0.0169	—	Matta and Ahern 2007
Equilibrium constant of temperature sensor	K	TRPV1, K	0.00182634	—	Matta and Ahern 2007
—	L	TRPV1, L	0.00042	—	Matta and Ahern 2007
—	P	TRPV1, P	750	—	Matta and Ahern 2007
TRPV1 maximal conductance	g_{TRPV1}	TRPV1, gTRPV1	0.0003	nS	Estimated from experimental data

Continued on next page

Table B.1: Parameter values in control conditions

Description	Name	Name in code	Values	Units	Reference
Controls if L-type (1.3) TRPV1 is enabled	—	TRPV1, on	1	—	—
Permeability of TRPV1	—	TRPV1, p_ca	2.23205e-49	μL/s	Estimated from experimental data
Gating charge	z	TRPV1, z	0.6	—	Matta and Ahern 2007
The duration of stimulating step current	DC_{dur}	action, APdur	0.03	s	From the experimental stimulation protocol
The amplitude of action current	AP_{max}	action, APmax	7020	pA	To reproduce bAP in experiments and in Elodie Fino, Paille, et al. 2010
The amplitude of stimulating step current	DC_{max}	action, DPmax	495	pA	From the experimental stimulation protocol
If action current is used in place of VSCC	—	action, action_as_VDCC	False	—	—
The time constant of action current	τ_{bAP}	action, tausbAP	0.001	s	To reproduce bAP in experiments and in Elodie Fino, Paille, et al. 2010
Scaling of voltage-dependent rate	$c^{\alpha}_{CaLv1.3}$	caL13, c	39.8	1/(s·mV)	Wolf et al. 2005
Scaling of voltage-dependent rate	$c^{\beta}_{CaLv1.3}$	caL13, cpr	990	1/s	Wolf et al. 2005
Time scaling factor of gating variable correcting for temperature	$q^{h}_{CaLv1.3}$	caL13, hqfact	3	—	Wolf et al. 2005
Slope of the steady-state Boltzmann fit	$h^{slope}_{CaLv1.3}$	caL13, hslope	11.9	mV	Wolf et al. 2005
Time constant of gating variable	$\tau^{h}_{CaLv1.3}$	caL13, htau	0.0443	s	Wolf et al. 2005
half-activation voltage of the steady-state Boltzmann fit	$h^{half}_{CaLv1.3}$	caL13, hvhalf	-13.4	mV	Wolf et al. 2005
Slope of the steady-state Boltzmann fit	$k^{\alpha}_{CaLv1.3}$	caL13, k	9.005	mV	Wolf et al. 2005
Slope of the steady-state Boltzmann fit	$k^{\beta}_{CaLv1.3}$	caL13, kpr	31.4	mV	Wolf et al. 2005
Slope of the steady-state Boltzmann fit	$m^{slope}_{CaLv1.3}$	caL13, mslope	-6.7	mV	Wolf et al. 2005
half-activation voltage of the steady-state Boltzmann fit	$m^{half}_{CaLv1.3}$	caL13, mvhalf	-33	mV	Wolf et al. 2005
Controls if L-type (1.3) VSCC is enabled	—	caL13, on	1	—	—

Continued on next page

Table B.1: Parameter values in control conditions

Description	Name	Name in code	Values	Units	Reference
Permeability of L-type (1.3) VSCC	$p_{CaLv1.3}$	caL13, pcaLbar	1.02e-06	μL/s	Value of Wolf et al. 2005 scaled to 5000 spines, radius 1 μm
Time scaling factor of gating variable correcting for temperature	$q^m_{CaLv1.3}$	caL13, qfact	3	—	Wolf et al. 2005
Reversal potential	$V_{CaLv1.3}$	caL13, vm	-8.124	mV	Wolf et al. 2005
Slope of the steady-state Boltzmann fit	h^{slope}_{CaT}	cat, hslope	6.7	mV	Wolf et al. 2005
half-activation voltage of the steady-state Boltzmann fit	h^{half}_{CaT}	cat, hvhalf	-80	mV	Wolf et al. 2005
Slope of the steady-state Boltzmann fit	m^{slope}_{CaT}	cat, mslope	-6.53	mV	Wolf et al. 2005
half-activation voltage of the steady-state Boltzmann fit	m^{half}_{CaT}	cat, mvhalf	-51.73	mV	Wolf et al. 2005
Controls if T-type VSCC are enabled	—	cat, on	0	—	—
Permeability of T-type VSCC	p_{CaT}	cat, pcatbar	9.6e-07	μL/s	Estimated from experimental data
Time scaling factor of gating variable	q^h_{CaT} and q^m_{CaT}	cat, qfact	3	—	Wolf et al. 2005
Extracellular Ca2+ concentration	Ca_{out}	common, Ca_out	5000	μM	Wolf et al. 2005
Faraday constant	F	common, F	96.5	kCol/mol	—
Absolute temperature	T	common, T	307.15	K	Directly measured in our experiments
Valence Ca2+	z_{Ca}	common, zS	2	—	—
Absolute tolerance for LSODA	—	integration, ATOL	1e-07	—	Set to yield correct integration in reasonable time
Maximal allowed integration time step	—	integration, HMAX	50	s	Set to yield correct integration in reasonable time
Maximal number of substeps per time step	—	integration, MXSTEP	1000	—	Set to yield correct integration in reasonable time
Relative tolerance for LSODA	—	integration, RTOL	1e-07	—	Set to yield correct integration in reasonable time

Continued on next page

Table B.1: Parameter values in control conditions

Description	**Name**	**Name in code**	**Values**	**Units**	**Reference**
End time	—	integration, t_end	250	s	Set to $N_{pairings}$/frequency+150, to let W_{pre} and W_{post} reach steady states
Initial time	—	integration, t_start	0	s	—
Time step for solution (actual time step is chosen by LSODA)	—	integration, t_step	0.001	s	Set for speed and low memory cost while sampling fast changes of variables
Membrane capacitance	C_m	mem, Cm	0.1	nF	From experiments
Resting membrane potential	V_L	mem, EL	-70	mV	Directly measured in our experiments
Leak conductance	g_L	mem, gL	10	nS	Estimated from experimental data
Total CaMKIIα concentration	$CaMK_{tot}$	post_CaMKII_plast, CaMKT	16.6	μM	Graupner and Brunel 2007
Total Calmodulin concentration	CaM_{tot}	post_CaMKII_plast, CaMT	0.07052	μM	Adapted from Graupner and Brunel 2007
Total I1 concentration	$I1_0$	post_CaMKII_plast, I10	1	μM	Graupner and Brunel 2007
CaM, phosphorylated CaMKII subunit dissociation constant	K_5	post_CaMKII_plast, K5	0.1	μM	Graupner and Brunel 2007
Michaelis constant	K_M	post_CaMKII_plast, KM	0.4	μM	Graupner and Brunel 2007
Calcium, calmodulin dissociation constant	K_1	post_CaMKII_plast, Ka1	0.1	μM	Graupner and Brunel 2007
Calcium, calmodulin dissociation constant	K_2	post_CaMKII_plast, Ka2	0.025	μM	Graupner and Brunel 2007
Calcium, calmodulin dissociation constant	K_3	post_CaMKII_plast, Ka3	0.32	μM	Graupner and Brunel 2007
Calcium, calmodulin dissociation constant	K_4	post_CaMKII_plast, Ka4	0.4	μM	Graupner and Brunel 2007
CaN half activation	K_{CaN}	post_CaMKII_plast, KdcanI1	0.053	μM	Graupner and Brunel 2007

Continued on next page

Table B.1: Parameter values in control conditions

Description	Name	Name in code	Values	Units	Reference
PKA half activation	K_{PKA}	post_CaMKII_plast, KdpkaI1	0.159	μM	Adapted from Graupner and Brunel 2007
Total PP1 concentration	$PP1_0$	post_CaMKII_plast, PP10	0.2	μM	Graupner and Brunel 2007
I1P, PP1 association rate	k_{11}	post_CaMKII_plast, k11	500	$1/(\mu\text{M}\cdot\text{s})$	Graupner and Brunel 2007
Dephosphorylation rate of CaMKII subunit	k_{12}	post_CaMKII_plast, k12	6000	1/s	Graupner and Brunel 2007
Probability of a phosphorylation step	k_6	post_CaMKII_plast, k6	6	1/s	Graupner and Brunel 2007
Probability of a phosphorylation step	k_7	post_CaMKII_plast, k7	6	1/s	Graupner and Brunel 2007
CaM-independent base CaN activity	k^0_{CaN}	post_CaMKII_plast, kcan0I1	0.05	1/s	Adapted from Graupner and Brunel 2007
Maximal CaM-dependent CaN activity	k_{CaN}	post_CaMKII_plast, kcanI1	20.5	1/s	Adapted from Graupner and Brunel 2007
I1P, PP1 dissociation rate	k_{-11}	post_CaMKII_plast, km11	0.1	1/s	Graupner and Brunel 2007
CaM-independent base PKA activity	k^0_{PKA}	post_CaMKII_plast, kpka0I1	0.0025	1/s	Adapted from Graupner and Brunel 2007
Maximal CaM-dependent PKA activity	k_{PKA}	post_CaMKII_plast, kpkaI1	4.67	1/s	Adapted from Graupner and Brunel 2007
CaN Hill exponent	n_{CaN}	post_CaMKII_plast, ncanI1	3	—	Graupner and Brunel 2007
PKA Hill exponent	n_{PKA}	post_CaMKII_plast, npkaI1	3	—	Decreased from Graupner and Brunel 2007, Ahn et al. 2007
Stimulation frequency	$Frequency$	stimulation, Freq	1	Hz	From the experimental stimulation protocol
Default value of Δt, actual value is varied	Δt	stimulation, dt_stim	0.02	s	From the experimental stimulation protocol
Number of pairings	$N_{pairings}$	stimulation, num_stim	100	—	From the experimental stimulation protocol
Controls if postsynaptic stimulation is enabled	—	stimulation, post_on	1	—	—

Continued on next page

Table B.1: Parameter values in control conditions

Description	**Name**	**Name in code**	**Values**	**Units**	**Reference**
Controls if presynaptic stimulation is enabled	—	stimulation, pre_on	1	—	—
Controls if regular stimulation protocol is used	—	stimulation, regular_on	1	—	—
Step for tabulation of linearly approximated functions	—	stimulation, tables_step	5e-05	s	Set for good linear approximation of functions and speed of computation
Delay before stimulation	—	stimulation, tpost	0.5	s	Set to have $t_{start} < t_{pre_1}$ for $\max(\Delta t)$
Delay to bAP outset	δ	stimulation, tsdt	0.015	s	From the experimental stimulation protocol

Table B.2: Parameters with EAAT2 block modified from control

Name	Name in code	Values	Units	Reference
α_{AMPAR}	AMPA, Alpha	1.02	$1/(\mu M \cdot s)$	Adapted from Alain Destexhe, Z. Mainen, and T. Sejnowski 1995
β_{AMPAR}	AMPA, Beta	10	1/s	Adapted from Alain Destexhe, Z. Mainen, and T. Sejnowski 1995
ϵ_{AMPAR}	AMPA, Epsilon	0.6	1/s	Adapted from Alain Destexhe, Z. Mainen, and T. Sejnowski 1995
γ_{AMPAR}	AMPA, Gamma	180	1/s	Adapted from Alain Destexhe, Z. Mainen, and T. Sejnowski 1995
g_{AMPA}	AMPA, gAMPA	6	nS	Estimated from experimental data
A_{LTD}	ECb, LTDMax	1	—	Estimated from experimental data
θ_{LTP}^{start}	ECb, LTPstart	0.1118	—	Estimated from experimental data
—	GABAA, gGABAA	20	nS	Estimated from experimental data
—	GABAA, on	True	—	—
—	GABA_release, on	True	—	—
G_0	Glu_release, BaseLevel	0.05	μM	Estimated from our experimental data
ξ_{VSCC}	I_to_Ca_flux, VDCC	81.48	μM/pCol	set to match Ca2+ amplitudes Carter and Bernardo L Sabatini 2004
g_{NMDA}	NMDA, gNMDA	1.8	nS	Estimated from experimental data ($\frac{g_{AMPA}}{g_{NMDA}} = 0.3$)
g_{NMDA}	NMDA_NR2B, gNMDA	10	nS	Estimated from experimental data
—	NMDA_NR2B, on	1	—	—
V_L	mem, EL	-55	mV	Directly measured in our experiments

Appendix C

Other results

C.1 Anti-Hebbian t-LTP with Graupner and Brunel (2007)

In the calcium-control hypothesis, no plasticity, LTD and LTP are caused by low, medium and high calcium concentration transients respectively. With this hypothesis applied to the hippocampal Hebbian STDP (fig. 1.10), NMDAR-CaMKII-dependent t-LTP, that is seen at small positive Δt, should be caused by a high calcium concentration. That is calcium influx via NMDAR must be highest at small positive Δt compared to that at any other Δt (and the lowest at small negative Δt where hippocampal t-LTD is observed).

To explain this dependence of calcium influx through NMDAR on Δt, a simple qualitative explanation is often evoked. NMDAR requires coincidence of both glutamate binding (for the opening of NMDAR's pore) and depolarization (to remove Mg^{2+} block of the pore). At positive Δt, glutamate is released from presynaptic neuron before the bAP arrives from postsynaptic soma; that is before the bAP delivers depolarization to synaptic site. Hence, glutamate binds to NMDAR before the time of the peak of depolarization (from bAP). Consequently, by the time peak depolarization arrives, NMDAR pore is ready to open due to previous glutamate binding. Therefore, when pre-before-post stimulus is delivered, NMDARs conductance noticeably increases causing high current and therefore high calcium influx. On the contrary, for negative Δt, depolarization from bAP arrives first and has started to vanish by the time glutamate binds. Thus, when glutamate binds, NMDAR is partly blocked by Mg^{2+}. Therefore, calcium influx in response to post-before-pre stimulus should be small.

However, this simple explanation implicitly assumes that depolarization and NMDAR conductance are linked by a monotonically increasing function (a higher depolarization leads to a higher

NMDAR conductance). If Ohm's law approximation is used for the calcium flux, the assumption is only true for a small range of membrane potential. In fact, the dependence of the steady-state current on voltage (so-called I-V curve) and therefore of calcium flux on voltage is highly nonlinear. This issue is even more pronounced for VSCC calcium channels, for which I-V curves are highly non-monotonic. The calcium influx through VSCC can be comparable to that through NMDARs. Therefore, along with NMDARs, VSCCs can substantially contribute to the outcome of calcium-controlled plasticity. The later can be especially pronounced when depolarization from bAP mostly stays in the range where VSCC current is maximal. To summarize, calcium current influx through NMDAR and VSCC depends on the combination of several factors: glutamate dynamics in the synaptic cleft (NMDAR), depolarization and calcium concentration inside of a spine and outside of the cell (both NMDAR and VSCC).

Applying calcium control hypothesis to cortico-striatal synapses, one would expect that the NMDAR-CaMKII-dependent t-LTP observed at negative Δt is caused by a higher calcium concentration than t-LTD at positive Δt. This t-LTD in turn should be caused by lower calcium concentration than for negative Δt but still higher than for Δt at which no plasticity is observed. This however contradicts the intuition arising from the simple idea described above. Below, I discuss how a higher calcium flux can be delivered by a post-before-pre stimulus compared to that of pre-before-post.

Without applying any stimulation protocols to the model, I studied the dependence of the steady state of the model on membrane potential. This is similar to the experimental method of obtaining I-V curves, whereby resting potential is manipulated by injecting a constant external current. The experimenter then waits for steady state and measures resulting trans-membrane current for each value of resting potential.

Fig. C.1A shows the dependence of steady state calcium fluxes on resting potential (voltage) in the model. These plots are equally valid when $GABA_AR$ current is included or not as $GABA_AR$ current only affects the voltage that in this case is fixed externally (fig. 2.2). I tested two alternative models for NMDAR and TRPV1 calcium fluxes, depending on either GHK or Ohm's law was used. When both NMDAR and TRPV1 calcium fluxes are modeled with GHK (fig. C.1A1), their steady dependence on voltage is described with monotonic function; the steady state calcium concentration takes its resting value at resting potential (-70 mV); it increases with the increase of voltage until it reaches its maximal value around -20 mV; with the further increase of voltage, it decreases back to its resting value at about 40 mV (dashed curve at fig. C.1B). When Ohm's law approximation is used to describe both NMDAR and TRPV1 calcium fluxes (fig. C.1A2), steady state calcium concentration decreases below the resting level for voltages above 10 mV (solid curve). This is due to the fact that NMDAR flux reverses its direction in the model (influx to outflux) at large voltages (V>0) (fig. C.1A2),

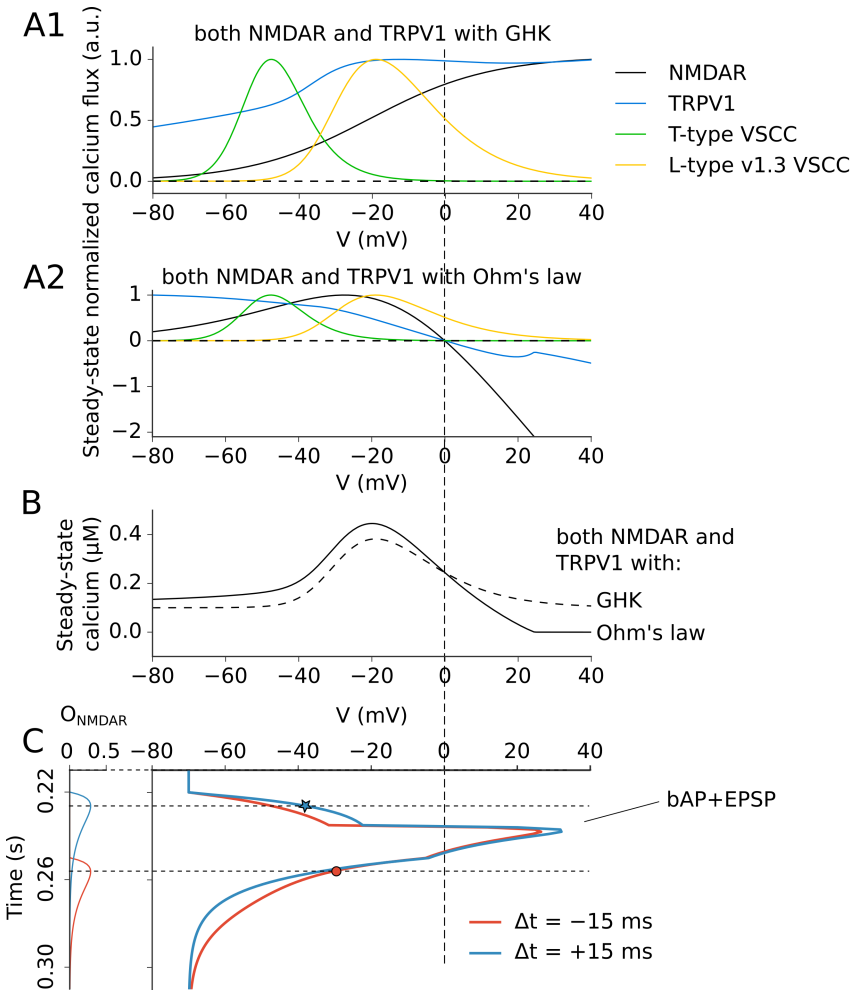

Figure C.1: **A.** The dependence of steady state calcium fluxes (normalized to their maximums) on the resting membrane potential (voltage). For each value of voltage, the glutamate concentration in the synaptic cleft is fixed to 10 μM, the model is simulated until steady-state is reached. NMDAR and TRPV1 calcium currents were modeled either with Ohm's law (**A2**) or with GHK (**A1**). In these two models, for low voltages, the steady-state calcium concentration (**B**) is lower for the model with GHK (dashed line) than for the model with Ohm's law (solid line). However, for high voltages (above 0), the steady-state calcium concentration is higher for the model with GHK than for that with Ohm's law. **C**, Right. Voltage transient in the model in response to single pairing with $\Delta t = \pm 15$ ms (blue/red). **C**, Left, The glutamate-controlled NMDAR opening probability (O_{NMDAR}) for the two Δt. Whereas voltage-transients are similar in both cases, the maximum of glutamate-dependent probability of NMDAR opening, O_{NMDAR}, happens at a higher voltage for Δt=-15 ms compared to Δt=+15 ms (higher voltage at red full circle than at blue star). However, for Δt=+15 ms, the decay phase of O_{NMDAR} that follows the maximum (when NMDAR are still conductive) occurs at higher voltages (including the bAP peak) compared to Δt=+15 ms.

thus yielding less steady-state calcium (fig. C.1C). Fig. C.1C,right shows voltage transient in response to a single pre-post pairing for $\Delta t = -15$ ms (post-before-pre pairing) and $\Delta t = +15$ ms (pre-before-post). For both cases, pairing of bAP and EPSP leads to voltage transients of similar shape and amplitude. However, the relative timing of glutamate release and the voltage transient differ (fig. C.1C,left). For $\Delta t = +15$ ms, glutamate release opens NMDAR during the voltage peak, i.e. the voltage range corresponding to calcium outflux (blue trace fig. C.1C). Calcium thus exits the cell through NMDA during the voltage peak. Whereas, for Δt=-15 ms, NMDAR opens *after* the voltage peak (fig. C.1B) and the possibility of calcium outflux. As a result, the global calcium influx for Δt=-15 ms is larger than for Δt=+15 ms.

In the framework of calcium-control hypothesis, this timing-dependence of calcium corresponds to anti-Hebbian STDP. Experiments of Paille et al. (2013) (sec. 1.1.7.2.2) demonstrate that anti-Hebbian versus Hebbian STDP at cortico-striatal synapses is decided by the state of postsynaptic $GABA_AR$. Thus, implementing postsynaptic $GABA_AR$ seems to be a good starting point to explain difference of calcium influx required to obtain anti-Hebbian STDP. Cortical stimulation during STDP protocol causes not only direct activation of MSN, but also indirect (therefore delayed) inhibition of MSN through direct activation of Fast Spiking (FS) interneurons. Thus, in response to a single cortical stimulus, the corresponding EPSP in the MSN should be followed by the IPSP caused by delayed $GABA_AR$ activation. The delay is determined by the time required for synaptic transmission through one more synapse (from cortex to FS interneurons and then to MSN, compared to the direct cortex to MSN transmission). Whereas $GABA_AR$ does not change directly steady state dependence of calcium fluxes on voltage, $GABA_AR$ activation affects voltage transients. This could change the region of the flux-voltage curves (fig. C.1A) that voltage transients explore during the STDP protocol, thus the total influx of calcium in the MSN. This idea delineates a potential mechanism for the $GABA_AR$-mediated plasticity switch (antiHebbian$\leftrightarrow$Hebbian) that still matches the calcium-control hypothesis: in control conditions ($GABA_AR$ not blocked), the calcium influx is larger for negative Δt than for positive Δt (anti-Hebbian) whereas $GABA_AR$ blockade alters the voltage trace in such a way that calcium influx becomes larger for positive Δt than for negative Δt (Hebbian). However, even after thorough numerical exploration and automated parameter optimization (see sec. A), I was not able to find an experimentally realistic set of parameters in support of this mechanism. In the model with GHK, calcium amplitude dependence on Δt corresponds to Hebbian plasticity: more calcium for pre-before-post (LTP) than for post-before-pre pairings (LTD). The addition of delayed GABA release (2-4 ms after glutamate release) produces almost no change of voltage transient for post-before-pre pairings with short Δt (LTD is kept). Indeed, in this case, AMPAR current (and therefore $GABA_AR$) appears after the peak of voltage transient for voltages <-30 mV (see fig. C.1C, red curve after red full circle). For these voltages close to reversal potential of GABA in MSNs (-60 mV), deviation from this reversal potential (driving force) and therefore

$GABA_AR$ current is small; hence, voltage transient is almost not altered.

Instead, for short pre-before-post parings, delayed $GABA_AR$ current coincides with the peak of voltage transient. For this reason, the driving force of GABA and $GABA_AR$ current are maximal. Hence, the amplitude of voltage transient is noticeably decreased. With GHK, this lower voltage decreases calcium influx via the major source, NMDAR (LTP is replaced by either LTP or if calcium transient reduced further by no plasticity). More calcium for post-before-pre than for pre-before-post pairings without GABA can be switched to less calcium for post-before-pre than for pre-before-post; however, Hebbian STDP, can be only switched to LTD or no plasticity for pre-before-post and LTD for post-before-pre because calcium amplitudes are decreased in the model with GABA. Hebbian $\rightarrow$ anti-Hebbian switch can be achieved if one either decreases plasticity thresholds with GABA signaling, or increases calcium currents (by increasing ξ_x and permeabilities, see eq. 2.17;eq. 2.18). Currently, such a change to thresholds or calcium currents is not supported experimentally. Therefore, I chose to use Ohm's law approximation to obtain calcium-dependence on Δt corresponding to anti-Hebbian STDP. This choice can be supported by the existence of the nano-domains of high calcium concentration (Higley and Bernardo L. Sabatini 2008). If calcium concentration in proximity of NMDAR and TRPV1 is close to that outside the cell, then Ohm's law approximation is valid. In recent modeling study, Griffith, Tsaneva-Atanasova, and Mellor (2016) simulated calcium diffusion in a spine in response to EPSP-bAP pairing. The calcium concentration in the nanodomain around NMDAR was more than 20 times larger than the concentration of calcium averaged over spine volume (see their Fig.1C). Whereas it is still not sufficient to make the local calcium concentration comparable to that outside of the cell, it suggest the possibility of higher compartmentalization of calcium concentration inside the spine. In their model, during EPSP-bAP pairing, high calcium concentrations were contained in nanodomains around NMDARs and VSCCs (their Fig.1B). Note that as in our model, they have used Ohm's law approximation for NMDAR calcium flux. This means that the EPSP-bAP triggered influx of extracellular calcium into NMDAR nanodomain was lower than it would have been with GHK model. With GHK, therefore, the difference between nanodomain concentration and the spine-volume averaged concentration could have been even higher in their model. The higher the local concentration of calcium (the closer to that outside of the cell) renders the Ohm's law approximation more applicable. We currently lack experimental data to directly support the idea of nanodomain calcium concentration comparable to that outside the cell. However, regardless of the way anti-Hebbian STDP is achieved, what matters for the calcium-controlled plasticity is calcium transients themselves; the way they were generated is of less crucial importance for our work. Thus, even if the part of the model generating calcium transients may turn out disputable, our modeling of plasticity downstream calcium transients can be still correct.

C.2 Preliminary work: a more realistic spiking

High jitter impairs regularity of both Δt and period. Spike-trains *in vivo* can have impaired periodicity (varied Inter Spike Interval, ISI), but individual spikes can still be well correlated with output spikes (Δt is almost not impaired). These spike-trains can as well have low average frequency over large time scales, altered with short periods of high-frequency spiking. This situation can be partially modeled by using two delayed (with the delay Δt) correlated Poisson trains as pre- and postsynaptic spike trains. The degree at which periodicity is impaired can be controlled if Poisson trains with refractory period are used. I simulated this situation with 200 pre- and postsynaptic homogeneous Poisson stimuli with expected frequency 0.5 Hz (expected 200 stimuli per 400-s-long stimulation). Pre- and postsynaptic spike trains were generated by removing spikes from the same "parent" sample of Poisson process. The expected frequency of the "parent" Poisson process was adjusted so that the expected frequency of the two "children" processes was 0.5 Hz after spike removal. The percentage of shared spikes between presynaptic Poisson spike train and Δt-shifted postsynaptic one was taken as a measure of "correlation" between the two trains. Let p be the probability of spike generation by "parent" Poisson at a single time step of numerical simulation. To generate "child" process, I remove spikes from a sample of "parent" process with probability, q. Then, the probability of finding a spike at a time step in the "child" process will be $p' = p(1-q)$. The expected fraction of the shared pulses for the two samples is given by $R = (1-q)^2$, expected frequency is given by p'/h=0.5 Hz, where h is the time step of numerical integration.

In this setting, the refractory period of the Poisson processes plays a crucial role since many of the time intervals between two successive presynaptic spikes will be comparable to the refractory period (by definition of a Poisson process). So when the refractory period is small, e.g. close to the pre-post pairing, the time interval between two successive presynaptic spikes, say $t_{pre}^{n+1} - t_{pre}^{n}$ will be of the same order as the spike timing defined as $\Delta t = t_{post}^{n} - t_{pre}^{n}$. If $t_{pre}^{n} < t_{post}^{n} < t_{pre}^{n+1}$ (a case that very frequently recurs), this definition of does not make much sense anymore since it does not take into account the spike timing between t_{post}^{n} and t_{pre}^{n+1}. Yet this latter spike timing is likely to be short enough to impact the synaptic weight if $t_{pre}^{n+1} - t_{pre}^{n}$ thus the refractory period is short.

In these conditions, the outcome of plasticity is determined neither by the spike-timing (defined as $\Delta t = t_{post}^{n} - t_{pre}^{n}$) nor by the correlation between the pre- and postsynaptic Poisson trains. However, if the refractory period is larger or equal to 50 ms (at the time scale where $CaMKII^*$ and y_{CB1R} almost do not depend on Δt), STDP has pronounced dependence on Δt even in the case when only 10% of pre- and postsynaptic spikes overlap at each Δt. These results suggest that in order for timing-dependent plasticity to be functional *in vivo*, the distribution of inter-spike

intervals (ISI) should be mostly contained in ISI>50 ms i.e. a frequency < 20 Hz. If this was found *in vivo*, this would suggest that learning might rely on spike-timing dependent plasticity. Moreover, modeling suggests that eCB-dependent plasticity, but not NMDAR-CaMKII-plasticity determines the STDP outcome in these more realistic conditions: no matter what refractory period (the degree of periodicity) was used (from highly irregular with 10 ms to close to periodic with 200 ms), STDP outcome in these conditions was completely determined by eCB-dependent presynaptic plasticity.

C.3 Experimental investigation of eCB-t-LTP regulation by dopamine

In the lab of Laurent Venance, our collaborators investigated the regulation of eCB-STDP by dopamine using experimental techniques including: Electrophysiology, Pharmacology, Lesioning, Opto-Genetics.

C.3.1 Dopamine is required during for eCB-t-LTP induction with a low number of pairings

Our experimental collaborators first examined whether eCB-t-LTP is affected in rat model of Parkinson's disease (hypodopaminergic rats). They performed unilateral lesion of the substantia nigra *pars compacta* (SNc) - the main source of dopaminergic innervation in the basal ganglia - by injecting 6-hydroxy-dopamine (6-OHDA). This treatment effectively destroys dopaminergic fibers of the SNc that deliver dopamine to the cortico-striatal synapse. As a control, they used sham-operated animals with saline injection. In adult sham-operated rats, 10 post-pre pairings induced t-LTP that was impaired in 6-OHDA treated rats (fig. C.2A). In 6-OHDA treated rats, t-LTP can be restored by treatment with dopamine precursor L-DOPA, a drug commonly used to treat Parkinson's disease (fig. C.2B). This restored t-LTP is CB1R-dependent since it is prevented by CB1R blocker (fig. C.2B).

Our collaborators then used more direct optogenetic approach to test if dopamine was required during the few pairings of the induction phase of eCB-t-LTP. During eCB-t-LTP induction protocol, they performed selective opto-inhibition of dopaminergic neurons in mice expressing archeorhodopsin-3 specifically in dopaminergic neurons (fig. C.3). In the protocol with 15 post-pre pairing, this opto-inhibition prevented the induction of t-LTP (fig. C.3B).

Therefore, eCB-t-LTP induction depends on dopamine during short stimulation and is impaired

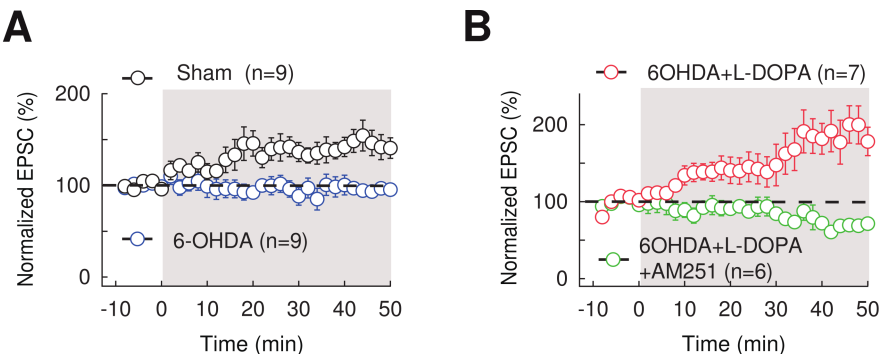

Figure C.2: eCB-t-LTP inducible with a low number of pairings is impaired when rat dopamine neurons are lesioned by 6-OHDA. **A**. 10 post-pre pairings induced eCB-t-LTP in sham-operated rats (control) (n=9) while no plasticity was observed in 6-OHDA-lesioned rats (n=9). **B**. Chronic L-DOPA treatment allowed to recover t-LTP (n=7) induced with 10 post-pre pairings; the treatment consisted in twice daily injection of L-DOPA (10mg/kg) for 10 days, two weeks after 6-OHDA lesion. The recovered t-LTP was CB1R-dependent since prevented by CB1R blocker AM251 (3μM, n=6) in 6-OHDA-lesioned rats treated with L-DOPA.

in the rat model of Parkinson's disease.

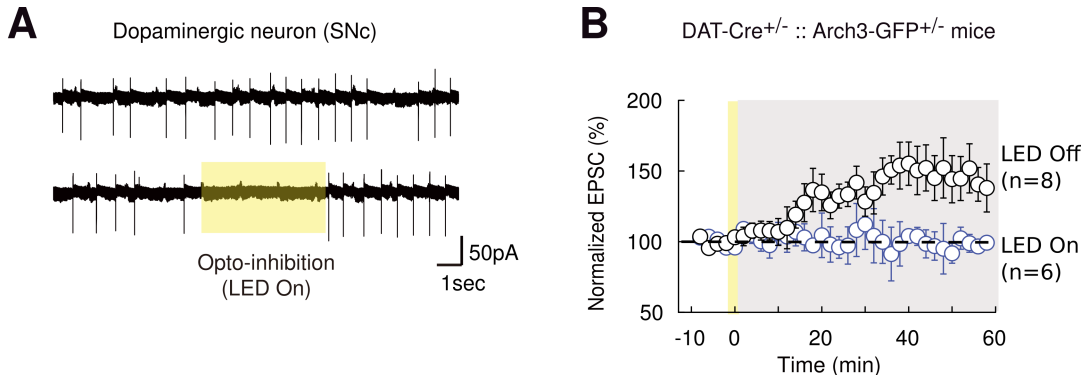

Figure C.3: Induction of eCB-LTP with a low number of pairings requires dopamine release during the STDP paired-activity paradigm. **A**. Spontaneous firing of dopaminergic neurons recorded in cell-attached mode in DAT-Cre$^{+/-}$ :: Arch3-GFP$^{+/+}$ mice with and without light (left traces). **B**. 15 post-pre pairings induced t-LTP (n=8) in DAT-Cre$^{+/-}$ :: Arch3-GFP$^{+/-}$ mice without opto-stimulation (LED Off), while opto-stimulation (LED On) during STDP pairings prevents t-LTP induction (n=6). This illustrates that eCB-t-LTP requires DA release during STDP pairings.

C.3.2 D2, but not D1 dopamine receptors are involved in eCB-t-LTP induced by a low number of pairings

Our collaborators then asked which types of dopamine receptors are involved in the eCB-t-LTP and where these receptors are located. In the dorsal striatum, the principal subtypes of dopamine receptors are D1 and D2 receptors (Gerfen and Surmeier 2011). They first questioned which dopaminergic receptor subtype was involved in eCB-t-LTP induced by 10 post-pre pairings. A mixture of D1R and D2R antagonists efficiently prevented the induction of eCB-t-LTP (fig. C.4A1). Block of D1R did not affect eCB-t-LTP, whereas blocking D2R prevented t-LTP

(fig. C.4A2). They then compared dopamine-dependence of eCB-t-LTP induced by 10 post-pre pairings to that of eCB-t-LTD induced by 100 pre-post pairings. Just like eCB-t-LTP, eCB-t-LTD was prevented with mixture of D1R and D2R antagonists. Unlike eCB-t-LTP, however, eCB-t-LTD was prevented by the block of D1R, but also by the block of D2R. Block of D2R not simply prevented eCB-t-LTD, but replaced it with t-LTP (its dependence on pre- and postsynaptic pathways remains unknown). Those experiments are summarized in tbl. 2.2 (see main text).

Altogether these experiments indicate that eCB-t-LTP induced by a low number of post-pre pairings is D2R-mediated but does not depend on D1R whereas eCB-t-LTD induced by 100 pre-post pairings is mediated by both D1R and D2R with unknown location.

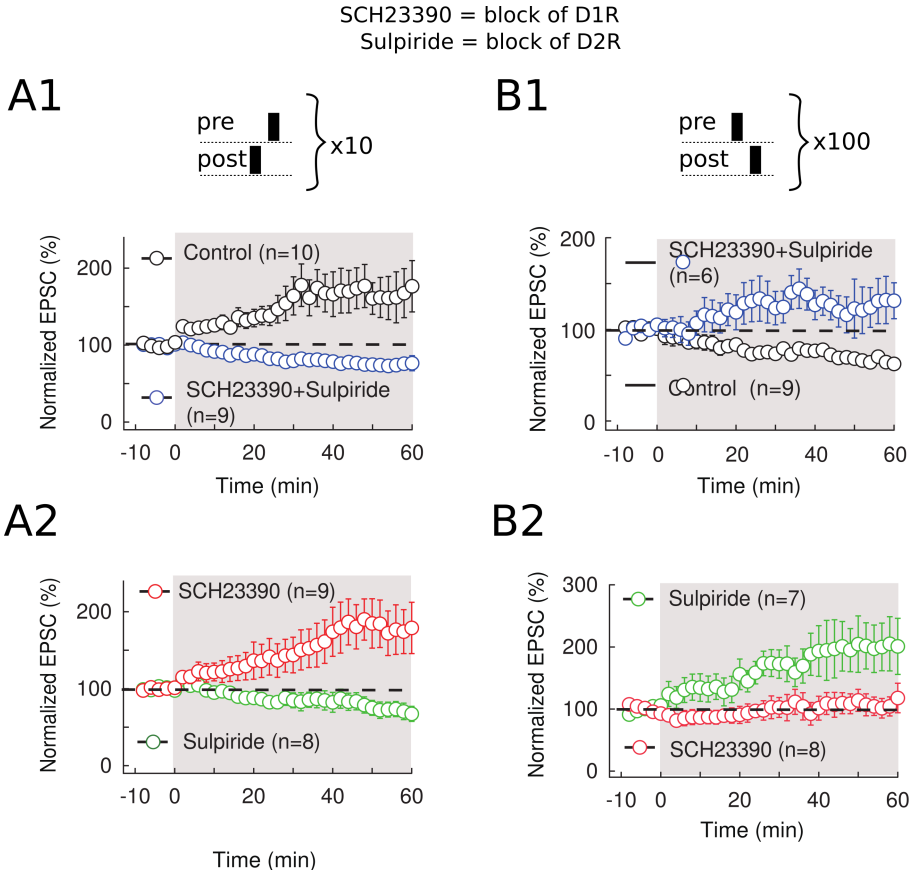

Figure C.4: eCB-t-LTP is D2R-activation dependent (but not D1R) whereas eCB-t-LTD relies on both D1R- and D2R. **A**. 10 post-pre pairings (-30<Δt<0ms) induced t-LTP is D2R-activation dependent. Summary of STDP experiments showing that eCB-t-LTP induced with 10 post-pre pairings (n=10) is prevented with the co-application of antagonists of D1R and D2R, SCH23390 (4μM) and sulpiride (10μM) (n=9) (**A1**), and with the D2R antagonist, sulpiride (10μM, n=8) but t-LTP was left unaffected by the sole application of the D1R antagonist, SCH23390 (4μM, n=9) (**A2**). **B**. t-LTD induced with 100 pre-post pairings (0<Δt<+30ms) is both D1R- and D2R-activation dependent. Summary of STDP experiments showing that t-LTD induced with 100 pre-post pairings is replaced by t-LTP with a mixture of D1R and D2R antagonists, SCH23390 (4μM) and sulpiride (10μM) (n=7) (**B1**) and impaired with either SCH23390 (4μM, n=8) or sulpiride (10μM, n=7) (**B2**); moreover, with sulpiride the t-LTD is replaced by t-LTP.

C.3.3 What is the location of D2R involved in eCB-t-LTP induced by a low number of pairings?

Next, out collaborators aimed to reveal the location of D2R required for the induction of eCB-t-LTP with 10 post-pre pairings. D2R are expressed at different locations in the striatum: postsynaptically in D2R-expressing MSNs (Gerfen and Surmeier 2011; Calabresi et al. 2014) and presynaptically in cholinergic interneurons (ChAT interneurons) (Hersch et al. 1995), nigrostriatal dopaminergic neurons (Sesack, Aoki, and Pickel 1994) and glutamatergic cortical afferents (H. Wang and Pickel 2002; Bamford et al. 2004) (fig. C.5A). To identify the D2R involved in the eCB-t-LTP, they opted for the following strategy: they selectively genetically-ablated D2R-expressing MSN (fig. C.5E) or cholinergic interneurons (fig. C.5D), selectively ablated dopaminergic cells (fig. C.5B1 trace labeled 6-ODHA) in the medial forebrain bundle (MFB) and specifically knocked-out the D2Rs expressed at cortico-striatal glutamatergic afferents, and then examined if eCB-t-LTP could still be expressed.

They first questioned the postsynaptic localization of the D2R involved in eCB-t-LTP at the level of the MSNs (fig. C.5C). Due to the segregation of expression of D1- and D2Rs among MSNs in mice (D1R and D2R in MSNs of the direct and indirect pathways, respectively)(Gerfen and Surmeier 2011; Calabresi et al. 2014), roughly half of the MSNs are expected to be D2R-expressing neurons. If eCB-t-LTP is due to D2R-MSNs, one would expect to induce eCB-t-LTP in ~50% of the (randomly chosen) recorded MSNs. This was not the case in the experiments of our collaborators. Indeed, eCB-t-LTP was successfully induced in 83% (n=27) of the (randomly chosen) recorded MSNs. To confirm that eCB-t-LTP is due to D2R-MSNs, they used transgenic D1-eGFP mice to induce eCB-t-LTP specifically in D1-eGFP$^+$ MSNs (D1-MSNs) or non-D1-eGFP$^+$ MSNs (D2-MSNs) (fig. C.5C). In both types of MSNs, t-LTP was observed (compare fig. C.5C1 and C2) Therefore, postsynaptic D2Rs in MSNs are likely not involved in eCB-t-LTP.

To further test the involvement of the D2R-MSNs, they selectively ablated these neurons. To do this, they expressed the diphteria toxin receptor (DTR) specifically in the D2R-expressing MSNs by putting the DTR gene under the control of the $A_{2A}R$ promoter (the expression of $A_{2A}R$ is specific to D2R-expressing MSNs). Injection of the diphtheria toxin in the striatum was then used to ablate the D2R-expressing MSNs. With the ablation of D2R-MSNs, t-LTP was still induced by 15 post-pre pairings (fig. C.5E). These results show that eCB-t-LTP does not depend on postsynaptic D2R-activation but thus should rely on the activation of presynaptically located D2R.

Using the same kind of genetic strategies, our collaborators then selectively ablated striatal cholinergic interneurons to test if D2Rs on these neurons are involved in eCB-t-LTP (fig. C.5D). With ablation of cholinergic interneurons, t-LTP was still induced by 15 post-pre pairing

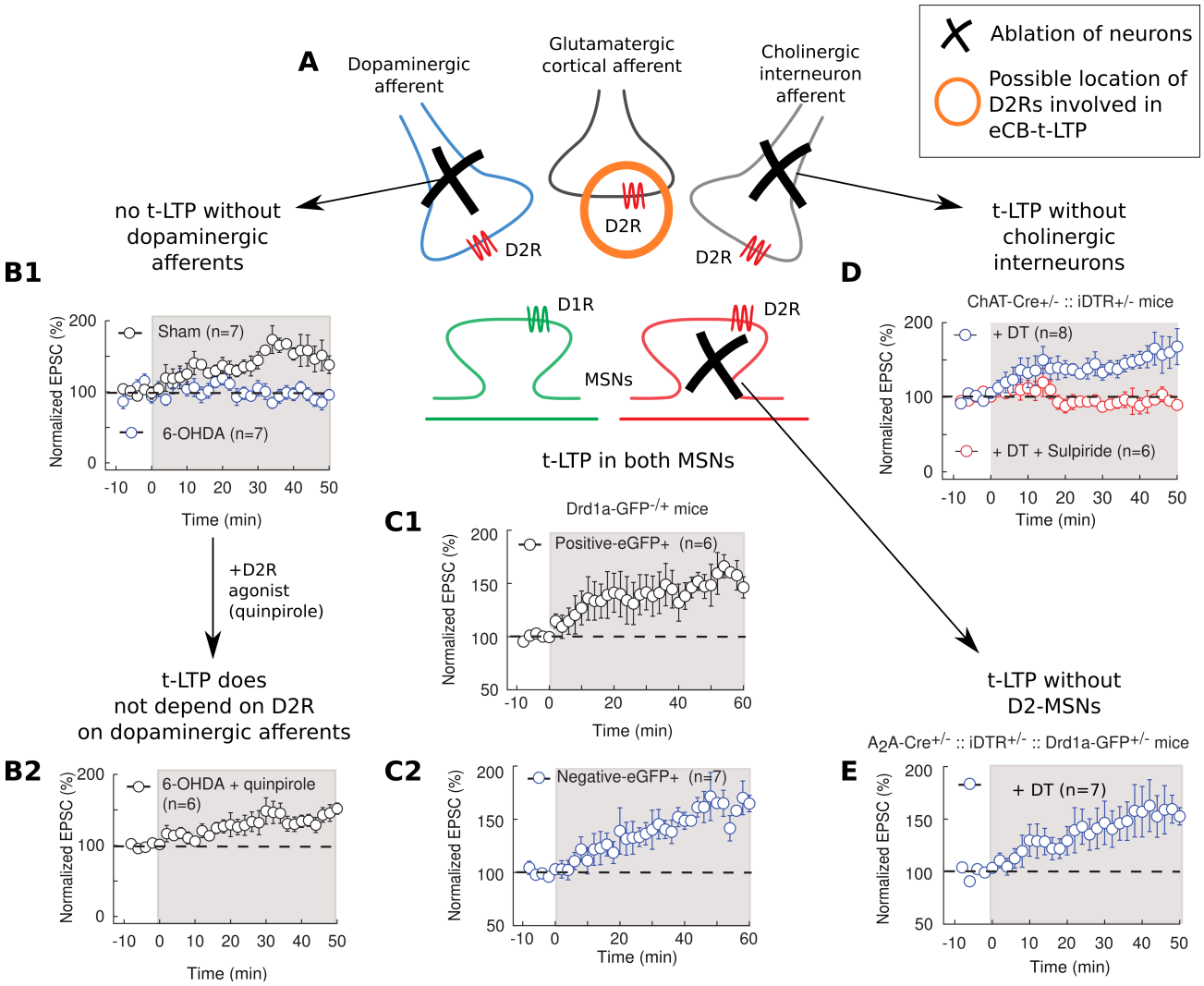

Figure C.5: eCB-t-LTP induced by a low number of pairings does not depend on D2R expressed by: MSNs belonging to the indirect pathway, striatal cholinergic interneurons or nigro-striatal dopaminergic neurons. **A**. Schematic view of the location of the D2Rs in striatum, which have been reported to be expressed in striato-nigral MSNs, cholinergic interneurons, SNc dopaminergic and cortical glutamatergic afferents. **B1**. 10 post-pre pairings induced t-LTP in sham-operated (n=7) rats whereas t-LTP was impaired in 6-OHDA-lesioned rats (n=7). **B2**. In 6-OHDA-lesioned rats, t-LTP was rescued with a D2R agonist, quinpirole (10 μM, n=6). **C**. t-LTP induced with 15 post-pre pairings is observed in both striato-nigral (D1R-eGFP positive neurons, D1R-eGFP^{+}, n=6) (**C1**) and striato-pallidal (D1R-eGFP negative neurons, non-D1R-eGFP^{+}, n=7) (**C2**) MSNs. **D**. t-LTP was induced with 15 post-pre pairings in mice with ablated cholinergic interneurons (ChAT-Cre$^{+/-}$ :: iDTR$^{+/-}$ mice). t-LTP observed in ChAT-ablated mice was D2R-mediated because it was prevented with sulpiride (10 μM, n=6). **E**. In mice in which D2R-expressing striatal neurons were ablated (A_{2A}-Cre$^{+/-}$ :: iDTR$^{+/-}$: Drd1a-GFP$^{+/-}$ mice injected with diphteria toxin stereotaxically in the dorsal striatum) t-LTP was induced with 15 post-pre pairings (n=7).

(fig. C.5D). These results indicate that eCB-t-LTP does not depend on D2R-activation located in cholinergic interneurons.

Taken together the results above suggest that among all possible locations of D2R that might be implicated in eCB-t-LTP depicted at fig. C.5A, the only location left unexplored is terminals of cortical afferents to MSNs (shown with orange circle at fig. C.5A). To check this last location, our collaborators selectively knocked-out the D2Rs expressed at cortico-striatal glutamatergic.

In these knockouts, no t-LTP was observed with 15 post-pre pairings (fig. C.6). Instead, a significant t-LTD was observed. These results indicate that eCB-t-LTP depends on the activation of presynaptic D2R located on cortico-striatal pyramidal cells.

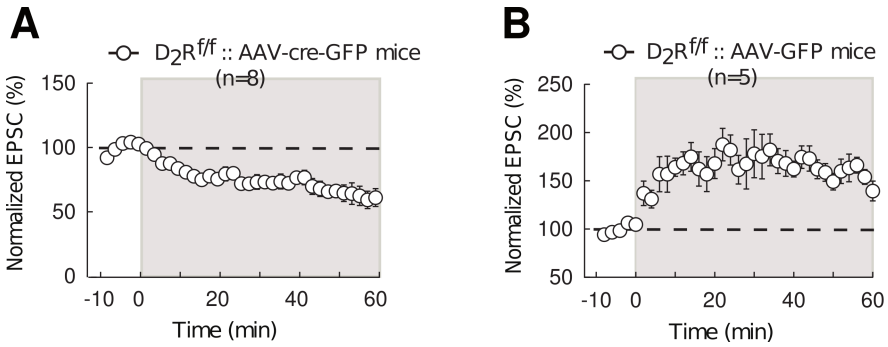

Figure C.6: eCB-t-LTP induced by a low number of pairings is dependent on D2R expressed by cortical pyramidal cells. Experiments of plasticity expression in knock-out mice for D2Rs expressed at cortico-striatal glutamatergic afferents. **A**. 15 post-pre pairings failed to induce significant t-LTP in $D2R^{f/f}$ mice injected with AAV-cre-GFP in somatosensory cerebral cortex (n=8). **B**. As a control, t-LTP was induced with 15 post-pre pairings in $D2R^{f/f}$ mice injected with AAV-GFP (n=5).

References

Abbott, L. F. and Nelson, S. B. (2000). "Synaptic Plasticity: Taming the Beast". *Nature neuroscience* 3, pp. 1178–1183.

Ahn, J.-H., Sung, J. Y., McAvoy, T., Nishi, A., Janssens, V., Goris, J., Greengard, P., and Nairn, A. C. (2007). "The B"/PR72 Subunit Mediates Ca2+-Dependent Dephosphorylation of DARPP-32 by Protein Phosphatase 2A". *Proceedings of the National Academy of Sciences* 104.23, pp. 9876–9881. DOI: 10.1073/pnas.0703589104. URL: http://www.pnas.org/cgi/doi/10.1073/pnas.0703589104.

Bamford, N. S., Robinson, S., Palmiter, R. D., Joyce, J. A., Moore, C., and Meshul, C. K. (2004). "Dopamine Modulates Release from Corticostriatal Terminals". *The Journal of neuroscience* 24.43, pp. 9541–9552.

Barrionuevo, G., Schottler, F., and Lynch, G. (1980). "The Effects of Repetitive Low Frequency Stimulation on Control and "potentiated" Synaptic Responses in the Hippocampus". *Life Sciences* 27.24, pp. 2385–2391. DOI: 10.1016/0024-3205(80)90509-3. URL: http://linkinghub.elsevier.com/retrieve/pii/0024320580905093.

Bell, C. C., Han, V. Z., Sugawara, Y., and Grant, K. (1997). "Synaptic Plasticity in a Cerebellum-like Structure Depends on Temporal Order." *Nature* 387.6630, pp. 278–81. DOI: 10.1038/387278a0. URL: http://www.nature.com/nature/journal/v387/n6630/pdf/387278a0.pdf.

Bellec, G., Galtier, M., Brette, R., and Yger, P. (2016). "Slow Feature Analysis with Spiking Neurons and Its Application to Audio Stimuli". *Journal of Computational Neuroscience* 40.3, pp. 317–329. DOI: 10.1007/s10827-016-0599-3. URL: http://link.springer.com/10.1007/s10827-016-0599-3.

Bender, V. A. (2006). "Two Coincidence Detectors for Spike Timing-Dependent Plasticity in Somatosensory Cortex". *Journal of Neuroscience* 26.16, pp. 4166–4177. DOI: 10.1523/JNEUROSCI.0176-06.2006. URL: http://www.jneurosci.org/cgi/doi/10.1523/JNEUROSCI.0176-06.2006.

Berridge, M. J., Bootman, M. D., and Roderick, H. L. (2003). "Calcium Signalling: Dynamics, Homeostasis and Remodelling." *Nature reviews. Molecular cell biology* 4.7, pp. 517–29. DOI: 10.1038/nrm1155. URL: http://dx.doi.org/10.1038/nrm1155.

Bhalla, U. S. and Iyengar, R. (1999). "Emergent Properties of Networks of Biological Signaling Pathways." *Science (New York, N.Y.)* 283.5400, pp. 381–7. PMID: 9888852.

Bi, G.-q. and Poo, M.-m. (1998). "Synaptic Modifications in Cultured Hippocampal Neurons: Dependence on Spike Timing, Synaptic Strength, and Postsynaptic Cell Type". *The Journal of Neuroscience* 18.24, pp. 10464–10472. URL: http://www.jneurosci.org/content/18/24/10464.short.

Bienenstock, E. L., Cooper, L. N., and Munro, P. W. (1982). "Theory for the Development of Neuron Selectivity: Orientation Specificity and Binocular Interaction in Visual Cortex." *The Journal of neuroscience : the official journal of the Society for Neuroscience* 2.1, pp. 32–48. PMID: 7054394.

Bliss, T. and Lømo, T. (1973). "Long-Lasting Potentiation of Synaptic Transmission in the Dentate Area of the Anaesthetized Rabbit Following Stimulation of the Perforant Path". *The Journal of physiology* 232.2, pp. 331–356. URL: http://jp.physoc.org/content/232/2/331.short.

Brunel, N. and van Rossum, M. C. W. (2007). "Quantitative Investigations of Electrical Nerve Excitation Treated as Polarization". *Biological Cybernetics* 97 (5-6), pp. 341–349. DOI: 10.1007/s00422-007-0189-6. URL: http://link.springer.com/10.1007/s00422-007-0189-6.

Calabresi, P., Picconi, B., Tozzi, A., Ghiglieri, V., and Di Filippo, M. (2014). "Direct and Indirect Pathways of Basal Ganglia: A Critical Reappraisal". *Nature neuroscience* 17.8, pp. 1022–1030.

Caporale, N. and Dan, Y. (2008). "Spike Timing–Dependent Plasticity: A Hebbian Learning Rule". *Annual Review of Neuroscience* 31.1, pp. 25–46. DOI: 10.1146/annurev.neuro.31.060407.125639. URL: http://www.annualreviews.org/doi/abs/10.1146/annurev.neuro.31.060407.125639.

Carter, A. G. and Sabatini, B. L. (2004). "State-Dependent Calcium Signaling in Dendritic Spines of Striatal Medium Spiny Neurons." *Neuron* 44.3, pp. 483–93. DOI: 10.1016/j.neuron.2004.10.013. PMID: 15504328.

Castillo, P. E., Younts, T. J., Chávez, A. E., and Hashimotodani, Y. (2012). "Endocannabinoid Signaling and Synaptic Function." *Neuron* 76.1, pp. 70–81. DOI: 10.1016/j.neuron.2012.09.020. PMID: 23040807.

Cho, K., Aggleton, J. P., Brown, M. W., and Bashir, Z. I. (2001). "An Experimental Test of the Role of Postsynaptic Calcium Levels in Determining Synaptic Strength Using Perirhinal Cortex of Rat". *The Journal of Physiology* 532 (Pt 2), pp. 459–466. pmid: 11306664.

Citri, A. and Malenka, R. C. (2008). "Synaptic Plasticity: Multiple Forms, Functions, and Mechanisms." *Neuropsychopharmacology : official publication of the American College of Neuropsychopharmacology* 33.1, pp. 18–41. DOI: 10.1038/sj.npp.1301559. PMID: 17728696.

Clements, J. D., Lester, R. a, Tong, G., Jahr, C. E., and Westbrook, G. L. (1992). "The Time Course of Glutamate in the Synaptic Cleft." *Science (New York, N.Y.)* 258.5087, pp. 1498–501. PMID: 1359647.

Clopath, C., Büsing, L., Vasilaki, E., and Gerstner, W. (2010). "Connectivity Reflects Coding: A Model of Voltage-Based STDP with Homeostasis." *Nature neuroscience* 13.3, pp. 344–52. DOI: 10.1038/nn.2479. PMID: 20098420.

Cormier, R. J., Greenwood, A. C., and Connor, J. A. (2001). "Bidirectional Synaptic Plasticity Correlated with the Magnitude of Dendritic Calcium Transients above a Threshold". *Journal of Neurophysiology* 85.1, pp. 399–406. pmid: 11152740.

Costa, R. P., Froemke, R. C., Sjöström, P. J., and van Rossum, M. C. W. (2015). "Unified Pre- and Postsynaptic Long-Term Plasticity Enables Reliable and Flexible Learning". *eLife* 4. DOI: 10.7554/eLife.09457. URL: http://elifesciences.org/lookup/doi/10.7554/eLife.09457.

Crick, F. (1984). "Memory and Molecular Turnover". *Nature* 312.5990, p. 101. pmid: 6504122.

Cui, Y., Paille, V., Xu, H., Genet, S., Delord, B., Fino, E., Berry, H., and Venance, L. (2015). "Endocannabinoids Mediate Bidirectional Striatal Spike-Timing Dependent Plasticity". *The Journal of Physiology*, n/a–n/a. DOI: 10.1113/JP270324. URL: http://onlinelibrary.wiley.com/doi/10.1113/JP270324/abstract.

Cui, Y., Prokin, I., Xu, H., Delord, B., Genet, S., Venance, L., and Berry, H. (2016). "Endocannabinoid Dynamics Gate Spike-Timing Dependent Depression and Potentiation". *eLife* 5, e13185. URL: https://elifesciences.org/content/5/e13185.

Dan, Y. and Poo, M.-m. (2006). "Spike Timing-Dependent Plasticity: From Synapse to Perception". *Physiological Reviews* 86.3, pp. 1033–1048. DOI: 10.1152/physrev.00030.2005. URL: http://physrev.physiology.org/cgi/doi/10.1152/physrev.00030.2005.

Danbolt, N. C. (2001). "Glutamate Uptake". *Progress in neurobiology* 65.1, pp. 1–105.

Dayan, P. and Balleine, B. W. (2002). "Reward, Motivation, and Reinforcement Learning". *Neuron* 36.2, pp. 285–298. DOI: 10.1016/S0896-6273(02)00963-7. URL: http://www.sciencedirect.com/science/article/pii/S0896627302009637.

De Pittà, M., Goldberg, M., Volman, V., Berry, H., and Ben-Jacob, E. (2009). "Glutamate Regulation of Calcium and IP3 Oscillating and Pulsating Dynamics in Astrocytes." *Journal of biological physics* 35.4, pp. 383–411. DOI: 10.1007/s10867-009-9155-y. URL: http://www.pubmedcentral.nih.gov/articlerender.fcgi?artid=2750743&tool=pmcentrez&rendertype=abstract.

Debanne, D., Gahwiler, B. H., and Thompson, S. M. (1994). "Asynchronous Pre- and Postsynaptic Activity Induces Associative Long-Term Depression in Area CA1 of the Rat Hippocampus in Vitro." *Proceedings of the National Academy of Sciences* 91.3, pp. 1148–1152. DOI: 10.1073/pnas.91.3.1148. URL: http://www.pnas.org/cgi/doi/10.1073/pnas.91.3.1148.

DeFelipe, J. and Fariñas, I. (1992). "The Pyramidal Neuron of the Cerebral Cortex: Morphological and Chemical Characteristics of the Synaptic Inputs". *Progress in Neurobiology* 39.6, pp. 563–607. DOI: 10.1016/0301-0082(92)90015-7. URL: http://linkinghub.elsevier.com/retrieve/pii/0301008292900157.

Destexhe, A., Mainen, Z. F., and Sejnowski, T. J. (1994). "Synthesis of Models for Excitable Membranes, Synaptic Transmission and Neuromodulation Using a Common Kinetic Formalism." *Journal of computational neuroscience* 1.3, pp. 195–230. PMID: 8792231.

Destexhe, A., Mainen, Z. F., and Sejnowski, T. J. (1998). "Kinetic Models of Synaptic Transmission". *Methods in Neuronal Modeling*.

Destexhe, A., Mainen, Z., and Sejnowski, T. (1995). "Fast Kinetic Models for Simulating AMPA, NMDA, GABA A and GABA B Receptors". *The Neurobiology of Computation*. URL: http://link.springer.com/chapter/10.1007/978-1-4615-2235-5_2.

Dunwiddie, T. and Lynch, G. (1978). "Long-Term Potentiation and Depression of Synaptic Responses in the Rat Hippocampus: Localization and Frequency Dependency." *The Journal of Physiology* 276.1, pp. 353–367. DOI: 10.1113/jphysiol.1978.sp012239. URL: http://doi.wiley.com/10.1113/jphysiol.1978.sp012239.

Dyson, F. (2004). "A Meeting with Enrico Fermi". *Nature* 427.6972, pp. 297–297. DOI: 10.1038/427297a. URL: http://www.nature.com/doifinder/10.1038/427297a.

Eccles, J. C. and McIntyre, A. K. (1953). "The Effects of Disuse and of Activity on Mammalian Spinal Reflexes". *The Journal of Physiology* 121.3, pp. 492–516. pmid: 13097388.

Fernandez, E., Schiappa, R., Girault, J.-A., and Le Novere, N. (2005). "DARPP-32 Is a Robust Integrator of Dopamine and Glutamate Signals". *PLoS Computational Biology* preprint.2006, e176–e176. DOI: 10.1371/journal.pcbi.0020176.eor. URL: http://dx.plos.org/10.1371/journal.pcbi.0020176.

Fino, E., Paille, V., Deniau, J.-M., and Venance, L. (2009). "Asymmetric Spike-Timing Dependent Plasticity of Striatal Nitric Oxide-Synthase Interneurons." *Neuroscience* 160.4, pp. 744–54. DOI: 10.1016/j.neuroscience.2009.03.015. PMID: 19303912.

Fino, E., Deniau, J.-M., and Venance, L. (2008). "Cell-Specific Spike-Timing-Dependent Plasticity in GABAergic and Cholinergic Interneurons in Corticostriatal Rat Brain Slices". *The Journal of Physiology* 586.1, pp. 265–282. DOI: 10.1113/jphysiol.2007.144501. pmid: 17974593. URL: http://jp.physoc.org/content/586/1/265.

Fino, E., Glowinski, J., and Venance, L. (2005). "Bidirectional Activity-Dependent Plasticity at Corticostriatal Synapses." *The Journal of neuroscience : the official journal of the Society for Neuroscience* 25.49, pp. 11279–87. DOI: 10.1523/JNEUROSCI.4476-05.2005. URL: http://www.jneurosci.org/content/25/49/11279.full.

Fino, E., Paille, V., Cui, Y., Morera-Herreras, T., Deniau, J.-M., and Venance, L. (2010). "Distinct Coincidence Detectors Govern the Corticostriatal Spike Timing-Dependent Plasticity." *The Journal of physiology* 588 (Pt 16), pp. 3045–62. DOI: 10.1113/jphysiol.2010.188466.

Fino, E. and Venance, L. (2010). "Spike-Timing Dependent Plasticity in the Striatum." *Frontiers in synaptic neuroscience* 2 (June), pp. 6–6. DOI: 10.3389/fnsyn.2010.00006. URL: http://www.pubmedcentral.nih.gov/articlerender.fcgi?artid=3059675&tool=pmcentrez&rendertype=abstract.

Freund, T. F., Katona, I., and Piomelli, D. (2003). "Role of Endogenous Cannabinoids in Synaptic Signaling". *Physiological Reviews* 83.3, pp. 1017–1066. DOI: 10.1152/physrev.00004.2003. pmid: 12843414.

Gazzaniga, M. S. and Bizzi, E., eds. (2009). *The Cognitive Neurosciences*. 4. ed. A Bradford book. Cambridge, Mass.: MIT Press. 1294 pp.

Gerfen, C. R. and Surmeier, D. J. (2011). "Modulation of Striatal Projection Systems by Dopamine". *Annual Review of Neuroscience* 34.1, pp. 441–466. DOI: 10.1146/annurev-neuro-061010-113641. URL: http://www.annualreviews.org/doi/abs/10.1146/annurev-neuro-061010-113641.

Gerstner, W., Kempter, R., van Hemmen, J. L., and Wagner, H. (1996). "A Neuronal Learning Rule for Sub-Millisecond Temporal Coding". *Nature* 383.6595, pp. 76–78. DOI: 10.1038/383076a0. URL: http://www.nature.com/doifinder/10.1038/383076a0.

Giese, K. P., Fedorov, N. B., Filipkowski, R. K., and Silva, A. J. (1998). "Autophosphorylation at Thr286 of the α Calcium-Calmodulin Kinase II in LTP and Learning". *Science* 279.5352, pp. 870–873.

Giuffrida, A., Parsons, L., Kerr, T., De Fonseca, F. R., Navarro, M., and Piomelli, D. (1999). "Dopamine Activation of Endogenous Cannabinoid Signaling in Dorsal Striatum". *Nature neuroscience* 2.4, pp. 358–363.

Goubard, V., Fino, E., and Venance, L. (2011). "Contribution of Astrocytic Glutamate and GABA Uptake to Corticostriatal Information Processing." *The Journal of physiology* 589 (Pt 9), pp. 2301–19. DOI: 10.1113/jphysiol.2010.203125. URL: http://www.pubmedcentral.nih.gov/articlerender.fcgi?artid=3098705&tool=pmcentrez&rendertype=abstract.

Graupner, M. and Brunel, N. (2012). "Calcium-Based Plasticity Model Explains Sensitivity of Synaptic Changes to Spike Pattern, Rate, and Dendritic Location." *Proceedings of the National Academy of Sciences of the United States of America* 109.10, pp. 3991–6. DOI: 10.1073/pnas.1109359109. URL: http://www.pubmedcentral.nih.gov/articlerender.fcgi?artid=3309784&tool=pmcentrez&rendertype=abstract.

Graupner, M. and Brunel, N. (2010). "Mechanisms of Induction and Maintenance of Spike-Timing Dependent Plasticity in Biophysical Synapse Models." *Frontiers in computational neuroscience* 4 (September), pp. 1–19. DOI: 10.3389/fncom.2010.00136. URL: http://www.pubmedcentral.nih.gov/articlerender.fcgi?artid=2953414&tool=pmcentrez&rendertype=abstract.

Graupner, M. and Brunel, N. (2007). "STDP in a Bistable Synapse Model Based on CaMKII and Associated Signaling Pathways." *PLoS computational biology* 3.11. Ed. by K. J. Friston, e221–e221. DOI: 10.1371/journal.pcbi.0030221. URL: http://www.pubmedcentral.nih.gov/articlerender.fcgi?artid=2098851&tool=pmcentrez&rendertype=abstract.

Graybiel, A. M. (2008). "Habits, Rituals, and the Evaluative Brain." *Annual review of neuroscience* 31, pp. 359–87. DOI: 10.1146/annurev.neuro.29.051605.112851. PMID: 18558860.

Griffith, T., Tsaneva-Atanasova, K., and Mellor, J. R. (2016). "Control of Ca2+ Influx and Calmodulin Activation by SK-Channels in Dendritic Spines". *PLOS Computational Biology* 12.5. Ed. by K. T. Blackwell, e1004949. DOI: 10.1371/journal.pcbi.1004949. URL: http://dx.plos.org/10.1371/journal.pcbi.1004949.

Grueter, B. A., Brasnjo, G., and Malenka, R. C. (2010). "Postsynaptic TRPV1 Triggers Cell Type–specific Long-Term Depression in the Nucleus Accumbens". *Nature Neuroscience* 13.12, pp. 1519–1525. DOI: 10.1038/nn.2685. URL: http://www.nature.com/doifinder/10.1038/nn.2685.

Gulyás, A. I., Megías, M., Emri, Z., and Freund, T. F. (1999). "Total Number and Ratio of Excitatory and Inhibitory Synapses Converging onto Single Interneurons of Different Types in the CA1 Area of the Rat Hippocampus". *The Journal of neuroscience* 19.22, pp. 10082–10097.

Gutenkunst, R. N., Waterfall, J. J., Casey, F. P., Brown, K. S., Myers, C. R., and Sethna, J. P. (2007). "Universally Sloppy Parameter Sensitivities in Systems Biology Models". *PLoS Comput Biol* 3.10, e189. DOI: 10.1371/journal.pcbi.0030189. URL: http://dx.plos.org/10.1371/journal.pcbi.0030189.

Gutierrez-Arenas, O., Eriksson, O., and Kotaleski, J. H. (2014). "Segregation and Crosstalk of D1 Receptor-Mediated Activation of ERK in Striatal Medium Spiny Neurons upon Acute Administration of Psychostimulants". *PLoS Computational Biology* 10.1. Ed. by A. Morrison, e1003445. DOI: 10.1371/journal.pcbi.1003445. URL: http://dx.plos.org/10.1371/journal.pcbi.1003445.

Haas, J. S., Nowotny, T., and Abarbanel, H. (2006). "Spike-Timing-Dependent Plasticity of Inhibitory Synapses in the Entorhinal Cortex". *Journal of Neurophysiology* 96.6, pp. 3305–3313. DOI: 10.1152/jn.00551.2006. URL: http://jn.physiology.org/cgi/doi/10.1152/jn.00551.2006.

Hansen, H. S., Lauritzen, L., Moesgaard, B., Strand, A. M., and Hansen, H. H. (1998). "Formation of N-Acyl-Phosphatidylethanolamines and N-Acetylethanolamines: Proposed Role in Neurotoxicity". *Biochemical Pharmacology* 55.6, pp. 719–725. pmid: 9586943.

Hebb, D. O. (1949). *The Organization of Behavior: A Neuropsychological Theory*. Vol. 34. New York: John Wiley and Sons, Inc. 335 pp.

Hersch, S. M., Ciliax, B. J., Gutekunst, C.-A., Rees, H., Heilman, C. J., Yung, K., Bolam, J., Ince, E., Yi, H., and Levey, A. (1995). "Electron Microscopic Analysis of D1 and D2 Dopamine Receptor Proteins in the Dorsal Striatum and Their Synaptic Relationships with Motor Corticostriatal Afferents". *The Journal of neuroscience* 15.7, pp. 5222–5237.

Higley, M. J. and Sabatini, B. L. (2008). "Calcium Signaling in Dendrites and Spines: Practical and Functional Considerations". *Neuron* 59.6, pp. 902–913. DOI: 10.1016/j.neuron.2008.08.020. pmid: 18817730. URL: http://www.cell.com/article/S0896627308007447/abstract.

Hillard, C. J. and Campbell, W. B. (1997). "Biochemistry and Pharmacology of Arachidonylethanolamide, a Putative Endogenous Cannabinoid." *Journal of Lipid Research* 38.12, pp. 2383–2398. pmid: 9458263. URL: http://www.jlr.org/content/38/12/2383.

Hille, B. (1992). *Ionic Channels of Excitable Membranes*. 2nd ed. Sunderland, Mass: Sinauer Associates. 607 pp.

Hodgkin, A. and Huxley, A. (1952). "A Quantitative Description of Membrane Current and Its Application to Conduction and Excitation in Nerve". *The Journal of physiology* 117.4, pp. 500–544.

Hopfield, J. J. (1982). "Neural Networks and Physical Systems with Emergent Collective Computational Abilities". *Proceedings of the National Academy of Sciences* 79.8, pp. 2554–2558. pmid: 6953413. URL: http://www.pnas.org/content/79/8/2554.

Hudmon, A. and Schulman, H. (2002). "Neuronal CA2+/Calmodulin-Dependent Protein Kinase II: The Role of Structure and Autoregulation in Cellular Function". *Annual review of biochemistry* 71.1, pp. 473–510.

Hunter, J. D. (2007). "Matplotlib: A 2D Graphics Environment". *Computing In Science & Engineering* 9.3, pp. 90–95.

Izhikevich, E. M. (2007). *Dynamical Systems in Neuroscience*. MIT press.

Jackson, M. B. and Redman, S. J. (2003). "Calcium Dynamics, Buffering, and Buffer Saturation in the Boutons of Dentate Granule-Cell Axons in the Hilus". *The Journal of neuroscience* 23.5, pp. 1612–1621.

Jacob, V., Brasier, D. J., Erchova, I., Feldman, D., and Shulz, D. E. (2007). "Spike Timing-Dependent Synaptic Depression in the In Vivo Barrel Cortex of the Rat". *Journal of Neuroscience* 27.6, pp. 1271–1284. DOI: 10.1523/JNEUROSCI.4264-06.2007. URL: http://www.jneurosci.org/cgi/doi/10.1523/JNEUROSCI.4264-06.2007.

Jahr, C. E. and Stevens, C. F. (1990). "Voltage Dependence of NMDA-Activated Macroscopic Conductances Predicted by Single-Channel Kinetics". *The Journal of Neuroscience* 10.9, pp. 3178–3182.

Jędrzejewska-Szmek, J., Damodaran, S., Dorman, D. B., and Blackwell, K. T. (2016). "Calcium Dynamics Predict Direction of Synaptic Plasticity in Striatal Spiny Projection Neurons". *European Journal of Neuroscience*. DOI: 10.1111/ejn.13287. URL: http://doi.wiley.com/10.1111/ejn.13287.

Jones, E., Oliphant, T., Peterson, P., et al. (2001). *SciPy: Open Source Scientific Tools for Python*. URL: http://www.scipy.org/.

Jones, M. V. and Westbrook, G. L. (1996). "The Impact of Receptor Desensitization on Fast Synaptic Transmission." *Trends in neurosciences* 19.3, pp. 96–101. PMID: 9054063.

Kandel, E. R. (2013). *Principles of Neural Science*. Ed. by E. R. Kandel. 5th ed. New York: McGraw-Hill. 1709 pp.

Karmarkar, U. R. and Buonomano, D. V. (2002). "A Model of Spike-Timing Dependent Plasticity: One or Two Coincidence Detectors?" *Journal of Neurophysiology* 88.1, pp. 507–513.

Kempter, R., Gerstner, W., and Van Hemmen, J. L. (1999). "Hebbian Learning and Spiking Neurons". *Physical Review E* 59.4, p. 4498.

Kincaid, A. E., Zheng, T., and Wilson, C. J. (1998). "Connectivity and Convergence of Single Corticostriatal Axons". *The Journal of neuroscience* 18.12, pp. 4722–4731.

Koch, C. (1999). *Biophysics of Computation: Information Processing in Single Neurons*. Computational neuroscience. New York, NY: Oxford Univ. Press. 562 pp.

Kotaleski, J. H. and Blackwell, K. T. (2010). "Modelling the Molecular Mechanisms of Synaptic Plasticity Using Systems Biology Approaches." *Nature reviews. Neuroscience* 11.4, pp. 239–51. DOI: 10.1038/nrn2807. URL: http://dx.doi.org/10.1038/nrn2807.

Kreitzer, A. C. (2005). "Dopamine Modulation of State-Dependent Endocannabinoid Release and Long-Term Depression in the Striatum". *Journal of Neuroscience* 25.45, pp. 10537–10545. DOI: 10.1523/JNEUROSCI.2959-05.2005. URL: http://www.jneurosci.org/cgi/doi/10.1523/JNEUROSCI.2959-05.2005.

LeCun, Y., Bengio, Y., and Hinton, G. (2015). "Deep Learning". *Nature* 521.7553, pp. 436–444. DOI: 10.1038/nature14539. URL: http://www.nature.com/nature/journal/v521/n7553/full/nature14539.html.

Li, Y. X. and Rinzel, J. (1994). "Equations for InsP3 Receptor-Mediated [Ca2+]i Oscillations Derived from a Detailed Kinetic Model: A Hodgkin-Huxley like Formalism." *Journal of theoretical biology* 166.4, pp. 461–73. DOI: 10.1006/jtbi.1994.1041. URL: http://www.sciencedirect.com/science/article/pii/S0022519384710411.

Lindskog, M., Kim, M., Wikström, M. a, Blackwell, K. T., and Kotaleski, J. H. (2006). "Transient Calcium and Dopamine Increase PKA Activity and DARPP-32 Phosphorylation." *PLoS computational biology* 2.9, e119–e119. DOI: 10.1371/journal.pcbi.0020119. URL: http://www.pubmedcentral.nih.gov/articlerender.fcgi?artid=1562452&tool=pmcentrez&rendertype=abstract.

Lisman, J. (1985). "A Mechanism for Memory Storage Insensitive to Molecular Turnover: A Bistable Autophosphorylating Kinase". *Proceedings of the National Academy of ...* 82 (May), pp. 3055–3057. URL: http://www.pnas.org/content/82/9/3055.short.

Lisman, J. (1989). "A Mechanism for the Hebb and the Anti-Hebb Processes Underlying Learning and Memory". *Proceedings of the National Academy of Sciences* 86.23, pp. 9574–9578.

Lynch, G. S., Dunwiddie, T., and Gribkoff, V. (1977). "Heterosynaptic Depression: A Postsynaptic Correlate of Long-Term Potentiation". *Nature* 266.5604, pp. 737–739. DOI: 10.1038/266737a0. URL: http://www.nature.com/doifinder/10.1038/266737a0.

Machta, B. B., Chachra, R., Transtrum, M. K., and Sethna, J. P. (2013). "Parameter Space Compression Underlies Emergent Theories and Predictive Models". *Science* 342.6158, pp. 604–607. DOI: 10.1126/science.1238723. pmid: 24179222. URL: http://www.sciencemag.org/content/342/6158/604.

Magee, J. C. and Johnston, D. (1997). "A Synaptically Controlled, Associative Signal for Hebbian Plasticity in Hippocampal Neurons." *Science (New York, N.Y.)* 275.5297, pp. 209–13. PMID: 8985013.

Malenka, R. C. and Bear, M. F. (2004). "LTP and LTD: An Embarrassment of Riches". *Neuron* 44.1, pp. 5–21. URL: http://www.sciencedirect.com/science/article/pii/S0896627304006087.

Manninen, T., Hituri, K., Kotaleski, J. H., Blackwell, K. T., and Linne, M.-L. (2010). "Postsynaptic Signal Transduction Models for Long-Term Potentiation and Depression." *Frontiers in computational neuroscience* 4 (December), pp. 152–152. DOI: 10.3389/fncom.2010.00152. URL: http://www.pubmedcentral.nih.gov/articlerender.fcgi?artid=3006457&tool=pmcentrez&rendertype=abstract.

Markram, H., Lübke, J., Frotscher, M., and Sakmann, B. (1997). "Regulation of Synaptic Efficacy by Coincidence of Postsynaptic APs and EPSPs". *Science* 275.5297, pp. 213–215. DOI: 10.1126/science.275.5297.213. URL: http://www.sciencemag.org/cgi/doi/10.1126/science.275.5297.213.

Martin, S. and Morris, R. (2002). "New Life in an Old Idea: The Synaptic Plasticity and Memory Hypothesis Revisited". *Hippocampus* 12.5, pp. 609–636. DOI: 10.1002/hipo.10107. URL: http://doi.wiley.com/10.1002/hipo.10107.

Mathur, B. N. and Lovinger, D. M. (2012). "Endocannabinoid–Dopamine Interactions in Striatal Synaptic Plasticity". *Frontiers in Pharmacology* 3. DOI: 10.3389/fphar.2012.00066. URL: http://journal.frontiersin.org/article/10.3389/fphar.2012.00066/abstract.

Matta, J. A. and Ahern, G. P. (2007). "Voltage Is a Partial Activator of Rat Thermosensitive TRP Channels." *The Journal of physiology* 585 (Pt 2), pp. 469–82. DOI: 10.1113/jphysiol.2007.144287. URL: http://www.pubmedcentral.nih.gov/articlerender.fcgi?artid=2375500&tool=pmcentrez&rendertype=abstract.

McCulloch, W. S. and Pitts, W. (1943). "A Logical Calculus of the Ideas Immanent in Nervous Activity". *The bulletin of mathematical biophysics* 5.4, pp. 115–133.

McKerns, M. and Aivazis, M. (2010). *Pathos: A Framework for Heterogeneous Computing*. URL: http://trac.mystic.cacr.caltech.edu/project/pathos.

McRory, J. E., Santi, C. M., Hamming, K. S. C., Mezeyova, J., Sutton, K. G., Baillie, D. L., Stea, A., and Snutch, T. P. (2001). "Molecular and Functional Characterization of a Family of Rat Brain T-Type Calcium Channels". *Journal of Biological Chemistry* 276.6, pp. 3999–4011. DOI: 10.1074/jbc.M008215200. URL: http://www.jbc.org/cgi/doi/10.1074/jbc.M008215200.

Morris, R. (1989). "Synaptic Plasticity and Learning: Selective Impairment of Learning Rats and Blockade of Long-Term Potentiation in Vivo by the N-Methyl-D-Aspartate Receptor Antagonist AP5". *The Journal of neuroscience* 9.9, pp. 3040–3057.

Nabavi, S., Fox, R., Proulx, C. D., Lin, J. Y., Tsien, R. Y., and Malinow, R. (2014). "Engineering a Memory with LTD and LTP". *Nature*.

Nägerl, U. V., Novo, D., Mody, I., and Vergara, J. L. (2000). "Binding Kinetics of Calbindin-D28k Determined by Flash Photolysis of Caged Ca2+". *Biophysical Journal* 79.6, pp. 3009–3018. DOI: 10.1016/S0006-3495(00)76537-4. URL: http://linkinghub.elsevier.com/retrieve/pii/S0006349500765374.

Nair, A. G., Bhalla, U. S., and Kotaleski, J. H. (2016). "Role of DARPP-32 and ARPP-21 in the Emergence of Temporal Constraints on Striatal Calcium and Dopamine Integration". *PLOS Computational Biology* 12.9. Ed. by J. J. Saucerman, e1005080. DOI: 10.1371/journal.pcbi.1005080. URL: http://dx.plos.org/10.1371/journal.pcbi.1005080.

Nakano, T., Doi, T., Yoshimoto, J., and Doya, K. (2010). "A Kinetic Model of Dopamine- and Calcium-Dependent Striatal Synaptic Plasticity." *PLoS computational biology* 6.2. Ed. by B. S. Gutkin, e1000670–e1000670. DOI: 10.1371/journal.pcbi.1000670. URL: http://dx.plos.org/10.1371/journal.pcbi.1000670.

Nelson, S. B., Sjostrom, P. J., and Turrigiano, G. G. (2002). "Rate and Timing in Cortical Synaptic Plasticity". *Philosophical Transactions of the Royal Society B: Biological Sciences* 357.1428, pp. 1851–1857. DOI: 10.1098/rstb.2002.1162. URL: http://rstb.royalsocietypublishing.org/cgi/doi/10.1098/rstb.2002.1162.

Neves, G., Cooke, S. F., and Bliss, T. V. (2008). "Synaptic Plasticity, Memory and the Hippocampus: A Neural Network Approach to Causality". *Nature Reviews Neuroscience* 9.1, pp. 65–75.

Nevian, T. and Sakmann, B. (2006). "Spine Ca2+ Signaling in Spike-Timing-Dependent Plasticity". *The Journal of Neuroscience* 26.43, pp. 11001–11013. DOI: 10.1523/JNEUROSCI.1749-06.2006. pmid: 17065442. URL: http://www.jneurosci.org/content/26/43/11001.

Okamoto, Y., Morishita, J., Tsuboi, K., Tonai, T., and Ueda, N. (2004). "Molecular Characterization of a Phospholipase D Generating Anandamide and Its Congeners". *Journal of Biological Chemistry* 279.7, pp. 5298–5305. DOI: 10.1074/jbc.M306642200. URL: http://www.jbc.org/cgi/doi/10.1074/jbc.M306642200.

Oliveira, R. F., Kim, M., and Blackwell, K. T. (2012). "Subcellular Location of PKA Controls Striatal Plasticity: Stochastic Simulations in Spiny Dendrites." *PLoS computational biology* 8.2. Ed. by O. Sporns, e1002383–e1002383. DOI: 10.1371/journal.pcbi.1002383. URL: http://dx.plos.org/10.1371/journal.pcbi.1002383.

Packard, M. G. and Knowlton, B. J. (2002). "Learning and Memory Functions of the Basal Ganglia". *Annual review of neuroscience* 25.1, pp. 563–593.

Paille, V., Fino, E., Du, K., Morera-Herreras, T., Perez, S., Kotaleski, J. H., and Venance, L. (2013). "GABAergic Circuits Control Spike-Timing-Dependent Plasticity." *The Journal of neuroscience : the official journal of the Society for Neuroscience* 33.22, pp. 9353–63. DOI:

10.1523/JNEUROSCI.5796-12.2013. URL: http://www.jneurosci.org/content/33/22/9353.full#F3.

Pandas: Python Data Analysis Library (2012). URL: http://pandas.pydata.org/.

Pawlak, V. and Kerr, J. N. D. (2008). "Dopamine Receptor Activation Is Required for Corticostriatal Spike-Timing-Dependent Plasticity." *The Journal of neuroscience : the official journal of the Society for Neuroscience* 28.10, pp. 2435–46. DOI: 10.1523/JNEUROSCI.4402-07.2008. URL: http://www.jneurosci.org/content/28/10/2435.long.

Pedregosa, F., Varoquaux, G., Gramfort, A., Michel, V., Thirion, B., Grisel, O., Blondel, M., Prettenhofer, P., Weiss, R., Dubourg, V., Vanderplas, J., Passos, A., Cournapeau, D., Brucher, M., Perrot, M., and Duchesnay, E. (2011). "Scikit-Learn: Machine Learning in Python". *Journal of Machine Learning Research* 12, pp. 2825–2830.

Piomelli, D. (2003). "The Molecular Logic of Endocannabinoid Signalling". *Nature Reviews Neuroscience* 4.11, pp. 873–884. DOI: 10.1038/nrn1247. URL: http://www.nature.com/doifinder/10.1038/nrn1247.

Puente, N., Cui, Y., Lassalle, O., Lafourcade, M., Georges, F., Venance, L., Grandes, P., and Manzoni, O. J. (2011). "Polymodal Activation of the Endocannabinoid System in the Extended Amygdala". *Nature Neuroscience* 14.12, pp. 1542–1547. DOI: 10.1038/nn.2974. pmid: 22057189.

Rochester, N., Holland, J. H., Haibt, L., and Duda, W. (1956). "Tests on a Cell Assembly Theory of the Action of the Brain, Using a Large Digital Computer". *Information Theory, IRE Transactions on* 2.3, pp. 80–93.

Rosenberger, T. A., Farooqui, A. A., and Horrocks, L. A. (2007). "Bovine Brain Diacylglycerol Lipase: Substrate Specificity and Activation by Cyclic AMP-Dependent Protein Kinase". *Lipids* 42.3, pp. 187–195. DOI: 10.1007/s11745-007-3019-7. URL: http://link.springer.com/10.1007/s11745-007-3019-7.

Rosenblatt, F. (1958). "The Perceptron: A Probabilistic Model for Information Storage and Organization in the Brain." *Psychological Review* 65.6, pp. 386–408. DOI: 10.1037/h0042519. URL: http://content.apa.org/journals/rev/65/6/386.

Rothstein, J. D., Martin, L., Levey, A. I., Dykes-Hoberg, M., Jin, L., Wu, D., Nash, N., and Kuncl, R. W. (1994). "Localization of Neuronal and Glial Glutamate Transporters". *Neuron* 13.3, pp. 713–725. DOI: 10.1016/0896-6273(94)90038-8. URL: http://linkinghub.elsevier.com/retrieve/pii/0896627394900388.

Rubin, J. E. (2005). "Calcium Time Course as a Signal for Spike-Timing-Dependent Plasticity". *Journal of Neurophysiology* 93.5, pp. 2600–2613. DOI: 10.1152/jn.00803.2004. URL: http://jn.physiology.org/cgi/doi/10.1152/jn.00803.2004.

Rutishauser, U., Mamelak, A. N., and Schuman, E. M. (2006). "Single-Trial Learning of Novel Stimuli by Individual Neurons of the Human Hippocampus-Amygdala Complex". *Neuron* 49.6, pp. 805–813. DOI: 10.1016/j.neuron.2006.02.015. URL: http://linkinghub.elsevier.com/retrieve/pii/S0896627306001322.

Sabatini, B. L., Oertner, T. G., and Svoboda, K. (2002). "The Life Cycle of Ca2+ Ions in Dendritic Spines". *Neuron* 33.3, pp. 439–452. DOI: 10.1016/S0896-6273(02)00573-1. URL: http://www.sciencedirect.com/science/article/pii/S0896627302005731.

Saltelli, A., Tarantola, S., Campolongo, F., and Ratto, M. (2002). *Sensitivity Analysis in Practice*. Chichester, UK: John Wiley & Sons, Ltd. URL: http://doi.wiley.com/10.1002/0470870958.

Schultz, W. (2002). "Getting Formal with Dopamine and Reward". *Neuron* 36.2, pp. 241–263. URL: http://www.sciencedirect.com/science/article/pii/S0896627302009674.

Schultz, W., Tremblay, L., and Hollerman, J. R. (2003). "Changes in Behavior-Related Neuronal Activity in the Striatum during Learning". *Trends in Neurosciences* 26.6, pp. 321–328. DOI: 10.1016/S0166-2236(03)00122-X. pmid: 12798602.

Schulz, J. M., Redgrave, P., and Reynolds, J. N. (2010). "Cortico-Striatal Spike-Timing Dependent Plasticity after Activation of Subcortical Pathways". *Frontiers in synaptic neuroscience* 2, p. 23.

Schwartz, B., Colon, M., Sanchez, I., Rodriguez, I., and Evans, S. (2002). "Single-Trial Learning Of "what" and "who" information in a Gorilla (Gorilla Gorilla Gorilla): Implications for Episodic Memory". *Animal Cognition* 5.2, pp. 85–90. DOI: 10.1007/s10071-002-0132-0. URL: http://link.springer.com/10.1007/s10071-002-0132-0.

Sesack, S. R., Aoki, C., and Pickel, V. M. (1994). "Ultrastructural Localization of D2 Receptor-like Immunoreactivity in Midbrain Dopamine Neurons and Their Striatal Targets". *The Journal of neuroscience* 14.1, pp. 88–106.

Shatz, C. J. (1992). "The Developing Brain." *Scientific American* 267.3, pp. 60–7. PMID: 1502524.

Shen, W., Flajolet, M., Greengard, P., and Surmeier, D. J. (2008). "Dichotomous Dopaminergic Control of Striatal Synaptic Plasticity". *Science* 321.5890, pp. 848–851. DOI: 10.1126/science.1160575. URL: http://www.sciencemag.org/cgi/doi/10.1126/science.1160575.

Shouval, H. Z., Bear, M. F., and Cooper, L. N. (2002). "A Unified Model of NMDA Receptor-Dependent Bidirectional Synaptic Plasticity." *Proceedings of the National Academy of Sciences of the United States of America* 99.16, pp. 10831–6. DOI: 10.1073/pnas.152343099. URL: http://www.pnas.org/content/99/16/10831.full.

Shouval, H. Z., Castellani, G. C., Blais, B. S., Yeung, L. C., and Cooper, L. N. (2002). "Converging Evidence for a Simplified Biophysical Model of Synaptic Plasticity." *Biological cybernetics* 87 (5-6), pp. 383–91. DOI: 10.1007/s00422-002-0362-x. PMID: 12461628.

Silva, A. J., Paylor, R., Wehner, J. M., and Tonegawa, S. (1992). "Impaired Spatial Learning in Alpha-Calcium-Calmodulin Kinase II Mutant Mice". *Science* 257.5067, pp. 206–211.

Sjöström, P. J., Turrigiano, G. G., and Nelson, S. B. (2003). "Neocortical LTD via Coincident Activation of Presynaptic NMDA and Cannabinoid Receptors". *Neuron* 39.4, pp. 641–654. pmid: 12925278.

Sjostrom, P., Turrigiano, G., and Nelson, S. (2001). "Rate, Timing, and Cooperativity Jointly Determine Cortical Synaptic Plasticity". *Neuron* 32.6, pp. 1149–64.

Song, S. and Abbott, L. F. (2001). "Cortical Development and Remapping through Spike Timing-Dependent Plasticity". *Neuron* 32.2, pp. 339–350. DOI: 10.1016/S0896-6273(01)00451-2. URL: http://www.sciencedirect.com/science/article/pii/S0896627301004512.

Song, S., Miller, K. D., and Abbott, L. F. (2000). "Competitive Hebbian Learning through Spike-Timing-Dependent Synaptic Plasticity". *Nature Neuroscience* 3.9, pp. 919–926. DOI: 10.1038/78829. URL: http://www.nature.com/neuro/journal/v3/n9/full/nn0900_919.html.

Sprekeler, H., Michaelis, C., and Wiskott, L. (2007). "Slowness: An Objective for Spike-Timing–Dependent Plasticity?" *PLoS Comput Biol* 3.6, e112. DOI: 10.1371/journal.pcbi.0030112. URL: http://dx.doi.org/10.1371/journal.pcbi.0030112.

Squire, L. R., ed. (2008). *Fundamental Neuroscience*. 3rd ed. Amsterdam ; Boston: Elsevier / Academic Press. 1256 pp.

Starowicz, K., Nigam, S., and Di Marzo, V. (2007). "Biochemistry and Pharmacology of Endovanilloids". *Pharmacology & Therapeutics* 114.1, pp. 13–33. DOI: 10.1016/j.pharmthera.2007.01.005. URL: http://linkinghub.elsevier.com/retrieve/pii/S0163725807000186.

Stent, G. S. (1973). "A Physiological Mechanism for Hebb's Postulate of Learning". *Proceedings of the National Academy of Sciences of the United States of America* 70.4, pp. 997–1001. pmid: 4352227.

Sterratt, D., ed. (2011). *Principles of Computational Modelling in Neuroscience*. Cambridge: Cambridge Univ. Press. 390 pp.

Tepper, J. M. and Bolam, J. P. (2004). "Functional Diversity and Specificity of Neostriatal Interneurons". *Current Opinion in Neurobiology* 14.6, pp. 685–692. DOI: 10.1016/j.conb.2004.10.003. URL: http://linkinghub.elsevier.com/retrieve/pii/S0959438804001552.

Tigaret, C. M., Olivo, V., Sadowski, J. H., Ashby, M. C., and Mellor, J. R. (2016). "Coordinated Activation of Distinct Ca2+ Sources and Metabotropic Glutamate Receptors Encodes Hebbian Synaptic Plasticity". *Nature Communications* 7, p. 10289. DOI: 10.1038/ncomms10289. URL: http://www.nature.com/doifinder/10.1038/ncomms10289.

Tsien, J. Z., Huerta, P. T., and Tonegawa, S. (1996). "The Essential Role of Hippocampal CA1 NMDA Receptor–dependent Synaptic Plasticity in Spatial Memory". *Cell* 87.7, pp. 1327–1338.

Tzounopoulos, T., Kim, Y., Oertel, D., and Trussell, L. O. (2004). "Cell-Specific, Spike Timing–dependent Plasticities in the Dorsal Cochlear Nucleus". *Nature Neuroscience* 7.7, pp. 719–725. DOI: 10.1038/nn1272. URL: http://www.nature.com/doifinder/10.1038/nn1272.

Urakubo, H., Honda, M., Froemke, R. C., and Kuroda, S. (2008). "Requirement of an Allosteric Kinetics of NMDA Receptors for Spike Timing-Dependent Plasticity". *Journal of Neuroscience* 28.13, pp. 3310–3323. DOI: 10.1523/JNEUROSCI.0303-08.2008. URL: http://www.jneurosci.org/cgi/doi/10.1523/JNEUROSCI.0303-08.2008.

Valtcheva, S. and Venance, L. (2016). "Astrocytes Gate Hebbian Synaptic Plasticity in the Striatum". *Nature Communications* 7, p. 13845. DOI: 10.1038/ncomms13845. URL: http://www.nature.com/doifinder/10.1038/ncomms13845.

Vilardaga, J.-P., Agnati, L. F., Fuxe, K., and Ciruela, F. (2010). "G-Protein-Coupled Receptor Heteromer Dynamics." *Journal of cell science* 123 (Pt 24), pp. 4215–20. DOI: 10.1242/jcs.063354. URL: http://www.pubmedcentral.nih.gov/articlerender.fcgi?artid=2995613&tool=pmcentrez&rendertype=abstract.

Volkow, N., Fowler, J., Wang, G., Baler, R., and Telang, F. (2009). "Imaging Dopamine's Role in Drug Abuse and Addiction". *Neuropharmacology* 56, pp. 3–8. DOI: 10.1016/j.neuropharm.2008.05.022. URL: http://linkinghub.elsevier.com/retrieve/pii/S0028390808001482.

Wang, H. and Pickel, V. M. (2002). "Dopamine D2 Receptors Are Present in Prefrontal Cortical Afferents and Their Targets in Patches of the Rat Caudate-Putamen Nucleus". *Journal of Comparative Neurology* 442.4, pp. 392–404.

Whitlock, J. R. (2006). "Learning Induces Long-Term Potentiation in the Hippocampus". *Science* 313.5790, pp. 1093–1097. DOI: 10.1126/science.1128134. URL: http://www.sciencemag.org/cgi/doi/10.1126/science.1128134.

Williams, S. R. and Mitchell, S. J. (2008). "Direct Measurement of Somatic Voltage Clamp Errors in Central Neurons". *Nature Neuroscience* 11.7, pp. 790–798. DOI: 10.1038/nn.2137. URL: http://www.nature.com/doifinder/10.1038/nn.2137.

Wittenberg, G. M. and Wang, S. S.-. H. (2006). "Malleability of Spike-Timing-Dependent Plasticity at the CA3-CA1 Synapse". *Journal of Neuroscience* 26.24, pp. 6610–6617. DOI: 10.1523/JNEUROSCI.5388-05.2006. URL: http://www.jneurosci.org/cgi/doi/10.1523/JNEUROSCI.5388-05.2006.

Wolf, J. A., Moyer, J. T., Lazarewicz, M. T., Contreras, D., Benoit-Marand, M., O'Donnell, P., and Finkel, L. H. (2005). "NMDA/AMPA Ratio Impacts State Transitions and Entrainment

to Oscillations in a Computational Model of the Nucleus Accumbens Medium Spiny Projection Neuron." *The Journal of neuroscience : the official journal of the Society for Neuroscience* 25.40, pp. 9080–95. DOI: 10.1523/JNEUROSCI.2220-05.2005. URL: http://www.jneurosci.org/content/25/40/9080.long.

Woodin, M. A., Ganguly, K., and Poo, M.-m. (2003). "Coincident Pre- and Postsynaptic Activity Modifies GABAergic Synapses by Postsynaptic Changes in Cl- Transporter Activity". *Neuron* 39.5, pp. 807–820. DOI: 10.1016/S0896-6273(03)00507-5. URL: http://linkinghub.elsevier.com/retrieve/pii/S0896627303005075.

Yger, M. and Girault, J.-A. (2011). "DARPP-32, Jack of All Trades... Master of Which?" *Frontiers in behavioral neuroscience* 5 (September), pp. 56–56. DOI: 10.3389/fnbeh.2011.00056. URL: http://www.pubmedcentral.nih.gov/articlerender.fcgi?artid=3168893&tool=pmcentrez&rendertype=abstract.

Yin, H. H. and Knowlton, B. J. (2006). "The Role of the Basal Ganglia in Habit Formation." *Nature reviews. Neuroscience* 7.6, pp. 464–76. DOI: 10.1038/nrn1919. PMID: 16715055.

Zhang, L. I., Tao, H. W., Holt, C. E., Harris, W. A., and Poo, M.-m. (1998). "A Critical Window for Cooperation and Competition among Developing Retinotectal Synapses". *Nature* 395.6697, pp. 37–44. DOI: 10.1038/25665. URL: http://dx.doi.org/10.1038/25665.

FOLIO ADMINISTRATIF

THESE DE L'UNIVERSITE DE LYON OPEREE AU SEIN DE L'INSA LYON

NOM : PROKIN
(avec précision du nom de jeune fille, le cas échéant)

DATE de SOUTENANCE : 2/12/2016

Prénoms : ILIA

TITRE :
Synaptic plasticity emerging from chemical reactions: modeling spike-timing dependent plasticity of basal ganglia neurons

NATURE : Doctorat

Numéro d'ordre : AAAALYSEIXXXX

Ecole doctorale : InfoMaths

Spécialité :Informatique

RESUME :

Notre cerveau prend en charge différentes formes d'apprentissage dans ses diverses parties. C'est par exemple le cas des ganglions de la base, un ensemble de noyaux sous-corticaux qui est impliqué dans la sélection de l'action et une forme spécifique de l'apprentissage / mémoire, la mémoire procédurale (mémoire des compétences ou d'expertise). A l'échelle du neurone unique, le support le plus plausible de l'apprentissage et de la mémoire est la plasticité synaptique, le processus par lequel l'efficacité de la communication entre deux neurones change en réponse à un pattern spécifique de conditions environnementales. Parmi les différentes formes de plasticité synaptique, la plasticité dépendante du timing des spikes (STDP) représente le fait que le poids synaptique (l'efficacité de la connexion) change en fonction du temps écoulé entre l'émission des deux potentiels d'action (spikes) présynaptiques et postsynaptiques consécutifs. Si la STDP est une forme de plasticité qui a récemment attiré beaucoup d'intérêt, on ne comprends pas encore comment elle emerge des voies de signalisation / biochimiques qui la sous-tendent. Pour répondre à cette question, nous combinons les approches expérimentales de nos collaborateurs (pharmacologie et électrophysiologie) avec la modélisation de la dynamique des réseaux de signalisation impliquées (décrite par des équations différentielles ordinaires). Après estimation des paramètres, le modèle reproduit la quasi-totalité des données expérimentales, y compris la dépendance de la STDP envers le nombre stimulations pré- et post-synaptiques appariées et son exploration pharmacologique intensive (perturbation des voies de signalisation par des produits chimiques). En outre, contrairement à ce qui était largement admis dans la communauté des neurosciences, notre modèle indique directement que le système endocannabinoïde contrôle les changements du poids synaptique de façon bi-directionnelle (augmentation et diminution). De plus, nous étudions comment une série de facteurs comme la recapture du glutamate régule la STDP. Notre modèle représente une première étape pour l'élucidation de la régulation de l'apprentissage et de la mémoire au niveau du neurone unique dans les ganglions de la base.

MOTS-CLÉS :plasticity, STDP, computational neuroscience, signaling pathways

Laboratoire (s) de recherche :LIRIS

Directeur de thèse:
Hugues BERRY

Président de jury :
Guillaume BESLON

Composition du jury :
KOTALESKI, Jeanette, Docteur, HDR, Institut royal de technologie, Rapporteure
TSANEVA-ATANASOVA, Krasimira, Docteur, HDR Université d'Exeter, Rapporteure
BESLON, Guillaume, D.R.2 LIRIS, INSA-LYON, Examinateur
GRAUPNER, Michael, C.R.1 Université Paris DescartesExaminateur
BERRY, Hugues, D.R.2 INRIA, Directeur de thèse